博士学位論文

動的メッシュ細分化法と反復サブストラクチャー法に基づく大規模熱弾塑性解析

黄　輝

2015 年 12 月

船舶海洋工学コース

地球総合工学専攻

大阪大学大学院工学研究科

Doctoral Dissertation

Large Scale Thermal Elastic-Plastic Analysis Based on Dynamic Mesh Refining Method and Iterative Substructure Method

Hui Huang

December 2015

Department of Naval Architecture and Ocean Engineering
Division of Global Architecture
Graduate School of Engineering, Osaka University

Table of contents

Abstract

In welded structures, deformation and residual stress are inevitable due to the concentrated heat effect. Effective prediction and control of those welding consequences is crucial for ensuring and improving the dimensional accuracy and strength of structures. Transient thermal elastic-plastic FEM which is an accurate numerical method is currently limited to solve small scale problems. Characteristics of welding phenomena is that the strongly nonlinear region is confined in a small area and it moves with the heat source. Also the location of fatigue initiation is limited to area with high stress concentration. Thus it is desirable to employ fine mesh only in these focused areas from computational efficiency point of view. For this, methods such as multi-level refining technique, dynamic mesh refining method and heat transfer localization method are proposed.

Chapter 1 reviews the history of computational welding mechanics and the current stage of numerical methods. The faced problems and challenges for computational welding mechanics are addressed. In addition, the outline of this research is described.

Chapter 2 introduces Multi-Level Refining Technique (MLRT) which allows flexible subdivision in different directions. The continuity of displacement between elements with different level of refinements is maintained with a transformation matrix. The mesh size required for the focused area to ensure accurate thermal analysis is investigated.

Chapter 3 presents the Dynamic Mesh Refining Method (DMRM) which employs locally fine computational mesh and generally fine background mesh. The advantage of this method is that the high resolution is maintained by background mesh and computational efficiency is achieved by computational mesh. Proposed DMRM is applied to fillet welding joint model with more than one million degree of freedom and the computational efficiency is improved by nine times compared to conventional FEM.

In Chapter 4, Heat Transfer Localization Method (HTLM) is proposed as an alternative acceleration method for welding thermal conduction analysis and compared with DMRM. In case of thermal analysis, HTLM is superior to DMRM in saving computing time and memory.

Chapter 5 proposes DMRM* which is a combination of DMRM and existing Iterative Substructure Method (ISM) for further improvement of computational efficiency. In case of pipe-to-flange welding model, it is demonstrated that DMRM* is

over fifty times faster than the commercial code ABAQUS.

Chapter 6 delivers the application of developed methods to large scale practical problems such as plate forming by line heating and manufacturing stiffened structure by welding. The numerical models have more than one million degree of freedom, and time steps are more than ten thousands. The analyses of such large scale problems are all completed in one week using single CPU. The effectiveness and high performance of DMRM and DMRM* are proved through comparison with experimental results.

Chapter 7 shows the application of proposed mesh refining method to fatigue analysis and stress measurement by contour method which requires locally fine mesh. In case of fatigue analysis, relatively coarse mesh used for welding simulation can be employed with local mesh refinement. In the case of contour method, the multi-level refinement technique is employed to generate fine mesh to achieve high resolution.

Chapter 8 summarizes the development and application of proposed numerical methods. The difficulties, pending problems and outlook regarding this research were also addressed.

Chapter 1 Introduction

1.1 Background of computational welding mechanics

Welding has been playing a very important role in manufacturing industry since the major advance of welding technology around 1920s. With the aid of welding, steel structures such as ships and bridges can be easily built in large scales and complex shapes. As a nature of the welding process, the welding distortion and residual stress are usually inevitable due to local shrinkage associated with concentrated heat applied to steel structures. Welding distortion causes misalignment between components to be joined and negatively affect the performance of welded structure. Residual stress has significant influence on the fatigue life of structures, local buckling strength and ultimate strength. Thermal cycles during welding can degrade material property such as fracture toughness greatly. The failure of welded structures are usually found to be consequences of welding induced heat effects. Therefore, it is essential to estimate welding distortion and residual stress in welded structures. For this purpose, the welding mechanics has been developed under the effort of several generations dating from 1930s.

Rosenthal[1] proposed the mathematical model for the quasi-steady state heat conduction during welding and cutting. In his model, the heat source is idealized as a point on the plate surface, and there is no heat transfer on surfaces. Tanaka[2] solved the heat conduction problem by considering the heat transfer which should be included in most welding cases. In 1950s-1960s, analytical solution for heat transfer was derived by Rykalin[3], and temperature field could be calculated for plates with finite thickness. The analytical formulae for welding deformation have been proposed by Okerblom[4] and Vinokurov[5]. Okerblom predicted the shrinkage and deflection of welded beams. He utilized the analytical heat transfer theory of moving heat source to estimate the distribution of thermal stress and strain around the weld.

Later in 1960-70s, numerical methods such as finite difference method[6] and finite element methods[7] have been employed to solve heat conduction problems. In the case of welding simulation, Ueda and Yamakawa[8] established the theoretical formulations and basic computation procedures of general welding mechanics. Nonlinear material properties were numerically modeled in the simulation, and computation of transient temperature field and stress-strain evolution became available from that time. Hibbitt H.D. and Marcal P.V. [9] developed a numerical model for the welding and subsequent loading of a fabricated structure. The temperature dependent material property and deposition process as a contact problem has been modeled in their code. Friedman[10],

Adderson[11] respectively applied the finite element method in solving transient temperature field and residual stress pattern in butt welding joints. Masubuchi[12] conducted comprehensive work related to welding mechanics such as the computer aided analysis of welding induced distortion and fracture.

Interestingly, residual stresses in multi-pass welded plate could be well solved based on the plane strain assumption. Ueda[13] investigated the residual stress in very thick joints induced by multi-pass welding by FEM and experiment. The entire history of welding passes and stress relief annealing has been theoretically analyzed. Rybicki[14][15] analyzed a two-pass girth-butt welded pipe, and good correlation of residual stresses and residual deflections between computation and measurement were observed. Welding crack problem had also received attention from numerical field. Maddox[16] analyzed a semi-elliptical surface crack locating at the fillet weld toe, the shallow crack shapes and welding residual stress were incorporated in the solution. Addersson[17] studied the hot cracking behavior at the end portion of a butt weld. They concluded that, the hot cracks may nucleate at high temperature around 1200℃ due to large transverse tensile strains, and the crack may propagate at a temperature around 400℃, where high transverse tensile stresses arise. Parker[18] reported the calculation of stress intensity factor, crack profiles and fatigue rack growth rates in residual stress fields. Kanninen[19] combined the elastic-plastic fracture mechanics with thermo-mechanical finite element analysis to examine crack growth in the welding induced residual stresses. It was concluded that crack growth in the welds needs to be computed more realistically for more reliable structural integrity assessment.

Before late 1980s, the models were limited to two dimensional cases, welding start and end effect thus cannot be considered. In 1986, three-dimensional model was introduced. Ueda[20] numerically computed the repair welding induced residual stresses by means of 3D nonstationary thermal elastic-plastic FEM analysis. The production mechanism and the distribution characteristic of residual stress has been revealed. Tekriwal[21] employed the finite element program Abaqus to analyze the gas metal arc welding process. The finite element mesh continuously growing in time to accommodate the heat transfer process has been realized in the simulation. Karlson[22] studied the temperatures, stresses and deformations in a single-pass butt-welded pipe with a full three-dimensional finite element model. Low-temperature solid-state phase transformation has been included in the material model to obtain realistic residual stress field.

Since 1990s, computational welding mechanics has been booming with the exponential growth of computer technology. In the past two decades, the thermal elastic-plastic finite element method has been successfully employed in simulation of

welding deformation and residual stress for typical welding joints. Wang[23] discussed about the mechanical behaviors of welded structure, and residual deformation of a compressor under plug welding has been accurately reproduced by simulation. Dean calculated the welding deformation in fillet-welded joint by means of Abaqus and compared with experimental measurements, good agreement has been observed and the distortion mechanism was explained.

Parallel to the development of transient thermo-mechanical simulation, the inherent strain concept was proposed and employed to solve residual stress and welding deformation problems. Fujimoto[24] presented the fundamental theory for the analysis of residual stresses and deformations based on the inherent strain. The concept of inherent stress and inherent deformations were also introduced. Ueda and Fukuda[25] succeeded in measuring three dimensional residual stresses based on the characteristics of distribution of inherent strain. The welding residual stress was estimated by combining physical measurement and FEM computation. Further, the reliability of estimated results were investigated by statistic approach. By extending the inherent strain distribution functions, a series of welding residual stresses problems had been solved (see Hill [26], Ueda and Yuan[27] [28], Nakacho[29], Ma[30]).

Furthermore, Murakawa and Luo[31] investigated the mechanism of inherent strain production, and developed an elastic FEM to predict the welding residual stresses and deformations. It was found that the inherent strain is closely related to the maximum temperature reached in the thermal cycle and the restraint during welding. Wang[32] studied the inherent deformations in thin plates of various material and dimension. The inherent strain concept was extended to inherent deformation[33] and inherent force[34], and these has been employed to build up powerful tools to solve welding deformation problems in the assembly process of structures. For analysis of large welded structures, inherent strain method is a very effective way to compute welding deformation. As typical applications, the structural deformation induced by line heating and welding have been calculated by inherent strain method (see Hata[35], Wang[36] [37]).

As stated in above paragraph, the inherent strain method has been widely accepted as an efficient computation approach for welding deformation. Another typical application of inherent strain concept is the planning of heating plan and prediction of heating deformation in line heating process. Line heating is an important plate forming technique as it can be used to bend flat plates into desired complicated shape. However, perhaps due to the complexity of the process, line heating is still performed by experienced workers in most manufacturing industries such as shipbuilding. Regarding numerical approaches, Moshaiov and W. S. Vorus[38] presented a theory for the thermo-elastic-plastic plate bending, and the difference between plate and beam

bending mechanism was shown. Nomoto[39] proposed a simplified nonlinear elastic model for bending of thick plates, and a simulator was developed. Shin and Moshaiov[40][41] presented a modified strip model for analyzing the line heating of elastic plates and thermal-elastic-plastic plates.

Ueda and Murakawa[42][43][44][45] conducted a series of work on computer-aided planning system for plate bending by line heating process based on the concept of inherent strain. With those knowledge, an automated plate bending system IHI-α had been developed (see Tango[46]). Shin et al.[47][48] also designed an automatic line heating system which included processes such as shell modeling, shell development, heating information computation, and surface comparison. More recently, a fully automated system IHIMU-α for line heating had been developed in IHI[49]. In this system, the heating plan for a target shape could be determined with the aid of inherent strain method. Articulated robots for handling the heating coil, adaptive plate supporting jacks, and a plate turn-over device were also introduced to replace the manual operation.

In general cases, the parallel effect[50], edge effect[51] and overlapping effect[52] between adjacent heating lines influence the accuracy of mechanical model of line heating. And the thick plates differ from thinner plates apparently in aspect of inherent strain distribution. As a straightforward numerical approach, the 3D thermal elastic-plastic finite element method (TEP-FEM) can be utilized to perform a complete simulation considering those effects. Further, TEP-FEM can provide also the information of residual stress which is vital for evaluation of ultimate strength and fatigue strength.

In order to improve the production efficiency and quality of products, it is now gaining more and more attention from engineers who aim to predict and control welding stresses and distortions. The needs for quick estimation or even real-time simulation of large scale welding problems are increasing. For instance, the nuclear plant has many components manufactured from thick plates. Pipe–to-plate joints also exist besides the butt and fillet joint. Generally, a multi-pass welding is necessary to join the different parts (see Mochizuki[53], Brickstad[54], Itoh[55], Maekawa[56]). In the case of ship building, a full simulation of welding process of single block is anticipated to evaluate the assembly deformation and residual stress. Often, the engineers of manufacturing industry aim to minimize the welding distortion by optimizing the assembly sequence or welding condition. Moreover, line heating is now being applied to produce ship hull plates in larger range of plate thickness and dimensions[49]. New technology and algorithm should be provided to fulfill those objectives.

1.2 Current simulation methods related to thermal-mechanical process

Nevertheless, computations with TEP-FEM usually take large amount of time due to the highly nonlinear and transient feature of thermo-mechanical problems. There have been several efforts to enhance the computation performance. This section briefly summarized existing notable works.

Adaptive mesh scheme applied to heat transfer and stress-strain analysis in welding has been reported. Brown[57] developed rezoning and dynamic substructuring technique to perform finite element analysis on laser welding of plate with shell element. L.-E. Lindgren[58] developed an automatic remeshing algorithm based on a graded hexahedral element (**Fig. 1.1**), and successfully performed three-dimensional finite element simulation of electron beam welding of a large copper canister. The element was designed to have variable shape function with different number of nodes. Duranton[59] proposed an adaptive meshing technique to decrease the computation costs when keeping good confidence in the results. The interface between graded elements were constrained using penalty method and Lagrange multiplier method.

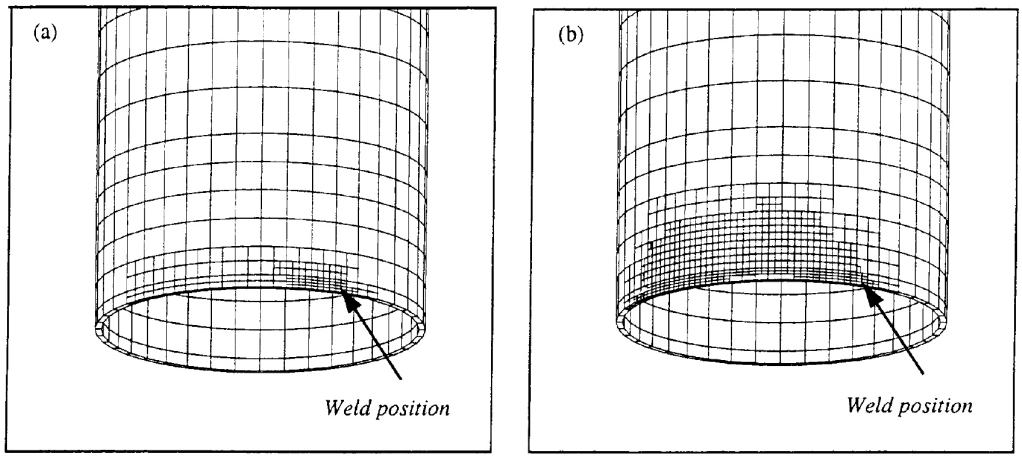

Fig. 1.1 Automatic remeshing: (a) thermal driven scheme (b) stress driven scheme

Goldak[60] created the composite mesh for a pipe welding model (**Fig. 1.2**), in which each mesh part is independent and the continuity of solution across the interface is maintained by constraints. The mesh part for weld was moved with the arc during the welding process. Compared with adaptive mesh, this scheme makes it much easier to modeling the welding structure.

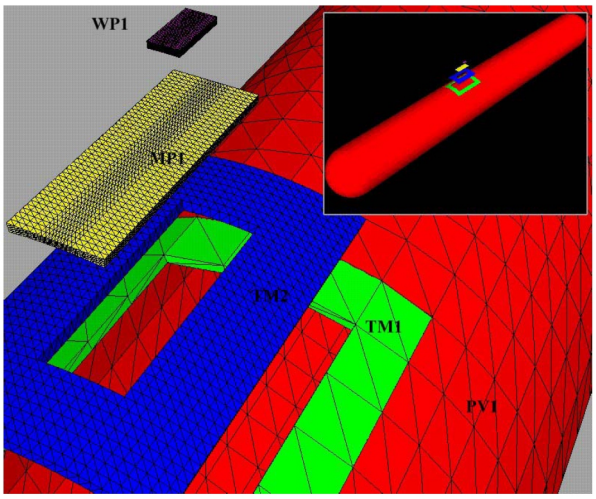

Fig. 1.2 Composite mesh of a welding pipe model

B. Souloumiac[61] developed a new local–global approach in combination with an inherent strain approach for predicting distortions of welded steel component (**Fig. 1.3**). The weld region is represented by a 3D local model assembled within a global shell model. They assumed that the residual plastic strains of the weld only depend on local mechanical and thermal conditions.

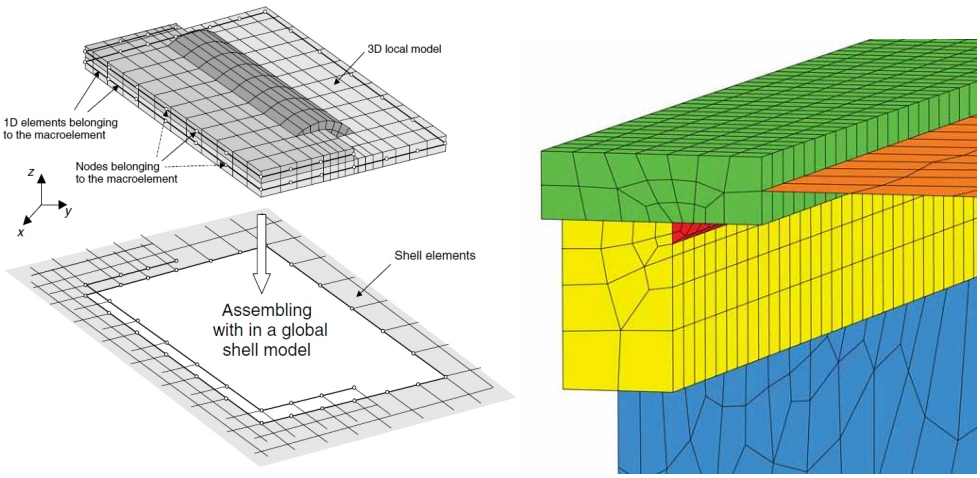

Fig. 1.3 Local-global approach for predicting welding distortion

M. Bellet[62] developed an adaptive mesh technique for thermal–metallurgical numerical simulation of arc welding processes. The refinement employs anisotropic and isotropic pattern with thermal based and combined thermal-metallurgical criterion, as shown in **Fig. 1.4**. In their study, linear tetrahedral elements are used and mechanical analysis is not carried out.

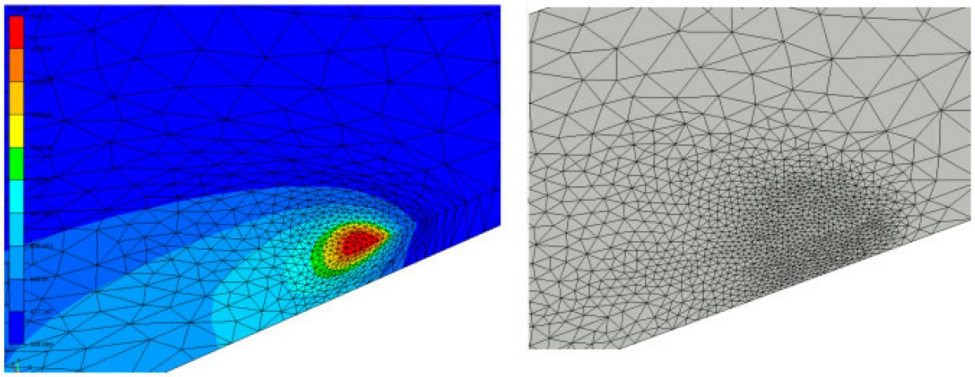

Fig. 1.4 Adaptive mesh with tethedral elements

Iterative substructure method (ISM) is developed by Murakawa[63] from the aspect of partitioning regions with different nonlinearity in the TEP model (**Fig. 1.5**). The regions are separated by setting a temperature limit, plasticity state and radius around heat source. After solving the strongly nonlinear region and weakly nonlinear region separately, the unbalanced force on the boundary will be equilibrated through iterative procedure. Simulations show that it is over 10 times faster than conventional method when the model consists of several hundreds of thousand elements. Hierarchical Multi-Grid Method[64] was combined with the ISM in solving welding problems.

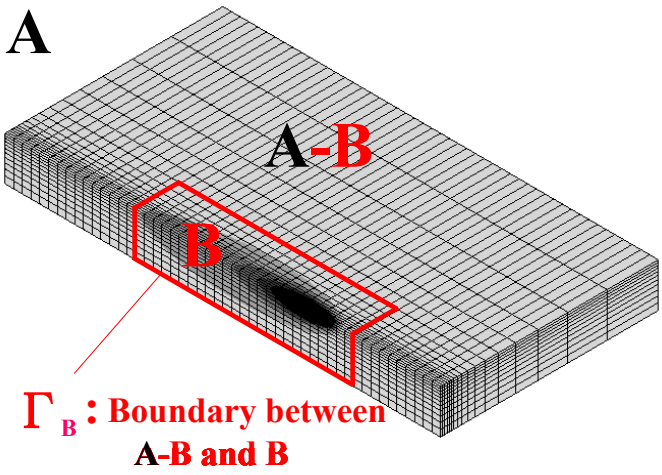

Fig. 1.5 Schematic drawing of regions in ISM: B. Strongly nonlinear region A-B., Weakly nonlinear region

Idealized explicit FEM (IEFEM) proposed by Shibahara[65] deals with welding problems by using dynamic explicit scheme, which allows performing the calculation for each degree of freedom (DOF) and element independently. The concept of the IEFEM was schematically shown in **Fig. 1.6**. Based on the characteristics, the parallelized IEFEM using a graphics processing unit (GPU) were also developed[66]. They have shown the high efficiency and good accuracy of IEFEM by a series of

study.

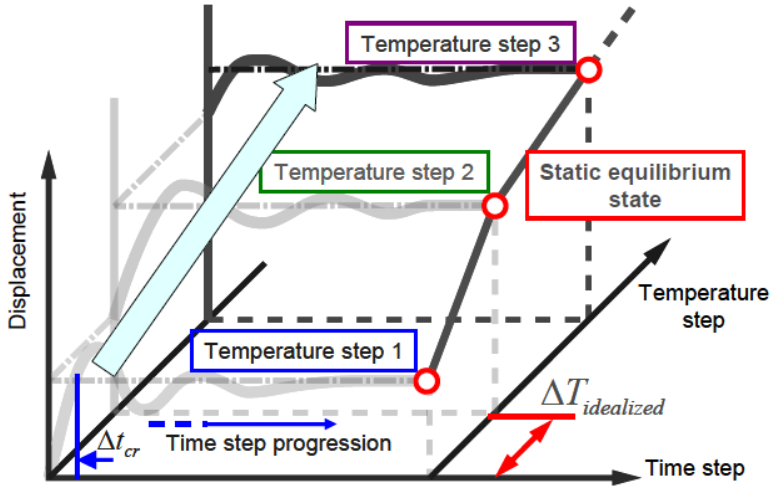

Fig. 1.6 Concept of the Idealized Explicit FEM

1.3 Faced problems and challenges

Due to the complexity of welding process, there are several main challenges in solving practical welding problems by computational welding mechanics. It is natural that model scale in simulation of welding has greatly increased with the aid of computer technology. Nevertheless, simulation on a real large scale welded structure by thermal elastic-plastic FEM is still rather challenging in aspect of computational efficiency and accuracy. The difficulties can be summarized as follows:

(1) ***Material property.***

The welding usually employs a heat source with high flux, which induces large temperature gradient around weld zone. As a result, the material property undergoes a drastic change with temperature. For accurate prediction of welding residual stresses, it is necessary to investigate the material constitutive model at high temperature range[67]. Elaborate measurement should be performed to evaluate the temperature dependent material property of base metal and filler metal. Although some of the tests such as gleeble test can provide some basic data about Young's modules and yield strength at different temperature. However, factors such as strain rate and thermal history all contribute to the variation of material property. Further, the metallurgical process introduces new phase which differs from base material in property. Appropriate mathematical description of the hardening and softening behavior need to be developed. Up until now, the reliable data of many materials remains unavailable.

(2) ***Process uncertainty.***

For accurate simulation of thermal process, exact mathematical modeling of the heat source is indispensable[68][69]. The welding heat input depends on the process parameters such as distance between cathode and work piece, pulse frequency and so on. The heat efficiency is related to heat transfer, radiation and interaction between arc and weld pool. To accurately estimate the value is difficult, thus calibration by penetration shape is usually needed. In prediction of structural welding deformation, there are various influential factors such as gap, misalignment, tack weld, and contact [70]. For thin plates, the initial state of the welding piece such as the geometrical imperfection and residual stress has large influence on the final shape of welded structures.

(3) *Coupled nonlinearity*.

During thermal cycle, several physical fields are usually coupled. Thermal process can strongly affect the phase transformation[71] process of microstructure and mechanical behavior in a macroscopic scale (displacement, stress, strain). The evolution of microstructure can induce latent heat which inversely affect the thermal process. In addition, the volume change due to phase transformation may influence the mechanical process especially stress evolution. The plasticity produced in the mechanical process in turn can provide heat to the thermal process, although this effect is negligible in most welding (one typical exception is friction stir welding). The microstructure evolution such as martensitic and bainitic transformations also depend on the mechanical deformation. A fully coupled thermo-metallurgical-mechanical simulation[72] is necessary to account all the effects, which significantly increase the difficulty in mathematical description and computation cost.

(4) *Computation cost*.

Because of the highly nonlinear behavior and transient phenomenon, the thermal mechanical analysis requires large amount of time and physical memory for large scale welding problems. Still, the analysis for most real scale welded structures is beyond the capability of modern computers in aspect of physical memory and computing time. There are three main reasons for this fact. Firstly, welding is a transient heat transfer process, large heat input is given to very local region, small time increment such as 0.1 sec are required to get smooth temperature field. Secondly, many elements shall be used to construct a finite element model because fine mesh is necessary near welding paths to fit the temperature gradient. Depending on the scale of structure, the total length of weld lines can reach several meters to hundred meters, which will lead to several thousand or even one million of elements and steps. As the third, temperature and stress analysis shows strongly nonlinear phenomenon, material properties such as

thermal capacity and yield strength changes rapidly with temperature. For one single step, many iterations will be used to reach convergence.

(5) *Numerical stability*

As mentioned in (2) *Material property* and (4) *Coupled nonlinearity*, the analysis process exhibits strong nonlinearity when a welding problem is solved in a fully coupled manner. There is a possibility that the analysis diverges if the material model is not carefully dealt with. For example, the curve of material property may not be smooth enough especially at austenite transformation point. In computation of thin-walled structure, the presence of geometrical nonlinearity in addition to material nonlinearity may cause severe numerical instability. Computation cost is increased because of poor convergence. In the current literatures, most of the analysis are carried out in a decoupled or sequentially couple manner for either computation efficiency or numerical stability.

1.4 Objective and outline of this study

The main objective of current research is to develop high performance modeling and solving algorithms for large scale thermal-mechanical problems. The algorithms are designed to be applicable to a wide range of problems, for instance, thick plates by multi-pass welding, thin plate structures with large deformation. Using the proposed methods, the detailed welding distortion and residual stress distribution in large-scale welded structures can be obtained, thus more accurate fatigue analysis and ultimate strength analysis become possible. The computation time and required physical memory of thermal elastic-plastic analysis are compared among different schemes.

Furthermore, this research included the high resolution of local stress concentration and the numerical reproduction of cutting process in contour method. Through combined use of welding simulator, mapping function, local refinement and contour method, the developed code provides an effective tool for accurate measurement of residual stress and efficient assessment of fatigue life in welded structures.

The thesis is organized as follows:

(1) Chapter 1 reviews the history of computational welding mechanics, and the current stage of numerical methods. The faced problems and challenges for computational welding mechanics are addressed. In addition, the outline of this research is listed here.

(2) Chapter 2 introduces a proposed multi-level refining technique (MLRT) which has flexible subdivision in different directions. The mesh size and time increment

required for a welding analysis is investigated, and transformation matrix for stiffness and load is also derived in explicit form.

(3) Chapter 3 presents the proposed dynamic mesh refining method (DMRM) which takes advantage of a background mesh. This chapter also discusses two different schemes about the solution updating on background mesh. The required computation time and physical memory for a thermal elastic-plastic analysis was used as indicators of the performance of numerical schemes. Fillet welding joints in different scales were analyzed by conventional FEM and dynamic mesh refining method, respectively.

(4) Chapter 4 shows the acceleration methods for welding thermal conduction analysis. Heat transfer localization method (HTLM) and dynamic mesh refining method (DMRM) are proposed. The simulation of welding and heating on large scale structures are examined by the two different techniques respectively.

(5) Chapter 5 demonstrates several efficient acceleration methods for welding thermal-mechanical analysis, including proposed inherent strain based iterative substructure method (i-ISM), modified ISM (mod-ISM) and combination of DMRM and ISM (DMRM*). Some comparative study are carried out to highlight the performance of each technique.

(6) Chapter 6 delivers the application of developed techniques to large scale thermal-mechanical problems. The multi-pass welding joint was analyzed by i-ISM, and rectangular plate with multiple heating lines and stiffened plate with fillet welding were analyzed by DMRM and DMRM*, respectively.

(7) Chapter 7 shows the application of mesh refining method in numerical problems of stress concentration and residual stress measurement by contour method. The influence of stress concentration on fatigue life evaluation was clarified numerically. A fatigue life estimation method based on local refinement and mapping solution was proposed. The influence of the position of cutting plane in measuring welding residual stress by conventional contour method is investigated. And a new contour method based on inherent strain was developed.

(8) Chapter 8 summarizes the current work about the development and application of numerical methods. The difficulties, problems and outlook regarding this research were also addressed.

Figure 1.7 schematically show the road map of the current research by highlighting developed numerical methods. Dynamic mesh refining method (DMRM) was focused, and the existing iterative substructure method (ISM) was extended. Thermal and mechanical analysis of welding and line heating were accelerated by various methods, especially the combined ISM and DMRM. Moreover, the heat transfer localization method (HTLM) and inherent strain based ISM were also developed as potential

approaches for further acceleration of DMRM. The fatigue analysis based on mapping of welding residual stress and multi-level refining technique (MLRT) was proposed from the viewpoint of computation efficiency and accuracy. A new contour method based on inherent strain theory was proposed for modeling convenience and a wider applicability.

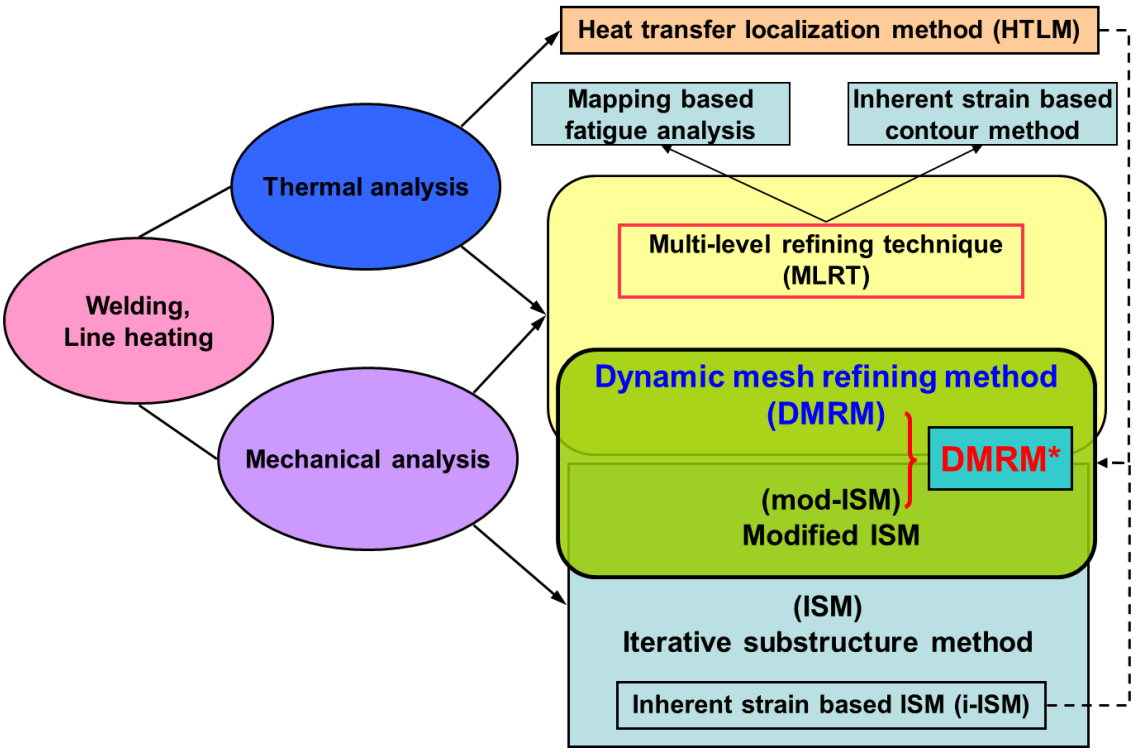

Fig. 1.7 Road map of the proposed numerical methods

Chapter 2 Development of multi-level refining method

Due to steep temperature gradient, the mesh size near the weld line should be small enough compared with the size of heat source model. For practical welded structure, the number of unknown required to describe the mathematical model is usually quite vast, larger than one million for instance. However, most part of the model away from the heat source has small temperature gradient and thus weak nonlinearity. It is a natural thinking to design a refined mesh according to the position of the heat source. In this chapter, the conventional remeshing techniques and new refining method are presented. The multi-level refinement is developed based on node property, and interface between elements at different refining level is connected by transformation matrix. Detailed finite element formulation is shown for thermal analysis and mechanical analysis. The effect of mesh size and time increment on solution accuracy is investigated in order to provide a guide line for modeling.

2.1 Refining techniques

In the finite element analysis, an important step is discretizing an object into finite elements—that is "meshing". For this purpose, numerous algorithms have been developed to generate the mesh automatically, especially for triangular and tetrahedral elements. However, the determination of the parameters in a mesh generation remains a task for the user. From the viewpoint of accuracy and efficiency, the mesh design should be done carefully from various aspects. The first aspect is the selection of element type and order. Compared with tetrahedral elements, hexahedral elements seems to have advantage in solution accuracy and efficiency[73] [74]. As the main merit of tetrahedron, full tetrahedral mesh generation can be easily achieved for arbitrary three-dimensional objects. **Figure. 2.1** shows an example of tetrahedral mesh of plate by friction stir welding[75]. Research on full hexahedral elements generation has shown some progress in the past decade[76][77]. Currently, commercial codes like Hypermesh is capable of meshing typical geometry by function of mapping or projection. For the sake of better solution accuracy in dealing with plasticity, the current research employed the hexahedral element. Higher order elements are preferable in aspect of improving accuracy of solution, but they tend to consume much more computer resources.

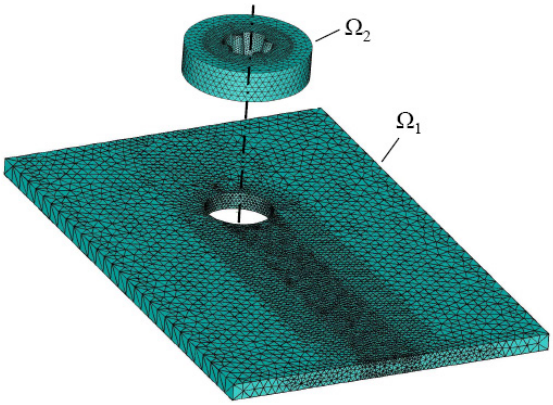

Fig. 2.1 Mesh for friction stir welding using tetrahedral elements

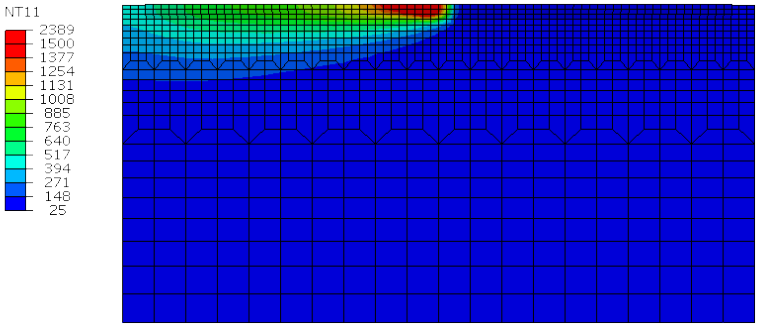

Fig. 2.2 Typical mesh transition using hexahedral elements

The second consideration is the mesh size and pattern. The mesh needs to reflect the geometry shape with enough accuracy. A region with large curvature (hole, etc.) requires dense mesh, which will result in increase of degrees of freedom. Recently, the iso-geometric analysis has been proposed by TJR Hughes[78] based on exact geometric model, and the scheme has shown great potential in optimization of the design and high precision solution. In addition, the mesh division should be able to well describe the stress and strain variation in cases like local stress concentration or singularity[79]. In the case of welding, the mesh is supposed to capture the external heat flux accurately. For instance, the laser beam usually has a diameter less than $1mm$, so element with smaller size should be used to fit the heat source model. Since local region near heat source experiences rapid heating and cooling, a fine mesh needs to be made for the region along the weld line to accurately reproduce the thermal-mechanical behavior (**Fig. 2.2**).

Alternatively, mesh design also depends on the purpose or accuracy needed from the simulation. Shell element, solid element both can be used in numerical analysis of welding and in simple cases they may generate solution with comparable accuracy[80]. If the global structural behavior is of interest, a shell element model could be an economical option while solid model can give local information at the expense of

longer simulation time.

In addition, the decision of mesh pattern relies on the available computer resources and tolerable simulation time. As for large scale models, the simulations usually failed due to limitation of computer memory or extremely long computation time.

As a compromise between efficiency and accuracy, a locally refined mesh is the ideal choice if a large and complex welded structures is to be analyzed. Some commercial software allow user to generate a hybrid mesh consist of different types of elements such as tetahedron, hexahedral and pentahedron. Nevertheless, extensive manual work such as domain decomposition and mesh seeds arrangement are required. In the SimuFact[81], adaptive mesh with non-compatible elements is possible, number of degrees of freedom in the numerical model can be reduced.

Here, a 3D remeshing in the framework of conventional FEM is introduced. Line heating on a rectangular plate was taken as an example. Firstly, it can be recognized that, the mesh of the typical welding joints can be designed with the concept that region near weld line is represented by finer elements and regions away by coarser elements. Thus the plate is roughly divided into three regions: (1) the strongly nonlinear region, (2) weakly nonlinear region and (3) linear region, as shown in **Fig. 2.3**. This is reasonable considering the fact that the metal will cool down to room temperature when the heat source moves away. The first region is represented by a small rectangular area with fine mesh. There are four divisions in the thickness direction but only two for other part around this area. Mesh size of the surface varies from 5mm to 50 mm through the three regions. In the remeshing model, linear iso-parametric hexahedral elements are used for the model to make it easier to setup the finite element model. Coarsening part is controlled by distance from the center of heat source. The process of generating nodes and elements at each stage of remeshing is formulated into a code which takes into account of position and orientation of heat source.

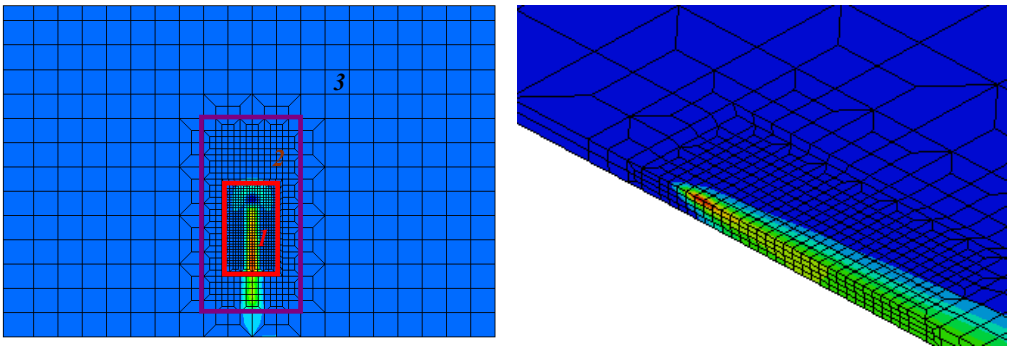

Fig. 2.3 Conventional remeshing method: (a) Mesh scheme for different regions, (b) Mesh pattern of region 1

In this type of refinement, the topology of the mesh changes with the time steps, therefore data must be mapped from the old mesh to the new mesh. For nodal variables such as temperature and displacement, exact data transfer can be accomplished by shape function because the nature of the iso-parametric element. However, for elemental variables such as plastic strain, the distribution does not follow the shape function of element. Inevitably, unexpected numerical error will be induced during the data mapping process. In engineering, the structures to be joined is usually made from many components, and the path of heating or welding lines is usually complicated. It is very difficult to design a mesh with local refinement in three directions. As a result, a mesh with large amount of fine elements would be the choice if the conventional TEP-FEM is employed to simulate the welding process of the structure.

2.2 Proposed multi-level refinement technique

In order to minimize the effort of modeling, mesh refining was developed for 3D thermal mechanical analysis. Hexahedral element was adopted for its robustness in dealing with plasticity. The multi-level refinement was realized with the concept of node property which distinguishes real node and dummy node. Firstly, all nodes in the initial mesh are assigned with real property holding a value of 1. After one level of refinement, the nodes created on the interface between two adjacent elements will have dummy property with a value of 0 if only the element on one side is refined (except for free surface case), as shown in **Fig. 2.4**. Then, for a new level of refinement, the element with all real nodes as shown in **Eq. 2.1** will be refined in order to keep the simplicity of problem. The initial coarse mesh is refined hierarchically based on the region of refinement and size of the element. Flexible refinement in single or multiple directions can be done for better computational efficiency. During the refinement, new nodes are created based on **Eqs. 2.2-2.3**:

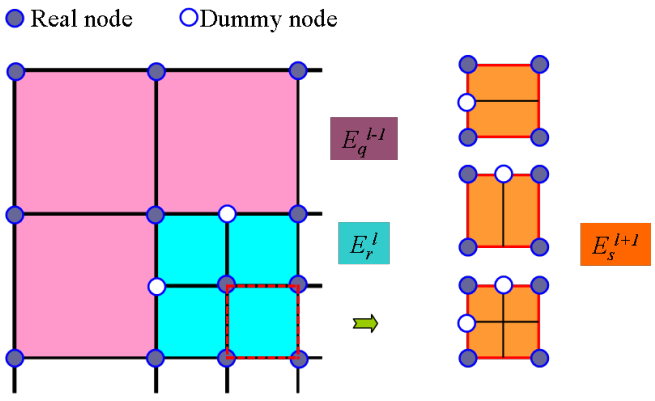

Fig. 2.4 Front view of three-dimensional refinement

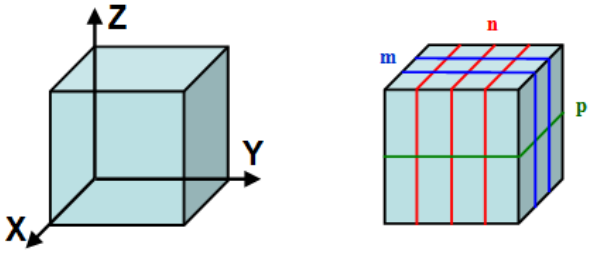

Fig. 2.5 Refinement schemes for a hexahedral element

As shown in **Fig. 2.5**, an orientation-based refinement was designed, so that the element was allowed to be subdivided into different divisions in desired directions. In the present study, the divisions were limited as ($1 \leqslant m,\ n,\ p \leqslant 2$) for simplicity of programming.

$$\forall n_i^r \in E_r^l, \quad p\left(n_i^r\right) = 1 \qquad \left(1 \le i \le 8, 1 \le r \le R_l, 1 \le l \le L\right) \tag{2.1}$$

$$X^m\left(n_j^s\right) = \sum_{i=1}^{8} N_i X^m\left(n_i^r\right) \qquad \left(n_j^s \in E_s^{l+1}, n_i^r \in E_r^l, E_s^{l+1} \subset E_r^l\right) \tag{2.2}$$

$$N_i = \frac{1}{8}\left(1+\xi_i\xi\right)\left(1+\eta_i\eta\right)\left(1+\zeta_i\zeta\right) \tag{2.3}$$

Where, $p(n_i^r)$ denotes the property of a node n_i^r which belongs to element E_r^l . E_r^l is the rth element at level l. R_l is the number of elements at level l, and L is the maximum level exist in the final refined mesh. N_i denotes the i-th component of element (E_r^l) shape function vector by substituting the normalized nodal coordinate of n_j^s (ξ, η, ζ). ξ_i, η_i, ζ_i represents the normalized local coordinates of node n_i^r, and they take a value either -1 or +1. X^m is the component of spatial coordinate at m-direction in global coordinate system.

The interface between a parent element E_p (level l element) and an adjacent child element E_c (level $l+1$ element) is connected through linear constraint relation (See next section **2.3**).

Here, two basic examples are demonstrated. **Figure 2.6** shows a cube been refined at one of its corners. Two levels of refinement were carried out. The minimum element size in three directions became one quarter compared with the coarse elements. This kind of refinement can be readily used for stress concentration problems and heating problems with a stationary heat source, such as spot welding.

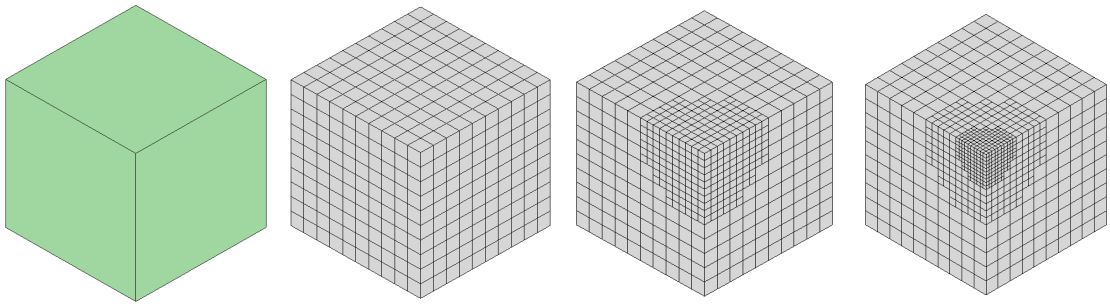

(a) Geometry (b) Coarse mesh (c) 1st level refining (d) 2nd level refining

Fig. 2.6 Refining of a cube at one of its corner

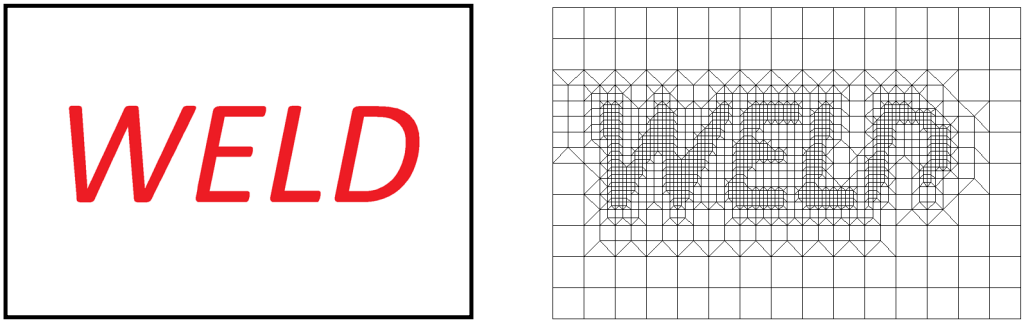

(a) Word 'WELD' on a board (b) Mesh representation

Fig.2.7 Refining around a word "weld"

Figure 2.7 shows the refinement around a word "weld". It should be noted that, the dummy nodes are eliminated, and the element with dummy node are transformed into element with pure real nodes. The refining zone is simply determined by sweep two spheres along the trace of the font. In the following chapters, more detail about refinement control for welding analysis will be discussed.

2.3 Transformation matrix for elemental stiffness and load vector

On the interface between refined element (child element) and non-refined element (adjacent parent element), there will be dummy nodes which are not shared by the two elements. In the studies[59][82], additional constraint equations were introduced in solution with penalty function method or Lagrange multiplier. These solving strategies generally break the symmetric property of global stiffness matrix. For simplicity, an interface between two different graded elements is connected by relating the dummy nodes of the child element to the real nodes of the parent element (**Fig. 2.8**). Similar to the linear constraint, the following transformations are firstly introduced:

$$\bar{u}_i = u(p) = N_j(p) u_j \quad (i, j = 1 \sim 8,\ p \in \Gamma) \tag{2.4}$$

Where, Γ is the interface between the child element and the adjacent parent element. i denotes a dummy node of the child element, and j is a node belonging to the parent element. p denotes a point on the interface Γ and meanwhile taking the same position of node i. Here u_i represents a scalar variable such as temperature value or displacement component in the parent element, and $\bar{u}_j$ is that in the child element. $N_j(p)$ is the jth component of interpolation function vector $\mathbf{N}$ of the refined parent element by evaluating at point p.

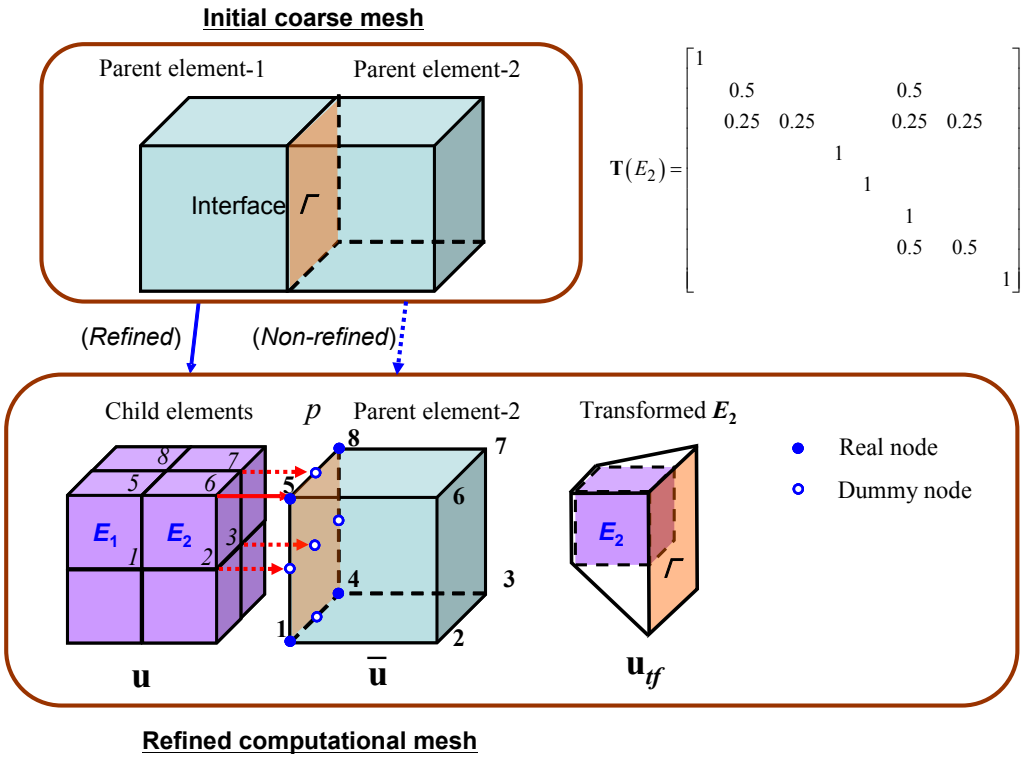

Fig. 2.8 The 3D refinement of element with single nodal degree of freedom

Following **Eq. 2.1**, we can write all nodal variables within a child element in the form of real nodes:

$$\bar{\mathbf{u}} = \mathbf{T}\bar{\mathbf{u}}_{\mathbf{tf}} \tag{2.5}$$

$\bar{\mathbf{u}}$ denotes the nodal variable vector of the child element (with both real and dummy nodes), and $\bar{\mathbf{u}}_{\mathbf{tf}}$ denotes that of the transformed child element (with only real nodes). The element is transformed by mapping dummy node to corresponding real node in the same nodal sequence on interface Γ, as shown in **Fig. 2.8**. $\mathbf{T}$ represents the transformation matrix between $\bar{\mathbf{u}}$ and $\bar{\mathbf{u}}_{\mathbf{tf}}$. It can be easily formed by judging the type (real or dummy) and position of nodes. Transformation matrix $\mathbf{T}$ can

be written into the following form by reference to **Fig. 2.4**:

$$T_{ij}^{T} = \begin{cases} N_i\left(n_j^s\right), \; if \; p\left(n_j^s\right) = 0 \\ \delta_{ij} \; , \; if \; p\left(n_j^s\right) = 1 \end{cases} \qquad \left(n_j^s \in E_s^{l+1}, 1 \le i, j \le 8\right) \tag{2.6}$$

Where, δ_{ij} is the *Kronecker delta*, N_i denotes the i-th component of the parent element E_r^l shape function vector by evaluating at node n_j^s.

To be more precise, the transformation matrix of child element E_2 is demonstrated. For real nodes, the i-th row in **T** matrix takes the corresponding ith row of a unit matrix; while for dummy nodes, the linear constraint relation **Eq. 2.4** can be directly observed. It can be seen from both **Fig. 2.8** and **Eq. 2.6**, there are many zero terms. Vector operation with prior recording positions of non-zero terms should be used to avoid costly matrix multiplication.

Obviously, the ordinary form can be arrived when dummy nodes do not exist in the element such as in element E1. In the finite element equations of thermal conduction and mechanical analysis, the equivalent stiffness matrix and nodal force (heat flux) can be obtained by transformation. The scalar variable $\bar{u}$ and its derivative $D\left(\bar{u}\right)$ at arbitrary position inside original child element can be represented by the following equation:

$$\bar{u} = \mathbf{N}\bar{\mathbf{u}} = \left(\mathbf{NT}\right)\bar{\mathbf{u}}_{\mathbf{tf}} \tag{2.7}$$

$$D\left(\bar{u}\right) = \mathbf{B}\bar{\mathbf{u}} = \left(\mathbf{BT}\right)\bar{\mathbf{u}}_{\mathbf{tf}} \tag{2.8}$$

As shown in above equations, nodal variables on dummy nodes can be eliminated by substituting **N** with **NT** and **B** with **BT** as:

$$\bar{\mathbf{N}} = \mathbf{NT}, \;\; \bar{\mathbf{B}} = \mathbf{BT} \tag{2.9}$$

Therefore, we can rewrite the stiffness matrixes and load vectors in the form of real nodes using relation **Eq. 2.9**. The transformation for heat transfer analysis and thermal-mechanical analysis are described as follows, respectively.

1. Heat transfer analysis

The temperature at position **x** within an element can be written as the interpolation form:

$$T\left(\mathbf{x}, t\right) = N_i\left(\mathbf{x}\right)\varphi_i\left(\mathbf{x}_0, t\right) = \mathbf{N}\boldsymbol{\varphi} \tag{2.10}$$

$$\mathbf{N}=\left[N_1,N_2,\cdots N_i\right],\quad \boldsymbol{\varphi}=\left\{\varphi_1,\varphi_2,\cdots \varphi_i\right\} \tag{2.11}$$

Where, N_i is the i-th component of element shape function vector evaluated at position **x**. φ_i is the temperature value at the i-th node of an element.

The complete finite element equations are summarized as shown in **Eqs. 2.12-2.14**:

$$\left(\mathbf{K}_1+\mathbf{K}_2\right)\boldsymbol{\varphi}+\mathbf{K}_3\dot{\boldsymbol{\varphi}}=\mathbf{Q}_1+\mathbf{Q}_2+\mathbf{Q}_3 \tag{2.12}$$

$$\mathbf{K}_1=\int_\Omega \mathbf{B}^T\lambda\mathbf{B}dV,\quad \mathbf{K}_2=\int_\Gamma \mathbf{N}^T\beta\mathbf{N}dS,\quad \mathbf{K}_3=\int_\Omega \mathbf{N}^T\rho c\mathbf{N}dV \tag{2.13}$$

$$\mathbf{Q}_1=\int_\Omega \mathbf{N}^T q_V dV,\quad \mathbf{Q}_2=\int_\Gamma \mathbf{N}^T q_S dS,\quad \mathbf{Q}_3=\int_\Gamma \mathbf{N}^T\beta T_a dS \tag{2.14}$$

Where $\mathbf{K}_1$ $\mathbf{K}_2$ $\mathbf{K}_3$ are coefficient matrix of heat conduction, heat transfer and heat capacity, respectively. $\mathbf{Q}_1$ $\mathbf{Q}_2$ $\mathbf{Q}_3$ are heat flux vector of volumetric heat source, surface heat source and heat transfer by reference temperature. ρ, c, λ is material density, specific heat and heat conductivity. These material properties are dependent of temperature. q_V is the volumetric heat source term generated by welding torch. q_S is heat flux going out from surface to environment. β is the heat transfer coefficient, T and T_a are current temperature at the point and the ambient temperature, respectively.

We can see that each component in both coefficient matrixes and heat flux vectors has a similar form. Thus, the equation **Eq. 2.9** can be used to transform the original terms of element with dummy nodes into equivalent terms. For instance,

$$\overline{\mathbf{K}}_1=\int_{\Omega^E}\overline{\mathbf{B}}^T\lambda\overline{\mathbf{B}}\,dV=\mathbf{T}^T\left(\int_{\Omega^E}\mathbf{B}^T\lambda\mathbf{B}dV\right)\mathbf{T}=\mathbf{T}^T\mathbf{K}_1\mathbf{T} \tag{2.15}$$

$$\overline{\mathbf{Q}}_1=\int_{\Omega^E}\overline{\mathbf{N}}^T q_V dV=\mathbf{T}^T\int_{\Omega^E}\mathbf{N}^T q_V dV=\mathbf{T}^T\mathbf{Q}_1 \tag{2.16}$$

$\overline{\mathbf{K}}_1$ and $\overline{\mathbf{Q}}_1$ is the equivalent element stiffness and heat flux vector after eliminating dummy nodes. The other items can be transformed in the same manner. It should be noted that, the matrix multiplication generally consumes significant computation time, optimization must be performed to compensate this effect. Since there are many zero elements in the transformation matrix, a local matrix which saves the non-zero elements is defined, so that number of floating point operation can be greatly reduced.

2. Thermal-mechanical analysis

The finite element equations for three dimensional case can be expressed as **Eqs. 2.17-19**: Note that, here **N**, **B** and **T** are the extended version of that in **Eq. 2.9**, since three degree of freedom exist on each node for mechanical analysis. The rank of the matrix is 24.

$$\left(\mathbf{K}^e + \mathbf{K}^p\right)\Delta\mathbf{u} = \Delta\mathbf{f}_s + \Delta\mathbf{f}_v + \Delta\mathbf{f}_t^e + \Delta\mathbf{f}_t^p + \Delta\mathbf{r} \tag{2.17}$$

Or simply $$\mathbf{K}\Delta\mathbf{u} = \Delta\mathbf{f} \tag{2.18}$$

With $$\mathbf{K} = \mathbf{K}^e + \mathbf{K}^p, \quad \Delta\mathbf{f} = \Delta\mathbf{f}_s + \Delta\mathbf{f}_v + \Delta\mathbf{f}_t^e + \Delta\mathbf{f}_t^p + \Delta\mathbf{r} \tag{2.19}$$

Here, **K** is tangential stiffness matrix which depends on the mechanical property and plasticity of the material, and it consists of elastic matrix $\mathbf{K}^e$ and plastic matrix $\mathbf{K}^p$. $\Delta\mathbf{u}$ is the incremental displacement vector and $\Delta\mathbf{f}$ is incremental nodal force vector due to residual stress and temperature increment. The explicit form of each term is given in **Eqs. 2.20-2.23**. In this study, phase transformation and work hardening behavior are currently not considered for simplicity of the problem.

$$\mathbf{K}^e = \int_{\Omega^E} \mathbf{B}^T \mathbf{D}^e \mathbf{B} dV, \quad \mathbf{K}^p = \int_{\Omega^E} \mathbf{B}^T \mathbf{D}^p \mathbf{B} dV \tag{2.20}$$

$$\Delta\mathbf{f}_s = \int_{\Gamma_\sigma^E} \mathbf{N}^T \Delta\mathbf{t} dS, \quad \Delta\mathbf{f}_v = \int_{\Omega^E} \mathbf{N}^T \Delta\mathbf{b} dV \tag{2.21}$$

$$\Delta\mathbf{f}_t^e = \int_{\Omega^E} \mathbf{B}^T \mathbf{D}^e \Delta\boldsymbol{\varepsilon}^t dV, \quad \Delta\mathbf{f}_t^p = \int_{\Omega^E} \mathbf{B}^T \mathbf{D}^p \Delta\boldsymbol{\varepsilon}^t dV \tag{2.22}$$

$$\Delta\mathbf{r} = \int_{\Gamma_\sigma^E} \mathbf{N}^T \mathbf{t} dS + \int_{\Omega^E} \mathbf{N}^T \mathbf{b} dV - \int_{\Omega^E} \mathbf{B}^T \boldsymbol{\sigma} dV \tag{2.23}$$

Where, $\mathbf{D}^e$ and $\mathbf{D}^p$ is elasticity and plasticity matrix for isotropic material, respectively. Ω^E is the domain of an element, and **N** is the matrix of shape function and **B** is the matrix of strain. $\boldsymbol{\sigma}$, $\boldsymbol{\varepsilon}^t$ are tensors of stress, thermal strain respectively. **t** and **b** are vectors of traction force and body force respectively. Since the stiffness terms have similar form, and also the load terms are similar to each other. Here, take the elastic terms of stiffness $\mathbf{K}^e$ and temperature induced load vector $\mathbf{f}_t^e$ as examples, it follows that:

$$\overline{\mathbf{K}}^e = \int_{\Omega^E} \overline{\mathbf{B}}^T \mathbf{D}^e \overline{\mathbf{B}} dV = \mathbf{T}^T \left(\int_{\Omega^E} \mathbf{B}^T \mathbf{D}^e \mathbf{B} dV \right) \mathbf{T} \quad \Rightarrow \quad \overline{\mathbf{K}}^e = \mathbf{T}^T \mathbf{K}^e \mathbf{T} \tag{2.24}$$

$$\Delta\overline{\mathbf{f}}_t^e = \int_{\Omega^E} \overline{\mathbf{B}}^T \mathbf{D}^e \Delta\boldsymbol{\varepsilon}^t dV = \mathbf{T}^T \left(\int_{\Omega^E} \mathbf{B}^T \mathbf{D}^e \Delta\boldsymbol{\varepsilon}^t dV \right) \quad \Rightarrow \quad \Delta\overline{\mathbf{f}}_t^e = \mathbf{T}^T \Delta\mathbf{f}_t^e \tag{2.25}$$

The integration domain does not change so that the original computation procedure of the program can be kept. The other terms such as plastic stiffness have the similar form, and consequently, the incremental force-displacement equation free of dummy nodes can be derived as:

$$\overline{\mathbf{K}}\Delta\overline{\mathbf{u}} = \Delta\overline{\mathbf{f}} \quad \text{with} \quad \overline{\mathbf{K}} = \mathbf{T}^T \mathbf{K} \mathbf{T}, \; \Delta\overline{\mathbf{f}} = \mathbf{T}^T \Delta\mathbf{f} \tag{2.26}$$

2.4 Mesh size and time increment in a thermal analysis

The accuracy of temperature field solved is critical to the evaluation of the penetration shape and stress-strain evolution. Necessary mesh size and time increment should be set to represent heat input correctly during thermal conduction analysis. Generally, suitable parameters for a specific welding model can be achieved through trial-error-trial analysis. However, it seems to be tedious when multiple heat sources with different parameters exist. Especially, the combining effect of the mesh size and time increment can hinder the trial analysis from the reliable solution. To simplify the problem, one dimensional model is considered here, and two dimensional case should have the same conclusion due to the axi-symmetric nature of the heat source. The planar Gaussian distribution is illustrated in **Fig. 2.9** to evaluate the effect of mesh size and time increment on heat input.

As the heat flux is usually calculated by Gauss-Legendre quadrature and then transferred to elemental nodes, the mesh size in the vicinity of heat source is important. Firstly, the ratio of total heat input Q_{num} calculated numerically to that integrated analytically Q_{ana} is defined as R_t which is given as **Eq. 2.27**. In the same way, the ratio of central heat input dQ_{num} (the shadow region in **Fig. 2.9**(a)) calculated numerically to that integrated analytically dQ_{ana} is defined as R_c given by **Eq. 2.28**.

$$R_t = \frac{Q_{num}}{Q_{ana}} = \sum_{i=1}^{\infty}\left(\sum_{j=1}^{n} w_j e^{-3\left(m/r_e\right)^2\left(i+0.5\left(x_j-1\right)\right)^2}\right) \Big/ \int_{-\infty}^{+\infty} e^{-3r^2/r_e^2}\,dr \tag{2.27}$$

$$R_c = \frac{dQ_{num}}{dQ_{ana}} = m e^{-3\left(m/r_e\right)^2\left(x_2-1\right)^2/4} \Big/ \int_{0}^{m/2} e^{-3r^2/r_e^2}\,dr \tag{2.28}$$

Where, m denotes the mesh size and r_e denotes the characteristic radius of heat source, n denotes the number of integration points within one element, w_j is the weight, and x_j is the position of integration point j. An one-dimensional estimation of the ratios defined here was computed with n=2, w_j=1 and x_j=$(-1)^j$*0.57735. R_c can be deemed as the accuracy of local heat distribution.

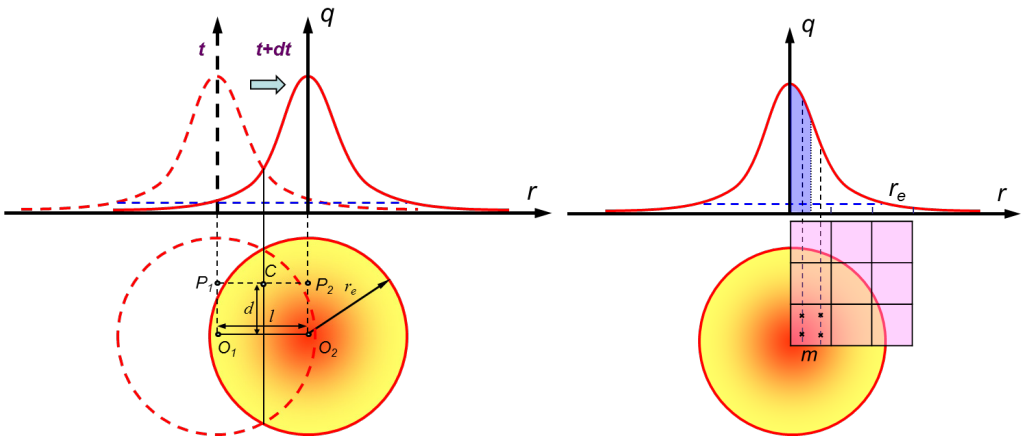

(a) (b)

Fig. 2.9 Estimation of mesh size and time increment: (a) Mesh size effect (b) Time increment effect

Figure 2.10 summarized the influence of mesh size on heat input. It can be concluded that, the total heat input conserves if m/r_e is less than 0.7, while a 5% error can still be found for the central heat input. By relating R_c to m, an exponential approximation for the mesh size can be obtained as:

$$m = r_e\sqrt{10\ln R_c} \quad (R_c \geq 1.0) \tag{2.29}$$

For a tolerance of 2% (R=1.02), it can be calculated that m=0.445 r_e, and similarly 1% (R=1.01), for m=0.315r_e. Based on **Eq. 2.29**, the mesh size can be determined from solution accuracy desired and computer resources in-hand, since the mesh size can greatly affect the scale of FEM model to be solved.

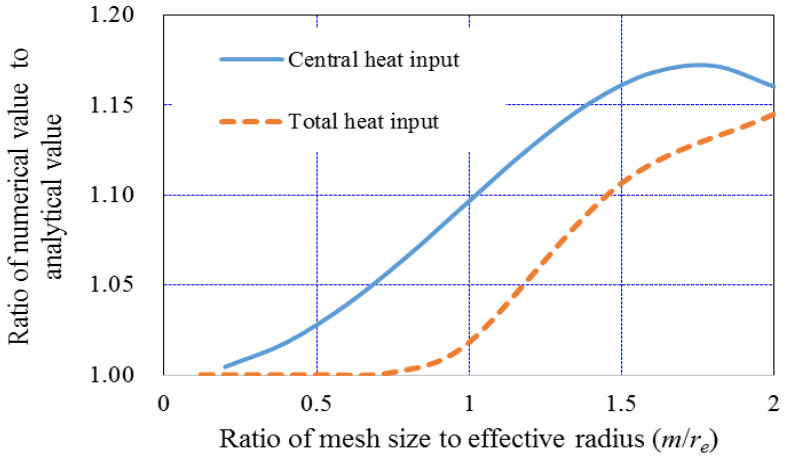

Fig. 2.10 Influence of mesh size on heat input

For the time increment dt, the resultant heat flux for successive time steps (-N, …,

0, …, *N*) are examined, and two adjacent time steps 0 and 1 are schematically shown in **Fig. 2.9**(b). In reality, the heat source moves continuously along the welding direction, thus heat will be deposited uniformly to each position on a fixed curve parallel to weld line. From this viewpoint, it is required that any heating surface on the welding path should get equivalent heat input during welding. In the estimation of maximum *dt*, the heat source is assumed to move $l=v*dt$. Obviously, the surfaces in the vicinity of three points P_1, C, P_2 should gain the same heat input during the whole welding process, so the following equation holds,

$$\sum_{i=-N}^{N} e^{-3\left(d^2+i^2l^2\right)/r_e^2} = 2\sum_{i=0}^{N} e^{-3\left(d^2+l^2/4+i^2l^2\right)/r_e^2} \tag{2.30}$$

It can be obtained for the critical length of l by solving the higher order nonhomogeneous equation by setting N=2, that

$$l \approx 0.9r_e \tag{2.31}$$

$$dt_{\max} = l / v = 0.9r_e / v \tag{2.32}$$

Interestingly, d can take an arbitrary value in this case, that means, all positions along the same line parallel to weld line have the same heat input during the whole time history if **Eq. 2.32** is satisfied.

The laser beam welding on two stainless plates was employed to numerically validate the equations. The thickness of the plates were both 1.33mm, and laser scanning speed were 1.2m/min and 2.0m/min, respectively. The power of laser is 1600W.

A moving heat source model is necessary to describe the time and space dependent heat flux. In the present study, a combined surface heat source and volumetric heat source[83] in Gaussian functions were adopted in the computation of transient temperature (**Fig. 2.11**). The heat flux for the two heat sources are described by the following equations:

$$q_S = \frac{3\eta_S Q}{\pi r_e^2} e^{-3\left[(x-x_0)^2+(y-y_0)^2\right]/r_e^2} \tag{2.33}$$

$$q_V = \frac{3\eta_V Q a}{\pi r_e^2\left(1-e^{-aT}\right)} e^{-3\left[(x-x_0)^2+(y-y_0)^2\right]/r_e^2} e^{-a(z-z_0)} \tag{2.34}$$

Where Q denotes the nominal laser power, η_s and η_v denotes the fractions of heat deposited in the surface heat source and volumetric heat source, respectively. x, y, z are global coordinates in three directions for a point where heat flux is to be evaluated, and x_0, y_0, z_0 are coordinates of heat source center at the current time. For the two heat sources, r_e is the effective radius on which heat flux is approximately 5% of that at the center of heat source, it is deemed as the same here. For the volumetric heat source q_v, a is the attenuation parameter which describes the variation of heat flux through plate thickness direction. In the case of full penetration, a large value of a can be used to model a relatively uniform distribution of heat flux in z direction. In the present study, the total laser absorptivity is defined as $\eta_s+\eta_v=0.32$ for each specimen after fitting the heat source model.

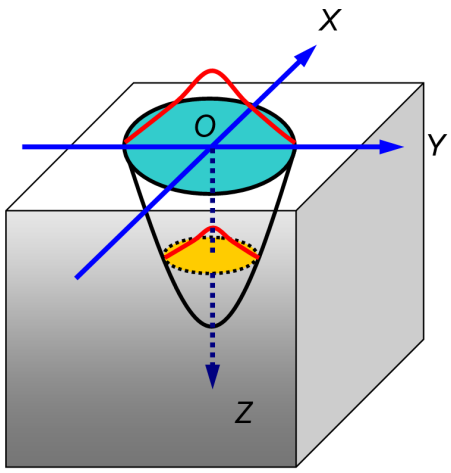

Fig. 2.11 Schematic drawing of heat source model for laser welding

Several thermal conduction computations were performed on a short model with welding length 10mm and scanning speed 2 m/min to investigate the influence of mesh size and time increment numerically. The transient (t=0.15s) temperature distribution on plate surface along transverse direction (X＝5mm) is plot in **Fig. 2.12**. It clearly shows that, reached maximum temperature is high when mesh size is large, which is the result of overestimation of central heat input. The difference gradually becomes smaller as mesh size decreases. In the case of $m=0.31r_e$, the error of peak temperature is about 1.5%, which is in accordance with estimation using **Eq. 2.29**. In the following computations, the mesh size is fixed as $m=0.21r_e$ for the purpose of high accuracy.

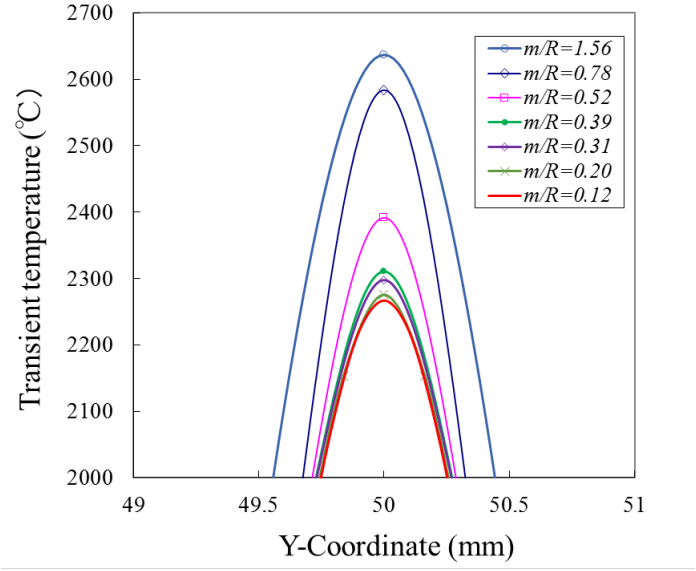

Fig. 2.12 Influence of mesh size '*m*' on transient temperature distribution

Figure 2.13 shows the transient (t=0.15s) temperature on plate surface along longitudinal direction (weld line). The dependence of peak temperature on time increment *dt* was found to be quite strong, and severe oscillation can be observed when *dt* is relatively large. For the estimated value of dt_{max} =0.0216s using **Eq. 2.32**, the related temperature profile will lay between the smooth and oscillatory profile predicted by *dt*=0.015s and *dt*=0.025s respectively. The coupling effect between mesh size and time increment is a reason for this phenomenon. dt=0.2~0.5*dt_{max} is recommended as the proper value of time increment, and the computations in the following sections were carried out with *dt*=0.01*s*.

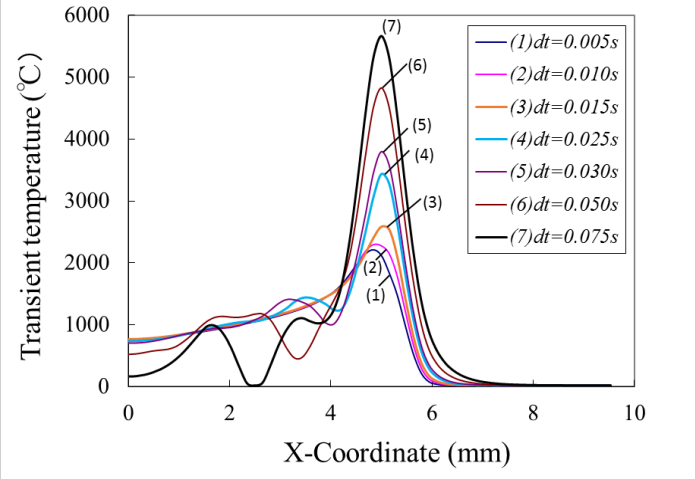

Fig. 2.13 Influence of time increment '*dt*' on transient temperature distribution

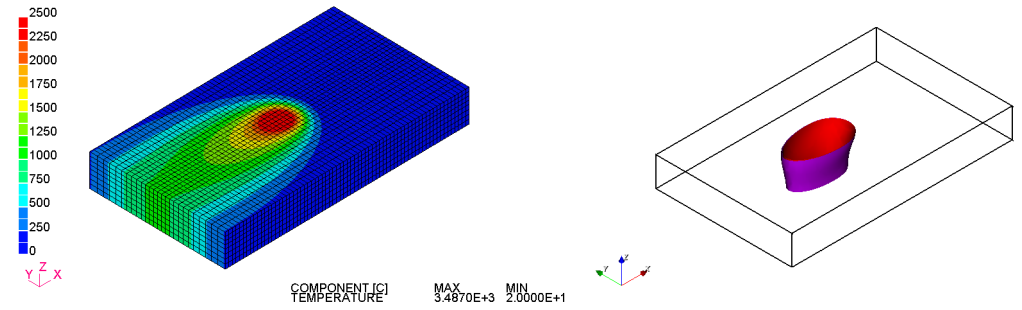

(a)

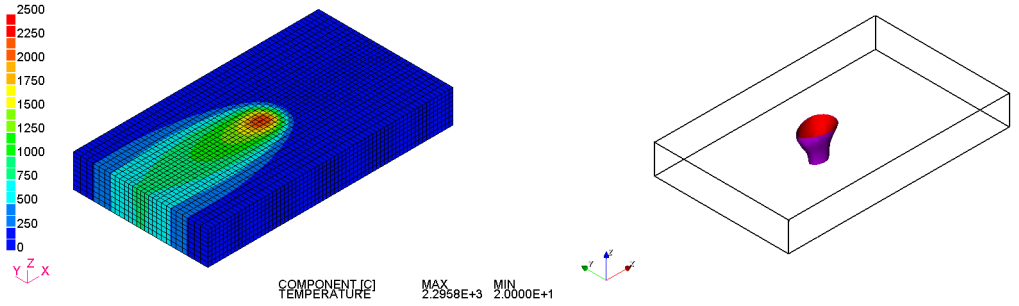

(b)

Fig. 2.14 Transient temperature distribution and molten pool: (a) v=1.2m/min (b) v=2.0m/min

The temperature field and molten pool when the laser beam scanned 5mm are plotted in **Fig. 2.14** for the two cases with different welding speed. It can be seen that, the region near heat source has steep temperature gradient, while the rear part showed relatively uniform distribution. The molten pool in the case of v=1.2m/min has larger size in both length and width than v=2.0m/min. For each model, the computed penetration is shown in **Fig. 2.15** in comparison with macrograph. The accuracy of heat source model and thermal analysis can be confirmed.

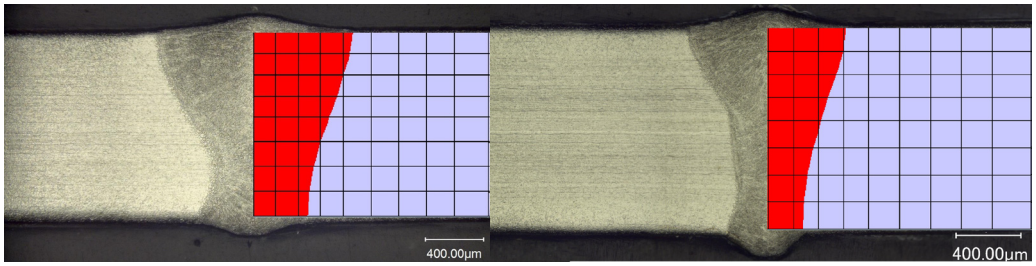

(a) (b)

Fig. 2.15 A comparison between experimental macrostructure and predicted penetration shape: (a) v=1.2m/min (b) v=2.0m/min

2.5 Summary

The refining techniques including general remeshing method, tetrahedral and hexahedral mesh generation, and special requirements in welding analysis were discussed. In order to minimize the modeling effort, the multi-level refinement based on real and dummy node property was proposed. An initial coarse mesh can be refined in hierarchical mode until desired levels. As another merit of this refining method, flexible refinement in single or multiple directions is allowed. It can be used for finite element model with small strain and finite rotation, since the topology of the mesh structure is not changed.

The interface between elements at different levels is connected through linear constraint. Different from penalty method and method of Langrange multiplier, direct finite element formulation of the linear constraint was realized by transformation matrix. The equivalent element stiffness matrix and load vector has been derived for both thermal analysis and mechanical analysis. The benefit of introducing such a transformation is keeping the structure of original program with minimum change. The reduction in solution cost can be anticipated since much fewer unknowns is needed for a model.

The mesh size and time increment for a thermal-mechanical analysis was investigated based on heat source characteristic. Conservation of heat input in global and local region was used to define parameters representing the quality of the heat input model with given mesh size and time increment. These simple parameters can serve as a guideline in mesh generation for analysis of welding problems. Numerical analysis of laser welding on thin sheets was carried out to validate the proposed parameters.

Chapter 3 Dynamic mesh refining method for welding simulation

Since the welding and heating process such as line heating utilizes a moving heat source, the mesh should be dynamically refined to reduce the number of degrees of freedom. As mentioned in the introduction of this thesis, several remeshing methods were proposed[93]. These schemes use mapping technique to transfer data from old mesh to new mesh, which generally introduced irreversible error for plastic problems. In this chapter, a new approach-dynamic mesh refining method, with the feature of maintaining high accuracy in stresses and strains, is presented. The refined fine and coarse mesh is termed as computational mesh (CM). A background mesh (BM) with fine elements near the weld is designed in addition to computational mesh, the solution is book kept and updated on this mesh if necessary.

Operation on the background mesh is crucial to computation accuracy and efficiency, since detailed information such as stress and strain are stored on it. Two different schemes in updating solution on background mesh are proposed considering the characteristics of welding problems. In the first scheme, stiffness matrix and load vector are always assembled and solved on the computational mesh, and solutions are just recorded on background mesh. Integration of elemental stiffness and load vector are carried out in different reduced schemes for elements at different level. Both computation time and required physical memory are reduced. In the second scheme, both global stiffness and load are assembled and solved on background mesh. The uniform reduced integration can be applied for elements at different level. Thus computation on mesh with multi-level refinement can be done without convergence and accuracy problem at the cost of computer memory. In this chapter, the computation flowchart and performance of each scheme is shown and discussed. Several numerical examples of typical thermal analysis and mechanical analysis are shown to verify the accuracy and efficiency of dynamic mesh refining method.

3.1 Computation flowchart and refinement control

The computation flow of dynamic mesh refining method (DMRM) is schematically shown in **Fig. 3.1**. Thermal mechanical analysis in sequentially coupled mode is employed. Initially, a coarse mesh is prepared for refinement, and the parameters for welding condition and solution control are defined as the input data.

The first module is mesh refinement for the current time step. Computational mesh and background mesh are created, and the relations regarding nodes and elements between the two meshes are established. A specific time interval determines the frequency to redefine the mesh. The interval should be designed from the view point of computational accuracy and efficiency. Relatively larger interval of refinement will

lead to more elements in the refined mesh and also lose accuracy by not updating solution on background mesh in time, while smaller one may result in slow computation speed due to frequently feedback on background mesh.

Secondly, the thermal conduction analysis is performed on computational mesh. Heat flux on elements is determined based on relative position with respect to the heat source. Node corresponding relation is necessary to map initial temperature from previous mesh to the current one. Temperature data for each node at every time step is written on a file, which will be read by mechanical analysis as thermal load. Here, temperature at the final step is transferred to background mesh for the purpose of bookkeeping.

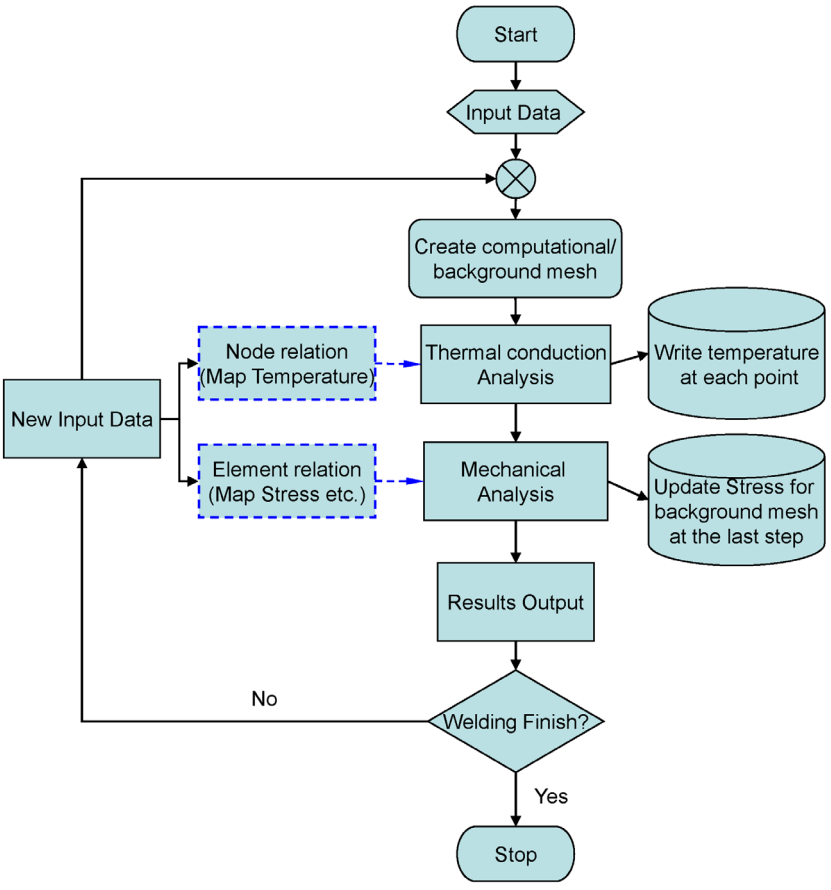

Fig. 3.1 Computation flowchart of dynamic mesh refining method

Thirdly, mechanical analysis is performed on computational mesh with the previously solved results as the initial condition. The number of analysis steps is automatically controlled by the temperature increment and maximum value allowed in one step. At the end of each time interval for mesh refinement, nodal forces and element stiffness matrix for computational mesh are assembled from background mesh. In the current study, the stress and strain for parent elements are obtained by averaging

that from their children elements. Solutions are updated and saved on background mesh as the input for subsequent analysis. After numerical results are output, it is necessary to judge if all welding lines have been finished by setting a global variable in the program. If the variable indicates the end, then the simulation will be terminated. Otherwise, the analysis will continue by returning to the beginning of the loop.

As the refining process costs non-negligible time compared with single step thermo-mechanical analysis. It is not efficient to generate a new mesh every time step. Instead, the coarse mesh is refined at the beginning of a time interval (time steps for refining Nr). **Table 3.1** shows the detailed information about each process at different time steps. More details about updating stress and strain, communication between computational mesh and background mesh are presented at the following sections.

Table 3.1 Operation on various meshes during thermal-mechanical analysis

Process	***Mesh***	***Time step***								
		1	**2**	**…**	**Nr**	**Nr+1**	**Nr+2**	**…**	**Nr+Nr**	**…**
Refinement	Initial mesh	R				R				
Thermal analysis	Computational mesh	T	T	T	T	T	T	T	T	
Mechanical analysis	Computational mesh	MC	C	C		MC	C	C		
	Background mesh				B				B	

R — Perform mesh refinement

T — Solve nodal temperature, interpolate results on background mesh

MC — Form stiffness matrix, map solution, solve stress/strain

C — Solve stress/strain, interpolate nodal variable on background mesh

B — Save (and solve) stress/strain, average stress/strain for coarse element

For welding and line heating problems, the main source of nonlinearity is plasticity due to thermal cycles, for which analytical solution can be approximately calculated. Meanwhile, the background mesh contributes in global equilibrium by correcting stress and strain in elements as long as displacement field has been obtained with high accuracy on the computational mesh. In this study, a simple refinement control is employed for the sake of fast computation with good accuracy. The elements to be refined for computational mesh were determined by sweeping a sphere along the welding path (**Fig. 3.2**). Two parameters namely radius of the sphere R and sweeping length L were defined for the analysis.

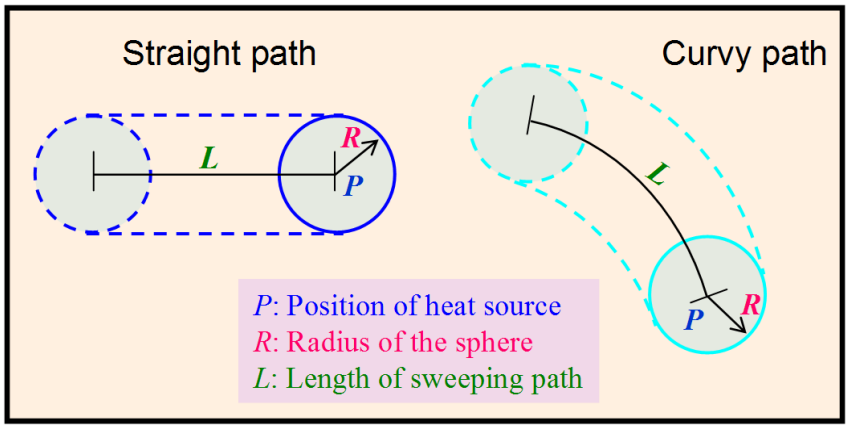

Fig. 3.2 Schematic drawing of mesh refinement control

Analytical form of the temperature distribution at quasi-steady state[93] was estimated by using **Eq. 3.1**. Although, the equation is derived from finite thickness plate with heating torch traveling along a straight path, it can also be applied in curvy path because traveling path is the key point for the refinement.

$$T = \sum_{i=1}^{N} \frac{Q}{2\pi\lambda R_i} \exp\left(-\frac{V(x_i + R_i)}{2a}\right) \tag{3.1}$$

In the above equation, λ is thermal conductivity and a is thermal diffusivity, they are assumed to be constants. Q is the net heat input, V is the travelling velocity of heat source. N denotes the number of periodically repeated layers. x_i is x coordinate of estimated point and R_i is distance from that point to center of heat source with respect to the ith layer.

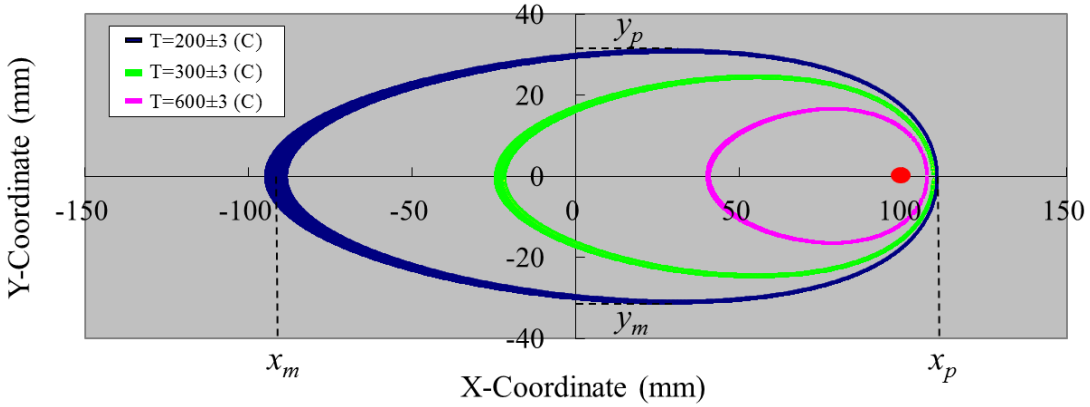

Fig. 3.3 Temperature contours depicted by analytical equation

The contours of temperature determined from **Eq. 3.1** is used to define R and L. With a predefined temperature value T_0, the points which have value close to T_0 can be sampled in the 2D space. As illustrated in **Fig. 3.3**, the points are searched for three temperature contours with a tolerance of $\pm 3℃$ on the x-y plane. It can be seen that the region near the heat source has steeper temperature gradient while the rear part

has smoother distribution as indicated by the band width of temperature distribution. By measuring the width and length of preferred temperature profile, the initial length L_0 and initial radius R_0 are obtained as (x_p - x_m) and (y_p - y_m)/2 respectively, as shown in **Fig. 3.3**. Then the initial values can be multiplied with a scaling factor to meet the requirement of non-uniform stress distribution at the front part of heat source as shown in **Eq. 3.2**. The scaling is conducted by considering effect of plasticity at rear part which is still under thermal load.

$$\begin{aligned} L &= f_L * (x_p - x_m) \\ R &= f_R * (y_p - y_m)/2 \end{aligned} \tag{3.2}$$

Where, f_L , f_R denotes the scaling factors of length and radius, respectively. In the following sections, refining process is operated with T_0 as 170 Celsius, scaling factors 3.0 for the radius, 1.0 for the length.

3.2 DMRM-1—Background mesh used for bookkeeping stress and strain

Figure 3.4 shows the sector graph of computation time in the case of a thermal-mechanical simulation with matrix solver Intel MKL PARDISO. Although advanced sparse linear solver was used, solving simultaneous equations dominates the whole analysis process. It is worth noting that, the cost of computing stress and strain (here called update solution), and factorization of stiffness matrix takes up around one quarter of total computation time, respectively.

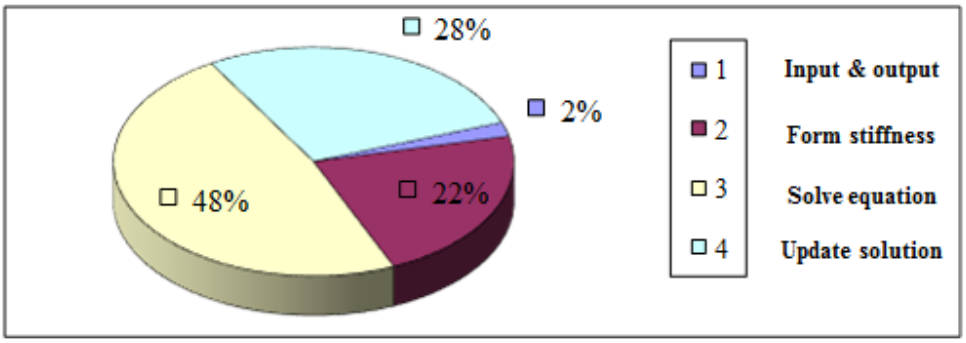

Fig. 3.4 Computation time consumed by a thermal-mechanical analysis using PARDISO

In the framework of DMRM, the number of DOFs in computational mesh is significantly fewer than that in background mesh. If the stress and strain is recorded on background mesh, and solution is always performed on computational mesh, the computation time can be largely reduced. For this purpose, several schemes have been tried as shown in **Table 3.2**.

Table 3.2 Various schemes for solving on computational mesh

Scheme	*Stiffness*	*Load*	*Convergence*	*Result*	*Reason*
I	CM	CM	Yes	Accurate	Consistent
II	BM→CM	BM→CM	Yes/No	Reducing Dependent	Inconsistent
III	CM	BM→CM	No	Not available	Inconsistent
IV	BM→CM	CM	No	Not available	Inconsistent

Where, CM denotes the computational mesh, BM denotes the background mesh, BM→CM means the stiffness or load are assembled from background mesh to computational mesh. It is clear that, the inconsistence between stiffness and load hinders the schemes III-IV to work for direct solution using computational mesh. In addition, the accuracy of scheme II shows some dependence on reduced integration which is important for plastic problem. The concept of reduced integration in Joining and Welding Research Institute ANalysis (JWRIAN) code is schematically shown in **Fig. 3.5**:

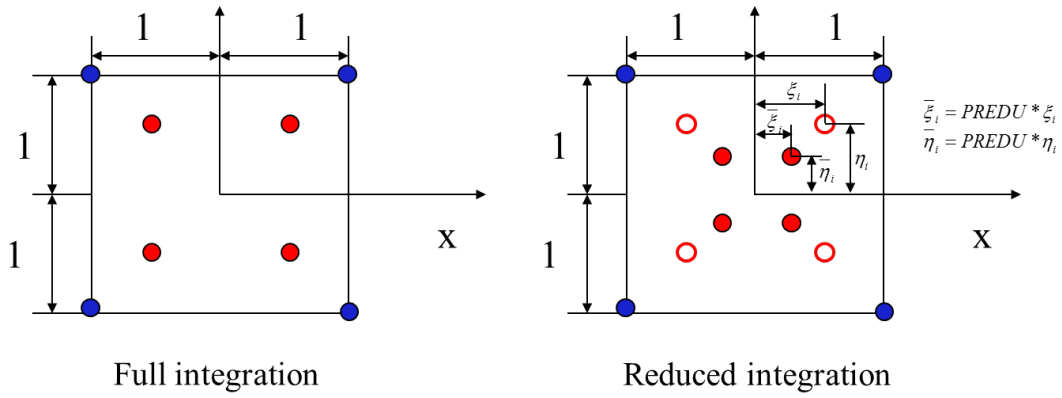

Fig 3.5 Integration schemes in JWRIAN

Different from one point integration, the second order integration points are still used, but they are moved towards the position of first order integration point (or element center). This integration can reduce the stiffness of the element and prevents the hourglass mode. As shown in **Fig. 3.5**, the parameter PREDU is called the reducing factor. In the case of normal thermal elastic-plastic analysis, PREDU takes a value around 0.1-0.2 which can ensure the solution accuracy. When stiffness or load of child elements in BM are calculated by reduced integration and then transformed to CM, it is equivalent to integrate the terms on the parent element in CM by full integration. Therefore, the hybrid integration using scheme II is potential to fulfill the consistence condition and make the analysis stable.

3.3 DMRM-2—Background mesh used for solving global simultaneous equations

The above hybrid integration scheme has advantage in saving computation time and physical memory, since the simultaneous equations are always solved on computational mesh. However, it has the disadvantage that, mesh refinement is limited to one finer level due to the integration. For large scale structure, the acceleration of computation can be further improved by reducing number of DOFs. In order to extend the mesh refinement to multiple levels, another alternative scheme was proposed. Besides the solution on computational mesh, the background mesh is also used to form global stiffness and solve equations. **Figure 3.6** depicts the communication between refined computational mesh and background mesh. For DMRM-2, the results solved by computational mesh is passed to background mesh as an approximation. Global equilibrium is carried out, and then corrected solution is feedback to computational mesh for the next step of analysis. In this calculation mode, the multi-level refinement and the same reduced integration can be used without any inconsistence problem.

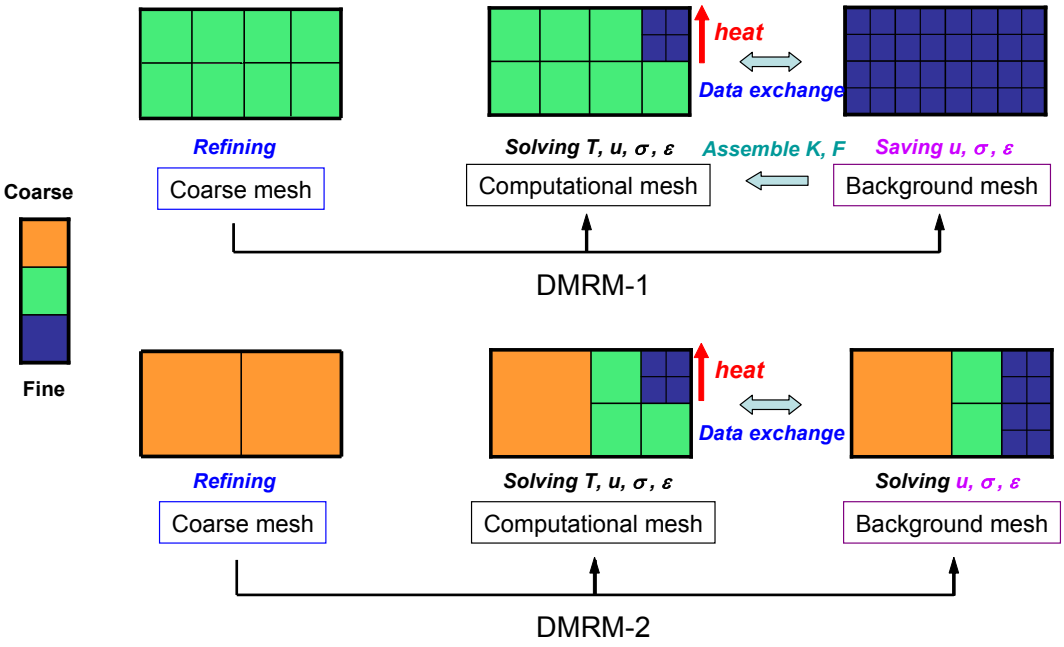

Fig. 3.6 Comparison of solution updating schemes in dynamic mesh refining method

Figure 3.7 shows the operations on background mesh under the framework of DMRM-2. Different from single level refinement, multi-level refinement may generate large number of elements. It is necessary to measure the maximum number of elements and nodes of the model, then allocate the memory for related arrays. Currently, refinement on initial coarse mesh by looping all welding/heating lines is carried out to form background mesh at the beginning of numerical analysis.

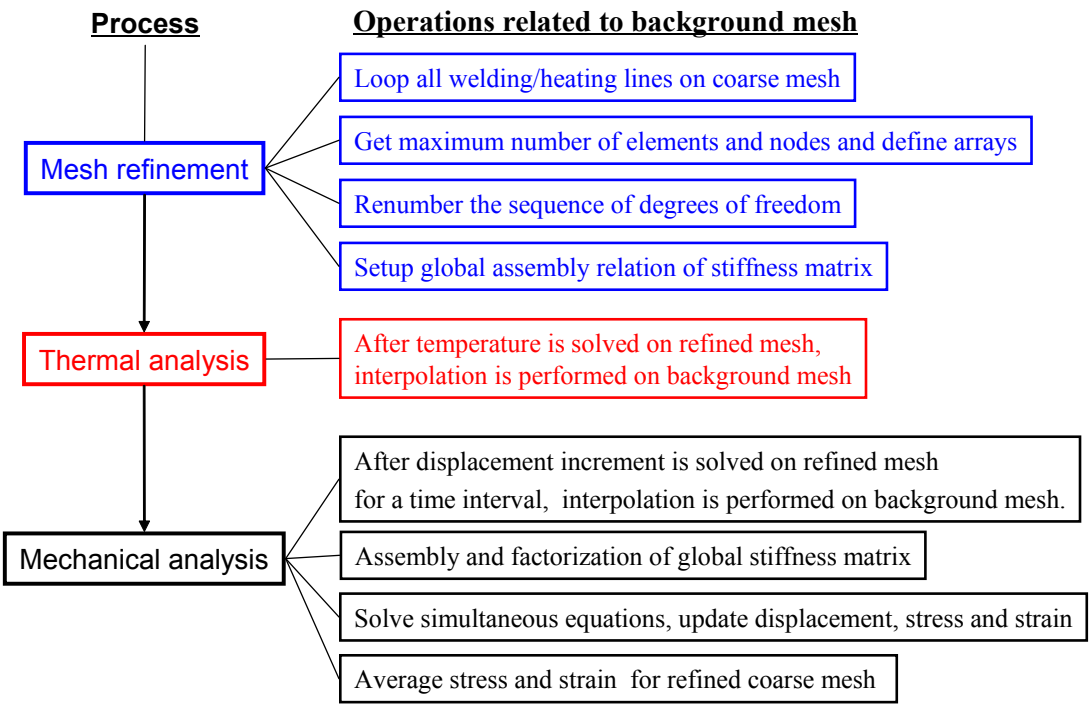

Fig. 3.7 Operations on background mesh in framework of DMRM-2

Nevertheless, the expense on computer memory is raised due to formation of global stiffness matrix on background mesh. In this research, the memory consumption of implicit analysis was optimized to keep the memory consumption of DMRM-2 as close to that of analysis without refining technique. Generally, selection of appropriate solution updating scheme is dependent on the computer platform such as physical memory and acceptable computation time. In the case of limited computer memory, DMRM-1 is preferable; when short solution time is desired, DMRM-2 is better.

3.4 Numerical examples and discussions

This section presents the simulation of fillet welding models by means of dynamic mesh refining method (DMRM). For comparison, the analysis without mesh refinement by conventional finite element method (C-FEM) was also performed. The C-FEM utilizes the same mesh as the background mesh in DMRM. The accuracy of proposed method was examined by the computation of transient temperature and welding deformations of a basic model. A series of simulations were then carried out to investigate the performance of DMRM in respect of shortening computation time when the model scale becomes larger.

3.4.1 Finite element model

The studied model consists of a bottom plate and L-shaped stiffener as shown in **Fig. 3.8**. The dimension of the basic model and welding condition are shown in **Table 3.3**. The stiffener is assumed to be welded simultaneously on both sides without

external constraint. Initial coarse mesh is also plotted in **Fig. 3.8**. The elements have a length of 10 mm in the welding direction. The finite element model holds 12555 nodes and 8160 elements for the initial mesh. Base metal and filler metal were supposed to be the same material, and the temperature dependent properties were shown in **Fig. 3.9**. To record temperature and displacements during welding, four virtual measured points P1~P4 in background mesh were selected at the middle cross section (**Fig. 3.10**).

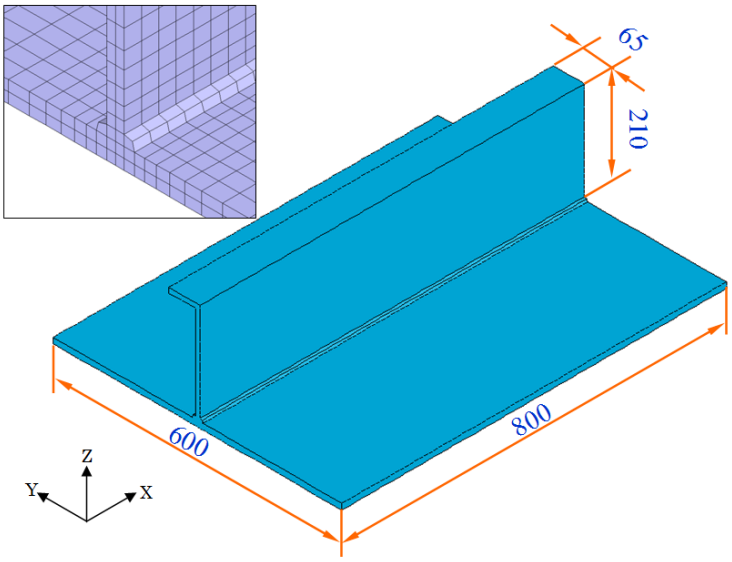

Fig. 3.8 Fillet welding model and initial coarse mesh

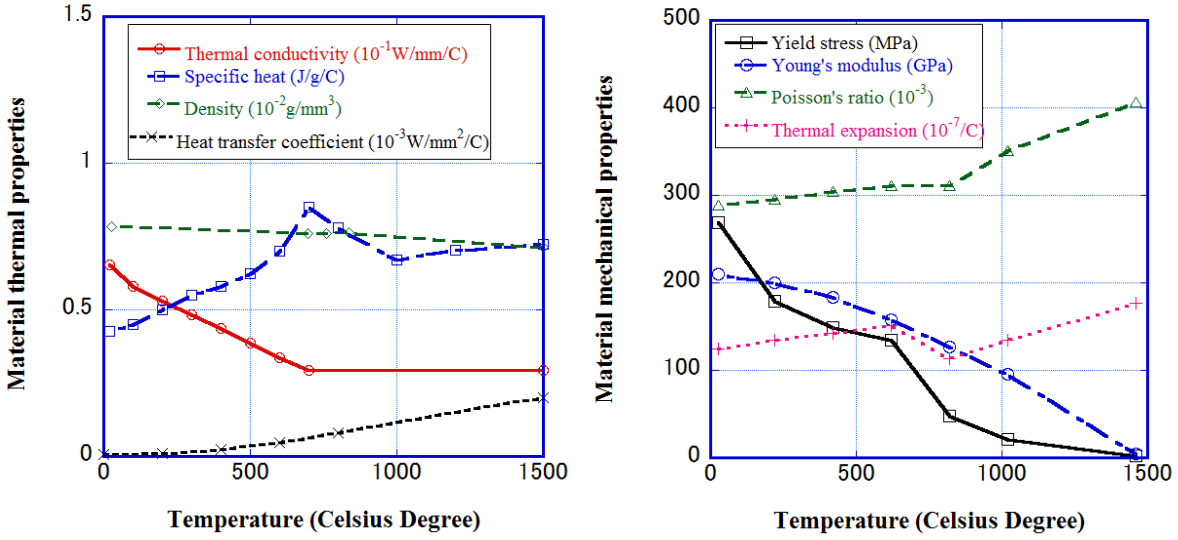

(a) (b)

Fig. 3.9 Temperature dependent material properties: (a) Thermal properties (b) Mechanical properties

Table 3.3 Welding condition of the basic fillet model

Flange Plate mm×mm×mm	Stiffener plate mm×mm×mm	Fillet size mm	Material	Voltage (V)	Current (A)	Velocity (cm/min)
800×600×12	800×210×10	6	SS400	26	150	30

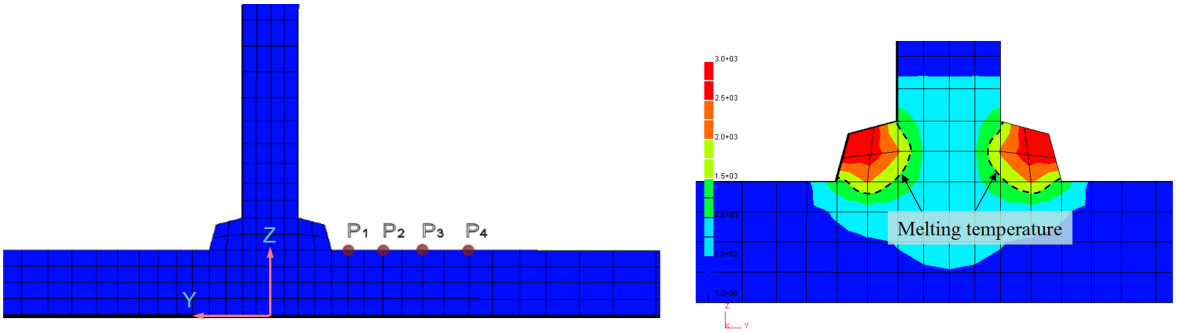

(a) (b)

Fig. 3.10 Thermal conduction analysis (a) Positions of measured points and (b) Penetration shape on background mesh

3.4.2 Results and discussion

The fillet model was welded for 160 seconds and then it cooled down to room temperature by heat transfer to the surroundings. The penetration shape is shown in **Fig. 3.10**. It can be seen that reasonable melting zone has been computed as indicated by the fusion line. The transient temperatures at four measured points were evaluated for the whole time history. From **Fig. 3.11(a)**, it can be observed that a sharp rising of temperature appears when welding torches passed by the points. As the distance from the welding line increases, the peak temperature of each point decreased due to heat diffusion. When the heat source moved away, the difference of temperature among the points gradually became smaller.

In addition, the transient displacements at the four points were measured as shown in **Fig 3.11(b)-(d)**. For the nodal displacements in XYZ directions, response of the model became smooth after heat source moved away from the plate (t＝160s) as it can be observed in the three figures. It can also be observed that most of the out-of-plane welding deformation occurred during the welding process as indicated by **Fig 3.11(d)**. The results from analysis of the DMRM-1 (P1'~ P4') were in excellent agreement with that of C-FEM (P1~ P4).

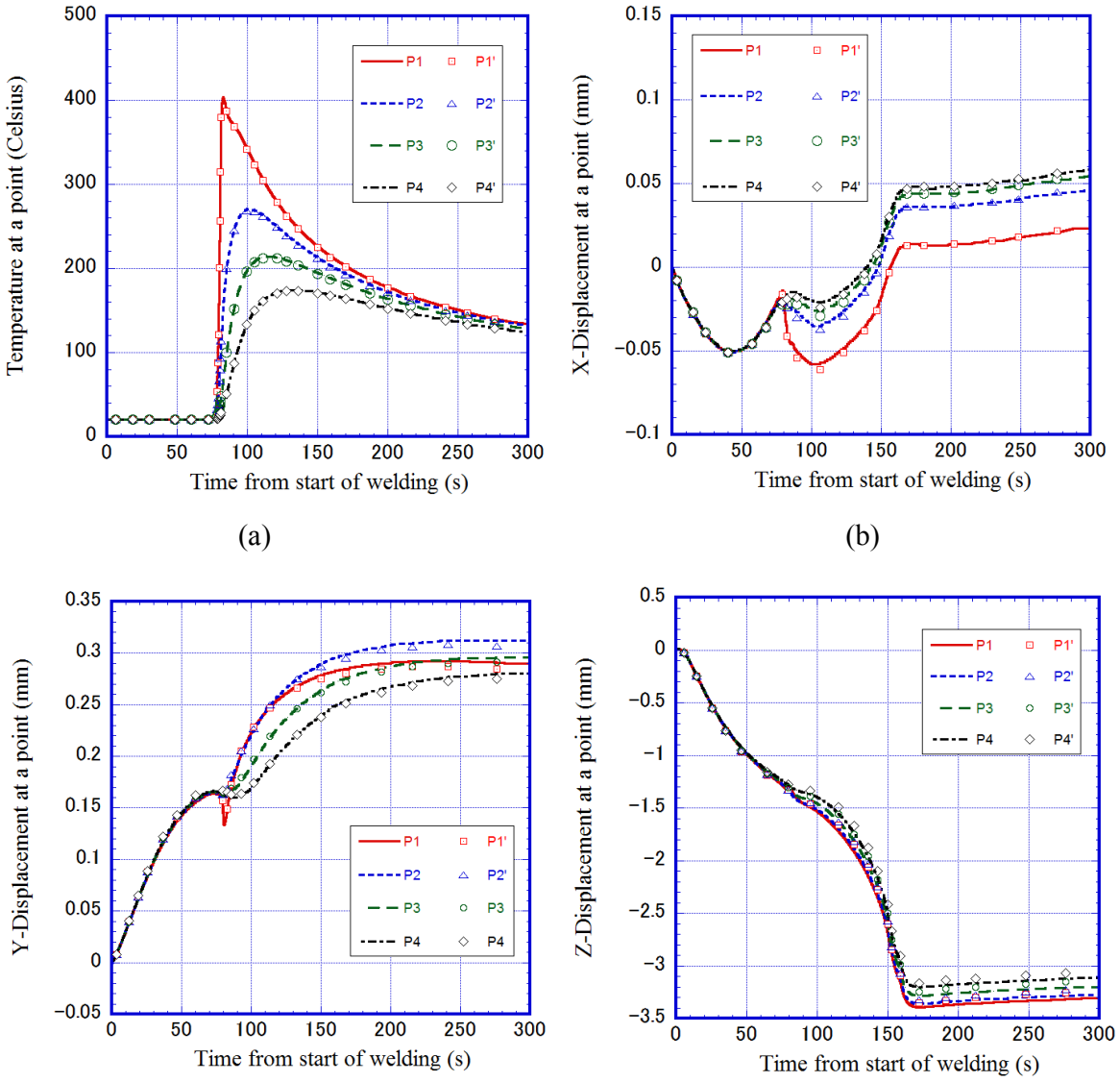

Fig. 3.11 Transient solution at typical points (a) Temperature (b) X-Displacement (c) Y-Displacement (c) Z-Displacement

The temperature and Mises stress contour at t=30s, 90s, and 3000s from the start of welding are plotted in **Figs. 3.12-14**. The stress contours of DMRM1, DMRM2 and C-FEM are all shown on background mesh, while temperature is plotted on computational mesh. As it can be observed from **Fig. 3.12** and **Fig. 3.13**, the temperature and stress field near the heat source stays in a quasi-steady state during the welding of intermediate part of the model. The stress field has large values in front of the heat source due to thermal expansion and restraints on local region. Perpendicular to welding direction, the stress contour has much wider region with high values than temperature contour does. The stress contours obtained by the DMRM-1 and DMRM-2 agreed very well with those by C-FEM at each time step.

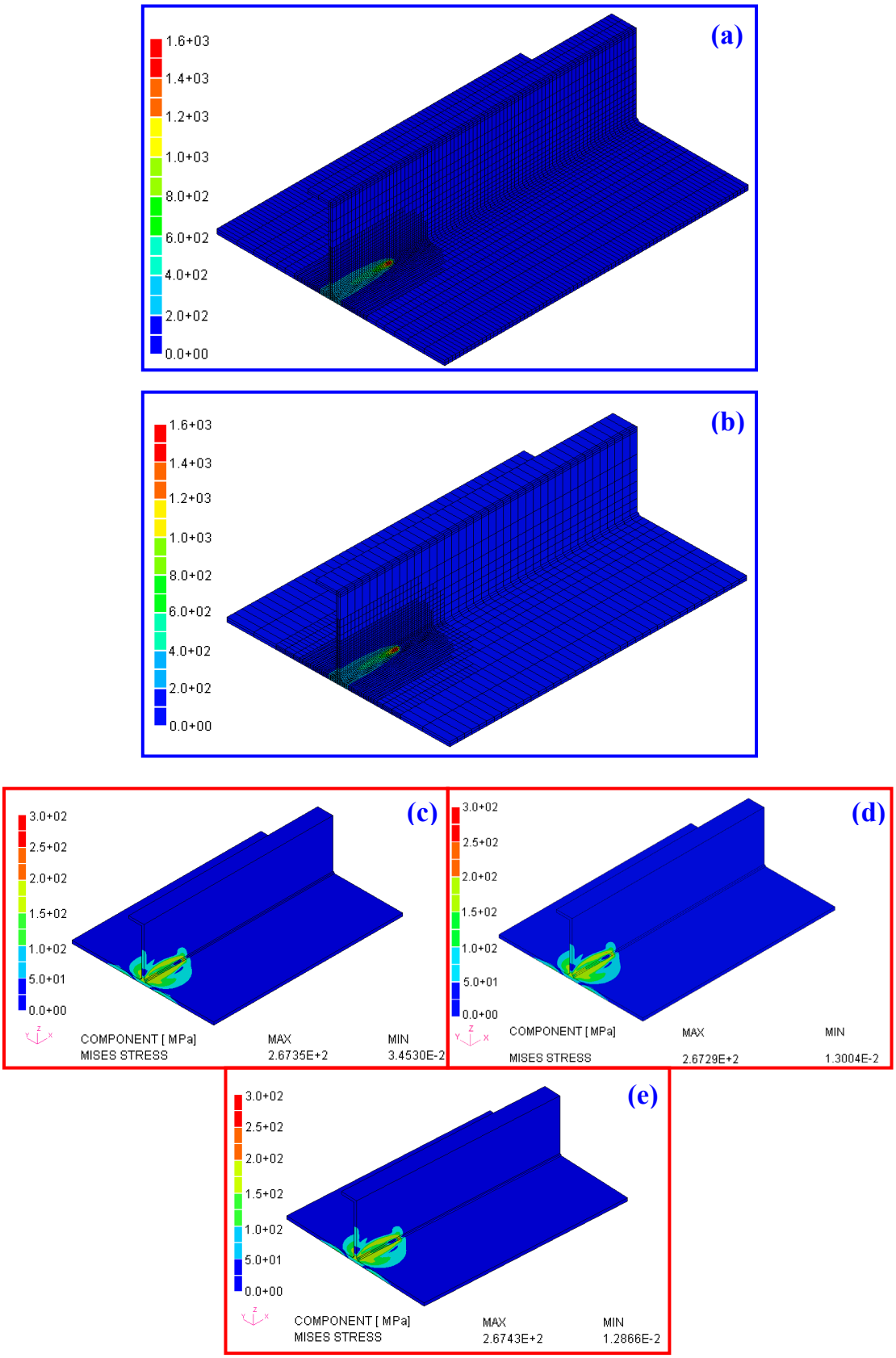

Fig. 3.12 Simulation results at 30s: (a) Temperature by DMRM-1 (b) Temperature by DMRM-2 (c) Mises stress by DMRM-1 (d) Mises stress by DMRM-2 (e) Mises stress by C-FEM

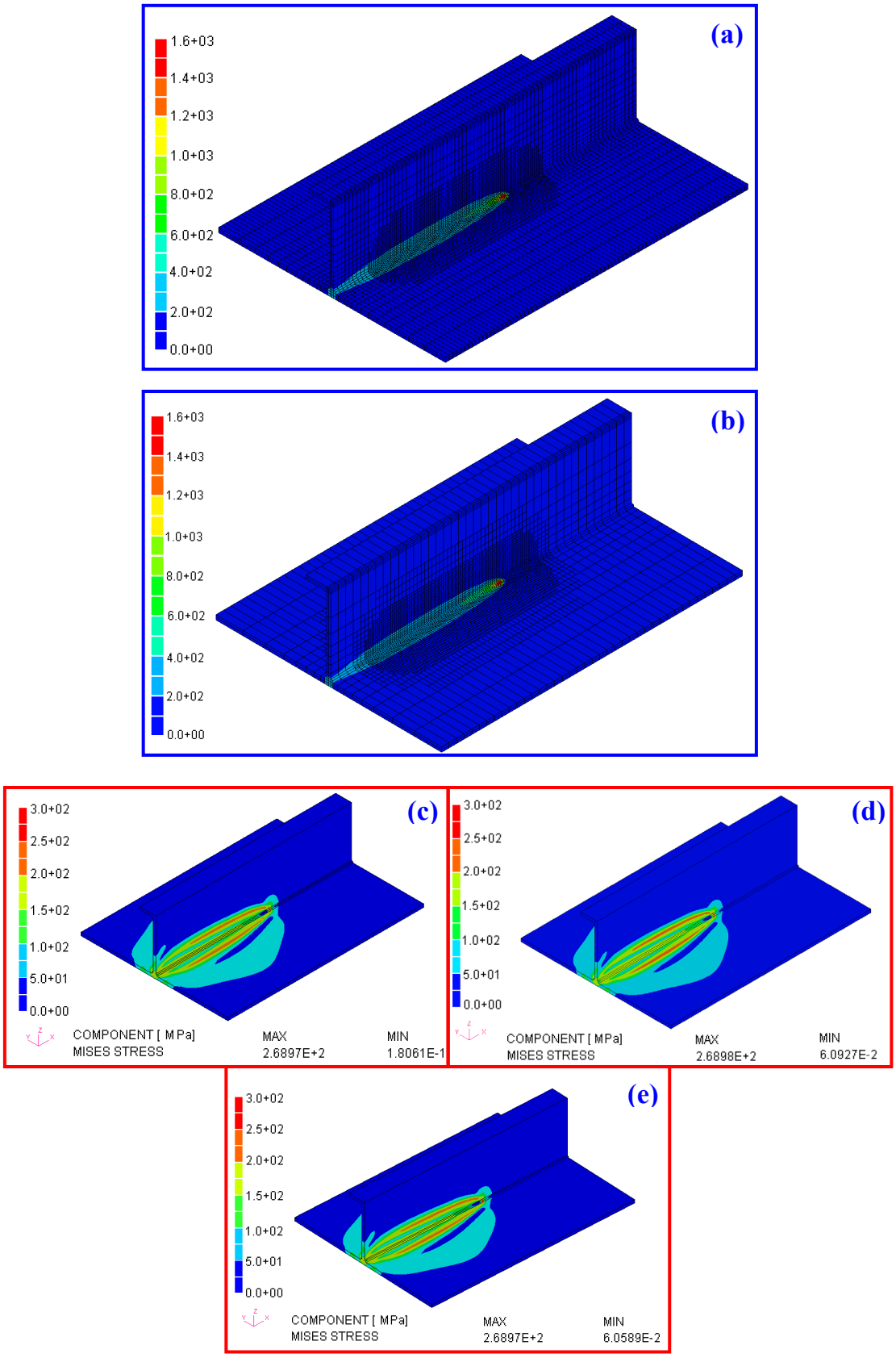

Fig. 3.13 Simulation results at 90s: (a) Temperature by DMRM-1 (b) Temperature by DMRM-2 (c) Mises stress by DMRM-1 (d) Mises stress by DMRM-2 (e) Mises stress by C-FEM

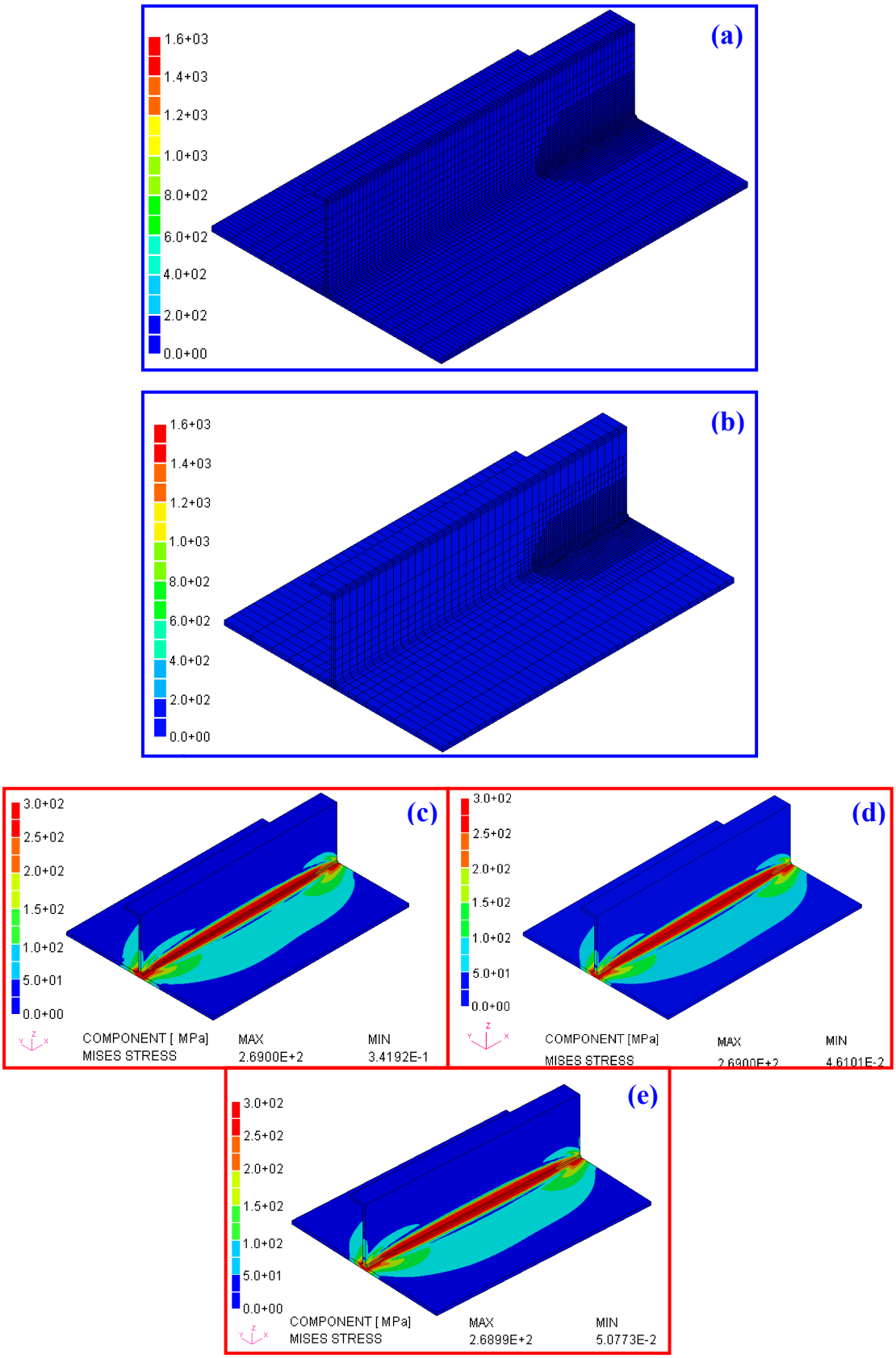

Fig. 3.14 Simulation results at 3000 s: (a) Temperature by DMRM-1 (b) Temperature by DMRM-2 (c) Mises stress by DMRM-1 (d) Mises stress by DMRM-2 (e) Mises stress by C-FEM

Two lines on the bottom of plate were used to extract the residual deformations and stresses. Line A is at center of plate along the welding direction and Line B is at the middle cross section as shown in **Fig. 3.15**. The longitudinal residual stresses along the two lines are shown in **Fig. 3.16**. Typical tensile stress distribution can be seen in the weld zone and heat affect zone excluding the welding start and end. The maximum value stress close to yield strength is almost constant in large part of Line-A. In the transverse direction, the stress is changed from tensile state to compressive state at about 40mm away from weld line, as shown on Line-B.

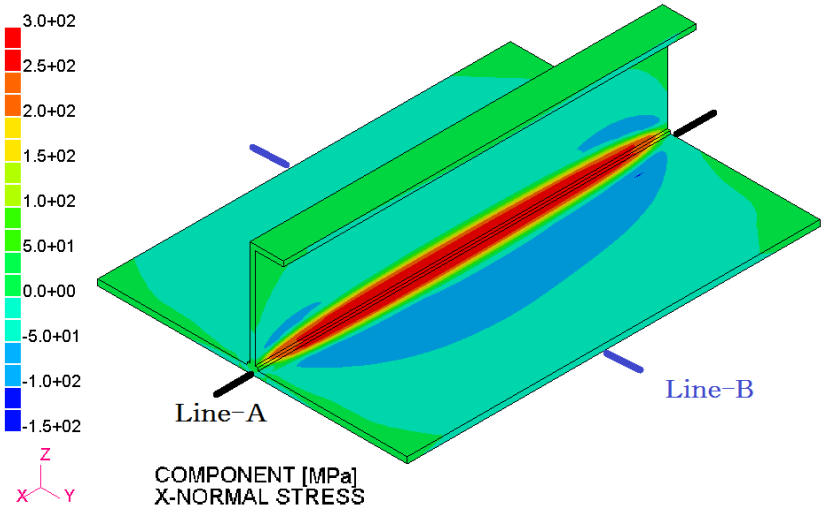

Fig. 3.15 Longitudinal stress contour and evaluating lines

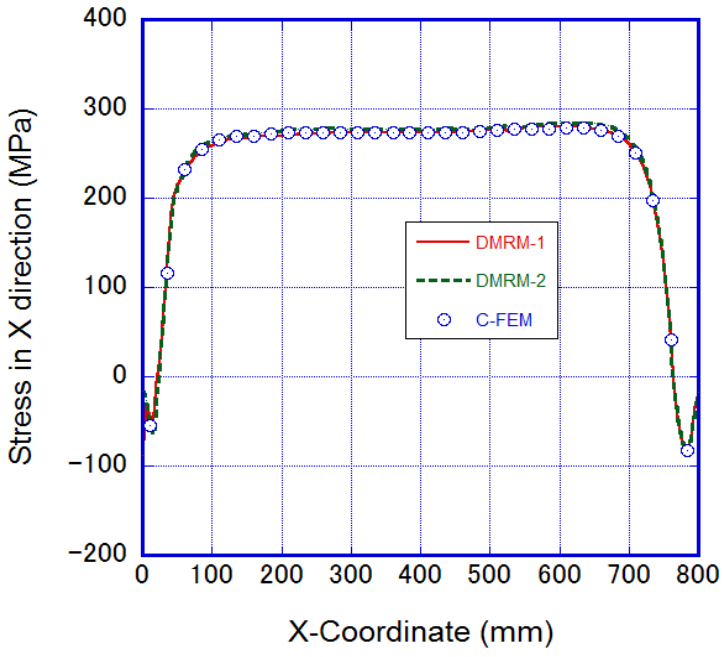

(a)

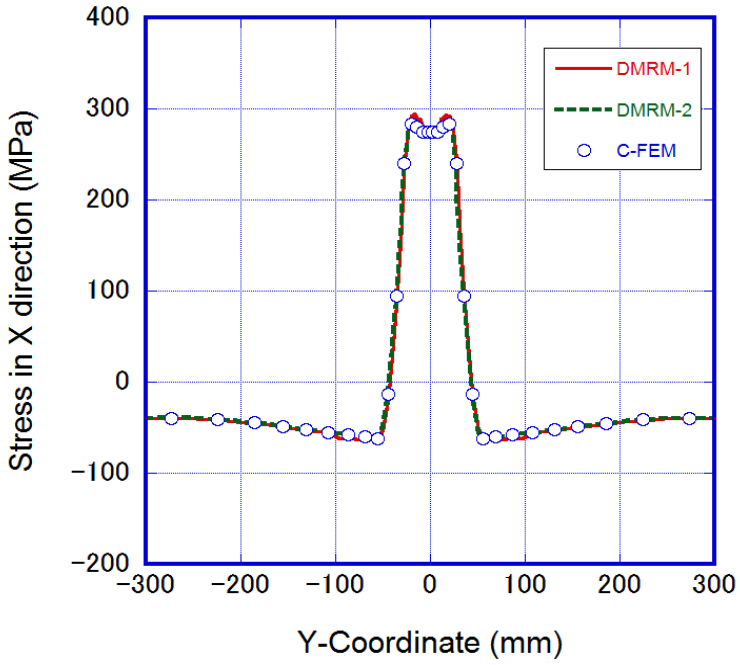

(b)

Fig. 3.16 Residual longitudinal stresses along the two lines: (a) Line-A (b) Line-B

Contours of residual deformations computed by dynamic mesh refining methods—DMRM-1 and DMRM-2 are plotted in **Fig. 3.17**. Longitudinal shrinkage (in X direction) near the weld line and transverse shrinkage (in Y direction) along the welding direction can be seen. The deflection (in Z direction) with a magnitude about 4 mm indicates the angular distortion. Longitudinal bending is not obvious since the ratio of stiffener height to plate size is large. All the deformation components are in good agreement between solution of DMRM-1 and DMRM-2.

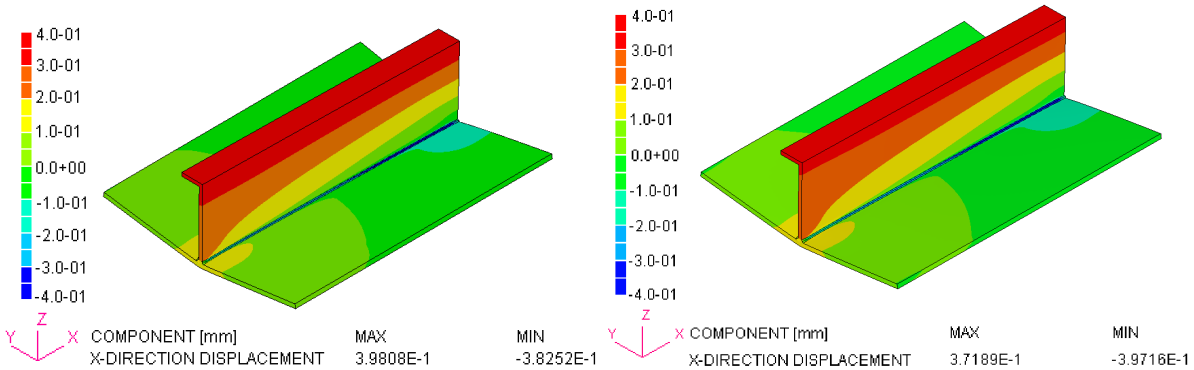

(a1) (a2)

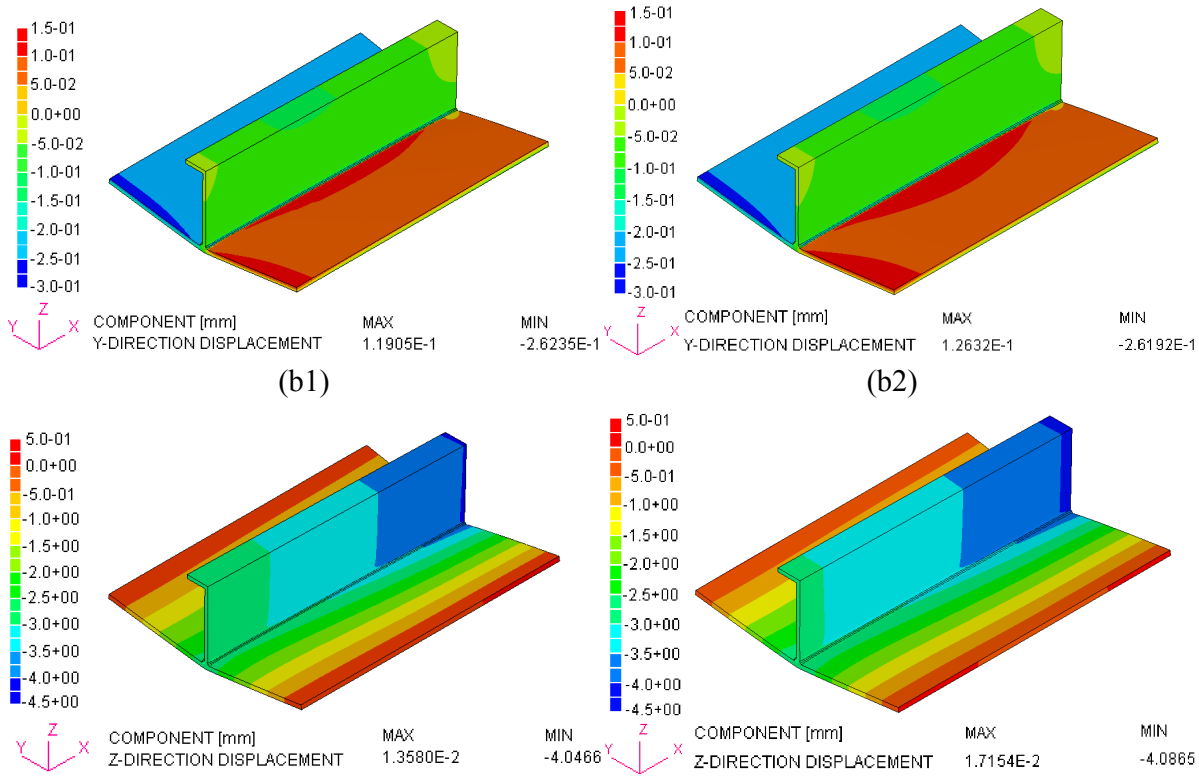

Fig. 3.17 Residual deformation computed by DMRM1 and DMRM2 (scaled by 12 times): (a1-a2) X-Displacement (b1-b2) Y-Displacement (c1-c2) Z-Displacement

The displacement profiles along Line-A are shown in **Fig. 3.18**. The displacement in X-direction indicates large longitudinal shrinkage in the heat affected zone (HAZ). Similarly, the transverse shrinkage is mostly produced in HAZ from the abrupt change of displacement in Y-direction. The region far away from the weld line exhibits decreased shrinkage, which is due to the angular distortion. The computational results suggest that the solution by C-FEM lies in between those of DMRM-1 and DMRM-2. However, the differences among the results are small.

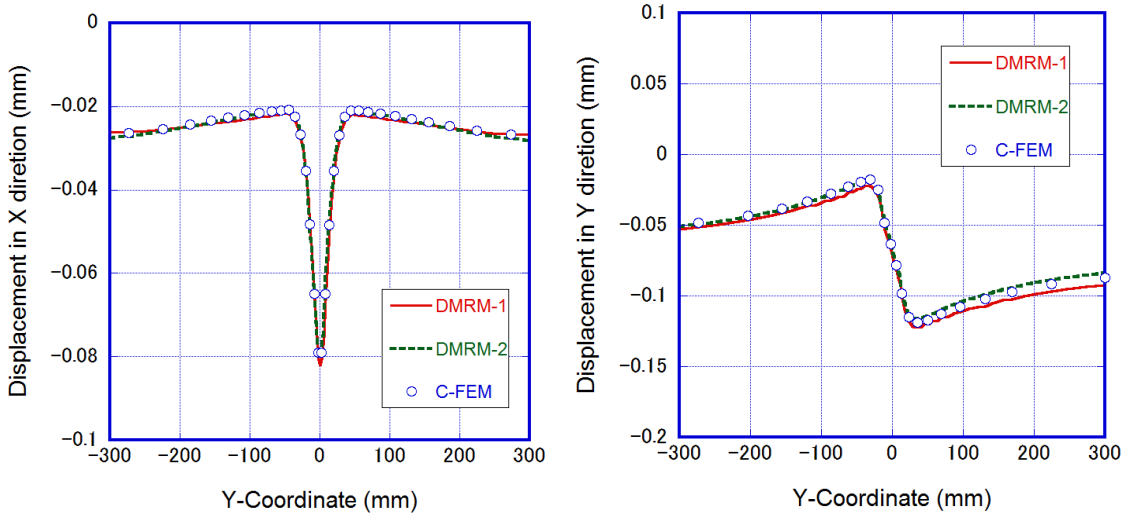

(a) (b)

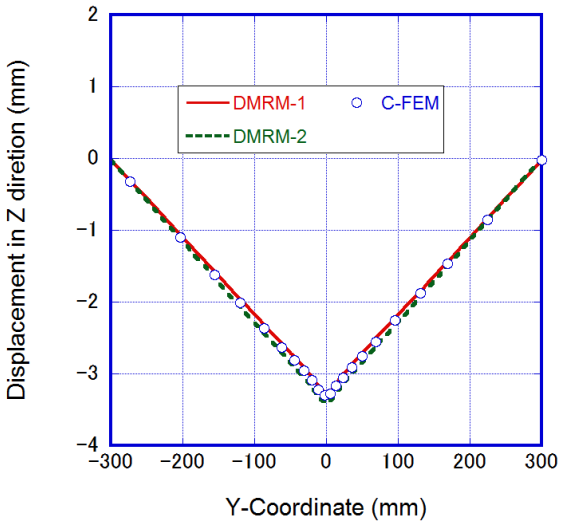

(c)

Fig. 3.18 Residual displacements along Line-A (a) X-Displacement (b) Y-Displacement (c) Z-Displacement

For the current model, computational time for the C-FEM is 13 hours, while those for DMRM-1 and DMRM-2 are 4.8 hours, and 3.6 hours respectively. Based on the results, it can be concluded that the DMRM reduces large amount of computational time while keeping good accuracy.

3.4.3 Performance on models in different scale

A series of models with the same cross-section and welding condition were analyzed to evaluate the performance of the proposed methods. The model dimension and mesh data of the models in the case of C-FEM are listed in **Table 3.4**.

Table 3.4 Model dimension and mesh data

Model No.	M1	M2	M3	M4	M5
Length (mm)	800	1600	2400	3200	4000
Nodes	82,593	164,673	246,753	328,833	410,913
Elements	65,280	130,560	195,840	261,120	326,400

The results of residual deformation and stresses are plotted in **Fig. 3.19, Fig. 3.20** and **Fig. 3.21**. Herein, the results solved by C-FEM, DMRM-1 and DMRM-2 were indicated by Mi, Mi' and Mi", respectively.

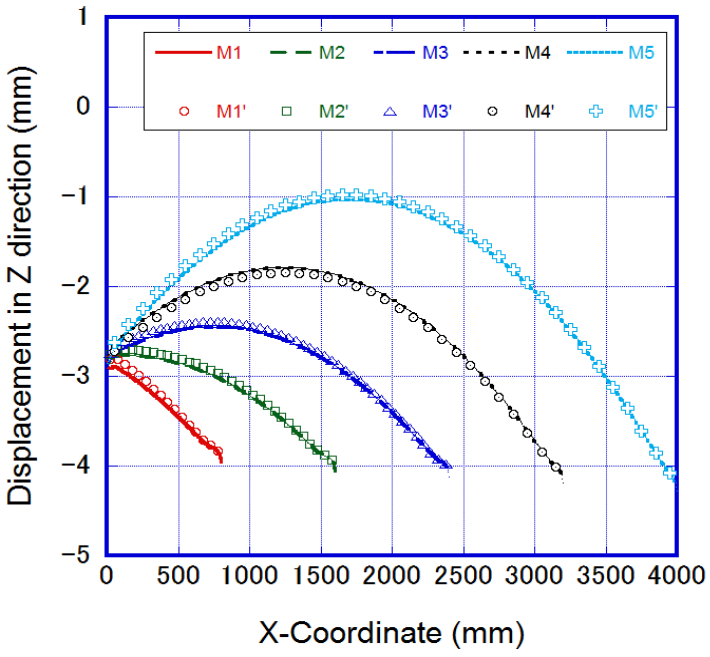

(a)

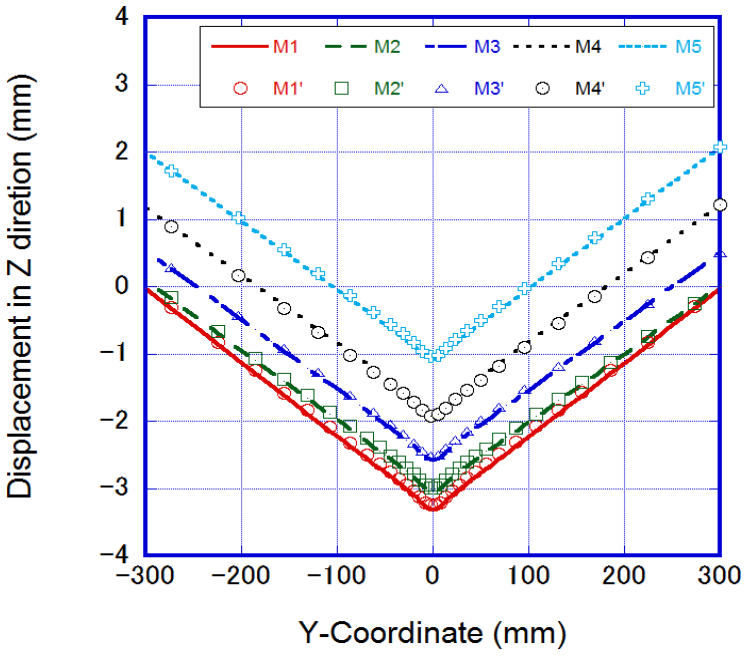

(b)

Fig. 3.19 Residual deflection along two lines: (a) Line A. (b)Line B

From **Fig. 3.19 (a)**, the deflection along the weld direction increases as the plate is longer. The longitudinal bending can be easily observed when the plate is longer than 2400mm. Nevertheless, the angular distortion at the middle cross section is almost the same among all models as shown in **Fig. 3.19(b)**. This is one of the natures of inherent strain which has been effectively utilized for numerical analysis of large welded structures.

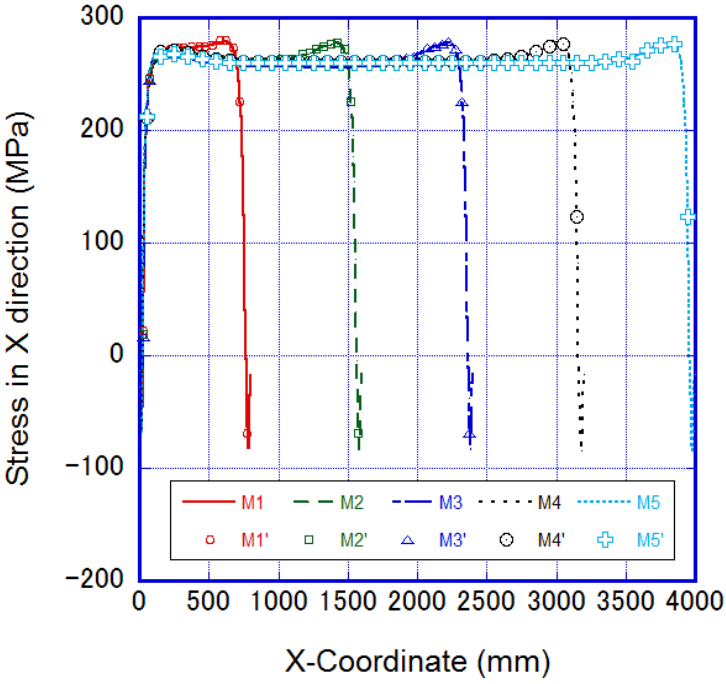

(a)

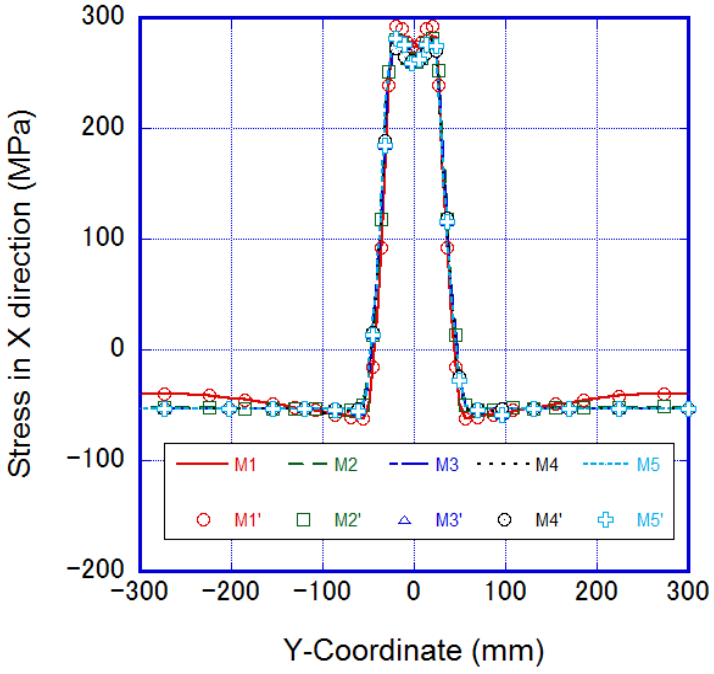

(b)

Fig. 3.20 Residual stress in X direction along two lines: (a) Line A. (b)Line B

From **Fig. 3.20(a)**, the longitudinal stress has a uniform distribution at the intermediate part of the length of plate. The stress near the welding start and finish ends is at compressive state. In **Fig. 3.20(b)**, the longitudinal stress along the transverse direction shows two peaks at the position near the weld bead on both sides. The stress profiles have small difference among the models with various length.

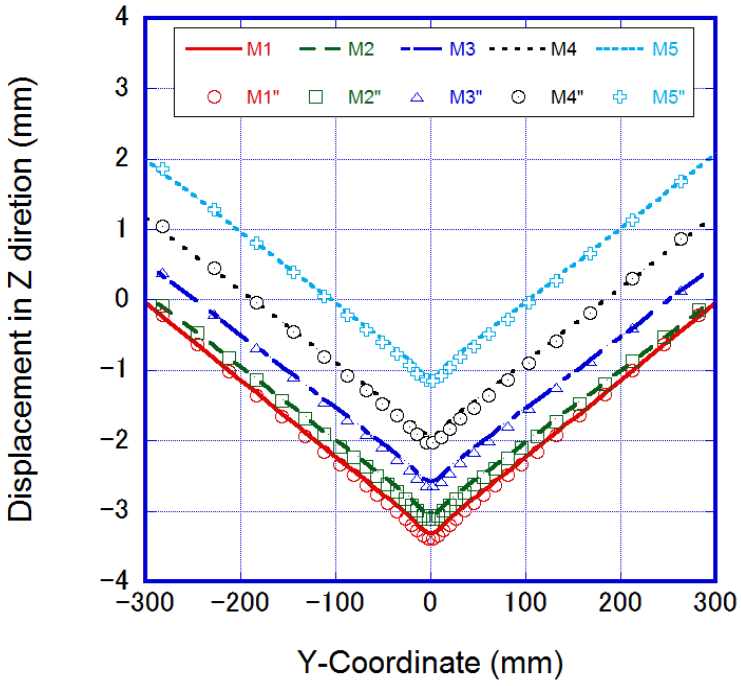

(a)

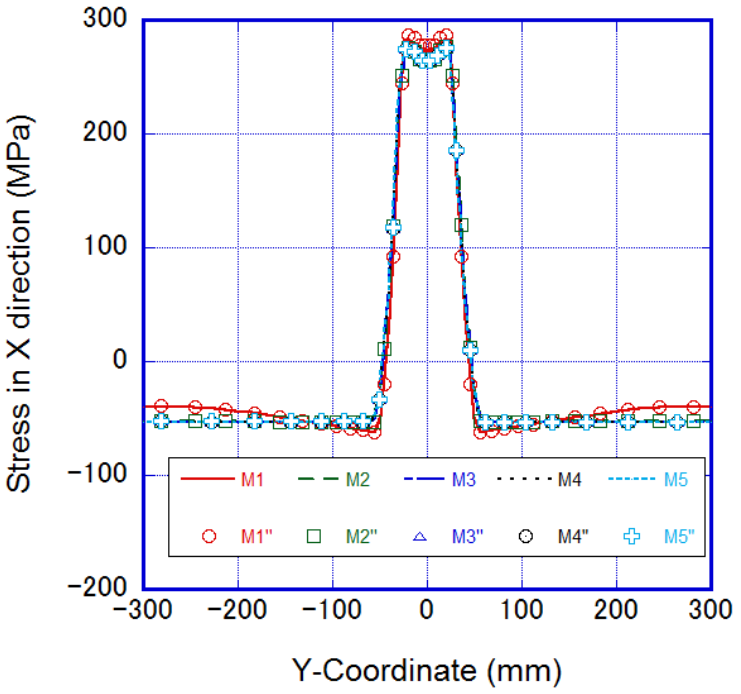

(b)

Fig. 3.21 Computational results along Line B: (a) Deflection. (b)Stress-X

Good agreement between results computed by DMRM-2 and that by C-FEM is also observed for both the displacement and the stresses, as shown in **Fig. 3.21**

Both computation time and physical memory cost in the simulations were tested. CPU in single core mode was used for each simulation on a Linux system. For a comparison, the same model was solved by means of DMRM-1 and DMRM-2. The computational information of all models are shown in **Table 3.5**.

Table 3.5 Computational information

Model No.	M1	M2	M3	M4	M5
Clock time (hour)	***13.0***	***40.1***	***77.9***	***139.2***	***199.4***
Memory cost (GB)	2.2	4.3	6.7	8.9	11.2
Model No.	M1'	M2'	M3'	M4'	M5'
Clock time (hour)	***4.8***	***10.6***	***17.1***	***26.2***	***35.3***
Memory cost (GB)	1.6	2.1	2.8	3.4	4.2
Model No.	M1"	M2"	M3"	M4"	M5"
Clock time (hour)	***3.6***	***7.4***	***11.8***	***16.7***	***21.9***
Memory cost (GB)	5.4	7.8	10.0	12.8	15.6

To clarify the relation between model scale and performance of DMRM, the ratios of element number, physical memory and CPU time among C-FEM, DMRM-1 and DMRM-2 were plotted in **Fig. 3.22**. Regarding element number, the maximum one among all computational meshes was used as the reference for DMRM. In each model, the element number in the computational mesh is much smaller compared with that in the background mesh.

In the case of DMRM-1, a reduction factor of about 6 in CPU time and 3 in physical memory was obtained in analysis of Model No.5, as shown in **Fig 3.22(a)**. Because the stiffness matrix is always formed and solved based on the computational mesh, computing time and memory can be both saved compared with conventional FEM. The ratio of CPU time is roughly the same with that of element number. Certainly, time spent on factorizing stiffness matrix takes a large proportion when the computational mesh increases in element number. For further improvement, a static condensation technique may be introduced to collect the elements around the heat torch as a super element. Then total number of DOFs for the computational mesh can be maintained at a lower level. Memory consumption has a weaker relation with model scale, as recording solution on the background mesh is necessary for all cases.

In the case of DMRM-2, the computation time was further reduced by a two-level refinement as shown in **Fig 3.22(b)**. The acceleration reached 9 times in the analysis of Model No.5. The ratio of CPU time shows a similar tendency to that of element number. Since the global stiffness matrix was formed on background mesh, the

memory consumption was increased, so that the ratio between C-FEM and DMRM-2 becomes 0.72 when the model is large. This deficiency could be improved by optimizing the program structure such as removal of local arrays. A hybrid computation scheme which solves background mesh with explicit method could help to enhance the dynamic mesh refining method.

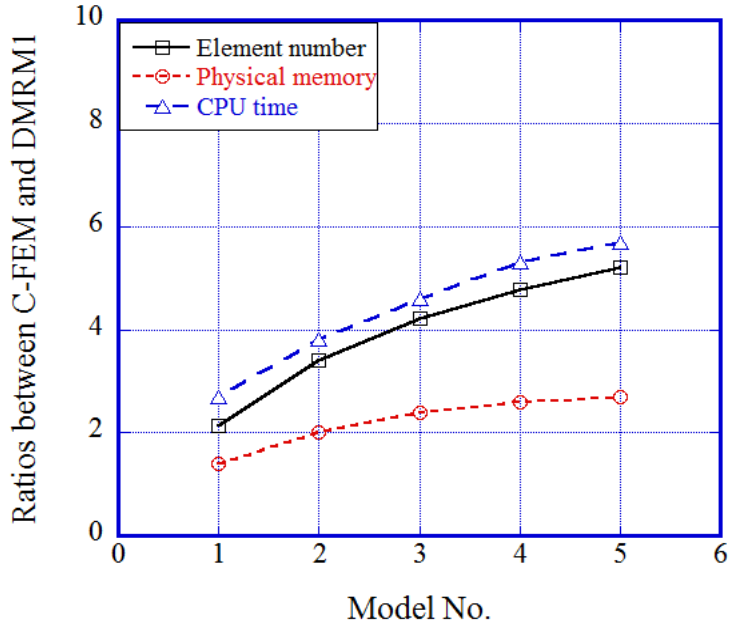

(a)

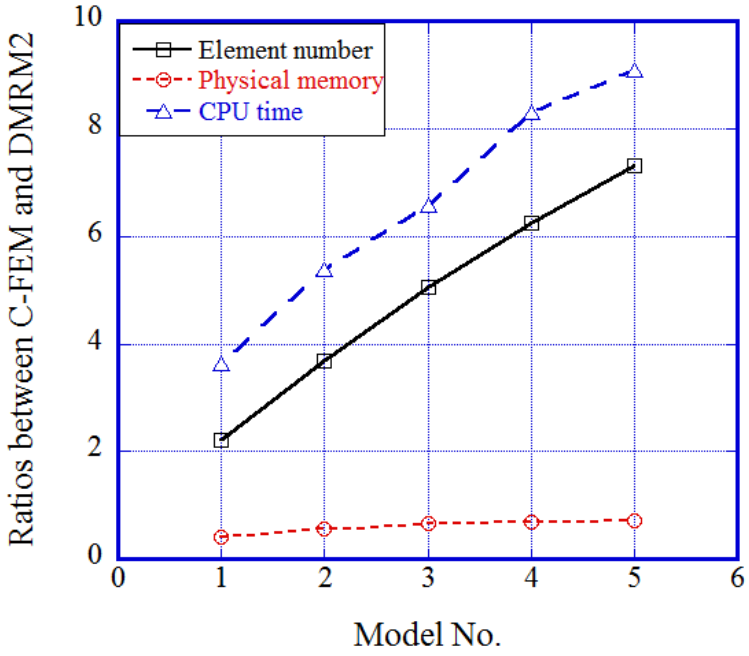

(b)

Fig. 3.22 Computation cost between conventional method and refining methods: (a) C-FEM vs DMRM-1 (b) C-FEM vs DMRM-2

3.5 Summary

To overcome the drawback of generally used remeshing methods, the dynamic mesh refining method (DMRM) has been developed considering the characteristic of welding problems. A background mesh is originally introduced into the numerical model, so that global solution can be book kept and updated on it. The computation flowchart and refinement control for a welding problem was described in detail.

The solution updating schemes on background mesh is important, when computation efficiency and required memory are considered. Two solution updating schemes were proposed. The first scheme (DMRM-1) aims to save both CPU time and memory cost, and computation was limited on computational mesh. Stiffness matrixes and load vectors are always assembled on the computational mesh, and solutions are just recorded on background mesh. Integration of stiffness matrix and load vector of an element are carried out in different reduced schemes for elements at different level. The numerical analysis of fillet joints indicated that acceleration ratio becomes almost 6 times and saving in memory is about 62.5%.

In the second scheme DMRM-2, global stiffness matrix and load vectors are also assembled on background mesh, and simultaneous equations are also solved on the mesh. The same reduced integration can be applied for elements at different level. Thus computation on mesh with multi-level refinement can be done without convergence and accuracy problem at the cost of computer memory. From the numerical examples, a two-level refinement could accelerate the computation by 9 times, and the additional memory required is just 39.3% of conventional FEM. The dynamic mesh refining method was proved to be efficient, accurate and robust.

Chapter 4 Thermal conduction analysis and acceleration methods

In most welding processes such as arc welding and laser welding, the heat directly deposited to the work piece is much larger than that produced by the plastic work. Thus the sequentially coupled scheme can be adopted for simplicity. Firstly, thermal analysis is carried out to compute the transient temperature field. Secondly, mechanical analysis is performed incrementally with the thermal load at corresponding time step. Because the number of DOFs in thermal analysis is just one third of that in mechanical analysis, and also the size of the matrix to be solved is much smaller, the computation time necessary for thermal analysis is usually shorter than mechanical analysis. However, when advanced solution method is applied in mechanical analysis, the computation time of thermal analysis becomes comparable with or even larger than that of accelerated mechanical analysis. In order to reduce the computation time, it is necessary to develop new algorithms for thermal analysis.

In this chapter, proposed efficient numerical schemes namely heat transfer localization method (HTLM) and dynamic mesh refining method (DMRM) will be introduced. The HTLM employs a fine mesh and a coarse mesh to solve the region near heat source and the region outside respectively. Mapping of temperature results in the coarse mesh onto the fine mesh is conducted to combine a full solution at each time step. The DMRM directly uses a locally refined mesh with transformation of elemental matrix and heat flux vector to solve temperature field. In addition, dynamic mesh refinement is necessary in this scheme, which makes the process much more complex than HTLM. The effectiveness of proposed schemes will be demonstrated through examples of large scale model.

4.1 Heat transfer localization method

4.1.1 Basic concept

In the recent decade, the thermal elastic-plastic analysis for welding was gradually extended to large scale models[102][103]. Although the stress analysis attracted strong interest in accelerating computation speed, the thermal analysis could be time consuming when the model is large. In order to save time and disk space, an efficient scheme takes advantage of the characteristic of thermal field was proposed.

Welding is a transient thermal process since the heat source moves along weld line and the welding pieces have finite dimensions. The region near heat source has large gradient of temperature while other regions have relatively uniform distribution of temperature. It is also well known that the material properties such as specific heat and

heat conductivity strongly depend on temperature. For simulation using conventional finite element method (C-FEM), the region near the weld line should be modeled with fine elements.

Recall that, it is not necessary to solve nodal temperature for the regions to be heated later or that already cooled down. Since most of the region has low temperature and weak heat transfer, the solution domain can be limited to region near the heat source using the same mesh as used in conventional method. The number of DOFs was reduced by temporary fixing nodes under specific criterions. The region which is not fixed can be solved with high accuracy as long as the fixed thermal boundary is far enough. This requires a dynamic relaxing and fixing nodes with the movement of the heat source. However, the region being fixed and that near the fixed thermal boundary lose accuracy in solution. The mesh density affects the temperature gradient greatly, but it affects the heat conduction around the heat source mildly. This is true because the heat transfer through convection and radiation is usually quite small than heat conduction. Therefore, the analysis on a coarse mesh will provide reasonable solution for the region far away from the heat source. As the solution near the heat source is obtained through analysis on a local region, the numerical scheme was called heat transfer localization method.

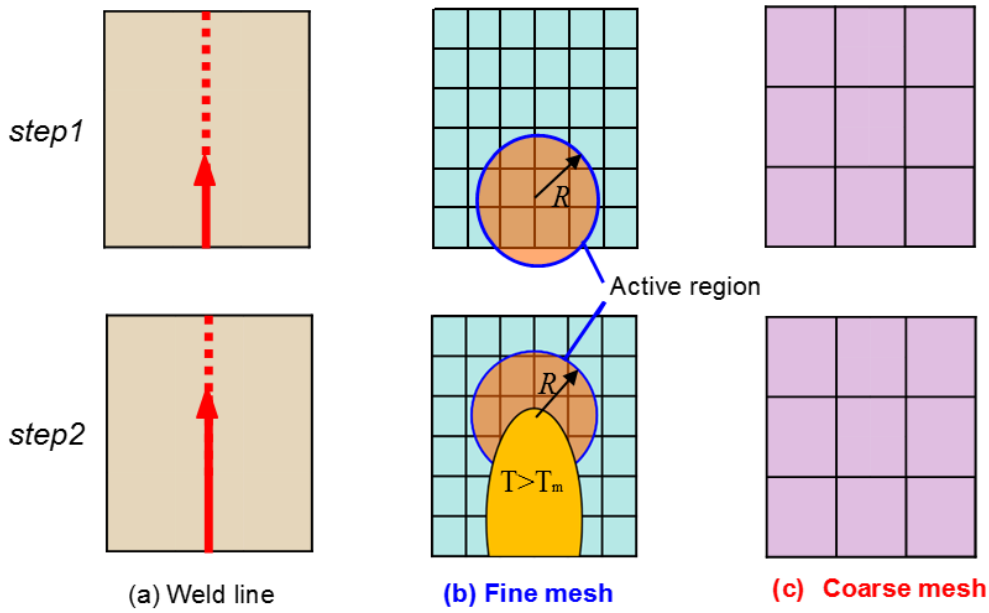

Fig. 4.1 Overview of heat transfer localization method

Figure 4.1 shows the overview of heat transfer localization method. It can be seen that, region around heat source are activated in analysis and other nodes are fixed. The region encompasses a zone covered by a sphere with radius R centering at the heat source and another zone with temperature higher than a predefined value T_m. If the nodes and elements in original mesh are sequentially numbered, those in the activated

region will not be in the same sequence. The band width of the matrix formed on disordered elements will be close to original global matrix. In order to minimize the band width, it is necessary to renumber the nodes and elements in natural sequence (abbreviated as Renum in the following sections). To recover the accuracy for outer region around heat source, a coarse mesh is utilized to overlap the results in that region solved by localization method. That is, the domain near heat source is solved by fine mesh while the region outside by coarse mesh. This kind of dual mesh analysis can be done much easier than the any refining or remeshing method.

The size of sphere which partitions active region and inactive region can be determined by the one dimensional heat conduction model[106] as illustrated in **Fig. 4.2**. The initial temperature of the domain is T_0, the temperature at the wall x=0 is suddenly raised to T_w at time t=0s, and the temperature at far-field x=∞ is fixed as T_0. The transient temperature at x can be solved analytically as shown in **Eq. 4.1**. Gauss error function $erf(\eta)$ is defined to obtain a curve with constant error value. In the present study, the variable η of error function was set as 2.0 to calculate the critical distance of x. The estimation has an error less than 0.5%. So the relation between evolution time t and distance was obtained as **Eq. 4.2**. In the case of stationary heat source, the critical distance between the heat source and the thermal boundary can be readily calculated. In order to consider the movement of heat source, the distance that traveled by heat source during time t needs to be added.

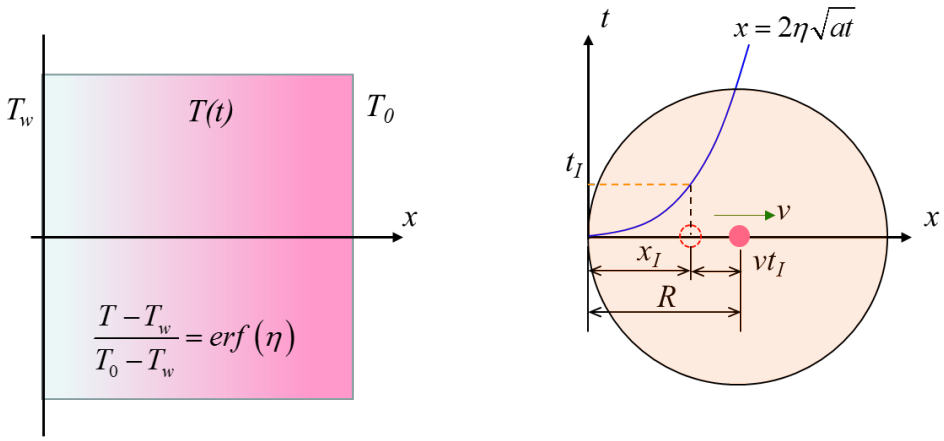

Fig. 4.2 Estimation of active region size by one dimensional thermal conduction analysis

$$\frac{T-T_w}{T_0-T_w}=\frac{2}{\pi}\int_0^{\frac{x}{2\sqrt{at}}}\exp\left(-s^2\right)ds=erf\left(\eta\right) \tag{4.1}$$

$$\eta=\frac{x}{2\sqrt{at}} \tag{4.2}$$

$$\eta = 2, \quad erf(\eta) = 0.99532 \tag{4.3}$$

For a mild steel, assume the thermal diffusivity is 12.0 mm^2/s, and the time interval t_{inv} for analysis with fixed region in fine mesh is 3 s, it can be calculated that minimum fixing radius R is 24mm. If the travelling speed of the heat source v is 6 mm/s, additional distance 18 mm should be added to R. The equation for evaluating R can be written as:

$$R = x(\eta, t_{inv}) + v * t_{inv} \tag{4.4}$$

After temperature is solved on fine mesh and coarse mesh, interpolation of results solved by coarse mesh onto fine mesh is performed. Similar to computation on fine mesh, the region which is fixed is dynamically recovered. Due to the structure of fine mesh and coarse mesh, the topology may not be in a hierarchical mode which has a single interpolation function. Here, an original data mapping method applicable for arbitrary mesh structures was employed. **Figure 4.3** schematically shows the basic processes of mapping, they are described as follows:

- Calculate normalized coordinates of each point in fine mesh corresponding to coarse mesh by Newton-Raphson method (**Location**).
- Obtain the temperature of the fine mesh nodes by **interpolation** of the temperature in coarse mesh using element shape function

In this process, nodal temperature is only necessary to be transferred, operation on integration points is not necessary.

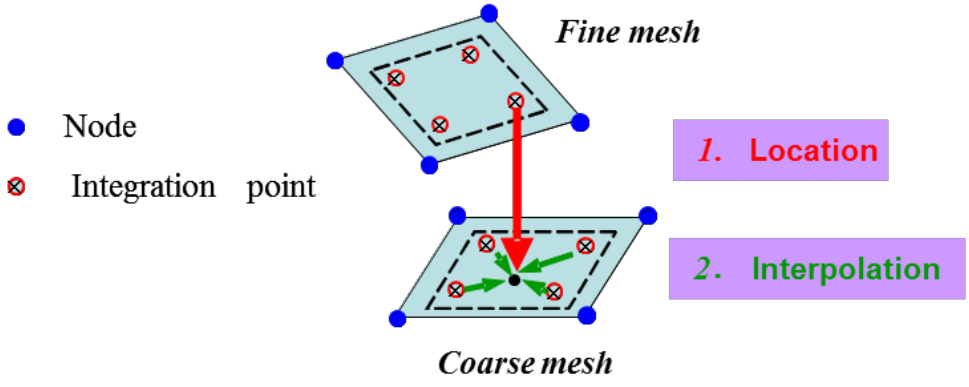

Fig. 4.3 Mapping results between two meshes

4.1.2 Verification Example

The proposed method was examined by butt joint welding model. The material of the welding plate is assumed to be the same as that described in **Section 3.3.4**. For the

heat transfer localization method, combined criterion for selecting solution domain was employed with temperature limit 300℃ and radius 50 mm.

(1) Welding condition

The welding model has a dimension of 200mm×200mm×6mm, and welding torch moves from position (0, 100) to position (200, 100), as shown in **Fig. 4.4** The model was meshed into uniform pattern with element size 4mm×4mm×1.5mm in the case of analysis by C-FEM, and the coarse mesh has double size in each dimension in the cases of HTLM and DMRM. The heat input was assumed to be 3900 W. Uniformly distributed ellipsoid heat source model with moving velocity 5 mm/s was employed. Heat radiation effect was not taken into account, and heat transfer coefficient follows the exponential relation with temperature[105].

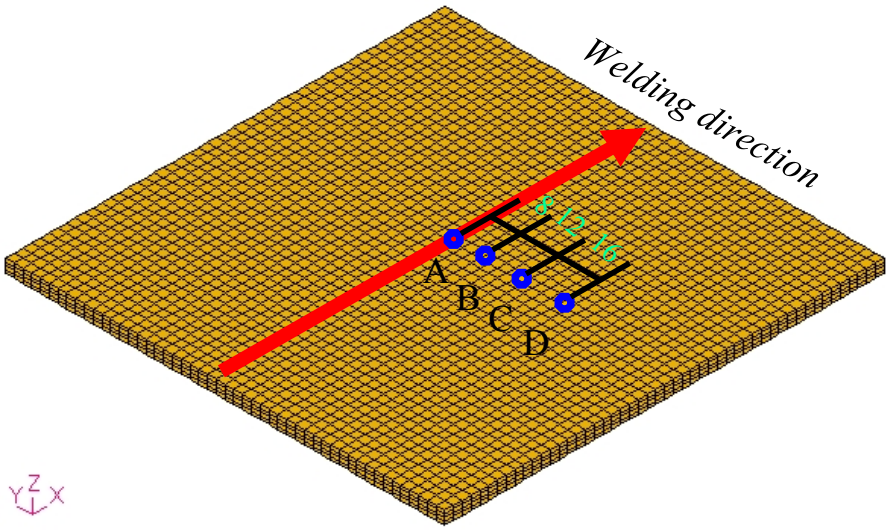

Fig. 4.4 Butt joint welding model and visual thermal couples

(2) Simulation results

Transient temperature was evaluated for four points at the middle cross section (**Fig. 4.4**). As shown in **Fig. 4.5(a)**, the nodal temperature has good correlation at heating stage between C-FEM using fine mesh and HTLM. This is because that the region near the moving heat source is always active. As expected, the results at cooling stage has large deviation. The difference can be minimized by increasing the radius limit or reduce the temperature limit. However, the reduction of computation time will not be significant. If the solution from the coarse mesh is interpolated to fine mesh, the accuracy of temperature at cooling stage was improved, as shown in **Fig. 4.5(b)**. The results obtained by HTLM exhibit very small deviation from the C-FEM.

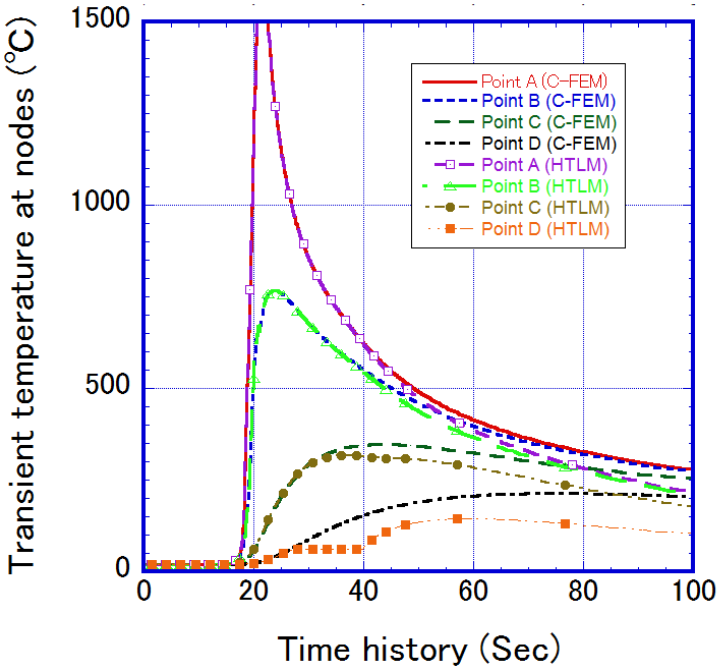

(a)

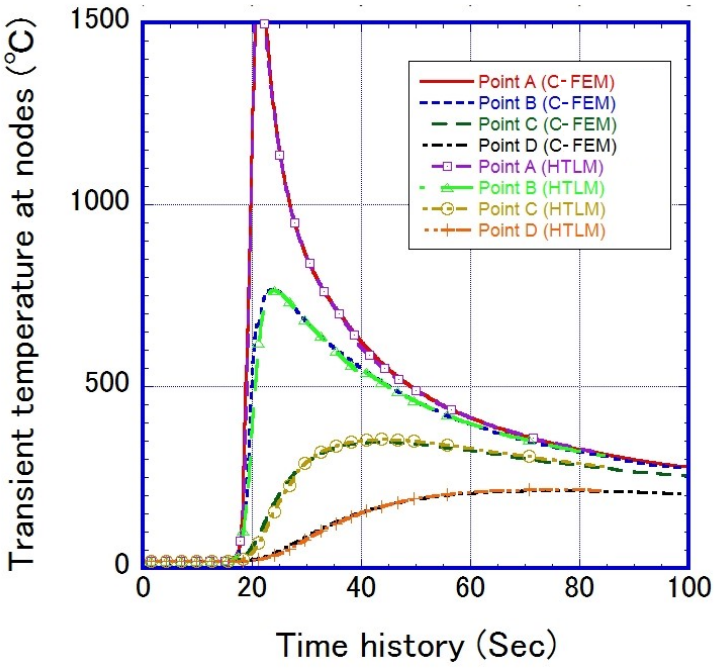

(b)

Fig. 4.5 Comparison of transient temperature between C-FEM and heat transfer localization method (a) Fine mesh only (b) After mapping

The computational results by HTLM at t=27*s* are shown in **Fig. 4.6**. Comparing solutions on fine mesh and coarse mesh, the temperature has a wider distribution in coarse mesh. This is caused by the temporary fixing of nodal temperature, so heat

cannot spread outside. And the thermal boundary is like a cold wall. The final mapped temperature contour is similar to that of coarse mesh, but the temperature around the heat source is similar to that of fine mesh.

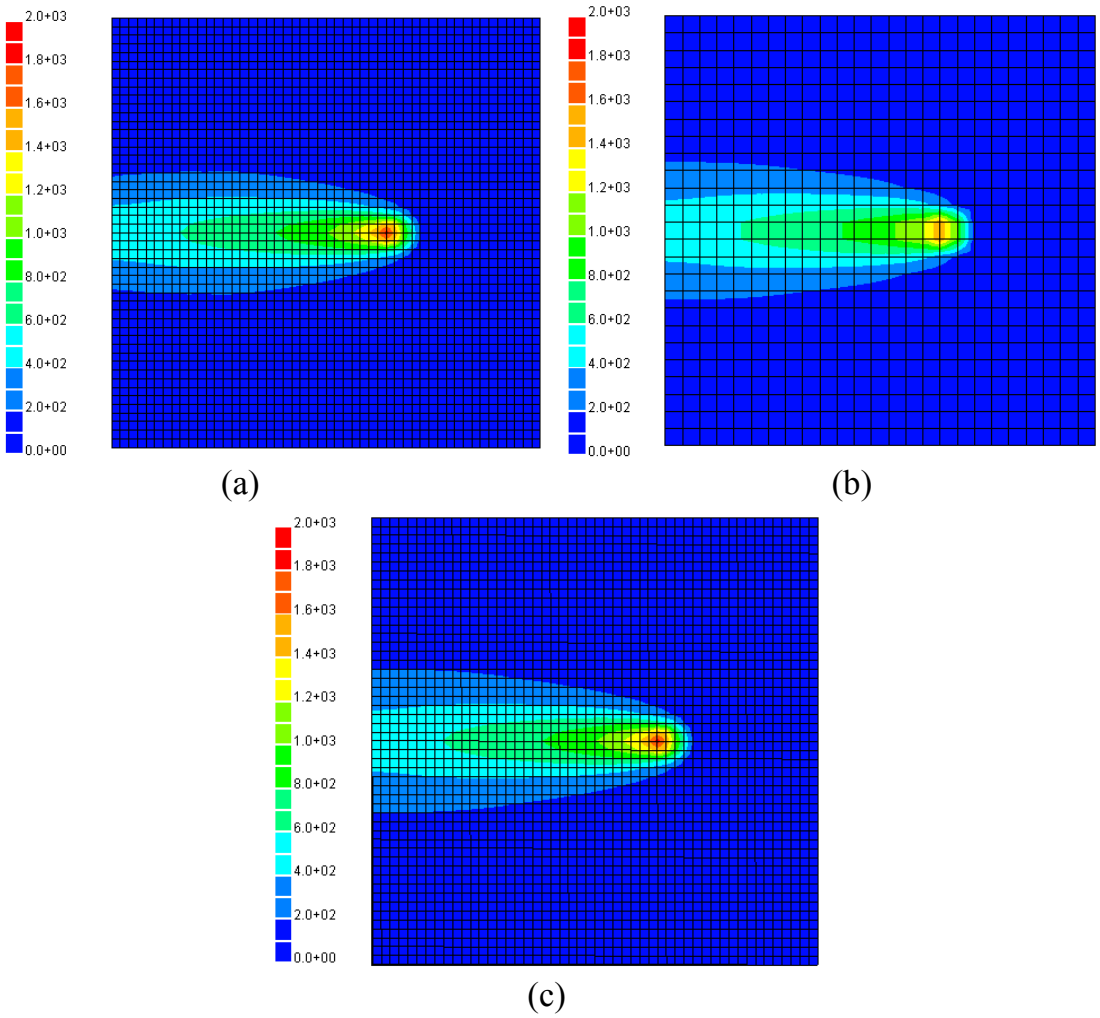

Fig.4.6 Temperature distribution at t=27s: (a) Fine mesh with localization (b) Coarse mesh (c) After mapping

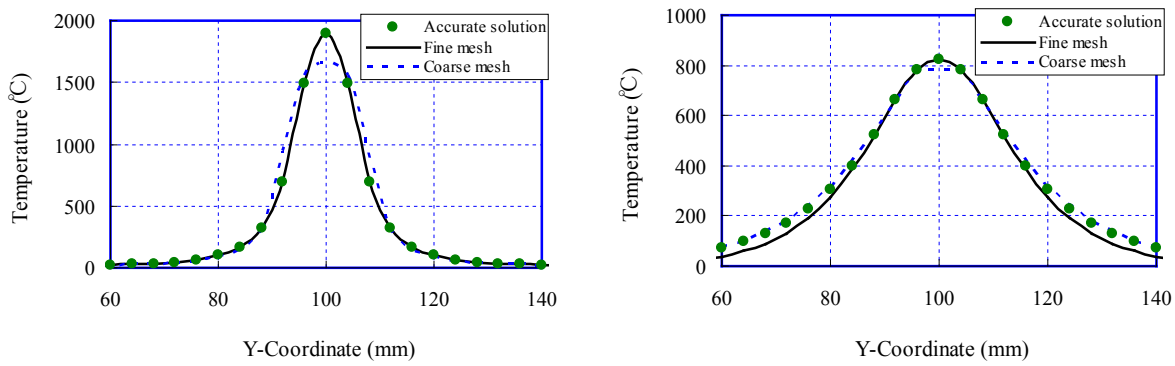

Fig. 4.7 Comparison of temperature profiles at transverse sections (a) X=128mm (b) X=80mm

To see the precise distribution of temperature, the profile of temperature at two transverse sections were evaluated at X=128mm (near heat source center at t=27s) and X=80mm, as shown in **Fig. 4.7**. The temperature predicted by the fine mesh with local active region has good accuracy near the weld line, whereas the deviation becomes obvious at the rear section in Fig. 4.7(b). In region behind heat source, the analysis by the coarse mesh gives reasonable solution.

4.2 Dynamic mesh refining method

4.2.1 Basic concept

In line heating or welding process, local region near heat source experience rapid heating and cooling. Therefore, an analysis model can be roughly divided into two regions, strongly nonlinear region (B) around the heat source and weakly nonlinear region (A-B), as shown in **Fig. 1.5**. To fit the temperature gradient, the element should be very fine at the region B while relatively coarse element can be designed in region A-B. Then the fine elements can be moved with the heat source in simulation. In the case of thermal analysis, a background mesh is also necessary to transfer the temperature for the whole model.

The computational mesh is designed based on the local refining around the heat source. Multi-level refinement can be performed on an initially coarse mesh. The temperature is then interpolated on background mesh since the nodal variables are directly determined on element nodes. For thermal-mechanical problems, the stress and strain will also be updated on background mesh. Generally, the values of interpolation function is readily known during refinement, it is not necessary to solve high order simultaneous equations during mapping process.

For welding thermal conduction analysis, the refining criterion can be limited as temperature driven scheme when refinement was conducted in every single time step. In the case of refining in the manner of multiple time steps, the combined criterion with the radius control can be employed.

4.2.2 Verification Example

The same model as illustrated in **Section 4.1.2** was employed to verify the accuracy of DMRM in calculating temperature results. For the dynamic mesh refining method, combined criterion is used, and the parameters are 300℃ and 30mm separately. The refined mesh of DMRM at t=9s and t=27s are shown in **Fig. 4.8**. Smooth distribution across fine and coarse elements can be observed.

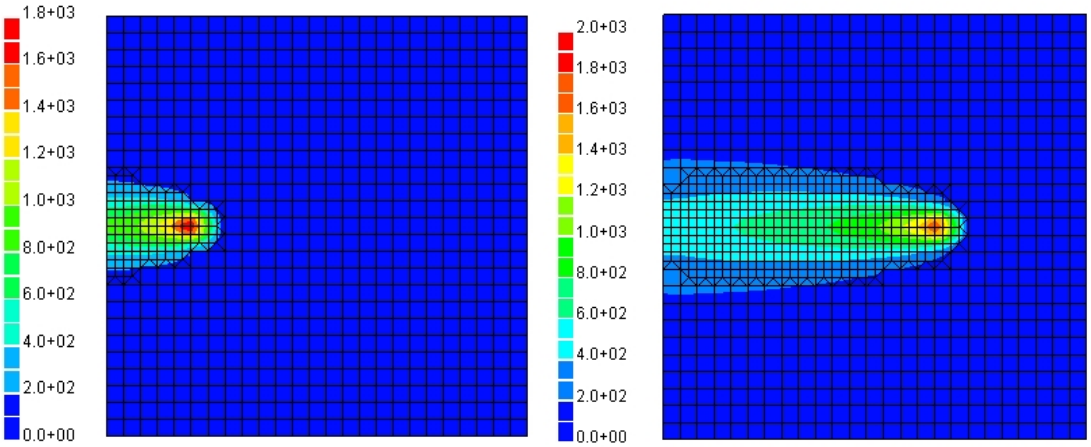

(a) (b)

Fig.4.8 Computational mesh with temperature distribution (a) t=9s (b) t=27s

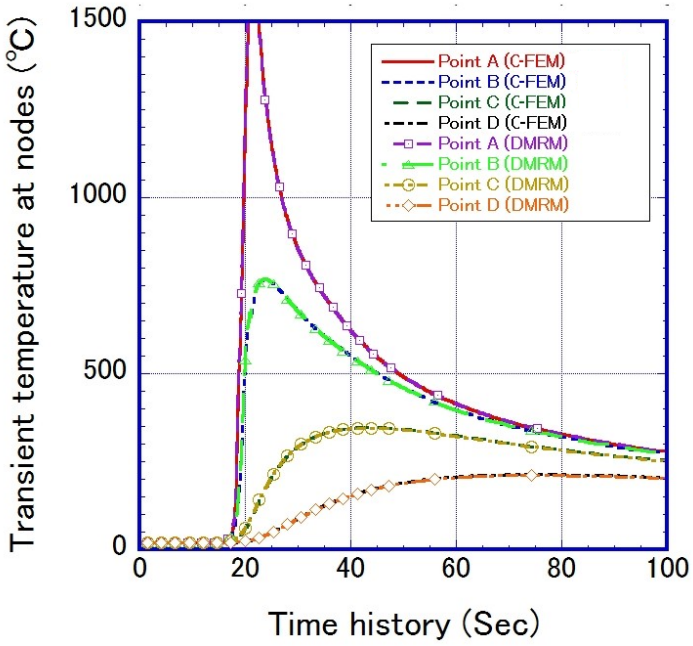

Fig.4.9 Comparison of transient temperature between C-FEM and DMRM

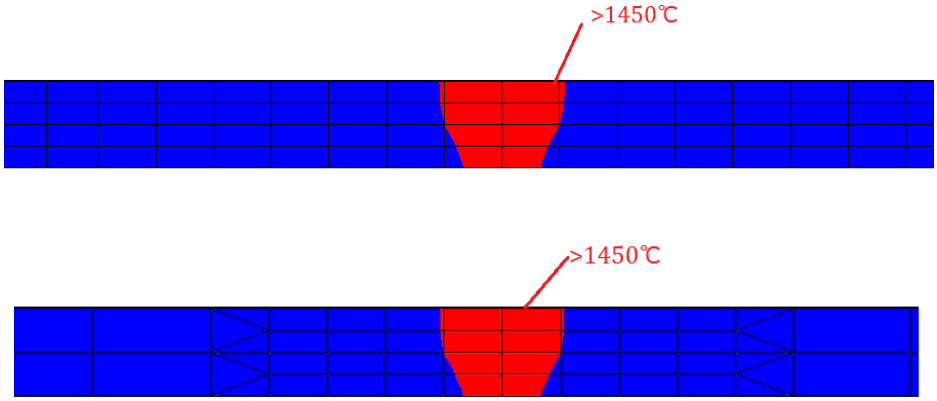

Fig.4.10 Penetration shapes predicted by C-FEM (top) and DMRM (bottom)

As shown **Fig. 4.9**, the transient temperature results by dynamic mesh refining method give almost the same solution as C-FEM for the whole time history. **Fig. 4.10** shows the penetration shape predicted by the two methods, good correlation can be confirmed.

4.2.3 Computation efficiency

The initial model was changed to another 9 models by scaling the length of plate and welding path while other conditions keep the same. The computation time versus number of degree of freedom was plotted in **Fig. 4.11**. It can be observed that computation time roughly grows with DOF number in a quadratic way for C-FEM. However, in the case of dynamic mesh refining method, CPU time just linearly increases with the model scale. Both DMRM and HTLM achieve higher acceleration effect as number of DOF increases. When the DOF is 127,755, the ratio of computation time between C-FEM and DMRM becomes 5.6 and that for HTLM becomes 3.0. However, if the nodes in the active region are renumbered, the acceleration of HTLM becomes 6.0.

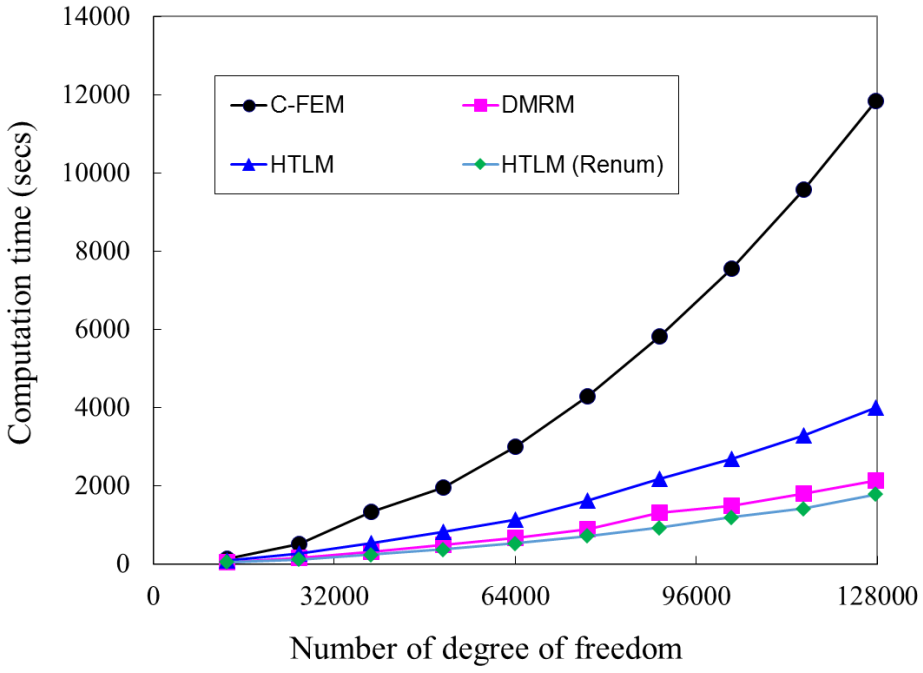

Fig.4.11 Relation between computation time and number of DOF

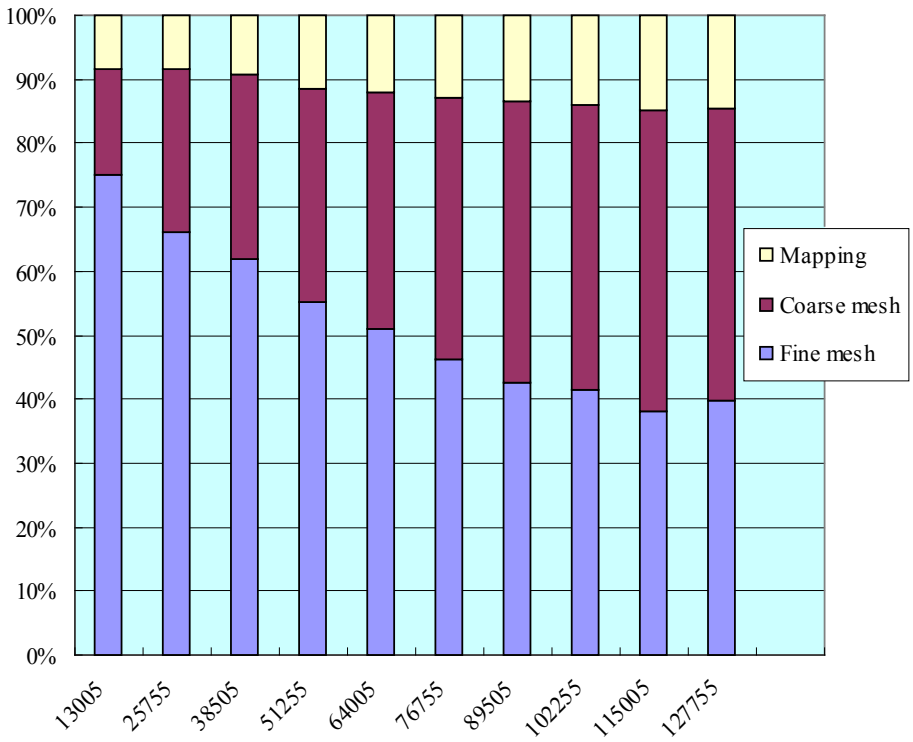

Fig. 4.12 CPU time constitution in HTLM

The computation time in HTLM mainly consists of three parts: solution on fine mesh, solution on coarse mesh and mapping process. **Fig. 4.12** summarized the CPU time constitution for analysis on different models (in terms of DOFs). It can be observed that, the mapping process almost takes 8-15% of total time for a model. Solution on fine mesh and coarse mesh cost almost the same amount of time when the model is large.

4.3 Application to Large Scale Model

4.3.1 Model description

A fillet model consisting of one panel and six stiffeners is shown in **Fig. 4.13**. The dimension of the model and welding condition are given in **Table 4.1**. The mesh employed by C-FEM has 1,051,200 elements and 1,404,954 nodes. Double side simultaneous welding was performed for each stiffener, and the stiffeners were welded sequentially. The welding heat input is 3900W, and heat source velocity is 5mm/s. Ellipsoidal heat source was used, and semi-axes are 5mm in welding direction, 4mm in both penetration width direction and depth direction. The local FE mesh was given in **Fig. 4.14**, fine mesh was used in the region near the weld line. The predicted penetration shape was also shown in the figure, reasonable heat input can be confirmed.

Table 4.1 Dimensions of stiffened panel structure

Panel(mm × mm × mm)	Stiffener (mm × mm × mm)	Fillet size (mm)
3000 × 3600 × 12	3000 × 200 × 10 (Web) 3000 × 120 × 10 (Flange)	6

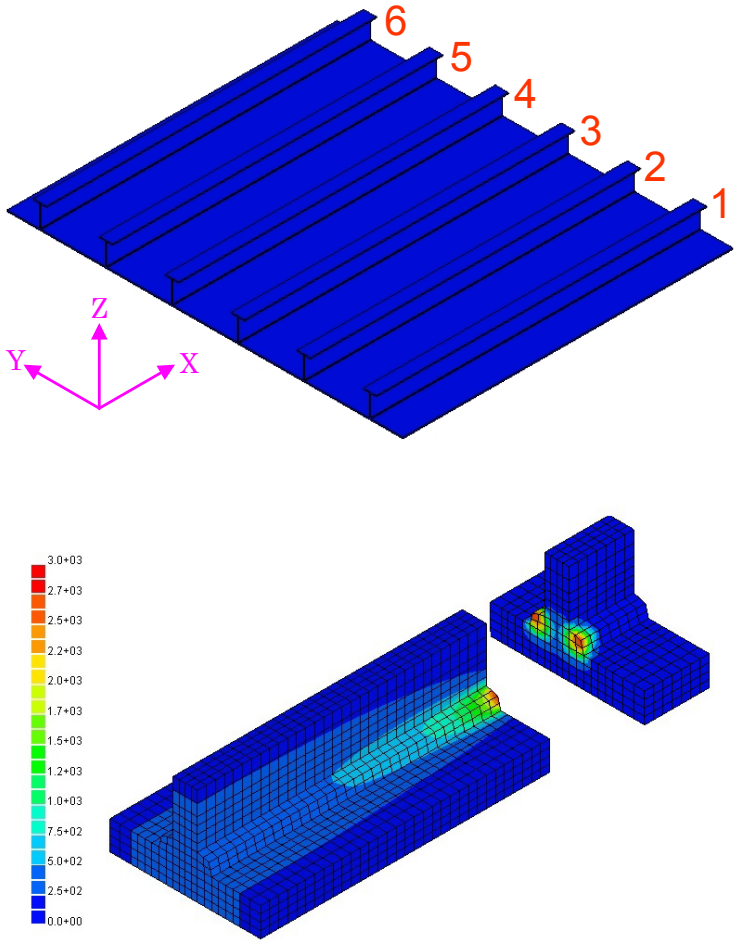

Fig. 4.13 Welded structure with six stiffeners

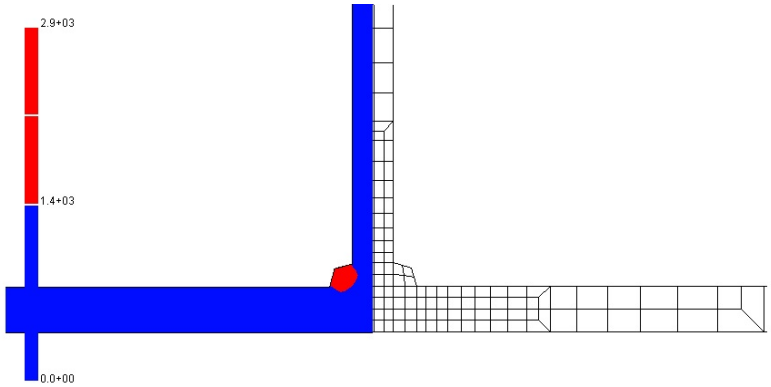

Fig. 4.14 Local fine mesh and penetration shape predicted by C-FEM

4.3.2 Analysis by proposed methods

The stiffener model was analyzed by proposed dynamic mesh refining method and heat transfer localization method. For both cases, the interval for updating active region or computational mesh is 15s during heating.

The initial coarse mesh and refined mesh for DMRM are given in **Fig. 4.15**. Two-level hierarchical mode is employed by radius control with parameter 95*mm* and 45*mm*, respectively. If the coarse mesh is refined along all the welds, the total number of elements and nodes after refining are close to those in model analyzed by C-FEM. Transient temperature distribution for DMRM at t=30*s* is shown in **Fig. 4.16**. The temperature accommodated well within the refined mesh.

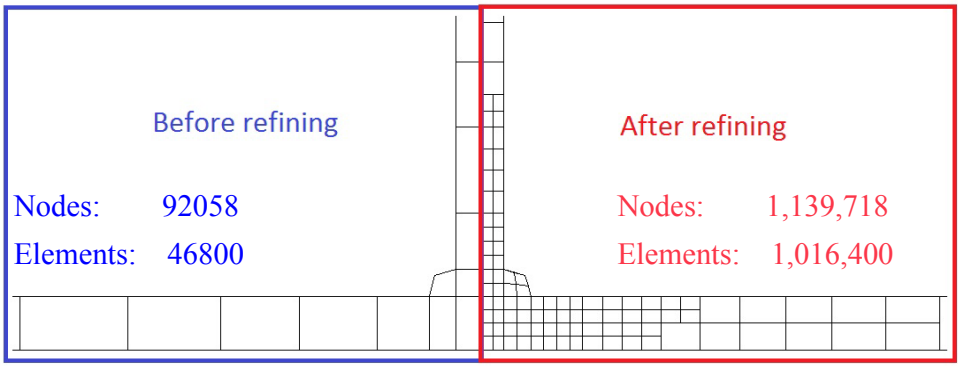

Fig. 4.15 Mesh pattern before and after refining

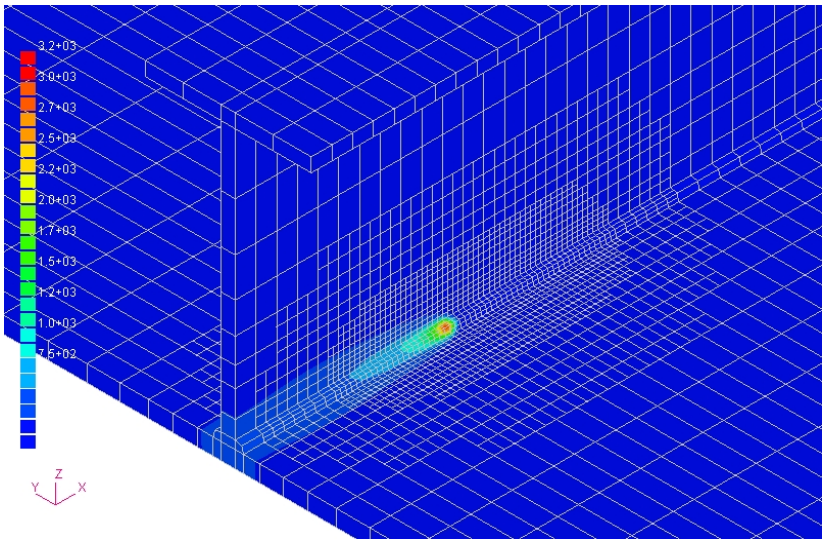

Fig. 4.16 Transient temperature distribution at welding time t=30s for the third stiffener

In the analysis by HTLM, the radius and temperature parameter was set as 80mm and 300℃. The solution domain at t=100s can be seen from **Fig. 4.17**. It clear shows

that region near heat source is selected by radius while rear part by temperature. The corresponding transient temperature distribution is shown in **Fig. 4.18**.

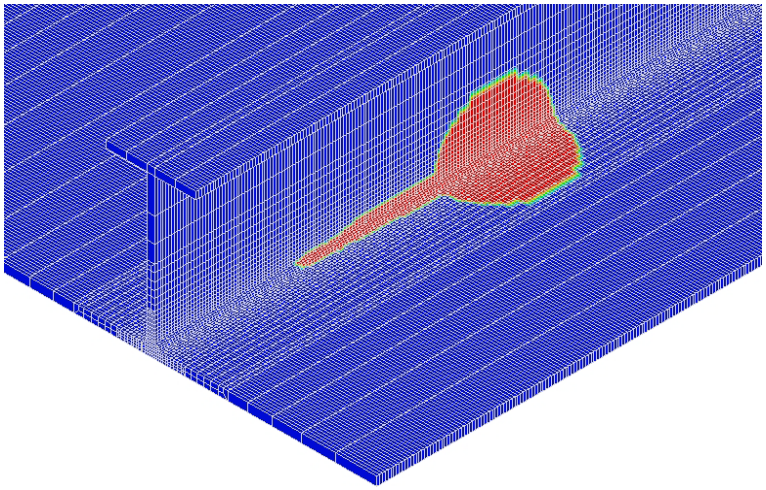

Fig.4.17 Computation domain within finite element model (HTLM)

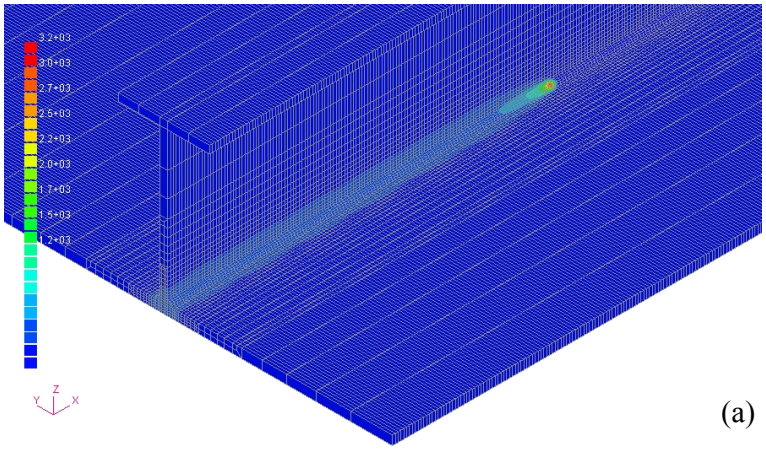

Fig.4.18 Transient temperature at t=100s for the 1st stiffener: (a) Solved by fine mesh (b) Solved by coarse mesh

A comparison among solutions by C-FEM, HTLM and DMRM was plotted in **Fig.4.19**. The maximum temperature, the shape of contour are all close to each other. The computational results confirm that, temperature has large gradient around the heat source. Mesh density can be designed based on the temperature distribution for efficient computation.

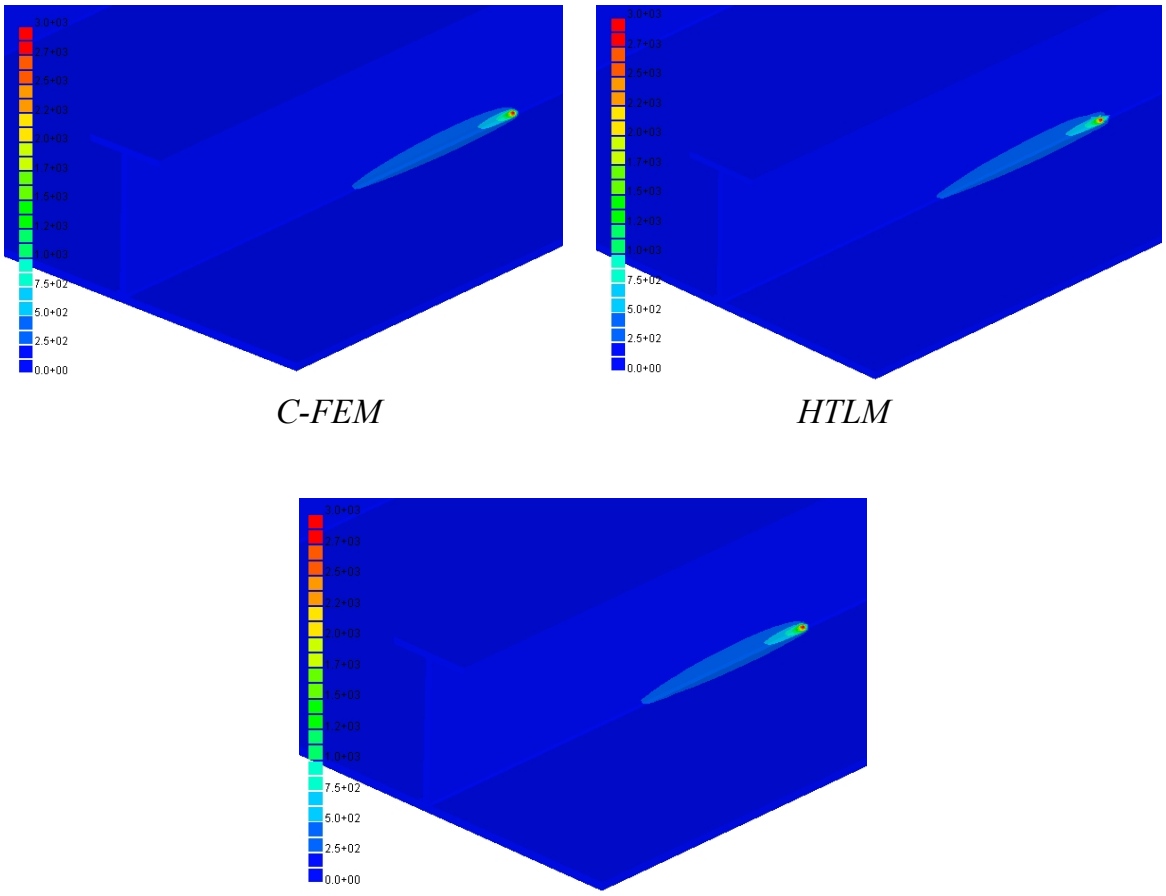

C-FEM *HTLM*

DMRM

Fig. 4.19 Comparison of temperature contours at t=150s

The computation information by different methods is summarized in **Table 4.2**. Compared with C-FEM, DMRM consumed just 1/7 of computation time and 1/5 of physical memory. In the case of HTLM without renumbering, the CPU time is reduced to about 1/3, while the memory was only 1/16 of that solved by C-FEM. With node renumbering, the CPU time is reduced to 1/12 (**Fig. 4.20**). Because the band width of the global matrix is narrower after renumbering, and the sparse solver becomes more efficient in solving simultaneous equations. It is confirmed that computation time and physical memory has been greatly reduced by the developed methods.

Table 4.2 Computation information

Computations	C-FEM	DMRM	HTLM	HTLM (Renum)
CPU time (h)	61.2	8.3	22.1	5.1
Memory (GB)	8.1	1.6	0.5	0.5

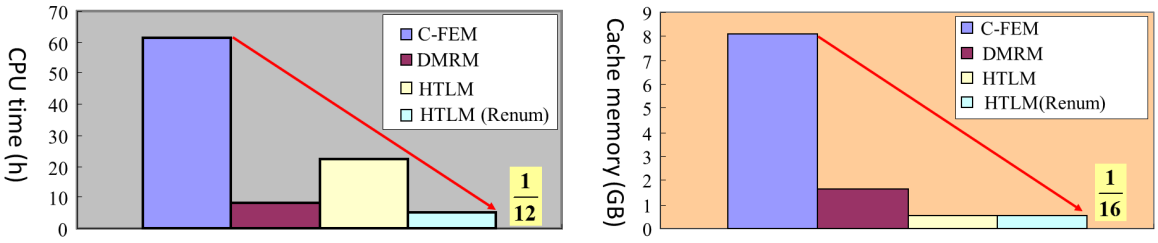

(a) (b)

Fig. 4.20 Comparison of cost by each method: (a) CPU time (b) cache memory

4.4 Summary

In this study, two efficient schemes for temperature analysis namely HTLM and DMRM were proposed and investigated. Based on the computational results, the following conclusions can be drawn:

(1) Heat transfer localization method (HTLM) employs a fine mesh to predict the temperature distribution around the heat source, and a coarse mesh to calculate temperature for outer region. The numerical results of the dual mesh analyses was combined through proposed mapping process. The size of region to be solved in the fine mesh can be effectively determined based on one-dimensional temperature conduction model.

(2) The mesh was refined with the movement of heat source using criterion of analytical temperature distribution and sweeping a sphere along welding path. Dynamic mesh refining method (DMRM) can accurately trace the temperature history at each point, and computation time is greatly reduced compared with C-FEM.

(3) The temperature analysis of a stiffener model with over 1 million elements has been completed in 8.3 hours and 5.1 hours using DMRM and HTLM, respectively.

(4) The CPU time and physical memory of temperature analysis has been dramatically reduced by the proposed computation schemes. More acceleration of computation was observed when the model scale grows larger.

Chapter 5 Mechanical analysis and acceleration methods

As mentioned in Chapter 4, the mechanical analysis process consumes most part of the computation cost in a thermal-mechanical analysis. Several notable work aiming to accelerate the process have been presented in Chapter 1. They have shown some extent of potential in solving large scale welded structures. For the purpose of more efficient or even real-time simulation, further development and combination of different techniques should be conducted. In this chapter, some advances towards this target are introduced. Firstly, the inherent strain based ISM and modified ISM are presented. The two methods show improvement in computation efficiency and capability in large deformation problem, respectively. Secondly, the DMRM with multi-level refinement function is demonstrated. The number of DOFs to be solved can be reduced dramatically. As a third, the effective combination of ISM and DMRM was demonstrated. The new code was closely examined with a comparison with a commercial software.

5.1 i-ISM and mod-ISM

In order to solve large scale models with various features, the original iterative substructure method (ISM) [63] was extended to inherent strain based version (i-ISM) and modified version (mod-ISM).

5.1.1 Inherent strain based ISM

The welding is a transient and nonlinear process. However, it has a special characteristic that the size of the nonlinear region is limited in a small area and the remaining large area behaves mostly elastically. Taking advantage of this characteristic, Iterative Substructure Method (ISM) was developed to solve large scale welding problems[99]. In ISM, the whole structure A under welding is divided into strongly nonlinear region B and weakly nonlinear region (A-B) as shown in **Fig. 1.5**.

The ISM is effective to solve large welding problems when the number of elements is less than several hundred thousand. This is due to the fact that analysis on (A-B) region will become comparable with that on B region in aspect of time as the model scale grows. To deal with structures modeled with more than one million elements, further improvement of computational efficiency is necessary. For such a huge problem, the computation of the displacement and the stress of region (A-B) becomes the dominant part of the analysis. To save the computational time for this part, Inherent strain based Iterative Substructure Method (i-ISM) was developed. The idea

of this method is that the inherent strain is produced and changes only in the area close to the current position of welding pool and not influenced by the restraint given in the portion of the structure away from the torch. If the welded structure to be solved is very large, it may not be necessary to solve the whole structure for each temperature step. In this case, only a part of the structure near the welding torch (Region-C) needs to be computed by constraining the boundary of this region as shown in **Fig. 5.1**. The size of the region C will be determined so that the restraint does not introduce an excessive error to the inherent strain. For example, the region to be fixed is determined by the domain swept by a sphere moving with the torch. It can be expected that the error becomes small but the computational time becomes large as the size of region C becomes large. To keep the size of the region C small with maintaining reasonable accuracy, the restraint given to the region outside C is relaxed every N_C steps.

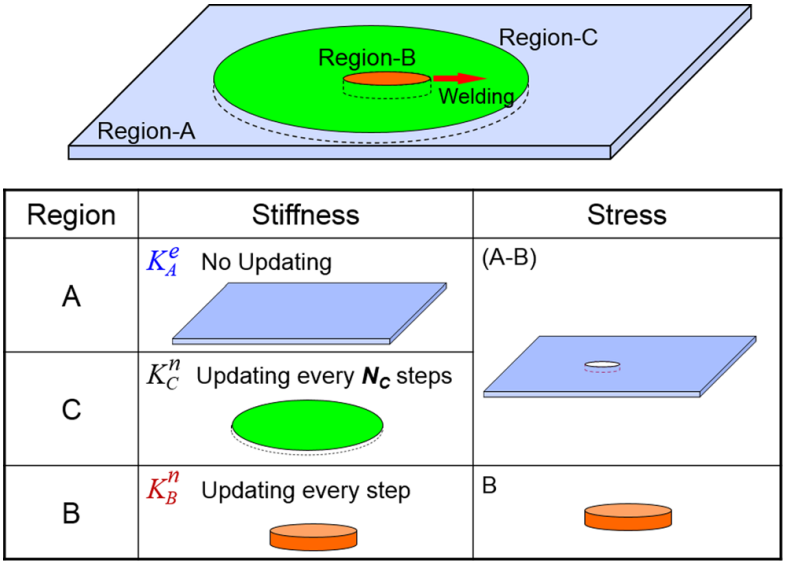

Fig. 5.1 Computation of stiffness and stress in i-ISM.

The initial elastic stiffness matrix of the whole structure $K_A{}^e$ and its inverse are constructed and used for the following computing steps unless they are necessary to be updated. In the case of small deformation problem where element birth is not considered, the stiffness matrix $K_A{}^e$ and its inverse are formed once in the entire computation process. The effect of the nonlinearity associated with the welding thermal cycle is taken into account by the region B which will move with the welding torch. The stiffness $K_B{}^n$ of the strongly nonlinear region B is updated in every temperature increment as shown in **Fig. 5.1**. Regarding the computation of stress, full nonlinear stress-strain relation is employed in both B and (A-B) regions. The continuity of the displacement on the boundary Γ_B between regions (A-B) and B can be maintained directly and the continuity of the traction is maintained through iterative

correction procedure. In this way, all necessary conditions, such as the compatibility condition, stress-strain relation and equilibrium, are satisfied in the whole model A, and the computed result has comparable accuracy as the straight forward FEM. Since the stiffness matrix is updated only for small region B at each step, the computation time can be greatly reduced.

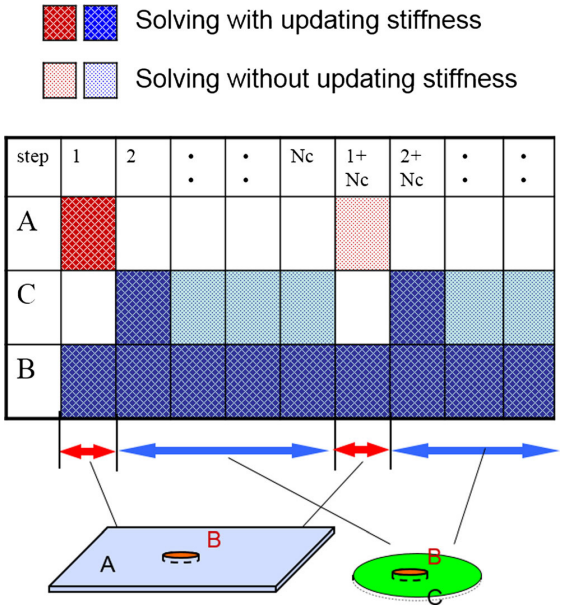

Fig. 5.2 Solution procedure in i-ISM.

Comparing with ISM and i-ISM from the aspect of computing stiffness matrix, the stiffness for the whole model K_A^n is usually constructed and solved in every time step when straightforward FEM is used. The stiffness of the whole model K_A^e is constructed at the beginning of computations and its inverse is saved. Comparing the temperature and its increment in a time step for those two regions, those in region (A-B) are smaller than those in region B. Thus the region (A-B) can be solved once at every $N_{A\text{-}B}$ steps using the saved inverse matrix of K_A^e, while region B is solved with updating stiffness K_B^n every step. In the case of i-ISM, the stiffness of the whole model K_A^e is also computed once as in ISM (**Fig. 5.2**). The difference is that the displacement in region (A-C) which is far enough from the torch is fixed and the region inside C is solved in the same manner as region A in ISM and the stiffness K_C^n of region C is updated every N_C steps. In each step within N_C, the region (C-B) is solved using the same stiffness and region B is solved for $N_{C\text{-}B}$ steps with updating stiffness K_B^n. Thus, the computation of stiffness K_C^n is introduced as an additional process compared to ISM. But the number of steps in which the whole model A is solved has been reduced to $1/N_C$. This is an effective way to reduce the computational time. Results showed that i-ISM is more efficient when the model to be solved is larger[102].

5.1.2 Modified ISM

The basic concept of ISM is that the regions in the whole finite element model with different levels of nonlinearity are divided and solved iteratively until the residuals on the interfaces of these regions converges to a small value. For a small deformation problem, speedup of solution by around ten times can be achieved if ISM is employed.

In the present study, a computation scheme named modified iterative substructure method (mod-ISM) was proposed to solve large deformation welding problems. As shown in **Fig. 1.5**, finite element analysis with ISM was performed in the regions (A-B) and B iteratively and the two regions are coupled during computation. Since the B region is very small, it was possible to find a solution Φ_B within a short time. After the solution Φ_B was obtained, analysis on the full model A was carried out using solution Φ_B as the initial condition. The computation flow of mod-ISM is shown in **Fig. 5.3**. In this study, the B region was defined by elements with a high transient temperature. The boundary between the B region and the remaining region (A-B) were fixed for each degree of freedoms. In the B region, the Newton method was employed in order to achieve a fast convergence. Another difference of mod-ISM from original ISM is that global stiffness matrix in the global region A is formed at previous step and it is updated only when the analysis tends to diverge. Therefore, the computation time can also be saved.

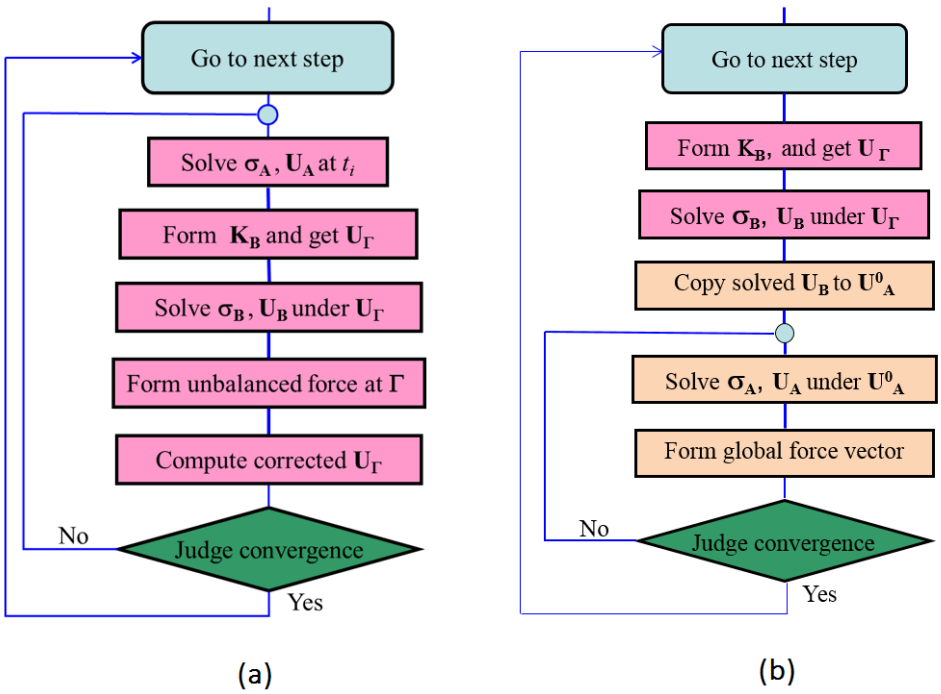

Fig. 5.3 Computation flow: (a) ISM, (b) modified ISM

$\boldsymbol{\sigma}_A$, the stress field of A region

$\mathbf{U}_A$, the displacement field of A region

$\mathbf{U}_\Gamma$, the displacement field at boundary Γ

$\boldsymbol{\sigma}_B$, the stress field of B region

$\mathbf{K}_B$, the stiffness matrix of B region

$\mathbf{U}_B$, the displacement field of B region

$\mathbf{U}^0_A$, $\mathbf{U}_A$ with the nodal solution at B region replaced by $\mathbf{U}_B$

t_i, the time step i

To validate the proposed method, the C-FEM and mod-ISM were employed to analyze the welding distortion of an arc welded lap joint. Two plates with the same material SPCC and the same dimensions (300mm×100mm×3.2mm) were tack welded before welding as shown in **Fig. 5.4**. The filler metal was MG-50T. A metal active gas (MAG) welding process with shield gas 80%Ar and 20%CO_2 was employed and the welding parameters were 160A for current, 18V for voltage, 9mm/s for speed.

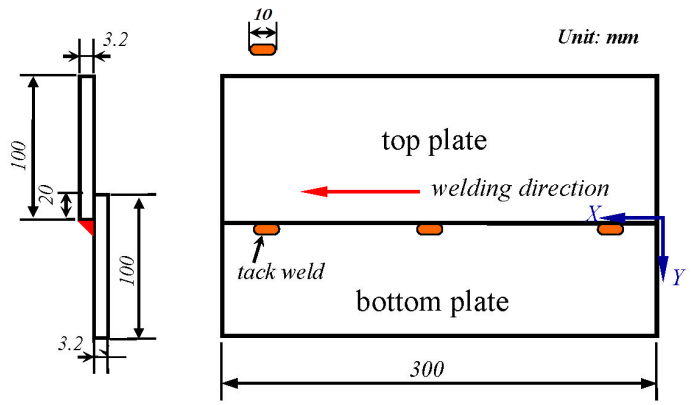

Fig. 5.4 Setup of welding for the lap joint

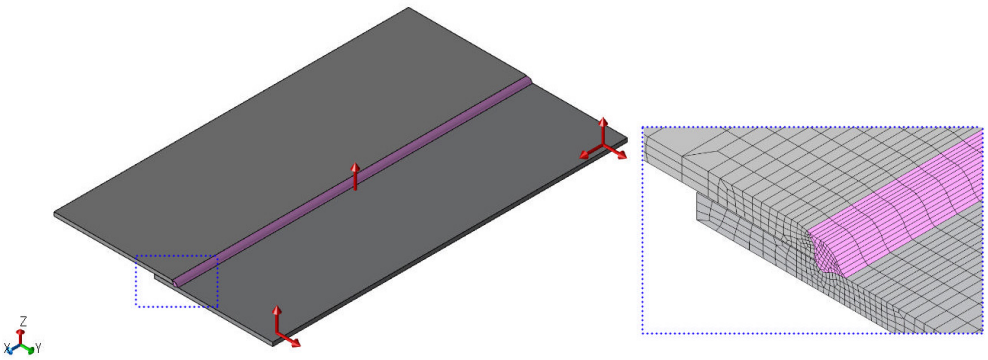

Fig. 5.5 Finite element model of lap welded plates

The finite element model for the lap welded plates is shown in **Fig. 5.5**. The numbers of elements and nodes are 33,800 and 41,145, respectively. Only six freedoms were constrained to prevent the rigid motion of the FE model. The

temperature dependent material properties are shown in **Fig. 5.6**.

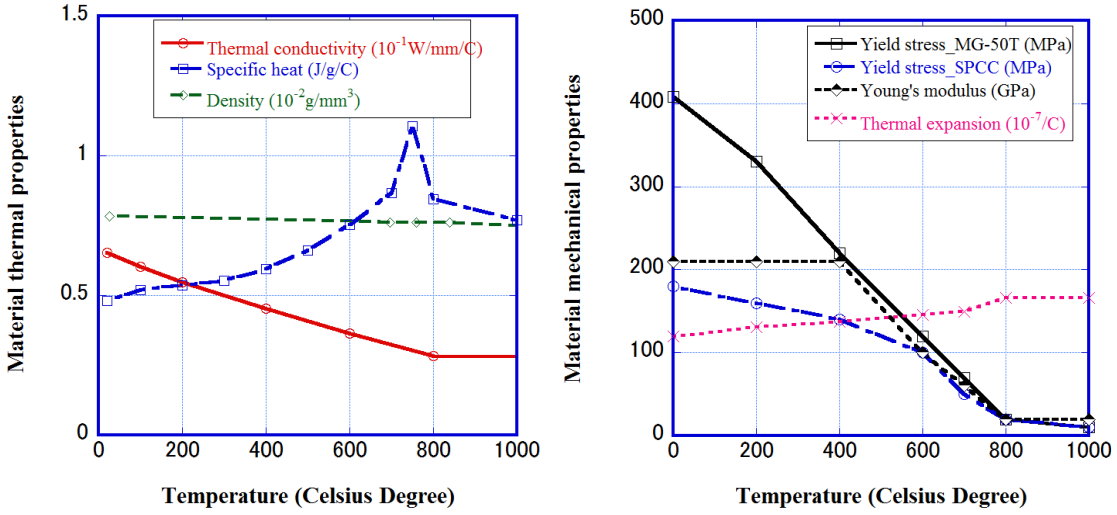

(a) (b)

Fig. 5.6 Material properties: (a) Thermal properties (b) Mechanical properties

After computation using mod-ISM, the transient out-of-plane displacement *Uz* at point A of the bottom plate and the point B of the top plate was compared with that using C-FEM as shown in **Fig. 5.7**. Due to the thermal expansion during heating stage, the top plate deflected to the positive *Z* direction and the bottom plate bent to the negative *Z* direction. After cooling, the opposite deflections at the top plate and bottom plate were induced by the thermal contraction. The deformation computed by C-FEM and mod-ISM has a very good correlation. The computation time for the arc welded lap joints was 5.2 hours by C-FEM and 1.3 hours by mod-ISM, respectively.

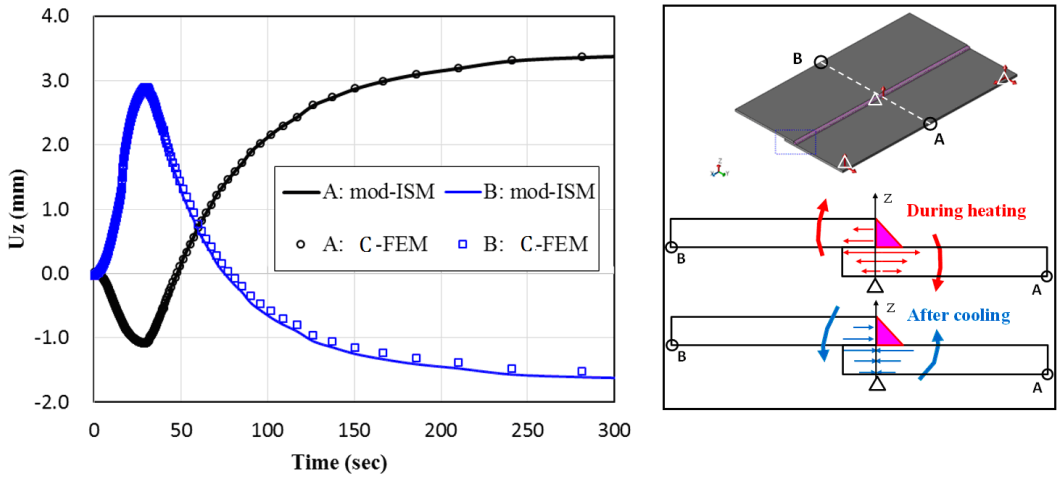

Fig. 5.7 Transient out-of-plane displacement at the evaluating points

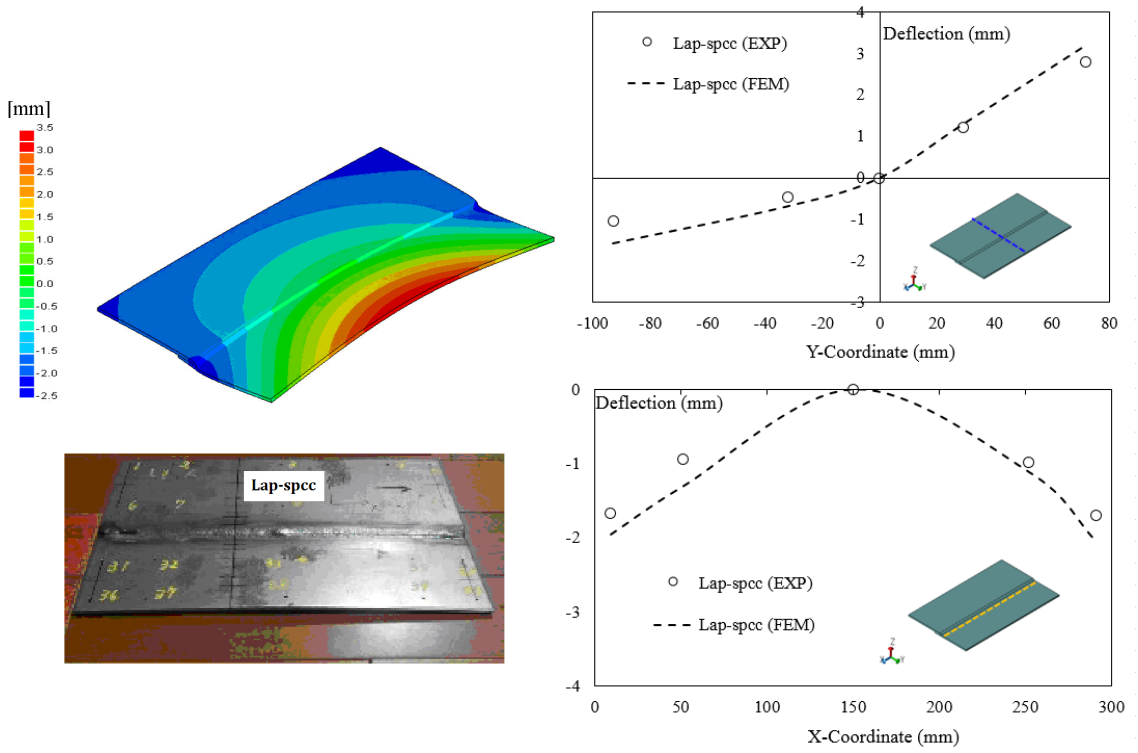

(a) (b)

Fig. 5.8 Welding distortion of lap joint: (a) Numerical prediction and experimental specimen (b) Comparison of deflection along lines

The out-of-plane deformation of the lap welded joint computed by mod-ISM using the large deformation theory was compared as shown in **Fig. 5.8(a)**. It can be observed that the bottom plate has much larger deformation than the top plate. Due to the fillet type weld of lap joint, the top plate was fully penetrated on the edge while the bottom plate was partially penetrated. Thus the bottom plate has a deformation behavior similar to a bead-on-plate welding, which can easily generate a saddle shaped distortion.

The deflection along longitudinal direction and transverse section are shown in **Fig. 5.8(b)**. It can be readily seen that the out-of-plane deformation mode has a convex shape along weld line. And the deformation mode has a concave shape along the transverse direction.

In order to examine the effect of the large deformation, the analysis with small deformation theory was also carried out for the Lap-spcc joint. **Figure 5.9** shows the comparison of out-of-plane deflection (displacement in the *Z* direction) solved under small deformation theory and large deformation theory, respectively. It can be found that the analysis with small deformation theory gave much smaller deflection.

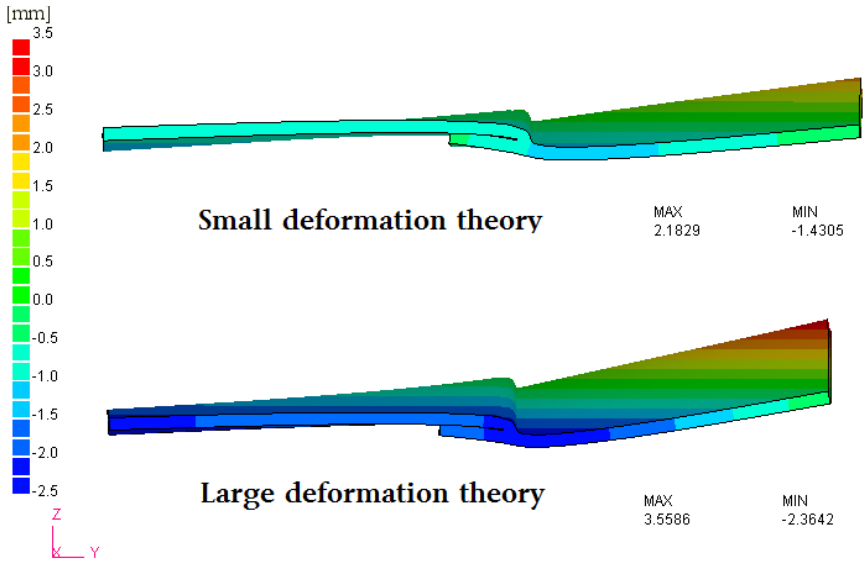

Fig. 5.9 Out-of-plane deformation (Scaled by 5 times) computed based on small deformation theory and large deformation theory

5.2 Dynamic mesh refining method with multi-level refinement

The basic idea of dynamic mesh refining method was addressed in Chapter 3, and here, application of DMRM in thermal-mechanical process employing multi-level refinement was focused. Its application to line heating was shown in the present study, and a comparison between in-house code DMRM and a general purpose code ABAQUS had been made to validate the accuracy and efficiency of proposed method.

5.2.1 Background mesh with multi-level refinement

In welding and line heating processes, the heat source travels along a predefined path. In the case of paths without overlapping or crossing of heating lines, all material points generally only involves single thermal cycle. It is reasonable to refine the region only when the heat source approaches. After the heat source travels away, the region can be coarsen until the end of process. The accuracy of solution especially displacement field could be guaranteed if the region to be refined is large enough. However, the stress and strain results usually scarifies in accuracy due to the mapping procedure. In the case of multi-pass welding where material points experience multiple thermal cycles, the error during remeshing becomes even larger. Furthermore, the resolution of numerical results strongly depends on the level of refinement. Since large number of data is carried by refined elements, the resolution disappears when the elements are combined into one coarse element. As the main advantage over conventional remeshing methods, a background mesh has been introduced in the

dynamic mesh refining method. The purpose is to record the stress and strain for all fine elements and update them when necessary.

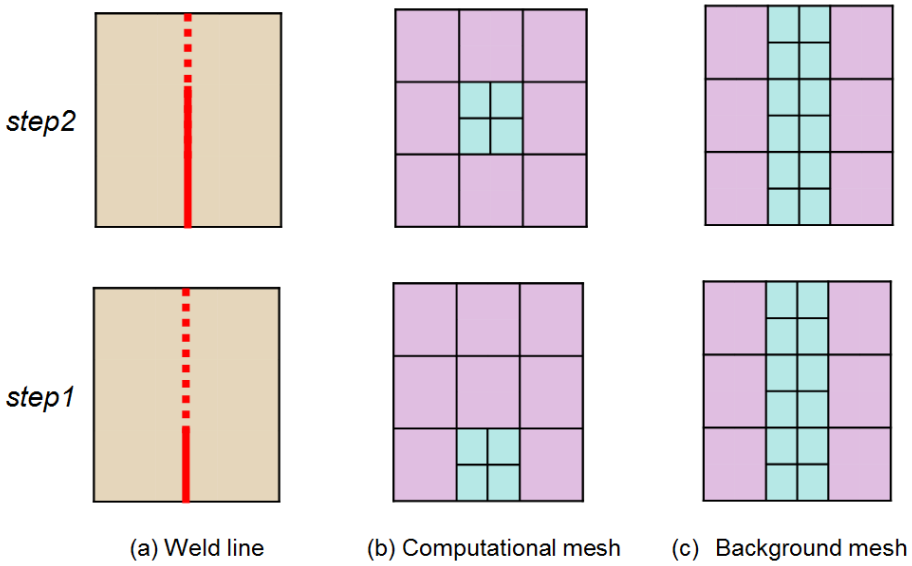

Fig. 5.10 Overview of dynamic mesh refining method (DMRM)

The background mesh can be designed in two ways. The first way is to refine each element in the coarse mesh into finest level. In this case, no interface exists in the refined mesh. It is easy to make comparison between conventional FEM like ABAQUS using the same finite element model. The second way is to refine elements near the weld lines only. That means, the background mesh consists of elements at different levels (**Fig. 5.10**), transformation matrix should be used in formation of element stiffness and load vector as discussed in **Section 2.3**. In this case, the mesh has fewer number of elements, and the computation is more efficient compared with the first case.

5.2.2 Verification by a line heating problem

A twisting type line heating model was analyzed, and a comparison between in-house code DMRM and a general purpose code ABAQUS had been made to validate the accuracy and efficiency of proposed method. The version of ABAQUS is 6.10 which is released on 2010. Similar to previous numerical examples, the decoupled thermal-mechanical analysis was performed in order to save computational cost. The user subroutine DFLUX was employed in the thermal conduction analysis. The ABAQUS standard module with New-Raphson method was adopted for both thermal and mechanical analysis. The automatic control in time increment was activated during the analyses. The input data for the two codes are the same.

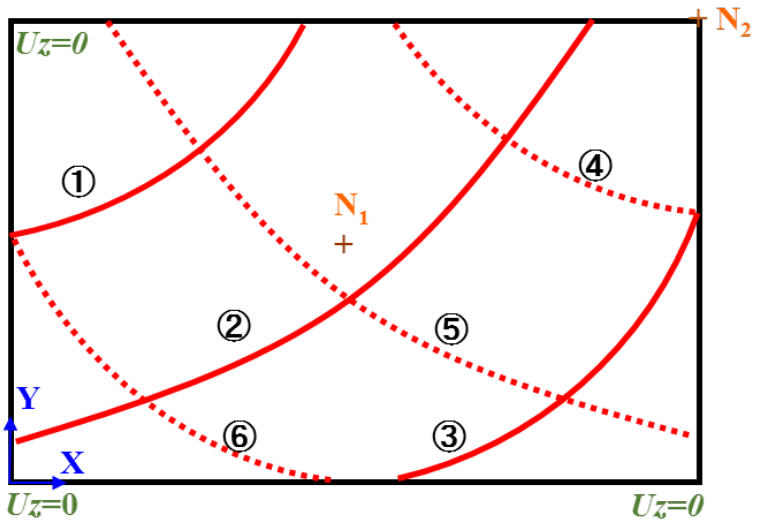

Fig. 5.11 Rectangular plate with 6 heating lines

Line heating on a rectangular plate as shown in **Fig. 5.11** was analyzed by in-house code DMRM and ABAQUS. Three heating lines are on the top surface and another three lines are on the bottom surface of plate. In the heat transfer analysis, the Gaussian surface heat source as shown in **Fig. 5.12** was adopted, and the characteristic radius r_e is =20 mm. The heating conditions for the plate are listed in **Table 5.1**.The boundary condition in mechanical analysis prevents rigid body motion only, with three corner points of plate fixed in out-of-plane direction. Two nodes N_1 & N_2 marked on the plate are used to record the transient displacement.

Table 5.1 Line heating conditions of the rectangular plate

Dimension	*Heat*	*Velocity*	*Material*
900×600×6mm	8000 W	16 mm/s	SM400A

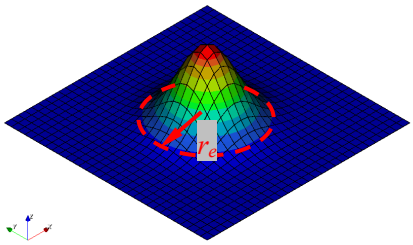

Fig. 5.12 Gaussian surface heat source

The corresponding equations of the heating lines are as follows:

$$y=\begin{cases} x^2/(500n+100)+(600-250n) & (1\le n\le 3) \\ (x-900)^2/(500n-1400)+(1350-250n) & (4\le n\le 6) \end{cases} \tag{5.1}$$

Size of an element in initial coarse mesh is $50\times 50\times 3mm$, and three levels of refinement was employed to generate computational mesh and background mesh. In the first and the third level refinement, elements were subdivided in X and Y directions; and in the second level refinement elements were subdivided in X, Y and Z

directions. Thus the minimum element size in BM and CM is $6.25 \times 6.25 \times 1.5mm$. The computational meshes at the intermediate stage of heating lines 1&2 are shown in **Fig. 5.13**. With multi-level hierarchical refinement, the number of DOF could be decreased significantly. The finest element in the numerical model for ABAQUS and DMRM are the same.

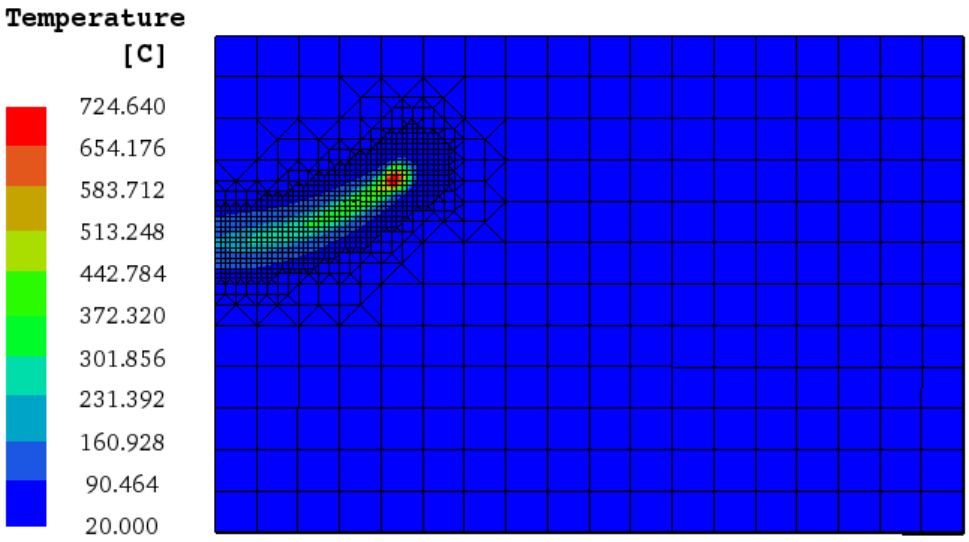

(a)

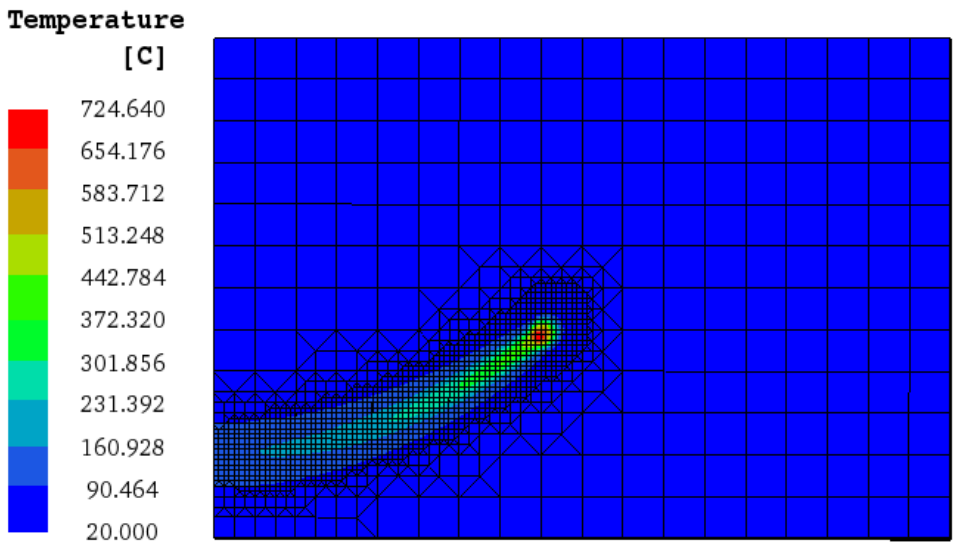

(b)

Fig. 5.13 Computational meshes: (a) Heating line ① (b) Heating line ②

Figure 5.14 shows the comparison of transient out-of-plane displacement at two evaluating nodes on the top of plate. Due to the angular distortion, the nodes displaced in the negative direction of Z axis. The heating of line ② has the largest contribution to

the final deformation, and heating of line ⑤ has the second largest contribution. It also can be observed that, the deformation mostly occurred during heating stage and early cooling stage. The slight discrepancy between solution of ABAQUS and DMRM came from the thermal analysis. Because the numerical modeling aspects such as transient heating region and integration scheme of thermal equation are different for the two codes.

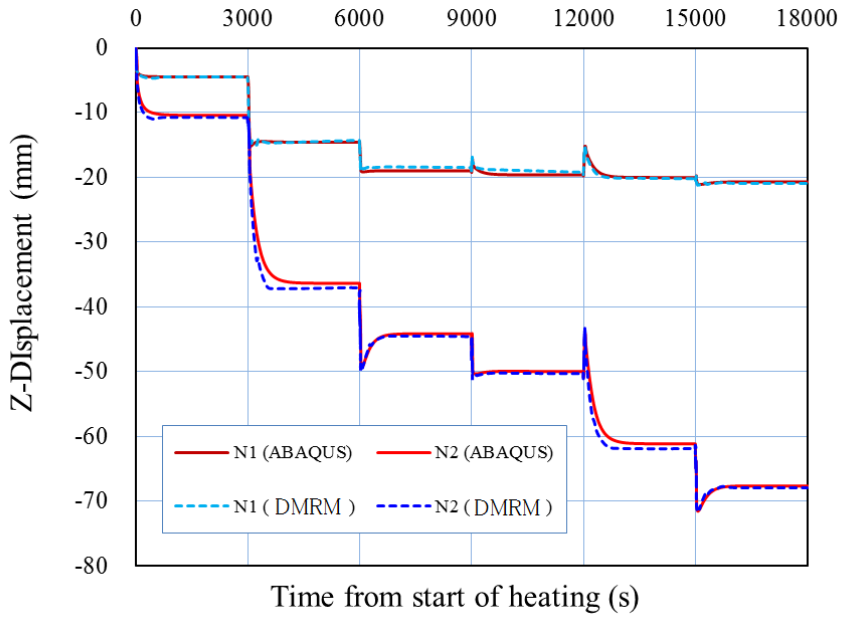

Fig. 5.14 Transient out-of-plane displacement at evaluating nodes N1 & N2

After the all heating lines were completed, the contour of out-of-plane displacement is plotted in **Fig. 5.15**. A typical twisted distortion was obtained with maximum deflection 67 *mm*. Comparing with the thickness of the plate 6 *mm*, the ratio of deflection to thickness is over 11 times. Large deformation theory was employed for the thermal elastic-plastic analysis. And the analysis under small deformation theory gave a much smaller defection as 45 *mm*. The final shape of the rectangular plate is not ideally smooth, because the contour lines is a form of segments. It can be confirmed that, the solution obtained by DMRM has comparable accuracy with that by ABAQUS.

The contour of residual Mises stress is plotted in **Fig. 5.16**. The results indicate that final heating lines dominate the distribution of Mises stress. Because the subsequent heating has a heat treatment effect on previous heated lines. In the case of stress on background mesh, fairly smooth distribution across elements in different level of refinements can be seen.

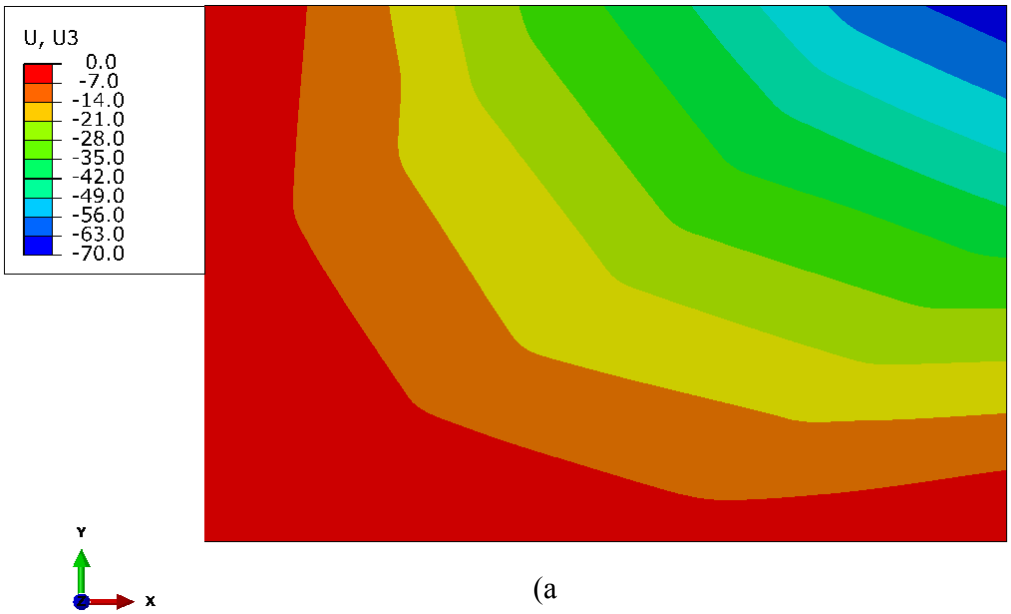

(a

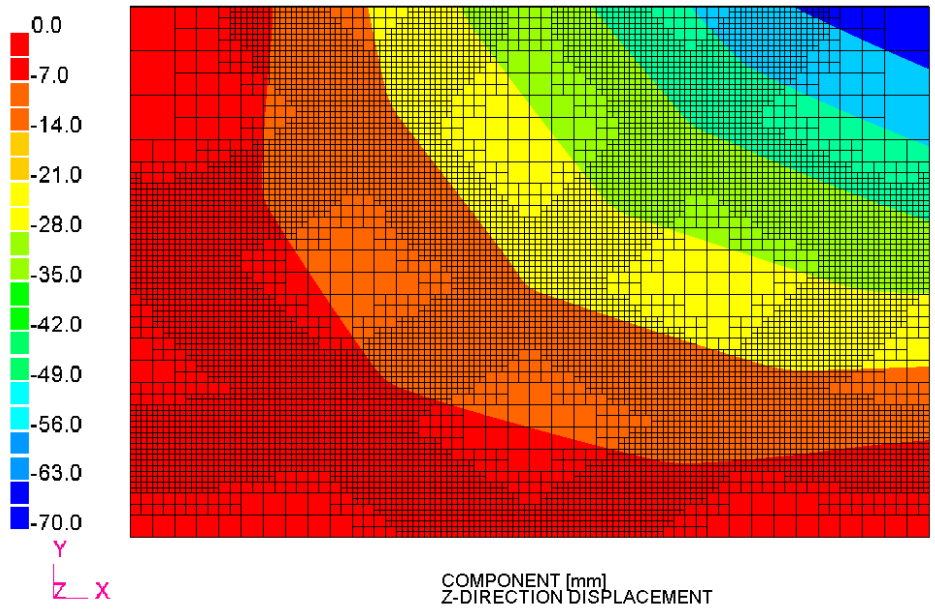

(b)

Fig. 5.15 Contours of residual out-of-plane deformation: (a) by ABAQUS (b) by DMRM

The distribution of Mises stress solved by ABAQUS has some discontinuity and oscillation, which may be induced by the large time increment as determined by automatic process. Because temperature is sampled at limited number of time steps, large time increment is bypassed if equilibrium is unilaterally satisfied for the mechanical analysis. It is advisable to set a upper limit for the time increment for ensuring smooth temperature and stress distribution.

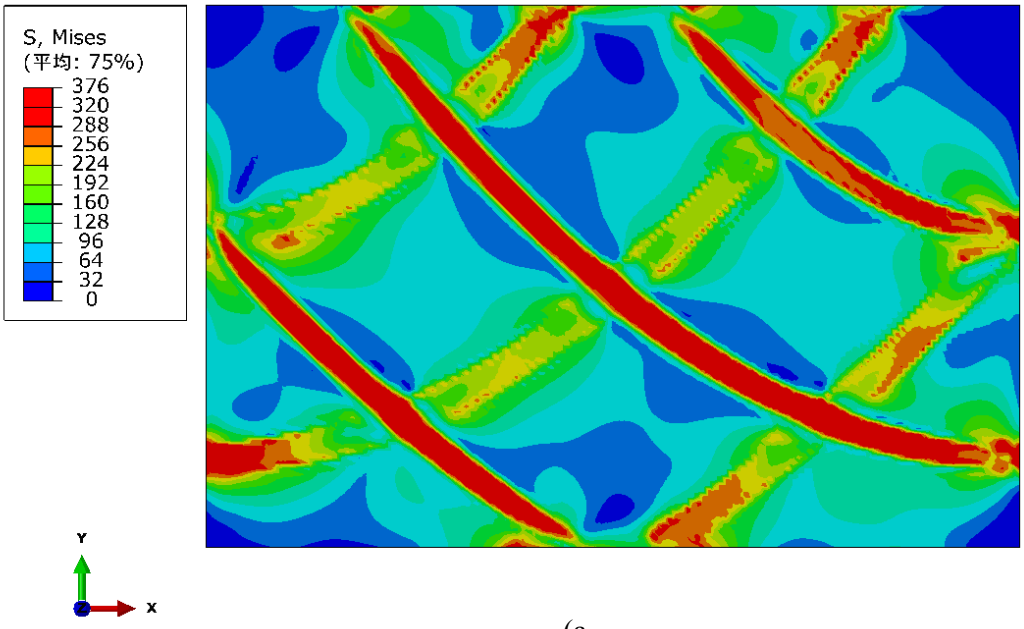

(a)

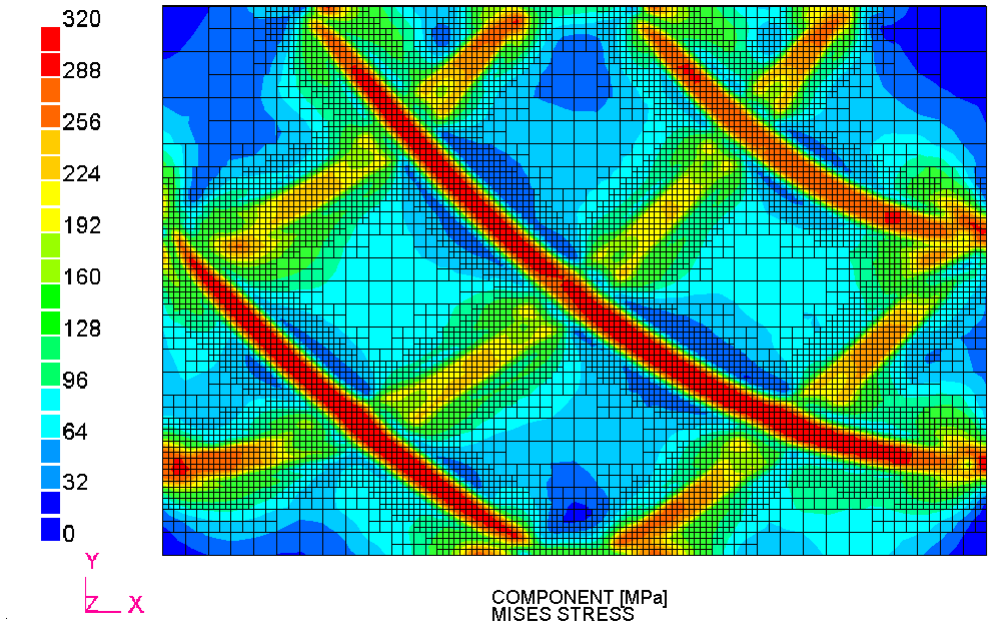

(b)

Fig. 5.16 Contours of residual Mises stress: (a) by ABAQUS (b) by DMRM

The average number of elements in the computational mesh during all time steps was 7,030 while the number of elements in the background mesh is 47,936. Since the temperature field and displacement field were frequently solved on CM which had much fewer degrees of freedom than BM, computation time necessary to solve large simultaneous matrix was greatly reduced. The analysis using DMRM and ABAQUS took 1.9 hours and 75.5 hours, respectively.

5.3 Combination of mod-ISM and DMRM

5.3.1 Features of two numerical methods

In many computation methods, including the DMRM, all regions are solved simultaneously as a whole. The iterations until convergence basically depends on the strongly nonlinear region B, which takes up just a small portion of the whole model. Therefore large amount of computation cost are spent to solve region A. To solve the two regions separately, the iterative substructure method has been developed. However, the mesh predefined with fine elements near the weld does not change during the whole analysis.

In the case of dynamic mesh refining method (DMRM), the mesh is adaptively created according to the transient position of heat source. Number of DOFs to be solved can be greatly reduced compared with a fixed mesh. Therefore, it can be understood that, the dynamic mesh refining method reduces the unknowns in the global region A and iterative substructure method deals with nonlinearity in the local region B. Combining these two different techniques has a great potential to solve large scale thermo-mechanical problems.

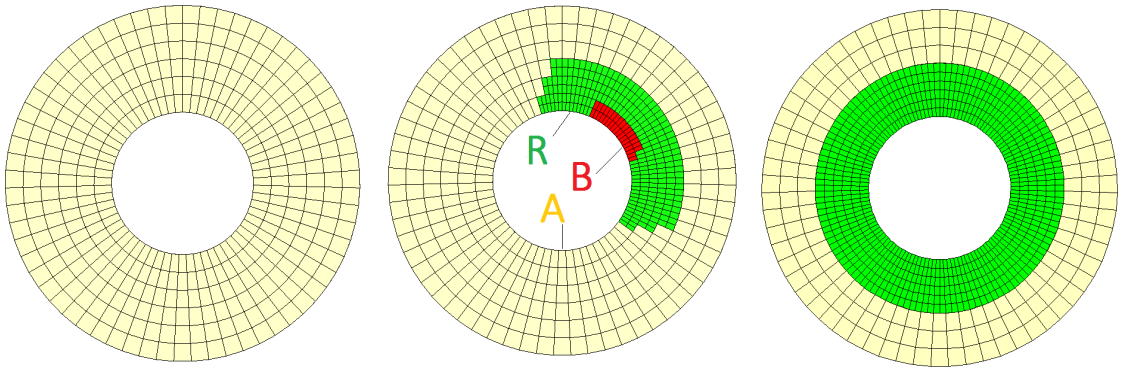

Fig. 5.17 Different meshes employed in the dynamic mesh refining and iterative substructure method

It becomes natural that, a fine mesh can be used in region B and the region nearby namely region R, and a coarse mesh can be used elsewhere (**Fig. 5.17**). For this purpose, refinement on an initial mesh (IM) with coarse elements is adopted. The fine mesh is then moved with the heat source, and the elements in the welded zone behind the heat source return back to coarse mesh.

5.3.2 Computation flowchart

Due to the complexity of original ISM program, the modified ISM which solves region B only at the beginning iteration was implemented in the current code DMRM*. Another advantage to use mod-ISM is that, large deformation problem can also be well solved because the strong coupling between region A and region B is removed.

The detailed computation flowchart of DMRM* is shown in **Fig. 5.18**. Three main modules including mesh refinement, thermal analysis and mechanical analysis are organized in a loop. Iterative substructure method is only employed in the mechanical analysis which generally takes up most part of computation time. The relation among initial mesh (IM), computational mesh (CM) and background mesh (BM) is depicted in the flowchart.

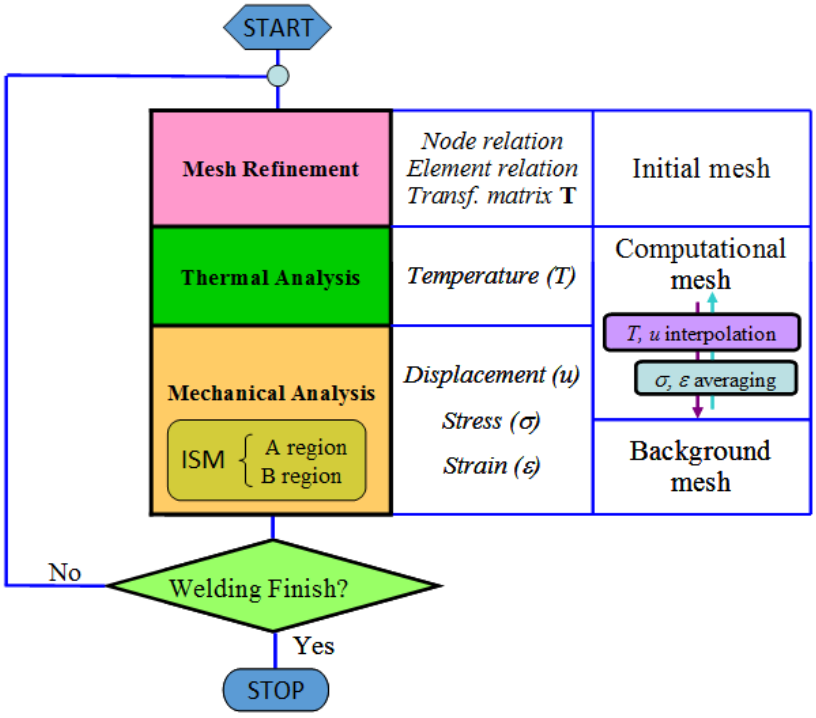

Fig. 5.18 Computation flow of DMRM*

5.3.3 Numerical validation by fillet welding of a flange to a pipe

A flange-to-pipe welding problem as shown in **Fig. 5.19** was analyzed by ISM, DMRM* and a general purpose code ABAQUS. ISM is the iterative substructure method which has been well validated for its accuracy. As introduced in previous section, DMRM* is the new version of program with combined mod-ISM and dynamic mesh refining method DMRM. Automatic time increment control was adopted in ABAQUS code to achieve the maximum speedup. Double ellipsoidal heat source was used to model the heat flux generated by welding torch. The weld metal

and based metal were assumed to be the same material SM400A. Four points on the section 90 degree from the welding start position were evaluated for temperature evolution. **Figure 5.20** shows the transient temperature distribution analyzed by DMRM*, and the different regions depicted by elements. B region was defined as elements with transient temperature over 300℃. R region was defined as elements within a sphere (radius 60mm) centered at the heat source position. As shown in **Fig. 5.21**, the temperature profiles calculated by the different codes have good correlation except for small deviation at peak values. The differences in numerical aspects such as heated region definition at each time steps and integration scheme of thermal equation could be reasons for this phenomenon.

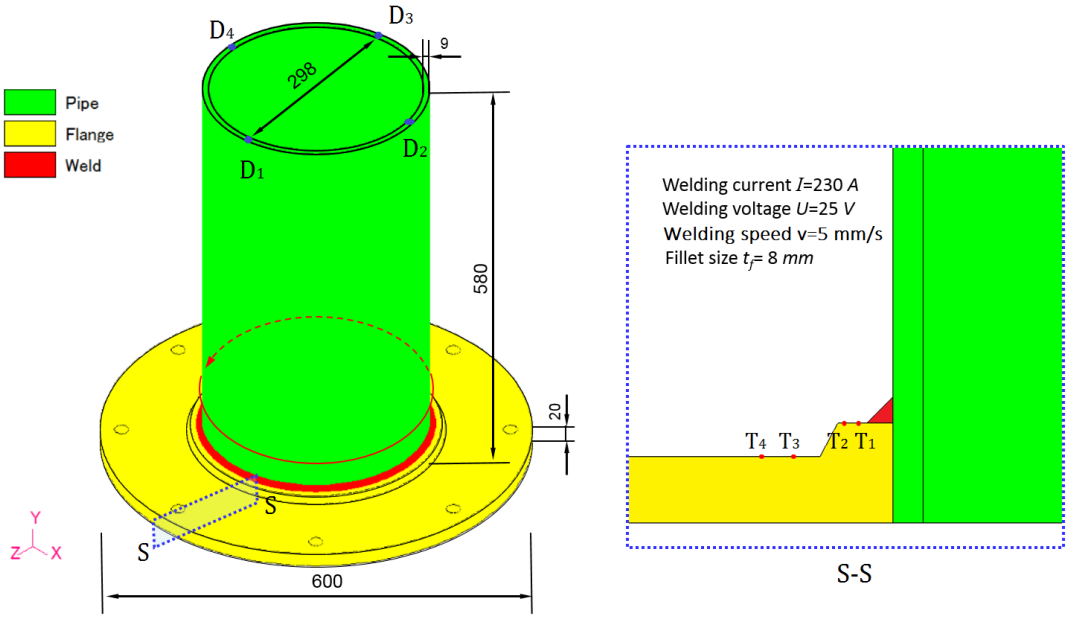

Fig. 5.19 Geometrical model of flange welding

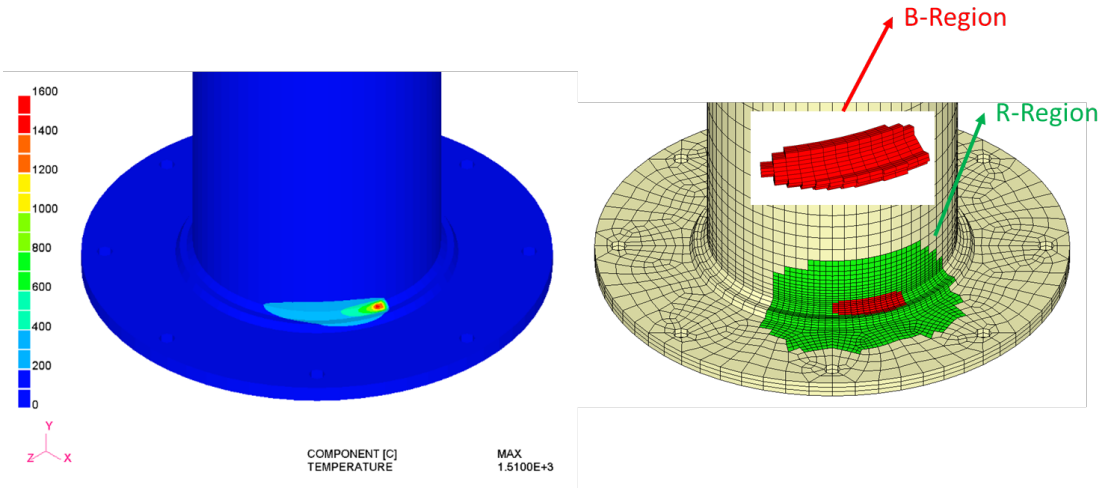

Fig. 5.20 Transient temperature distribution and different regions depicted by elements

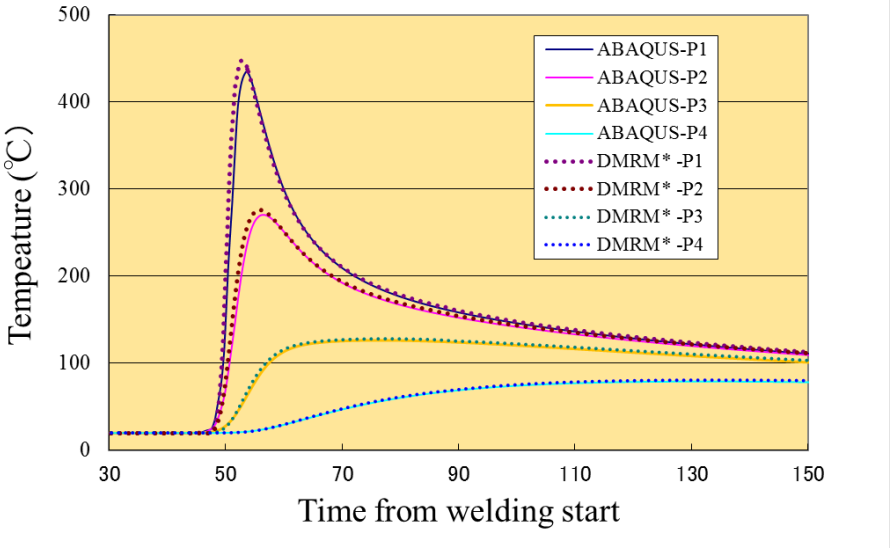

Figure 5.22 shows the comparison of transient axial displacements at another four points on the top of pipe. The points displaced in the negative direction of Y axis due to the angular distortion between pipe and flange. After the welded component completely cooled down, the contour of hoop stress on section S-S is plotted in **Fig. 5.23**. The inner part of the pipe shows higher tensile stress than the outer part. The weld zone exhibits a relatively lower tensile stress compared with the heat affected zone. It can be confirmed that, the solution obtained by DMRM* has almost the same accuracy with that by ABAQUS.

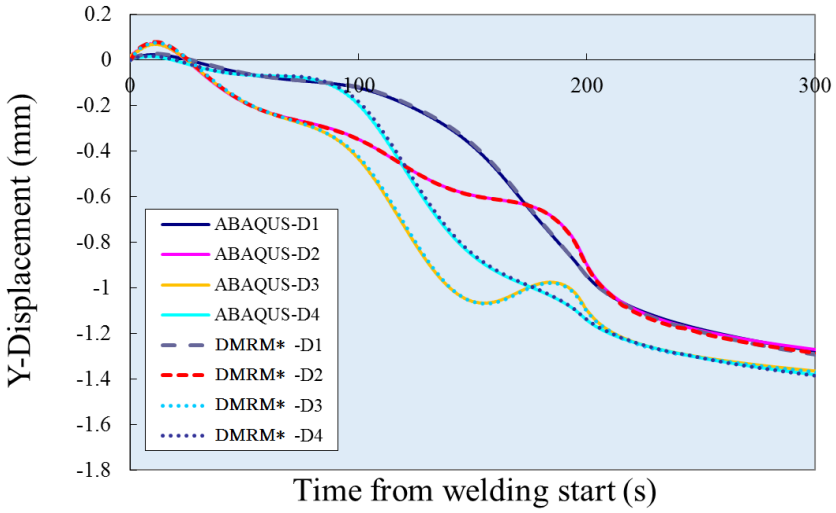

Fig. 5.22 Transient displacements at evaluating points D1-D4

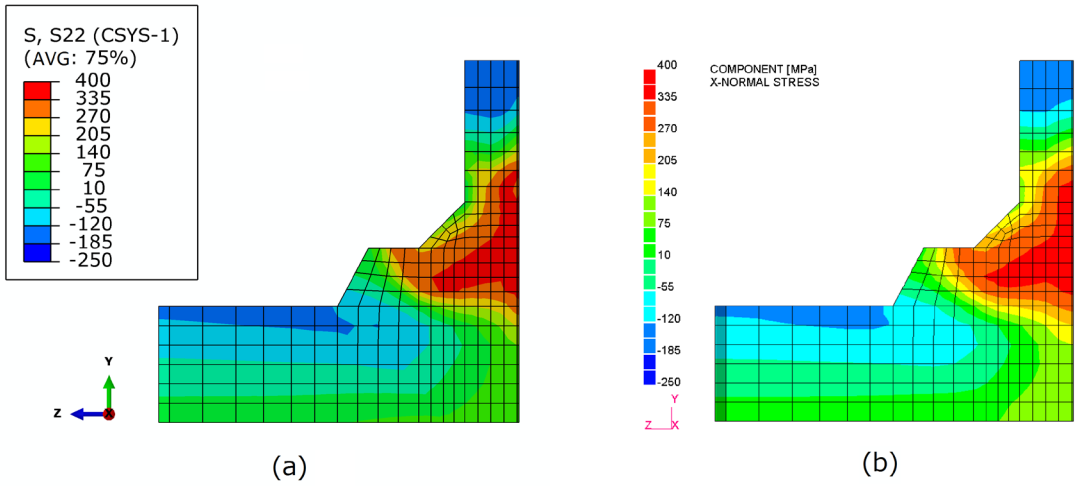

Fig. 5.23 Contours of residual hoop stress: (a) by ABAQUS (b) by DMRM*

The number of elements involved in B region and those in computational mesh during each time step is summarized in **Fig. 5.24**. At the start of welding, the number of elements in both regions increased; while at the intermediate welding stage, the number of elements did not change appreciably due to the quasi-steady state of temperature field. The averaged ratios E_B/E_{BM} and E_{CM}/E_{BM} are 1.7% and 27.9% respectively. Where, E_B, E_{CM} is the average number of elements during all time steps in B region and computational mesh, respectively. E_{BM} is the number of elements in the background mesh. As indicated by **Table 5.2**, the analysis using ISM took much less time than ABAQUS, and the time ratio was about 1/18. By introducing ISM in DMRM*, the computation time was further reduced to 1/56.

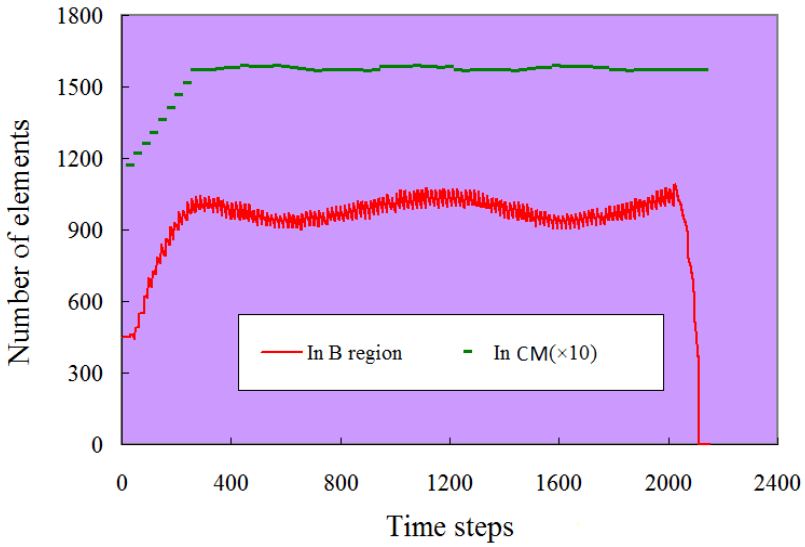

Fig. 5.24 Evolution of elements in B region and computational mesh

Table 5.2 Computation time for each code (unit: hour)

Code used / Analysis process	ABAQUS	ISM	DMRM*
Mesh refinement	*NA*	*NA*	0.04
Thermal analysis	19.6	0.9	0.15
Mechanical analysis	53.3	3.2	1.10
In total	72.9	4.1	1.29

5.4 Summary

In this chapter, the existing advanced method — iterative substructure method (ISM) was extended to solve large scale problem by combining with the concept of inherent strain. The inherent strain based ISM (i-ISM) was developed. The region at a lower temperature is constrained for a time interval and solution is conducted on the region at higher temperature. The stiffness and stress updating schemes on each region was shown and discussed. The i-ISM suggests a good way for future development on fast computation of large-scale problems.

Also, a modified iterative substructure method (mod-ISM) with consideration of the large deformation theory was developed. The welding deformation of a lap joint with the low strength steel was investigated by experimental measurement and numerical simulation. The welding deflection of the lap joint computed under large deformation theory agreed well with the measured one, but that computed by small deformation theory was much smaller. The out-of-plane deformation mode along weld line has a convex shape and that along the transverse section has a concave shape. Same phenomena was observed in the welded specimen. The modified ISM shows a good accuracy in computation of large deformation problem and consumes much less time than the conventional FEM.

In the case of DMRM, mesh refinement in single/multiple direction mode was realized in three-dimensional model. Multi-level refinement could bring large amount of reduction in degrees of freedom. Line heating process on a rectangular plate was analyzed. The refined mesh was easily generated for the curved heating lines. However, in the case of commercial software like ABAQUS, such refinement is currently not available. The computation time of DMRM is much shorter than ABAQUS, and the accuracy of solutions are very close to each other.

Furthermore, the novel techniques—dynamic mesh refining method and iterative

substructure method were successfully combined to solve thermo-mechanical problems in a short time. The feature of welding problems was fully taken advantage to reduce the computation cost. By analyzing a flange-to-pipe welding model with 207,090 unknowns, it was demonstrated that, the computation time of latest version DMRM* consumes just 1/56 of time that used by ABAQUS, while the solution accuracy of the two codes are comparable.

Chapter 6 Typical applications in large scale line heating and welding problems

For large scale line heating and welding problems, the straightforward computation by TEP-FEM has several difficulties: (1) Generation of a finite element model is difficult when there are curved or crossed welding or heating lines. Local refinement in the vicinity of welding lines are cumbersome for general software. (2) Practical structures have dimensions of several meters or more in length and width; it will lead to millions of elements which take quite large memory for global stiffness matrix in the FEM model. (3) Long computation time is required due to large number of elements and time steps. In Chapter 4 and Chapter 5, dynamic mesh refining method and enhanced iterative substructure methods were proposed as efficient numerical schemes in solving thermal-mechanical problems. In this chapter, simulation of large scale line heating and welding problems with these methods especially dynamic mesh refining method were demonstrated.

6.1 Plate Forming by multiple heating lines

Ship hull especially the bow and stern part is assembled by many pieces of plates with complex geometry. These plates usually has a non-developable shape, and it is difficult to be formed to the designed shape from the flat plate by conventional mechanical process using press machine or rolling and bending machine. In most shipyards, the plate forming are manually carried out by skilled workers using line heating. Line heating along multiple paths can generate necessary inherent strain to achieve the target shape. The line heating process needs considerable experience, so the decrease of skilled workers in this area is an urgent problem in shipbuilding. As a substitution, automated system for line heating has now been employed in some shipbuilding companies. It is recognized to be a much more efficient way compared with that operated by skilled workers. To automate all plate forming processes, it is necessary to predict the distortion quantitatively before performing line heating.

The planning of line heating in automated system generally employs the inherent strain method. Stretching strain component and bending strain component are firstly computed based on the initial surface and target surface. And then heating paths can be determined by the distribution of the strain components. Since inherent strain method is an elastic FEM and there are usually some iterative procedures required to obtain the final target shape. On the other hand, combining line heating process with pressing and water cooling can help to improve the work efficiency, for which it is difficult to apply

inherent strain method. Especially, the thick plates (t>25mm) and target curved plates with large curvature require higher computational accuracy. Three dimensional thermal elastic-plastic FEM has flexibility to account for those physical processes. Heating deformation and residual stress are available by transient thermal-mechanical analysis, provided that the large scale simulation can be completed in reasonably short term.

Similar to welding problems, line heating also employs a moving heat source and thermal-mechanical process occur with the progress of the heat source. The accurate heat source model of gas torch has been proposed by Osawa[100][101]. Here, for simplicity, the Gaussian surface heat source was employed. To examine the performance of the proposed DMRM on large scale line heating, a rectangular plate as shown in **Fig. 6.1** was analyzed. The plate had dimensions of 4,500mm in length, 2,000mm in width and 17mm in thickness direction. There were 18 heating lines on top surface and 15 heating lines on the bottom surface of the plate. The scale of the plate and the pattern of heating lines were close to practical cases [49].

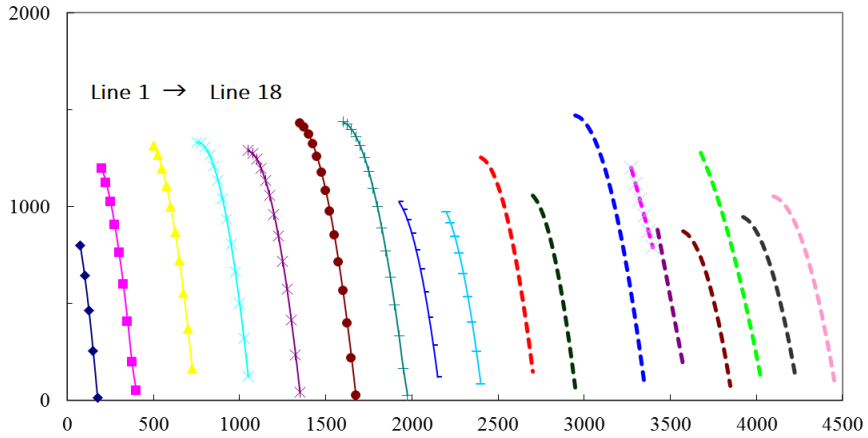

(a)

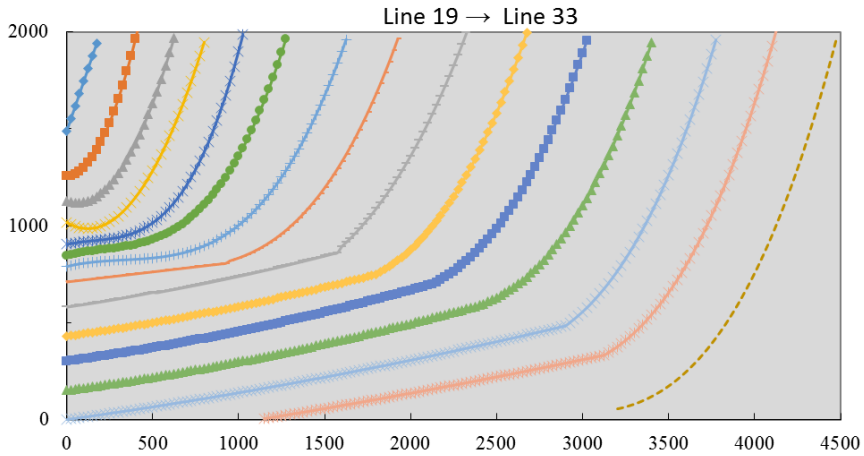

(b)

Fig. 6.1 Dimension of the plate and configuration of heating lines: (a) Top surface (b) Bottom surface

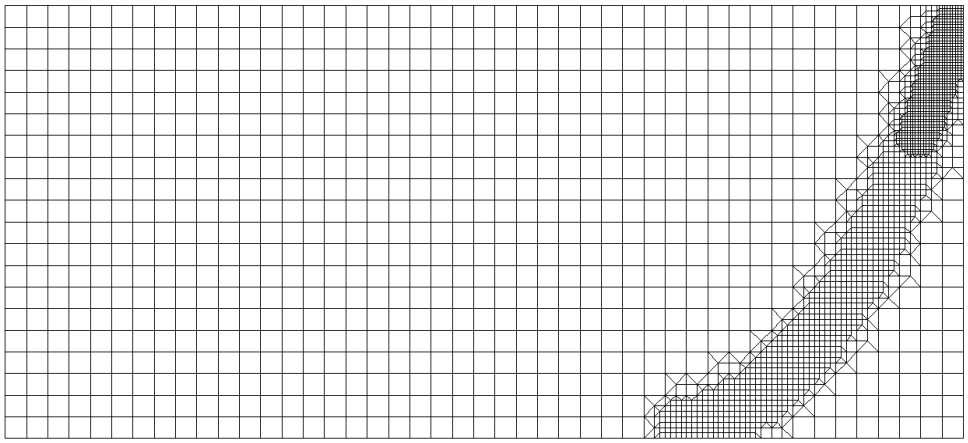

(a)

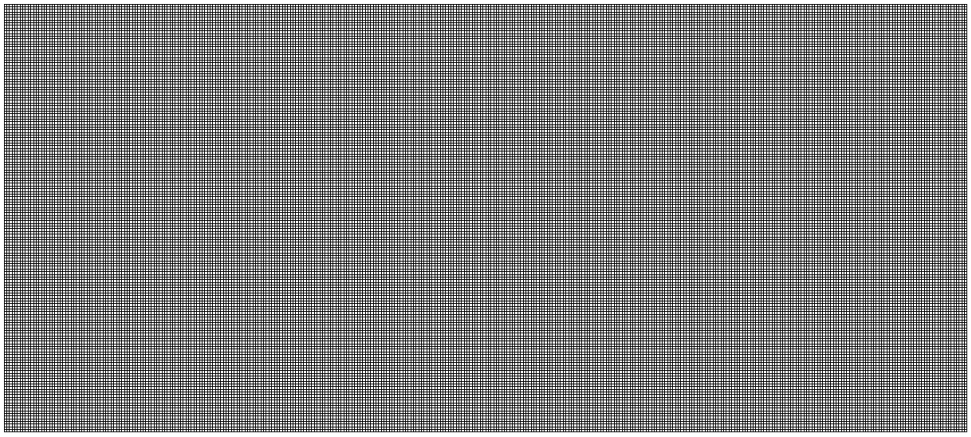

(b)

Fig. 6.2 (a) Computational mesh at final welding stage, and (b) Background mesh

Gaussian surface heat source with characteristic radius r_e=50mm was employed in the thermal analysis. The net heat input was 23,000W, and heating speed was 16mm/s for all heating lines. In this simulation, gravity force and supporting system which exist in practical case had been neglected. Each heating line was started after the previous heating line completely cooled down to room temperature. The same refinement method as the previous example in **Section 5.2** was employed for the computational mesh, while the background mesh had uniform fine elements for easy post processing. The background mesh as shown in **Fig. 6.2** consisted of 406,847 nodes and 345,600 elements with same size 12.5×12.5×2.83 mm. There were 6 divisions in plate thickness direction. Large deformation theory was used to consider the geometrical nonlinearity.

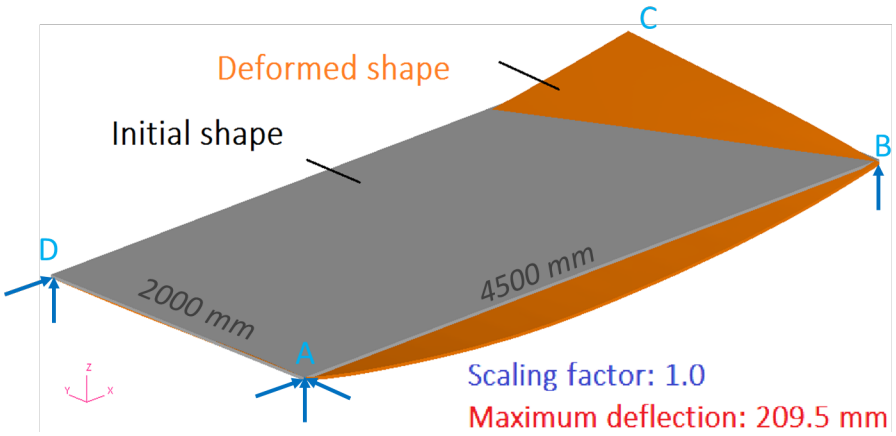

Fig. 6.3 Comparison of initial and deformed shape after heating on top surface

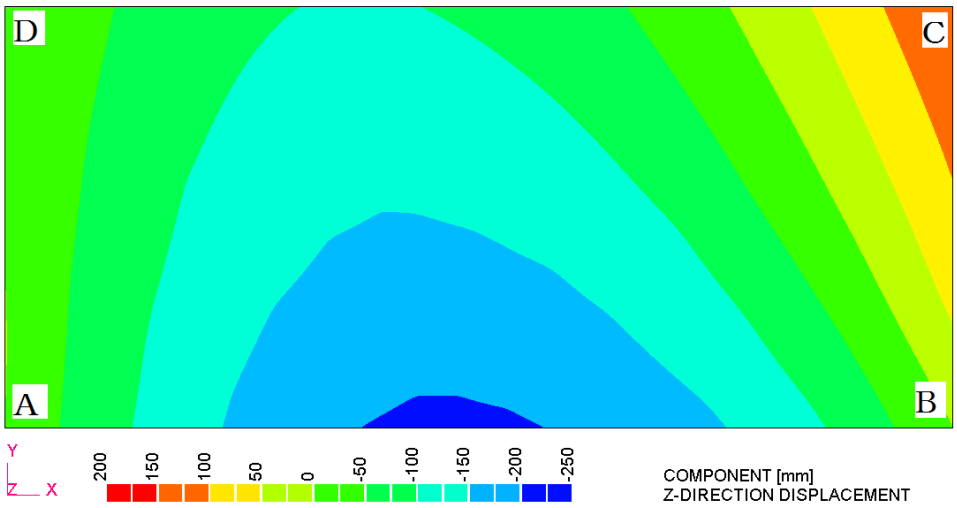

Fig. 6.4 Contour of out-of-plane deformation after heating on top surface

A combined bending and twisting distortion occurred after heating lines on the top surface were completed, as shown in **Fig. 6.3** and **Fig. 6.4**. The deformation along A-B was mainly caused by longitudinal bending, and the magnitude reached 200mm. On the other hand, the deformation along B-C was caused by twisting, and the magnitude reached about 100mm. Meanwhile, the contour of residual Mises stress is shown in **Fig. 6.5**. It is clear that, the stress distribution near the start and end positions of each heating line deviated from the stress at the intermediate part of the heat line, and the stress between two heating lines close to each other had a complex distribution.

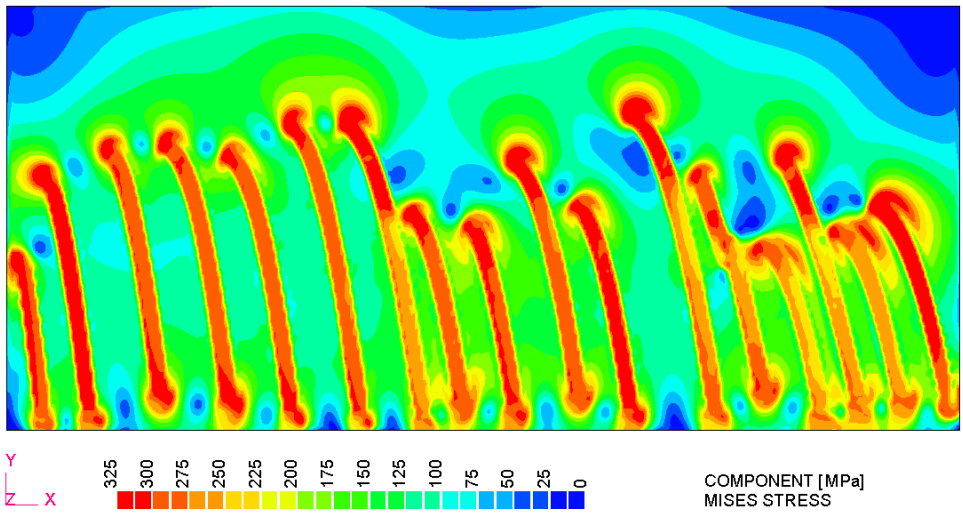

Fig. 6.5 Contour of Mises stress after heating on top surface

The deformed plate shape after the line heating on the bottom surface was finished was shown in **Fig. 6.6**. The maximum deflection occurred near the intermediate part along the plate length, and the value reached 600mm which is almost 13.3% of the plate length. From the deformation contour as shown in **Fig. 6.7**, it can be seen that, deflection due to longitudinal bending appearing along A-B and the deflection due to twisting appearing along B-C were both close to 400mm.

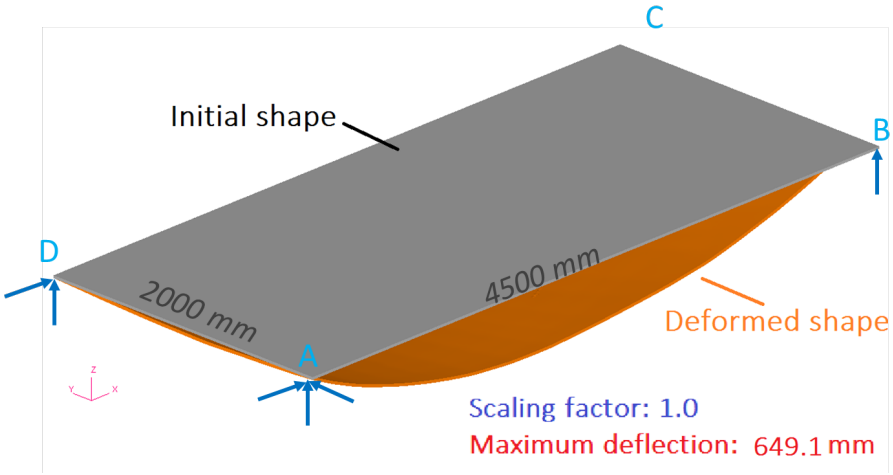

Fig. 6.6 Comparison of initial and deformed shape after heating on bottom surface

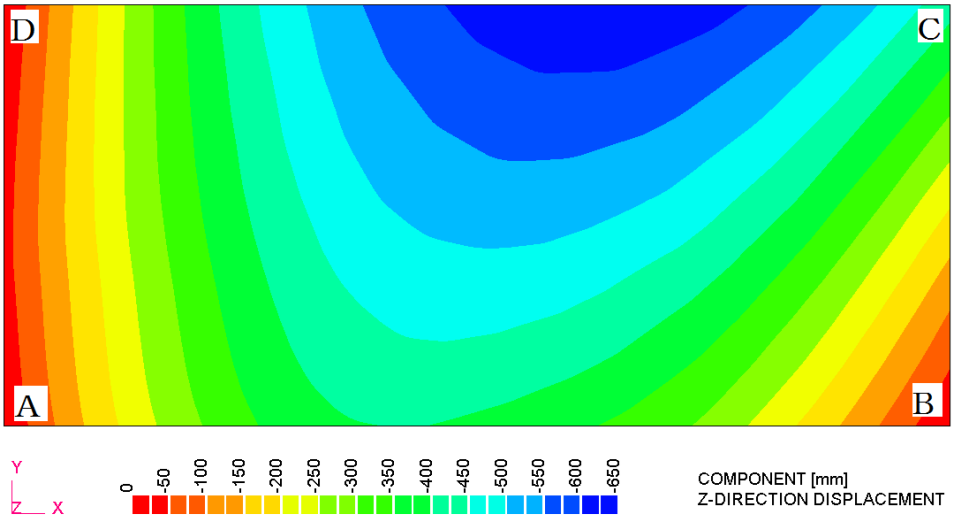

Fig. 6.7 Contour of out-of-plane deformation after heating on bottom surface

The contours of residual Mises stress and equivalent plastic strain were shown in **Fig. 6.8** and **Fig. 6.9**, respectively. It is clear that, the heating of lines at bottom surface had an annealing effect over stresses induced by heating on top surface. The crossing effect was indicated by the plastic strain distribution which has large values at regions near cross points of heating lines. Those interaction effects should be considered in evaluating inherent strains, especially when the interval between heating lines is small. Contours of stress in X-direction and Y-direction are shown in **Fig. 6.10** and **Fig. 6.11**, respectively.

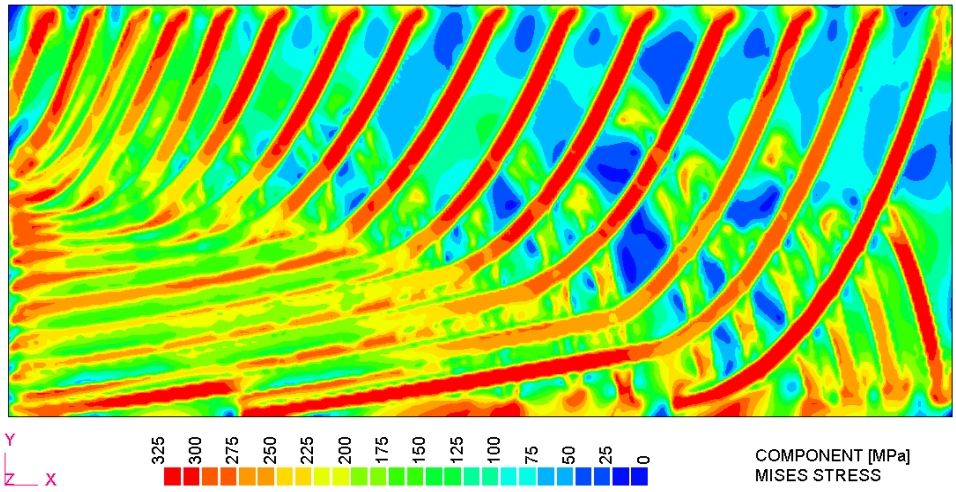

Fig. 6.8 Contour of Mises stress after heating on bottom surface

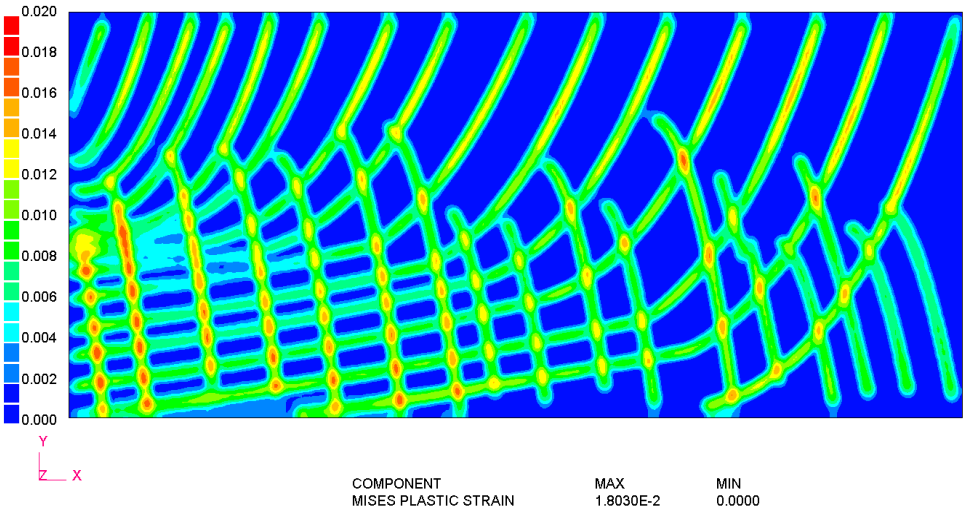

Fig. 6.9 Residual equivalent plastic strain

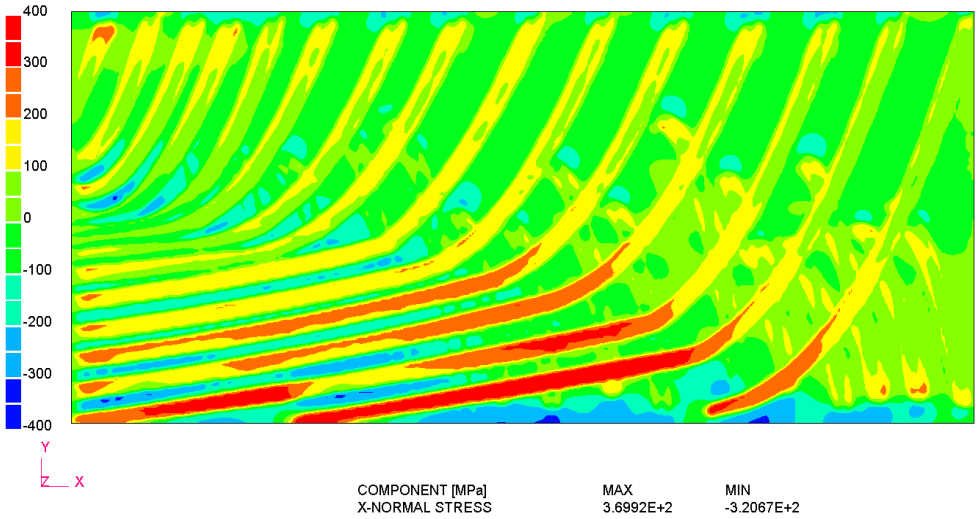

Fig. 6.10 Residual stress distribution in X direction

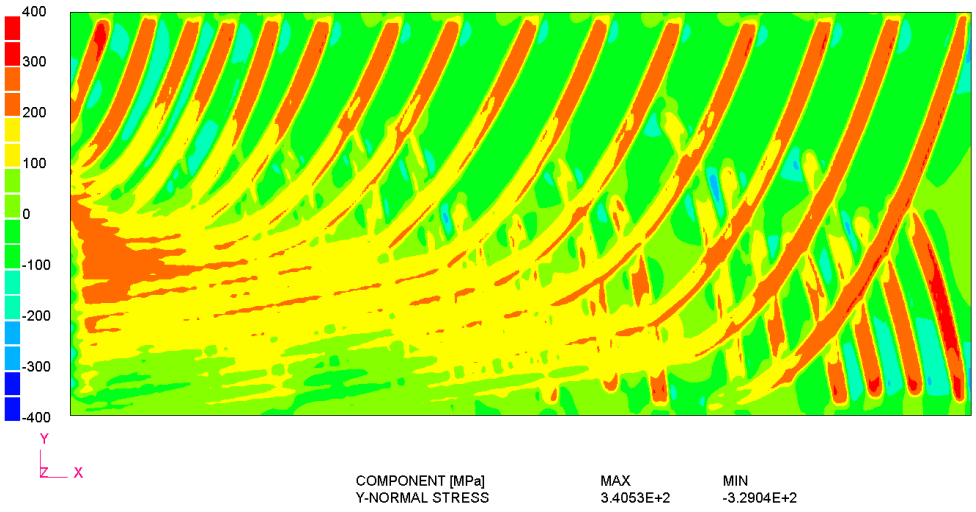

Fig. 6.11 Residual stress distribution in Y direction

To clarify the effect of large deformation, analysis employing small deformation

theory (small-D) was also performed. The deflection along two lines at different stages of heating were plotted in **Fig. 6.12** and **Fig. 6.13**. The deflection along Line-A was mainly produced by longitudinal bending. From deflections along Line-B, the twisting deformation of the rectangular plate can be confirmed. The direction of twisting was reversed from the stage of heating on the top surface to heating on the back surface. The analysis under small deformation theory seemed to underestimate the deformation compared with that under large deformation theroy (large-D). The difference was relatively small when the heating was completed on top surface of plate. However, it became quite large at the final stage, and deflection at the end of Line-B predicted by small-D was just half of that by large-D.

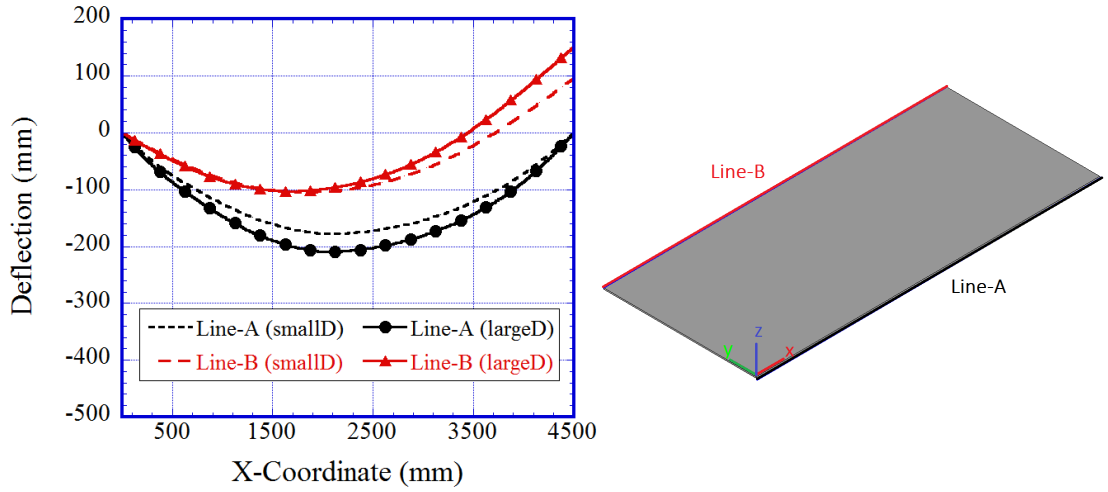

Fig. 6.12 Deflection along two lines after heating on top surface of plate

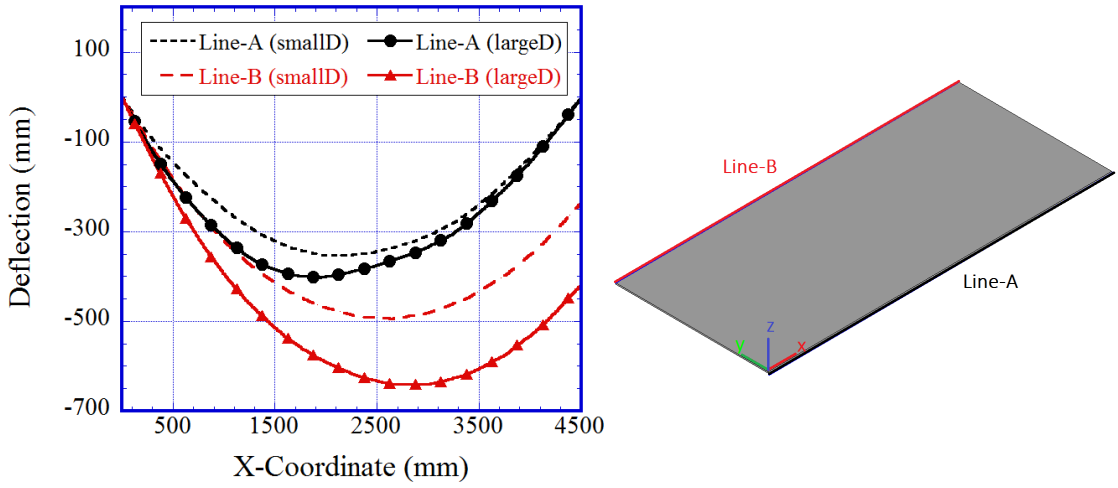

Fig. 6.13 Deflection along two lines after heating on back surface of plate

The analysis using dynamic mesh refining method (DMRM) took about 3.7 days. There were 1006 times of mesh refining during the computation, and the total number

of time steps was 33480. While, the analysis using conventional FEM cost roughly 119.2 days, which was estimated by analyzing the problem until the first 450 time steps. Currently, single CPU was employed for the analysis. Parallelization technique can be incorporated into the code to further improve the computation efficiency.

6.2 Welding of large scale stiffened panel structure

Stiffened panel structures are commonly used in shipbuilding owing to the good flexural rigidity. Fillet welding of stiffeners generally introduces visible deformation on panel, and in the case of thin plate welding, buckling distortion may occur. Thus, a virtual welding by simulation can help to make prior investigation on the structure to be designed under specific welding condition. By analyzing different welding sequences, the welding deformation may be minimized. In practical engineering, the gap and misalignment is inevitable due to the initial geometrical error of the parts. It is necessary to consider those factors in assessment of final welding deformation.

In order to investigate the thermal-mechanical behavior under welding assembly of large structures such as ship blocks, numerical model consisting of elements up to several millions needs to be solved. For large scale simulation, the mesh generation could become very difficult to for a model with complex welding paths. Because the region near the weld line need to be refined, and overall refinement will result in unrealistically large number of elements. Moreover, it usually requires long computation time to complete a single case study. For these reasons, high performance numerical method is indispensable for solving practical scale problems. In this research, the large stiffened panel structures [97] with/without initial gap were analyzed by proposed DMRM*.

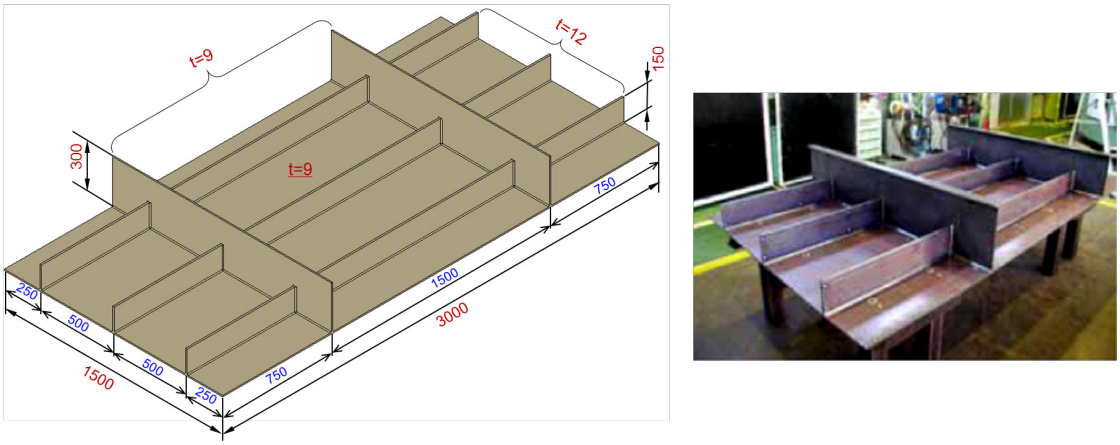

Fig. 6.14 Dimension of the stiffened panel structure and experimental model A after welding

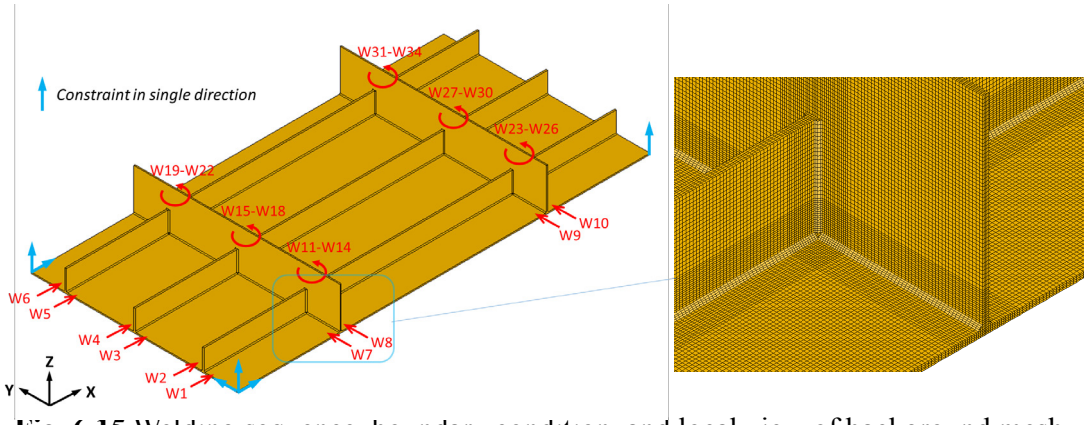

Fig. 6.15 Welding sequence, boundary condition, and local view of background mesh

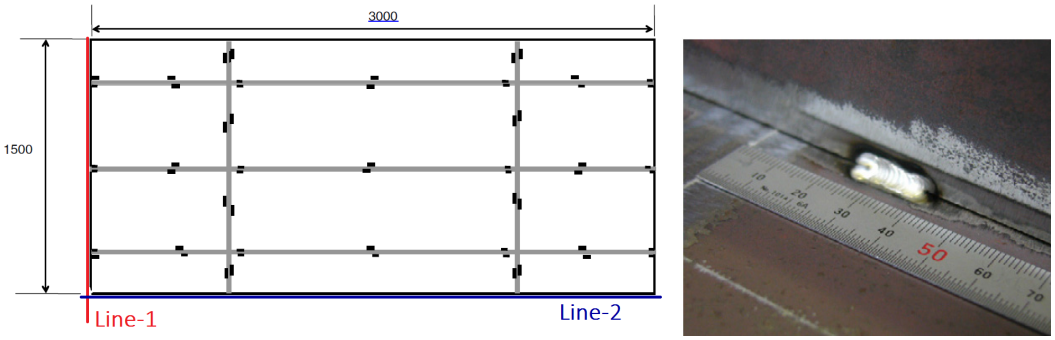

Fig. 6.16 Locations and length of tack weld.

The stiffened panel structure consists of a rectangular skin plate, two transverse stiffeners and three longitudinal stiffeners. The dimension of each part is shown in **Fig. 6.14**. The single-pass welding is performed firstly on panel-stiffener connections (T-joint) and then stiffener-stiffener connections (Cross-joint). The detailed welding sequences are shown in **Fig. 6.15**. Material of the base metal is SM400A. The net heat input for Cross-joint and T-joint are 585 J/mm and 940 J/mm, respectively. In the numerical model, uniform heat flux was given to elements enclosed by double ellipsoids. Material properties of filler metal was assumed to be the same as base metal, and work hardening effect was considered.

Two models were welded in experiment and corresponding numerical analysis were carried out. Before welding, there was no initial gap between the stiffeners and plate in Model-A. All parts are tack welded, and then welding was performed. The locations and the length of tack weld are shown in **Fig. 6.16**. The length of each tack weld is approximately 15mm. In Model-B, gap with a maximum value of 10mm at the edge existed in Model-B as shown in **Fig. 6.17**. Firstly, the initial gaps are closed by correction process. Then, all the parts are tack welded. Finally, the welding is

performed. In the numerical model, initial imperfection has been introduced and the gap was closed then welding was carried out. The gap correction was simulated by introducing an artificial temperature gradient in the stiffeners.

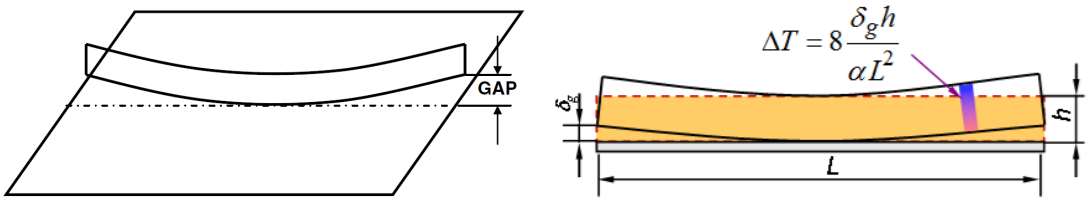

Fig. 6.17 Initial gap between skin plate and longitudinal stiffener.

The mesh preparation and refinement was similar to that presented in **Section 3.4**, but three levels of refining was employed. For each model, the background mesh had 4,988,535 unknowns, and the total number of time steps was 42,057.

The Mises stresses contour and out-of-plane deformation of Model-A after tack weld was shown in **Fig. 6.18** and **Fig. 6.19**, respectively. Locally distributed stress and slight angular distortion around the tack welds can be observed. The simulation of tack weld is important when the gap and misalignment between stiffeners and skin plate is large. In addition, the tack weld induced deformation and stress tends to be significant if the length of tack weld is large. In numerical model, tack welding was analyzed using stationary heat sources, and maximum reached temperature was control to be nearly melting point.

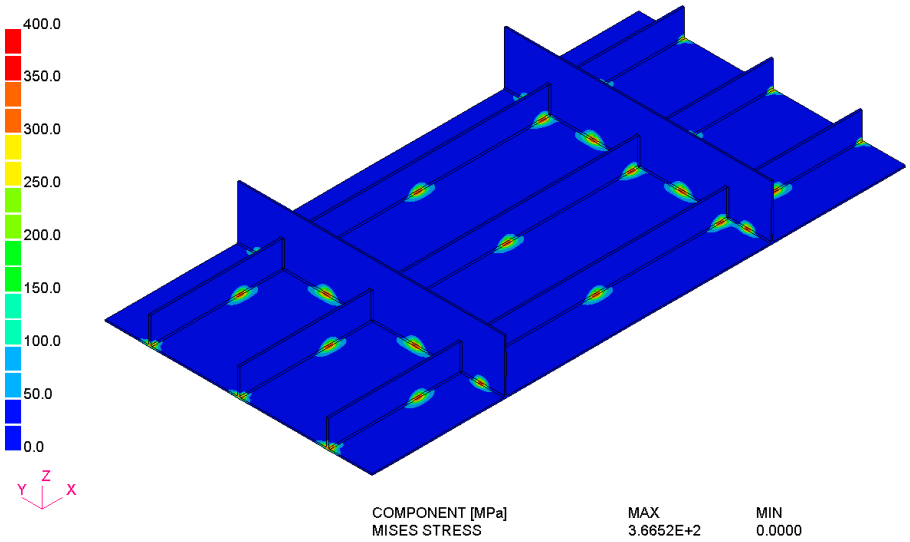

Fig. 6.18 Mises stress distribution of Model-A after tack weld.

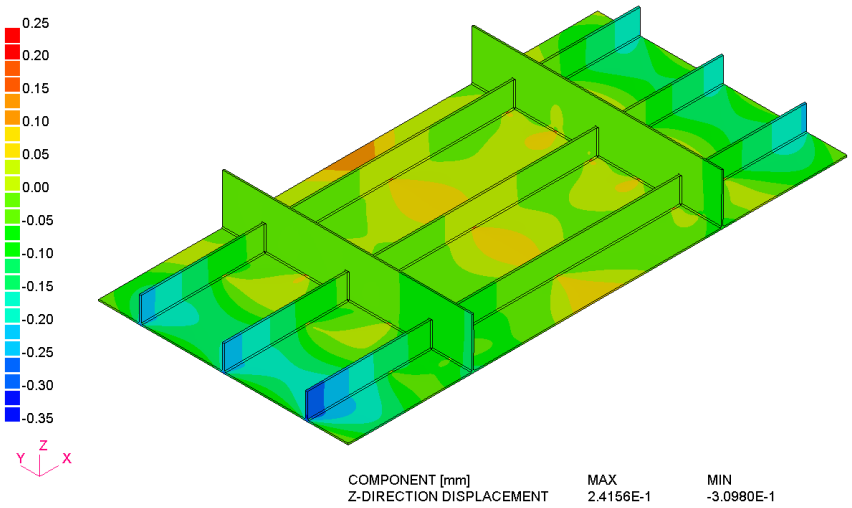

Fig. 6.19 Out-of-plane deformation of Model-A after tack weld

The Mises stresses contour and out-of-plane deformation of Model-A at final welding stage was shown in **Fig. 6.20** and **Fig. 6.21**, respectively. It can be found that, the stress distribution near the tack weld was not continuous, the maximum stress value is close to the tensile strength of base material. The mode of welding distortion can be separated into two. One is the hungry-horse mode deformation produced by the angular distortion along the stiffeners, and the region near the free edges shows the largest deformation. The other is the longitudinal bending of the longitudinal stiffeners produced by the shrinkage of the weld line. The maximum deflection is about 12mm.

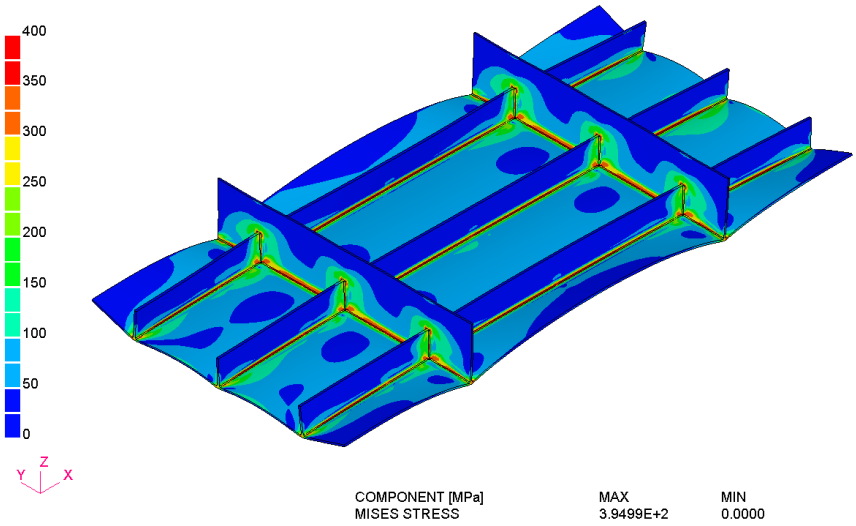

Fig. 6.20 Mises stress distribution of Model-A at final stage

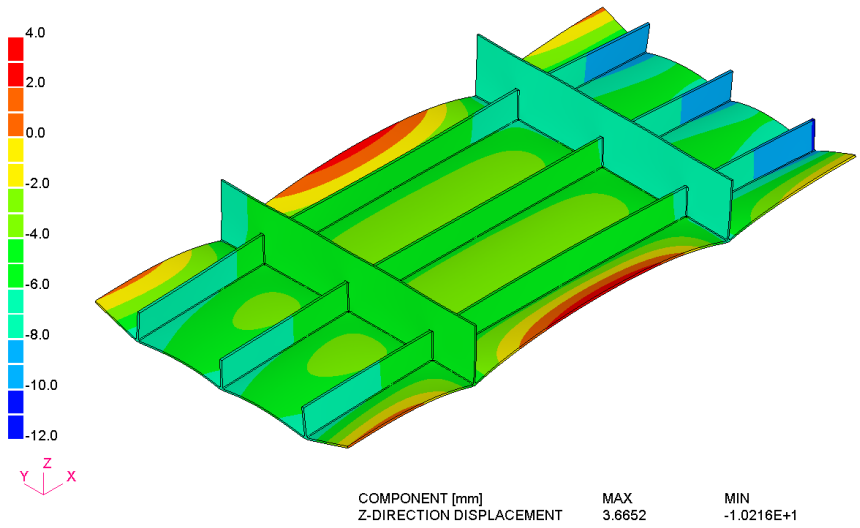

Fig. 6.21 Out-of-plane deformation of Model-A at final stage (Scaled by 10 times)

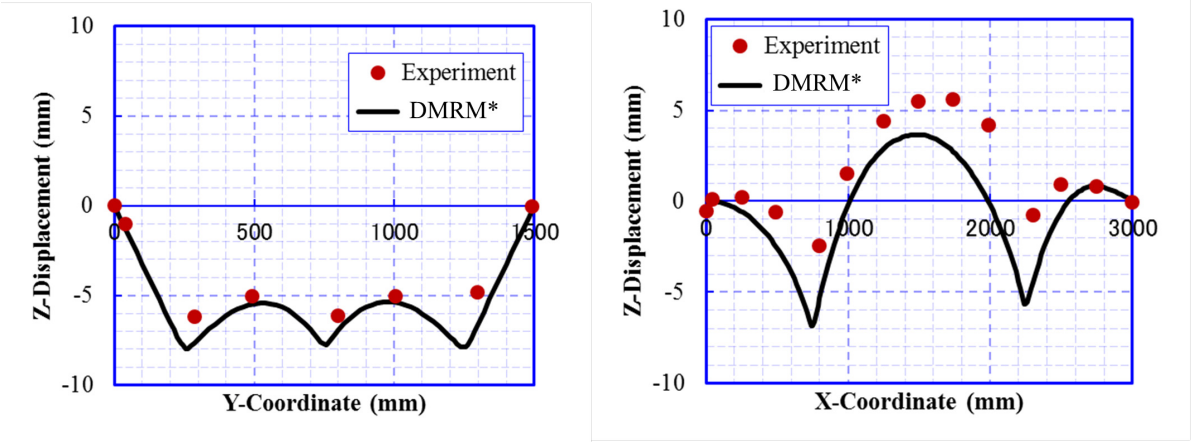

(a) (b)

Fig. 6.22 Comparison of edge deflection in Model-A: (a) Line-1 (b) Line-2

The deflection along two lines (as illustrated in **Fig. 6.16**) in Model-A is plot in **Fig. 6.22** which show experimental and computational results. From the deflection along Line-1, it can be concluded that deformation near the edge is much larger than that in other places. This is due to difference in constraint. The span between two stiffeners is narrow, so the constraint to resist inherent strain is large. From the deflection along Line-2, the computational results indicate a wave pattern deformation with relatively uniform amplitude, and the experimental results has a larger central deflection. The difference between numerical and measured deflection may come from the merging of the gap during the welding process. The dynamic contact behavior between stiffeners and skin plate are also influential to this phenomenon.

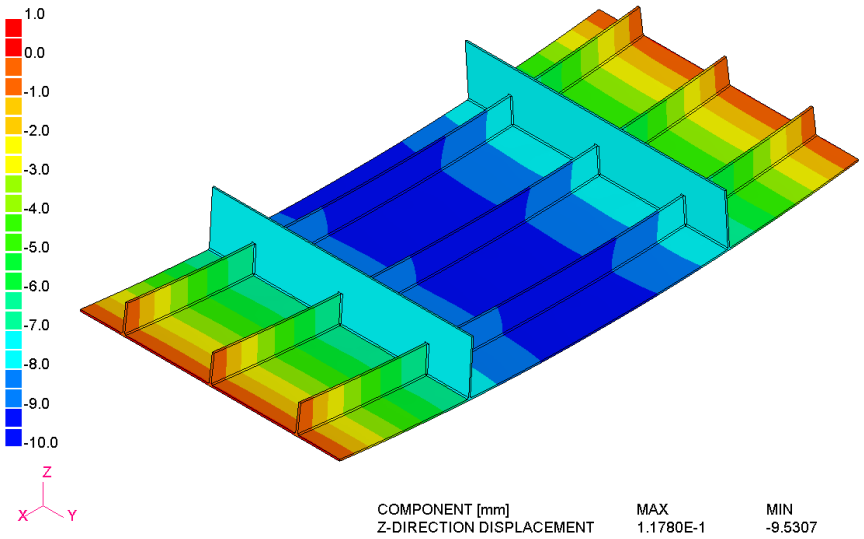

Fig. 6.23 Out-of-plane deformation of Model-B after positioning and tack weld (Scaled by 10 times)

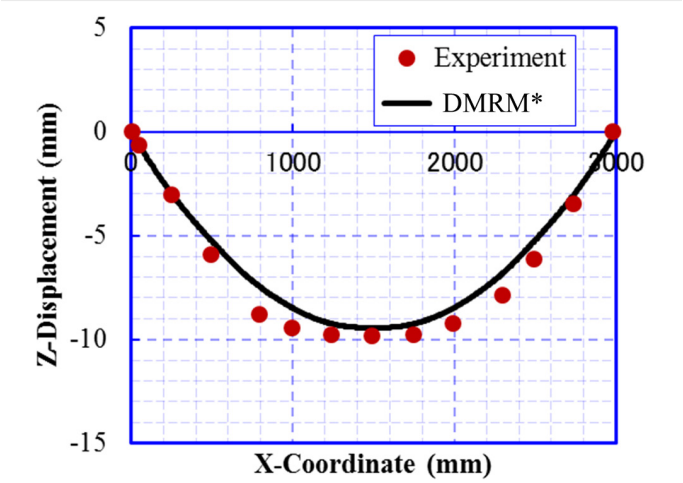

Fig. 6.24 Comparison of deflection along Line-2 after positioning in Model-B

In the case of Model-B, the contour of out-of-plane deformation after positioning is shown in **Fig. 6.23**. Longitudinal bending deformation is large due to the configuration of the gap between longitudinal stiffeners and skin plate. A quantitative comparison of deflection along Line-2 was shown in **Fig. 6.24**. Good agreement between computation and measurement was confirmed. The maximum deflection is close to the size of initial gap 10mm. The artificial temperature gradient is effective in simulation of gap mitigation.

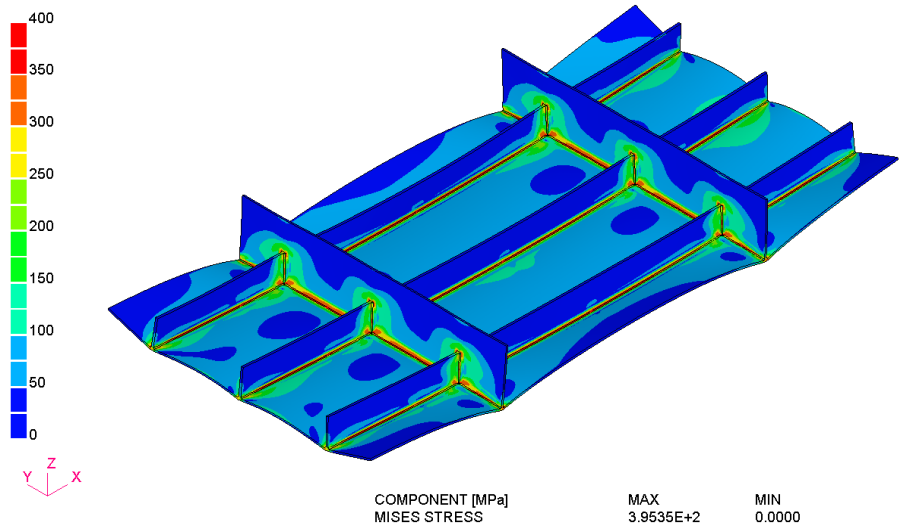

Fig. 6.25 Mises stress distribution of Model-B at final stage

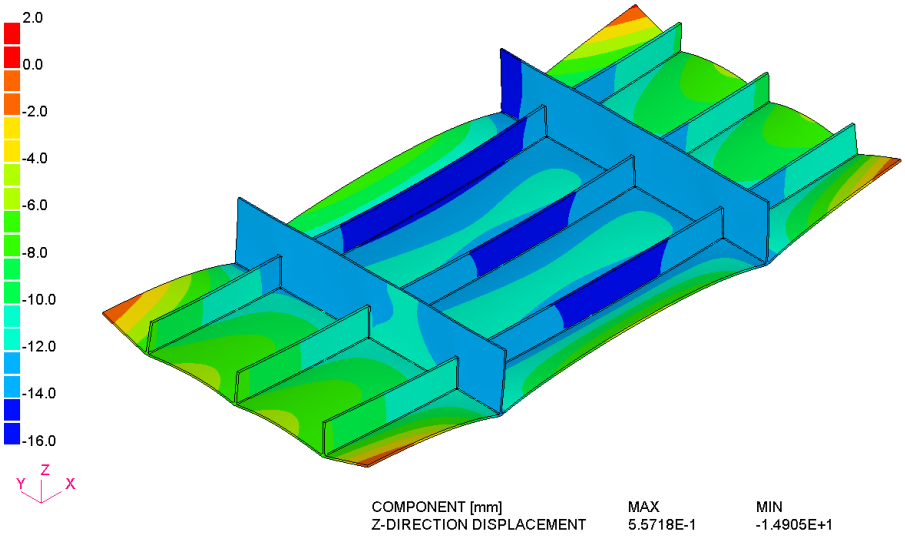

Fig. 6.26 Out-of-plane deformation of Model-B at final stage (Scaled by 10 times)

The contours of Mises stress and out-of-plane deformation at the final stage of welding is shown in **Fig. 6.25** and **Fig. 6.26**. Comparing the residual stress results between Model-A and Model-B, the difference is very small. However, the two models have large difference in out-of-plane deformation. **Fig. 6.27** depicts the deflection along the edges in Model-B. The Line-1 in transverse direction has a similar deflection to that in Model-A, as the size of gap among the three stiffeners are the same. The Line-2 shows a much larger deflection compared with the case without intial gap. The maximum deflection as indicated by computed results is about 7mm in Model-A and 14 mm in Model-B. The experimental results show the same tendency.

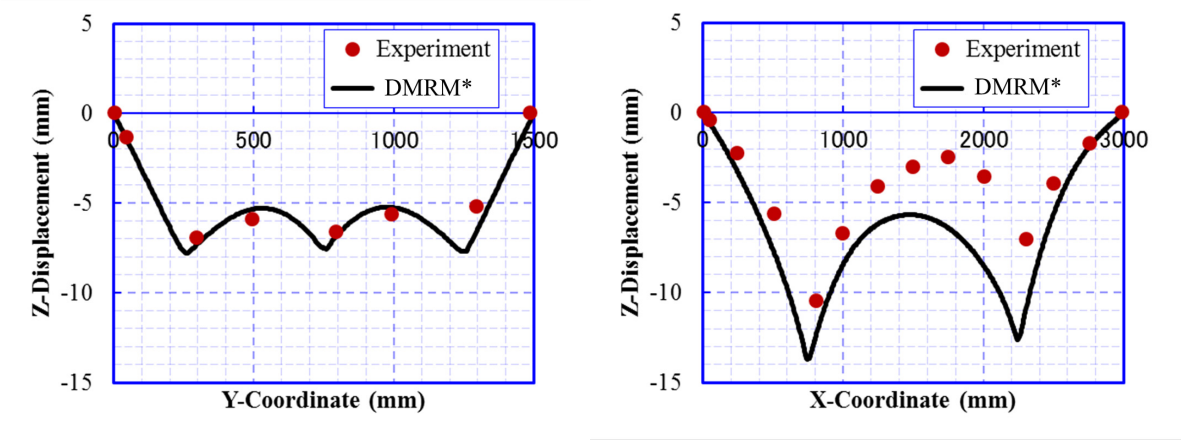

(a) (b)

Fig. 6.27 Comparison of edge deflection in Model-B: (a) Line-1 (b) Line-2

The computation time for models with and without initial gap using DMRM* are both about 3.6 days, while time of analysis using conventional FEM cost roughly 149 days. The computation time for the case was estimated by analyzing the problem until the first 356 time steps. Currently, only single CPU was employed for the analysis.

6.3 Simulation of welding on thick plate

It can be understood that i-ISM is effective for large thin-plate structures in which weld beads are scattered widely, such as ships and automobiles. To examine its effectiveness for thick welded components, a multi-pass welding of a thick plate weld joint is taken as an example. The size of the plate model is 450 mm, 360 mm and 180 mm in width, length and thickness directions for Model-M1, as shown in **Fig. 6.28**. And for Model-M2, all dimensions are the same with Model-M1 except that the length is 2160 mm, which is six times larger than Model-M1. As a test case, the final welding pass on the top surface is performed. In both models, welding speed is assumed to be 1.5 mm/s, and welding power is 2300W.

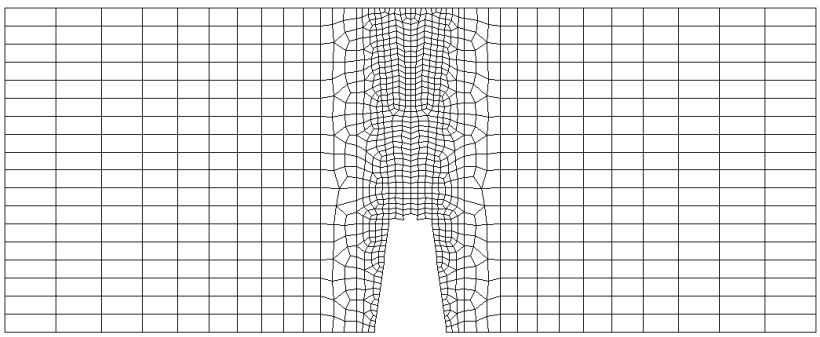

(a)

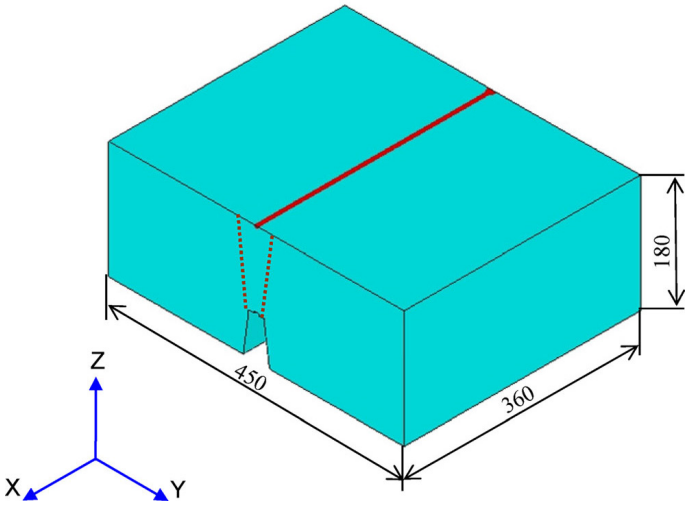

(b)

Fig. 6.28 Multi pass welding model for FE analysis: (a) Mesh (b) Geometry

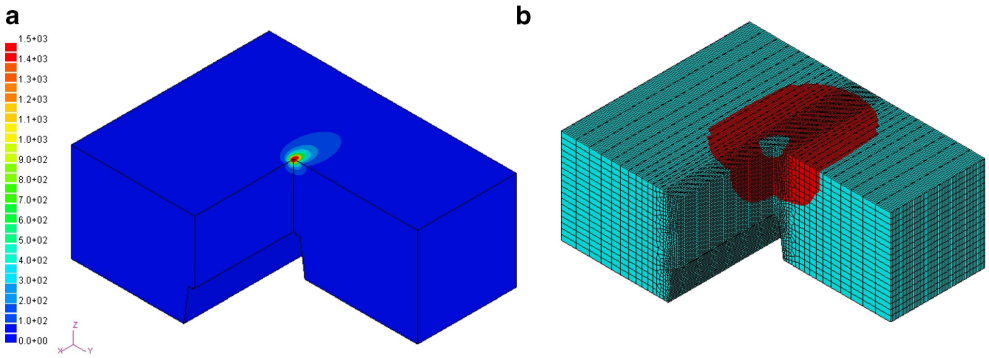

(a) (b)

Fig. 6.29 Transient temperature and regions B and C in Model-M1.

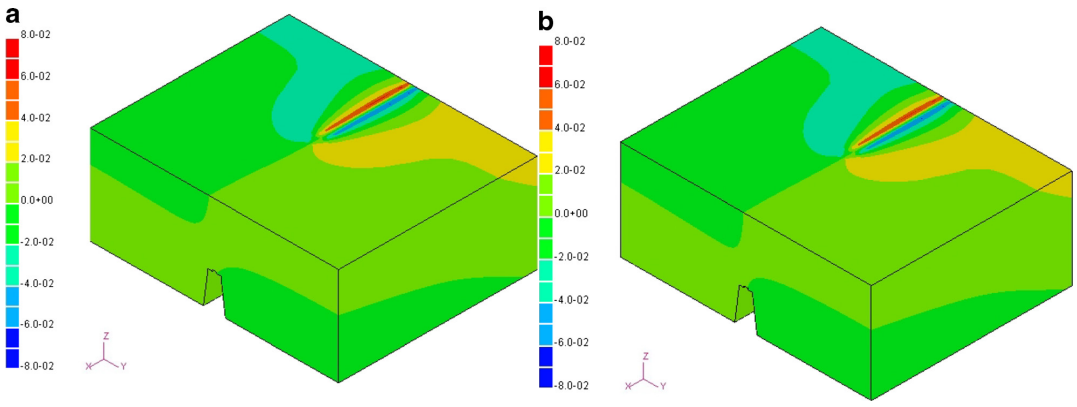

(a) by ISM (b) by i-ISM

Fig. 6.30 Contour of transient displacement (mm) in y direction computed by ISM and i-ISM for Model-M1.

As for the nonlinear region B, region where the temperature is higher than 300 ^{o}C and contained in a sphere with radius of 20 mm locating at the position of heat source

is selected in ISM and i-ISM for the two models (**Table 6.1**). As for the size of C in i-ISM analysis, radius of the sphere R is 80 mm in both models but the length of its tail is $1\times R$ mm and $3\times R$ mm, respectively. **Figure 6.29 (a)** and **Fig. 6.29 (b)** show the transient temperature distribution and regions B and C in Model-M1. **Figure 6.30** shows the comparison between transient displacements in y direction computed by ISM and i-ISM. For the quantitative comparison, distributions of the displacements along width direction at center on the top surface are compared between ISM and i-ISM in **Fig. 6.31**. Also, the distributions of stress components are compared in the same manner in **Fig. 6.32**. Good agreements can be observed between ISM and i-ISM for all components of displacement, stress and plastic strain. For Model-M2, the Mises stress contour and the transverse displacement computed by ISM and i-ISM are compared in **Figs. 6.33-6.34**.

Table 6.1 Definition of regions B and C for Multi-pass welding

Model Name	Model-M1		Model-M2	
Simulation Method	ISM	i-ISM	ISM	i-ISM
Temperature for B	300 C			
Radius for B	20 mm			
Radius for C	NA	80 mm	NA	80 mm
Tail for C	NA	80×1 mm	NA	80×3 mm

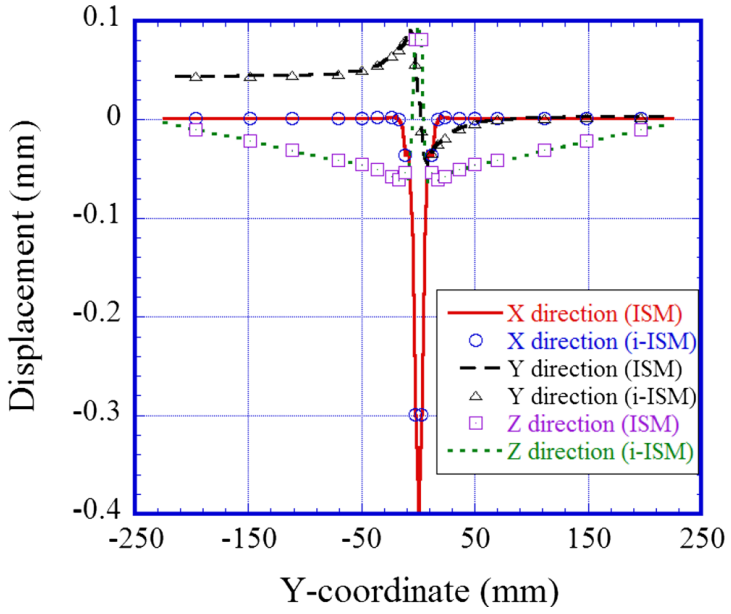

Fig. 6.31 Distribution of displacements computed by ISM and i-ISM

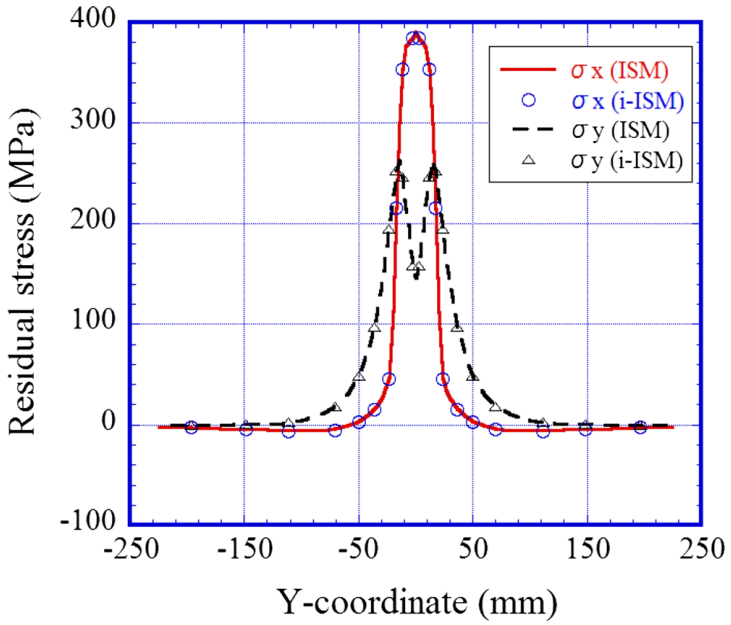

Fig. 6.32 Distribution of stresses computed by ISM and i-ISM

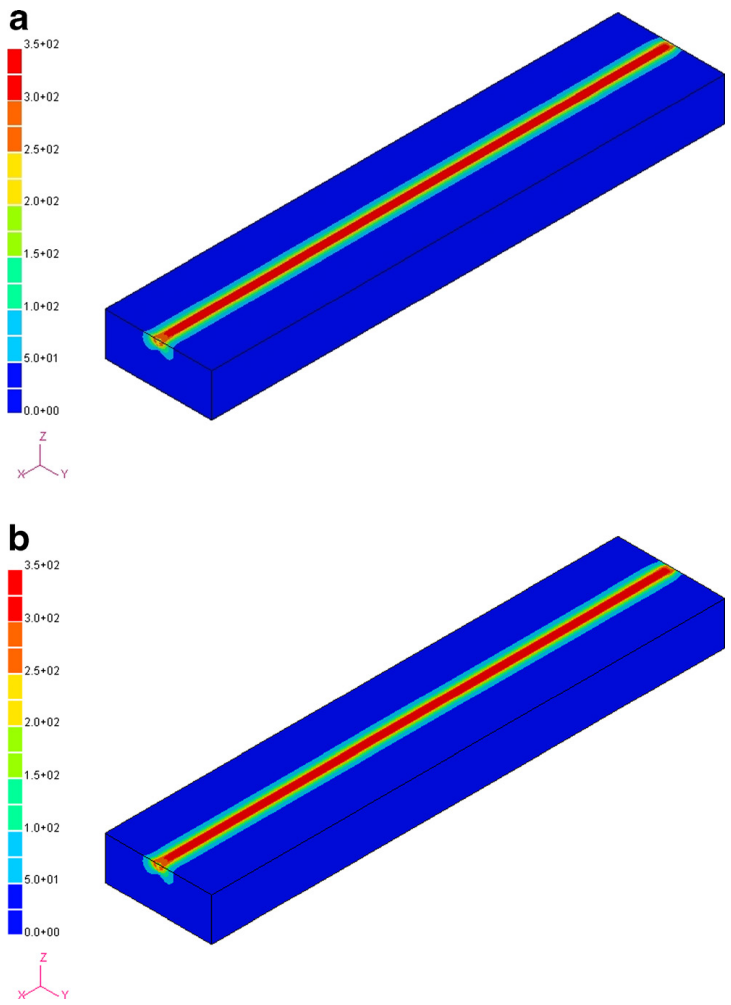

Fig. 6.33 Contour of Mises stress (MPa) for Model-M2: (a) by ISM, (b) by i-ISM

The computational time is summarized in **Table 6.2**. In case of Model-M1, the whole model consists of 139,920 elements and roughly 563 elements are contained in region B. Since the region B and the welding time are the same in both ISM and i-ISM, computational time spent for region B is almost the same. The difference in computational time comes from the rest of the computation mostly spent for solving regions A and C. Since the number of elements contained in region C is roughly 43,072 and it is very small compared with that for region A, the computational time for the rest is reduced to 35% compared with ISM. As a result, total computational time is reduced to 39 %. If the size of the model becomes large, the computational time can be greatly reduced by i-ISM. In case of Model-M2, the number of elements inside region B in ISM and i-ISM is about 592 which is almost the same with that in Model-M1. And averaged number of elements for C region increased to about 3 times of that in the previous model, but it took only 16% of the whole elements. The computation time for regions out of B has been reduced to 22%, and the simulation has achieved 3.6 times faster speed by i-ISM.

Table 6.2 Computation time for mechanical analysis of Model-M1 and Model-M2.

Model Name	Model-M1		Model-M2	
Simulation Method	ISM	i-ISM	ISM	i-ISM
Elements in A	139,920		974,880	
Elements in B	563*		592*	
Elements in C	*NA*	43,072* (31%)+	*NA*	154,332* (16%)+
CPU Time for B	0.2 h	0.2 h	8.0 h	9.4 h
CPU Time for the rest	2.6 h	0.9 h (35%)#	120.6 h	26.3 h (22%)#
Total CPU Time	2.8 h	1.1 h (39%)#	128.6 h	35.7 h (28%)#

* indicates average value over all steps

( )+ denotes percentage of elements in C region over elements in A region

( )# denotes percentage of CPU time using i-ISM over that by ISM

From the results, it can be concluded that the reduction of the computational time becomes significant when the size of the model becomes large, and it reaches 72% in the case of welding on large scale thick plate. Its potential capability has been demonstrated through the thick plate welding problems which contain around 1,000,000 elements.

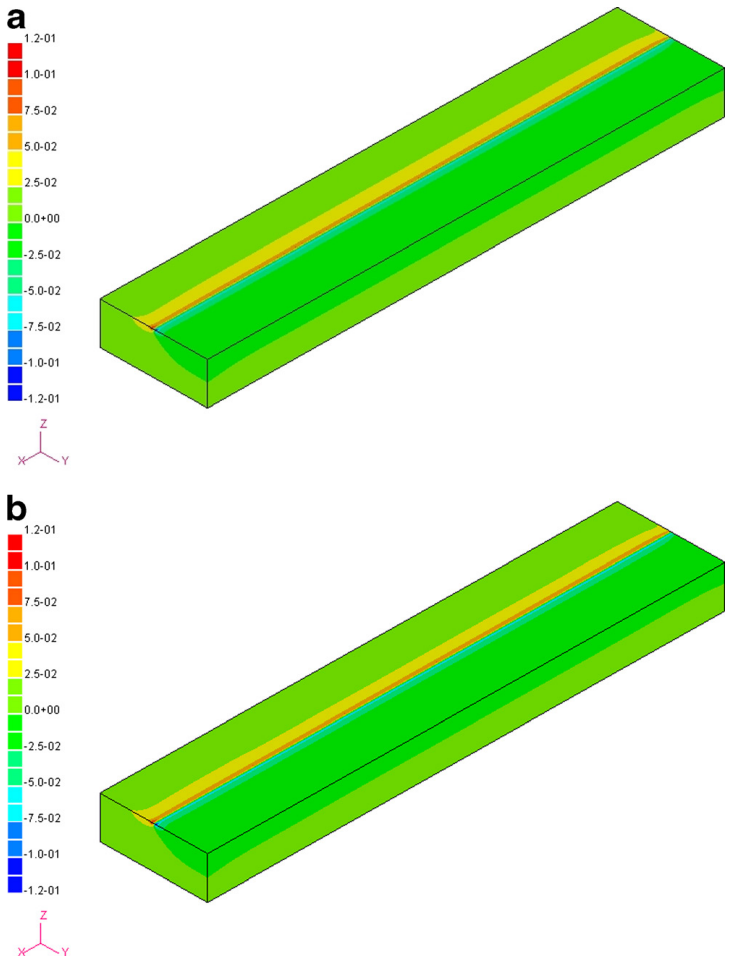

Fig. 6.34 Contour of transverse displacement (mm) for Model-M2: (a) by ISM, (b) by i-ISM

6.4 Summary

For practical application, the high-performance numerical methods were employed to analyze large scale thermal elastic-plastic problems. Different welding and heating problems are solved to demonstrate the capability of developed methods.

Line heating on a rectangular plate close to realistic engineering was computed by DMRM using three levels of refinement. There are 33 curved heating lines locating on both top surface and bottom surface of the plate. After heating, a combined twisting and bending deformation mode was observed. The numerical analysis has 1,220,535 unknowns and 33,480 time steps. The computation has been successfully accomplished in 3.7 days by the dynamic mesh refining method, which suggests a computation speed of over 30 times faster than original method. Computational results also revealed that, large deformation theory is necessary to be employed in the case line heating on large scale plate.

The stiffened panel structure joined by fillet welding was also simulated by 3D

transient thermal-mechanical analysis using DMRM*. The number of unknowns in the numerical model was nearly 5 million, and the total time steps of the analysis was 42,057. The computation for such a large scale model was completed within four days. The effect of initial gap on final welding deformation was investigated. Temperature gradient in stiffeners was proposed to model the mitigation of gap between skin plate and stiffener. Through comparison with experimental measurement, the computation results were validated.

Multi-pass welding joints of thick plates were analyzed by original ISM and i-ISM. The thick plates has large internal constraint thus inherent strain method can be effectively introduced into ISM. The computation results suggest that, the time cost in solving B region is nearly the same between ISM and i-ISM. The computational time in solving rest of analysis was greatly reduced since the elements in C region is obviously fewer than those in A region. In the case of a welding joint with 2160mm in length, the computation cost was reduced to 28% of that cost by original ISM. The residual stress and deformation had good agreement between the two numerical methods.

In the above cases of study, the number of degrees of freedom exceeds one million. It can be confirmed that, the computations accelerated by developed numerical methods consumed much less time than original and commercial codes while keeping good accuracy in results. The numerical approaches can be readily used to solve large scale welding and heating problems.

Chapter 7 Application to fatigue life evaluation and residual stress measurement

Extensive research have clarified that welding residual stresses have large influence on crack initiation and fatigue life. Due to nonlinear properties and phase transformation of material, the welding residual stresses usually have complex distribution. It is necessary to obtain realistic results using advanced techniques instead of simple assumptions. Numerical simulation and experimental measurement can be employed to obtain accurate distribution of residual stress. When a transient thermal-elastic-plastic simulation was carried out, detailed three-dimensional residual stress field is available. Based on the residual stress, the fatigue life of welded structure can be predicted using a rough estimation method or more elaborate analysis.

Accurate measurement of welding residual stress is important for clarifying the stress distribution and validating a numerical model. The contour method has been proved to be effective in measuring residual stress in thin and thick plates. In this chapter, the influence of mesh size on fatigue life evaluation was investigated with the refining method. An efficient local refining and mapping procedure was developed for fatigue life evaluation. The mesh refining method was also employed to minimize the effort in generating FE mesh for contour method. In addition, an inherent strain based contour method has been proposed to reproduce the residual stress in welding joint with complex and asymmetric geometry.

7.1 Fatigue life prediction with local refinement and mapping solution

A gusset welding joint as illustrated in **Fig. 7.1** was investigated. The dimensions of the welding joint are also shown in the figure. The base metal is a mild carbon steel and the filler metal is DW-100. The heat input along weld line is 1.5 kJ/mm. The size of the fillet around the gusset is 6mm in height and 8mm in width. The two gussets were welded sequentially, and they were symmetrical to the center of base plate.

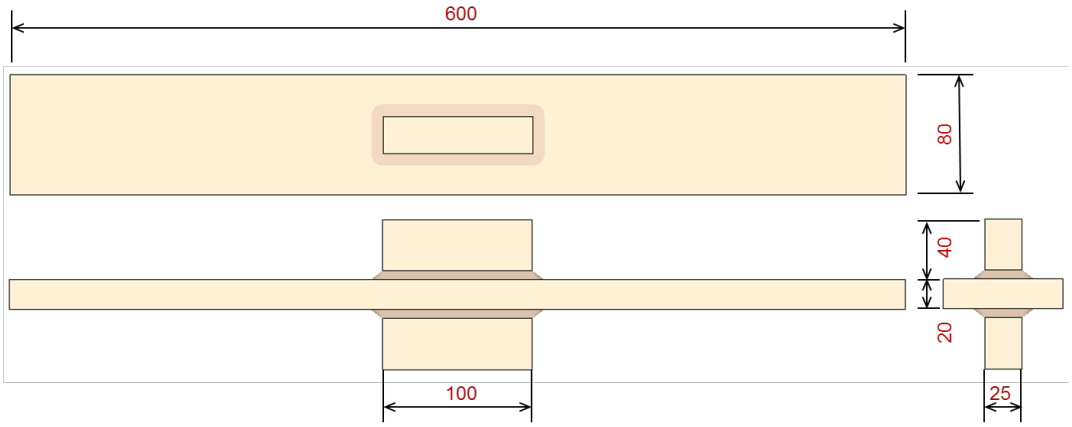

Fig. 7.1 Dimensions of the gusset welding joint

For the purpose of fatigue life estimation [107], transient thermal elastic-plastic analysis was performed to compute welding residual stress. Static elastic analysis was performed to compute the stress concentration in the welded joint under external loading (loading stress in x direction with 150MPa nominal stress). The two stress fields can be used for a rough prediction of fatigue life. In this study, two separate estimations were carried out for the welding joint. The first estimation employed the initially prepared mesh for both welding and loading. The element size in weld zone is about 1mm×1mm×2.5mm which is considered to be fine enough for welding simulation. The second estimation employed a mesh refined near the weld to a higher level in both welding residual stress computation and external loading computation. Double-ellipsoidal heat source model with uniform heat flux was employed for the welding thermal analysis.

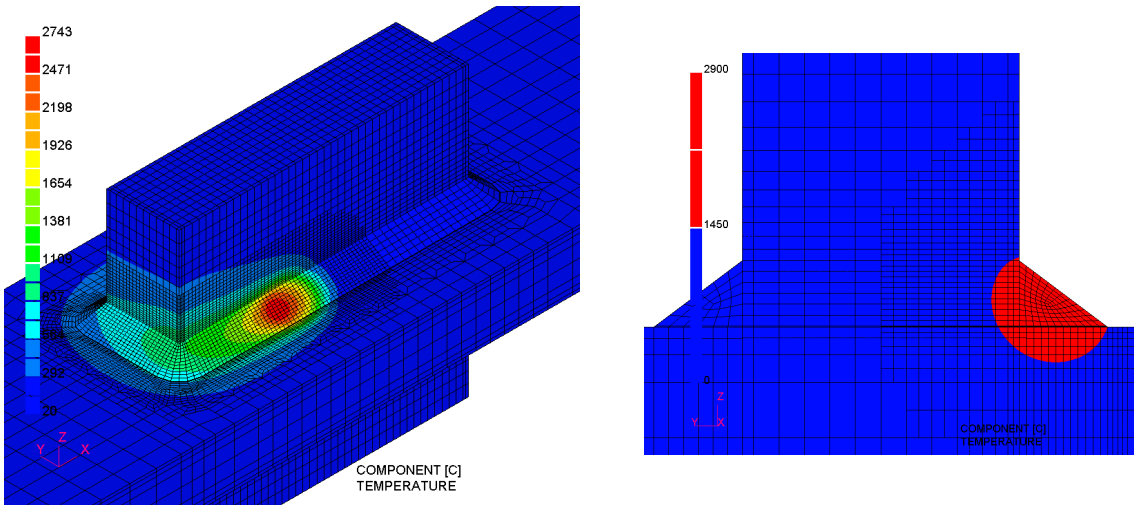

(a) (b)

Fig. 7.2 Thermal analysis by DMRM: (a) transient temperature distribution, (b) penetration shape

Figure 7.2 shows the transient temperature distribution and the penetration shape when the top gusset was welded. One level refining was conducted by sweeping a sphere along the weld. The radius of the sphere is 16mm. Accuracy of the computed temperature field and reasonable penetration shape were confirmed.

The contours of residual stress in X-direction and Mises stress are shown in **Fig. 7.3** and **Fig. 7.4**, respectively. It can be found that, the residual stress distribution with and without mesh refining do not show much difference. On the other hand, the stress induced by loading shows large dependence on mesh size, as shown in **Fig. 7.5**. The maximum values of stress in the case without refinement and with refinement are 279.62MPa and 346.62MPa. Therefore, the stress concentration is significantly influenced by the mesh size. The results suggest that, the welding residual stress is less sensitive to mesh size than stress concentration.

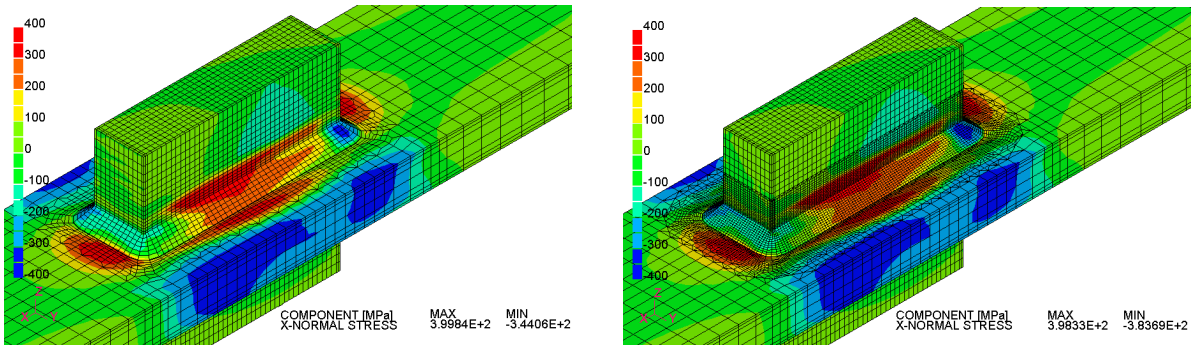

(a) Maximum=399.84 MPa (b) Maximum=398.33 MPa

Fig. 7.3 Contour of residual stress in X-direction: (a) Without refinement (b) With refinement

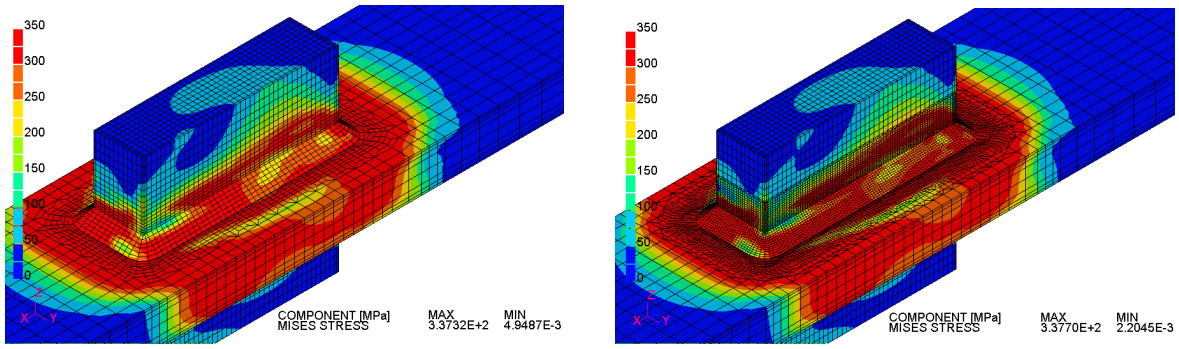

(a) Maximum=337.32 MPa (b) Maximum=337.70 MPa

Fig. 7.4 Contour of residual Mises stress: (a) Without refinement (b) With refinement

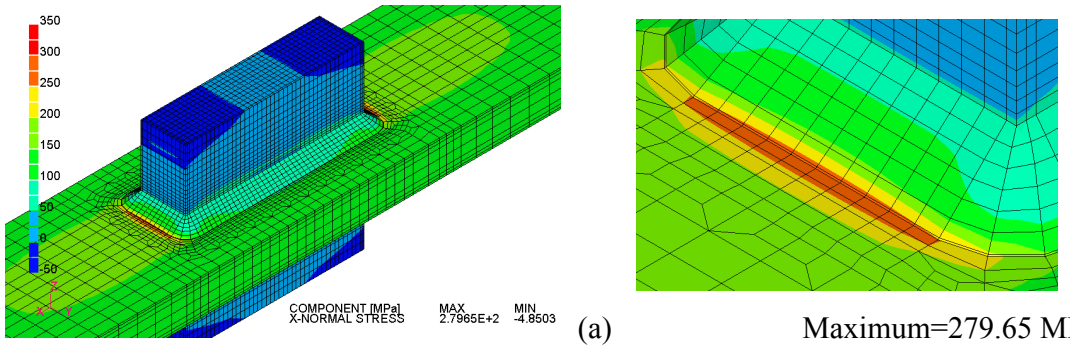

(a) Maximum=279.65 MPa

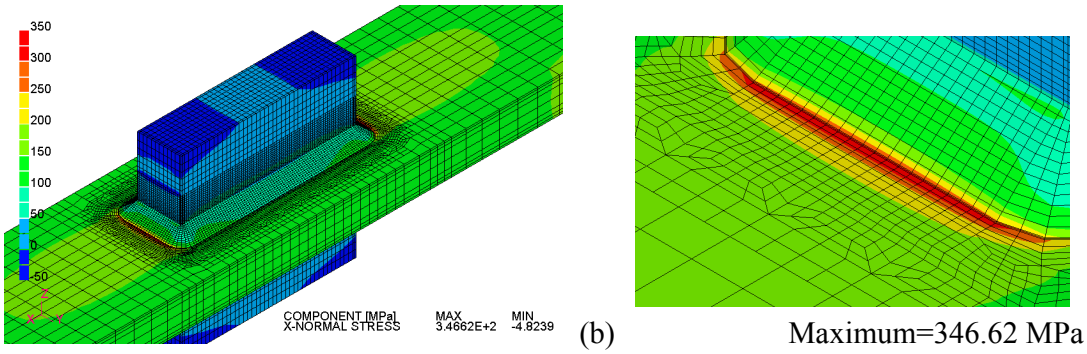

(b) Maximum=346.62 MPa

Fig. 7.5 Stress induced by external loading: (a) without refinement (b) with refinement

The fatigue life predicted by rough estimation theory was plotted in **Fig. 7.6**. The estimation using the refined mesh gives conservative results compared with that using a relatively coarse mesh. The difference between the two predictions is about 400% in crack initiation life and 50% in propagation life. The fatigue life calculated without consideration of residual stress σ_W is also shown in the same figure. Obviously, the prediction overestimated the initiation life and failure life if the residual stress is not considered.

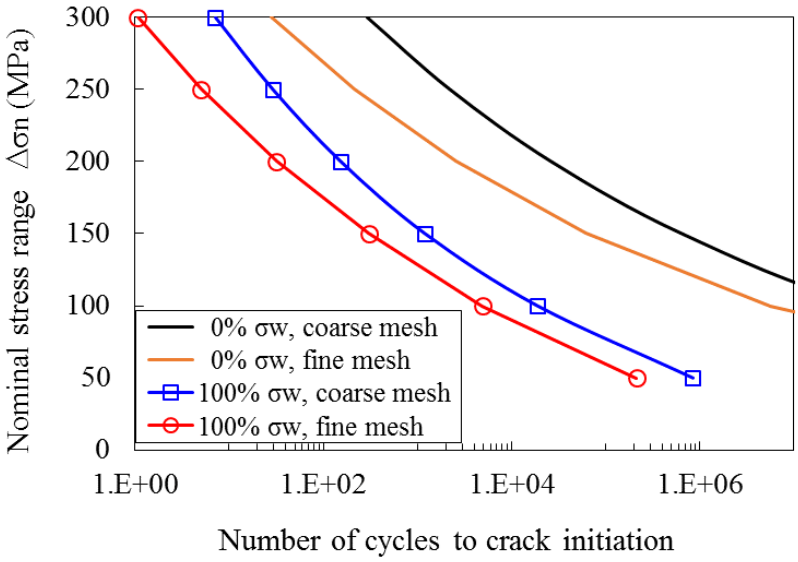

(a)

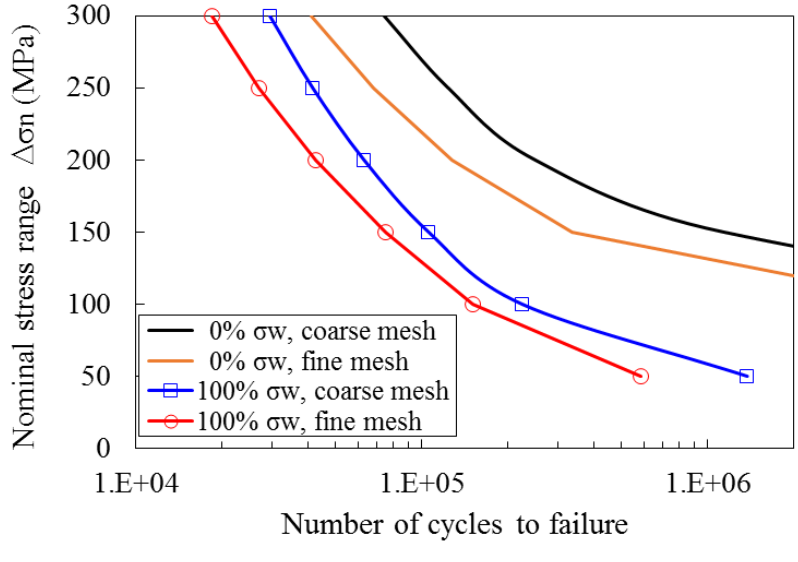

(b)

Fig. 7.6 Fatigue life of welded gusset joint: (a) Initiation life (b) Failure life

It was demonstrated that, a fine mesh should be employed in static elastic analysis.

However, the welding simulation using such a fine mesh will be rather time consuming especially for large scale structure, this type of analysis will be not practical. Since the computed welding residual stress is less sensitive to mesh size, it is reasonable to map the residual stress computed by a relatively coarse mesh onto a finer mesh, and then carried out the fatigue analysis based on the fine mesh. For this purpose, a refining and mapping process was employed to transfer results between different meshes. The region to be refined was determined based on the results of static stress analysis on the coarse mesh. The Mises stress was taken as the indicator, which allows elements to be refined when its stress value exceeds a given value (**Fig. 7.7**). In the mapping process, the welding residual stresses of a coarse element are passed directly to its refined elements. **Fig. 7.8** shows mapping results of residual stress from coarse mesh to locally refined mesh. The stress distribution across different level of elements is smooth, and the difference from the previous results is very small.

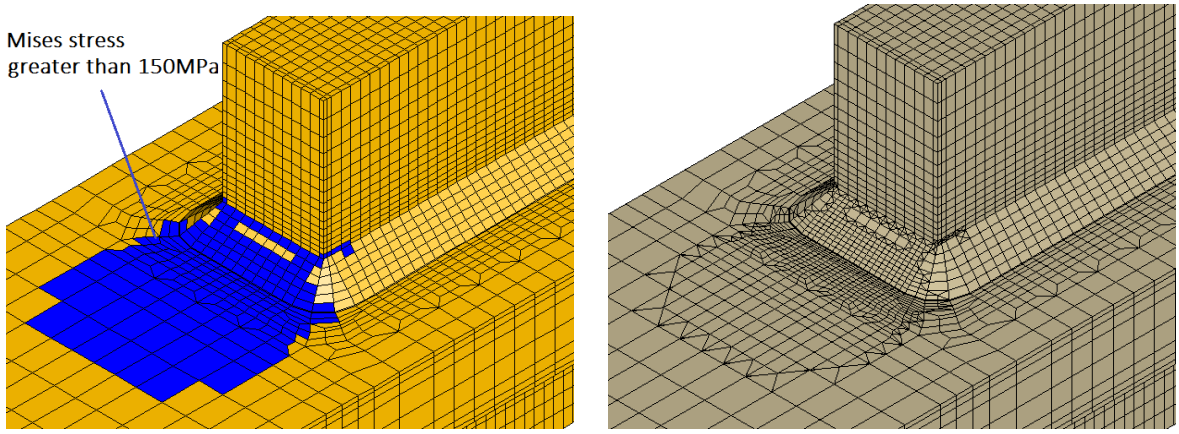

Fig. 7.7 Local refinement based on Mises stress computed by static loading analysis

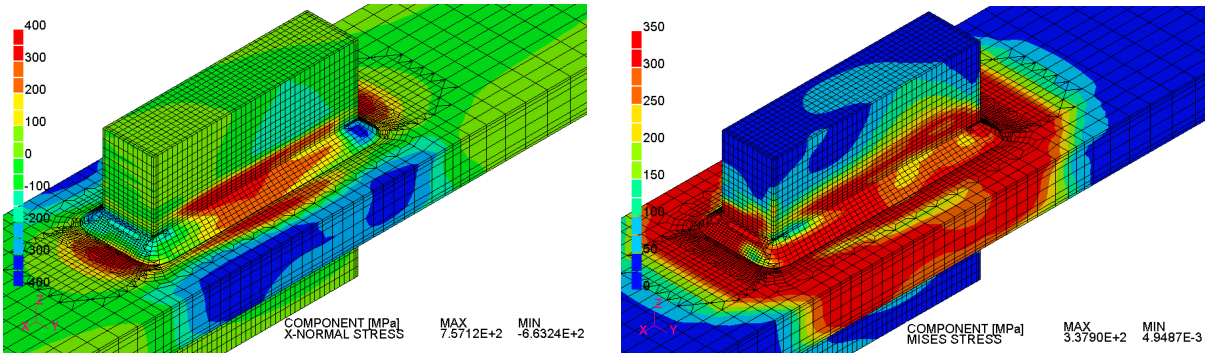

(a) (b)

Fig. 7.8 Residual stress mapped from coarse mesh to local refined mesh: (a) Stress in X-direction, (b) Mises stress

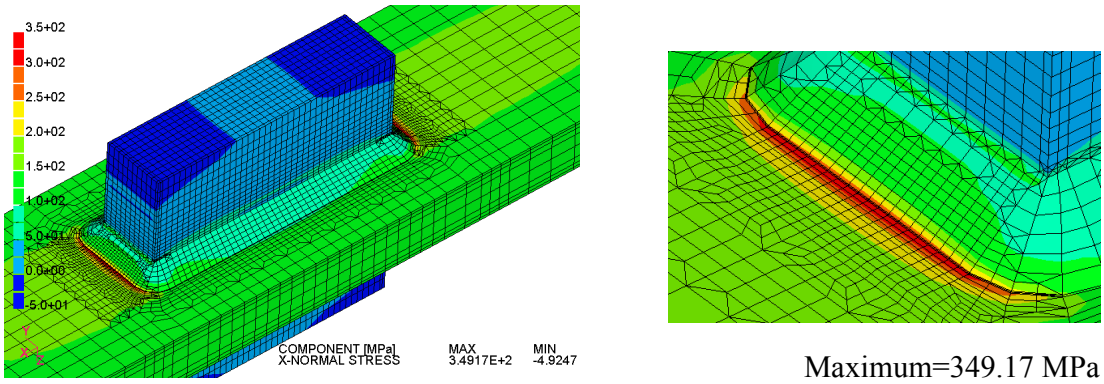

Fig. 7.9 Stress induced by external loading on the model with local refinement

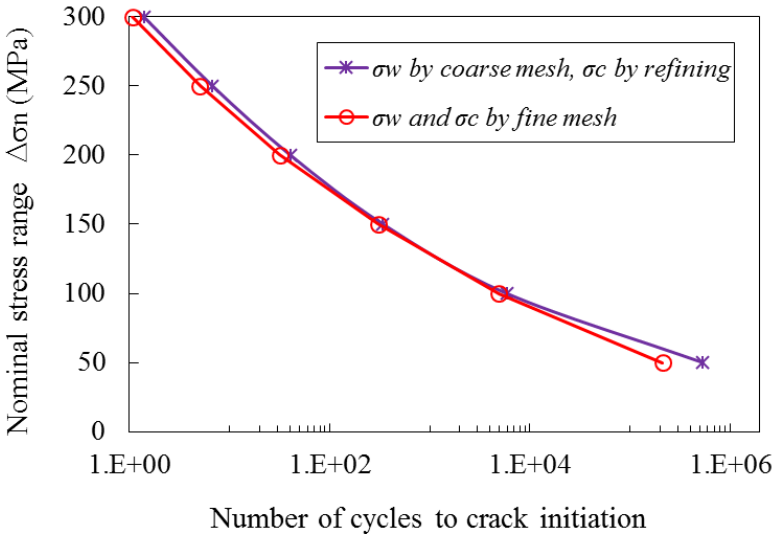

(a)

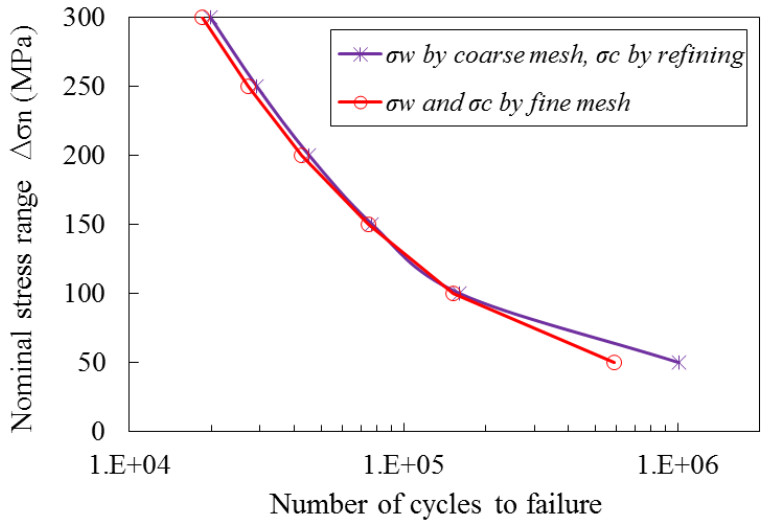

(b)

Fig. 7.10 Fatigue life of welded gusset joint with refining and mapping: (a) Initiation life (b) Fracture life

Figure 7.9 shows the stress in X-direction induced by external loading. Compared with results in **Fig. 7.5(b)**, the stress distribution is very similar, and the maximum value of stress is 349.17 MPa which is close to that (346.62 MPa) in the model uniformly refined along the weld line. For such a refinement analysis, only several minutes are enough. The fatigue life predicted by refined stress concentration and mapped residual stress results is plotted in **Fig. 7.10**. Both initiation life and fracture life agreed well with those estimated by using fine mesh model. The slight error is caused by mapping process, it can be avoided if residual stress was analyzed on the same locally refined mesh. Higher level of refinement can be introduced for more accurate prediction.

7.2 Local refinement for reproducing residual stress by contour method

Contour method was proved to be a simple but effective measuring technique for welding residual stresses in thin and thick plates[104]. The stress component normal to cut surface of welded joint can be calculated by an elastic analysis. Usually, a thin layer is firstly removed from the position of interest by electrical discharge machining (EDM). The flatness of cut surfaces are then measured by 3D macroscopic measuring devices. The elastic deformation can be determined as the difference between the deformations on two distorted surfaces, and it is introduced on a stress-free model as the forced displacement. In order to obtain high resolution of residual stress, the size of mesh near the cut surface should be very fine. For a welded joint with complex geometry, it is difficult to generate such a mesh with minimum number of DOFs. Especially, when the welding joint has complex geometry, the preprocessing becomes rather troublesome and time consuming. In this research, the mesh refining method was employed to minimize the effort in generating FE model for contour method. Different from the case in welding simulation, the mesh is not dynamically refined according to the position of heat source. The mesh is subdivided according to the position of cutting plane and then remain unchanged in the following analysis.

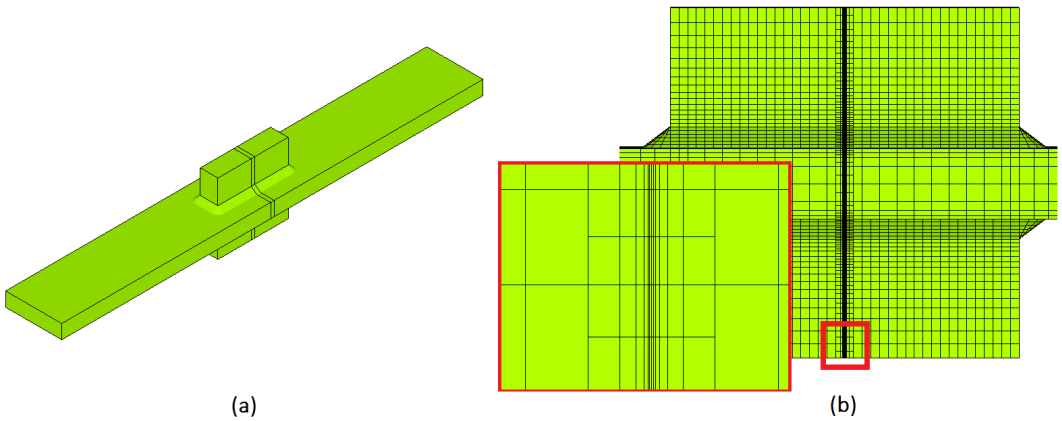

Fig. 7.11 Gusset welding joint after mesh refining: (a) Geometry (b) Mesh

The effectiveness of the proposed method is examined through numerical simulation of contour method. **Figure 7.11** shows the refined mesh for gusset joint. The region which was refined is near the central section with 5mm in width. Five levels of refining was performed, and the minimum element has a 0.078mm size in the direction normal to the cut plane. The residual stresses and plastic strains were mapped from initial mesh to refined mesh.

The longitudinal residual stress before and after cutting is shown in **Fig. 7.12**. Clearly, the stress near the cutting plane was released due to the cutting. And there are still large internal stresses in the region away from the cutting plane. The elastic deformation occurred in the cutting process was plotted for the two separated parts, as shown in **Fig. 7.13**. It can be observed that, the deformation is relatively symmetric about the cutting plane. The difference is mainly caused by the released shear forces which is not symmetrical (actually is anti-symmetrical) about the cutting plane, as shown in **Fig. 7.13(c)**. The produced deformation by shear on the two cut surfaces will cancel out by averaging the deformations on two sides. Other minor reasons are mapping of residual stress from coarse mesh to refined mesh, and also the numerical error by element size (because it is not infinite small).

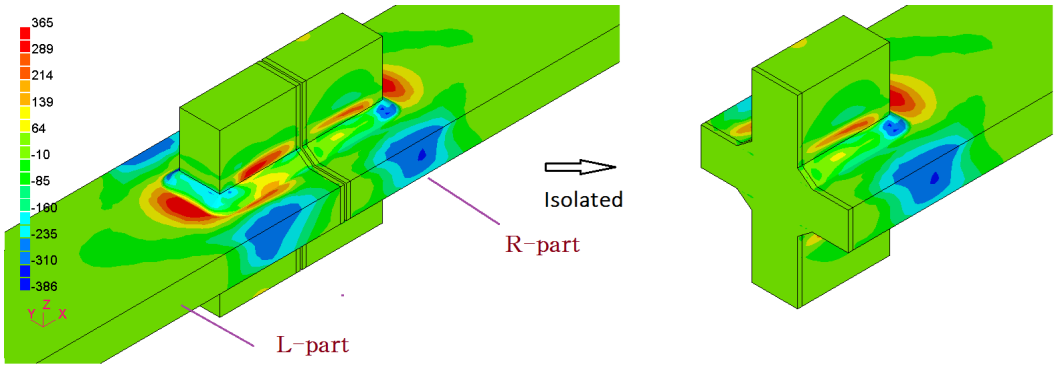

Fig. 7.12 Longitudinal stress (X-direction) after cutting at the middle cross section

It should be noted that, the deformations on both sides of the cut are usually quite different in practical EDM cutting. The primary reason is the winding of the cutting path and the second reason is the fluctuation of cutting width. The former can be removed by averaging the measured deformation on both sides of cut. The latter can be removed by smoothing of measured data to certain extent. In this research, it is assumed that, the additional deformation by thermal-mechanical process is negligible.

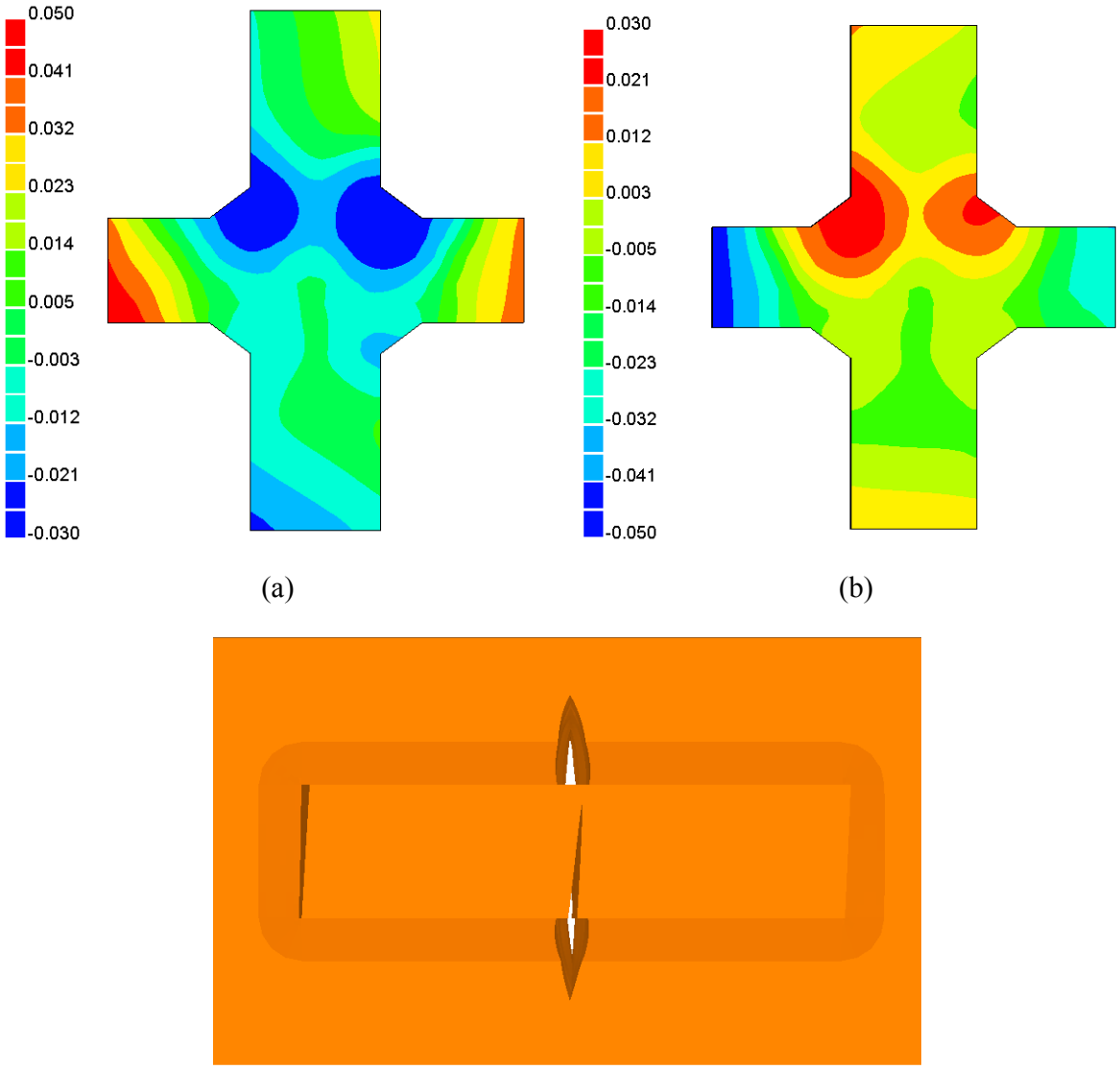

Fig. 7.13 Elastic deformation produced during cutting process: (a) L-part (b) R-part (c) Top view of deformed shape scaled by 100times

The averaged elastic deformation is applied to the separated parts as forced displacement. Only displacement in normal direction of the cut plane was employed, since the in-plane displacements are difficult to be measured during cutting. Elastic analysis is then carried out from the stress free state. Due to the geometric symmetry of cut parts, only L-part is used for elastic analysis by contour method. **Figure 7.14** shows the comparison of contours of original welding residual stress and the reproduced stress. The difference is quite small between the two results.

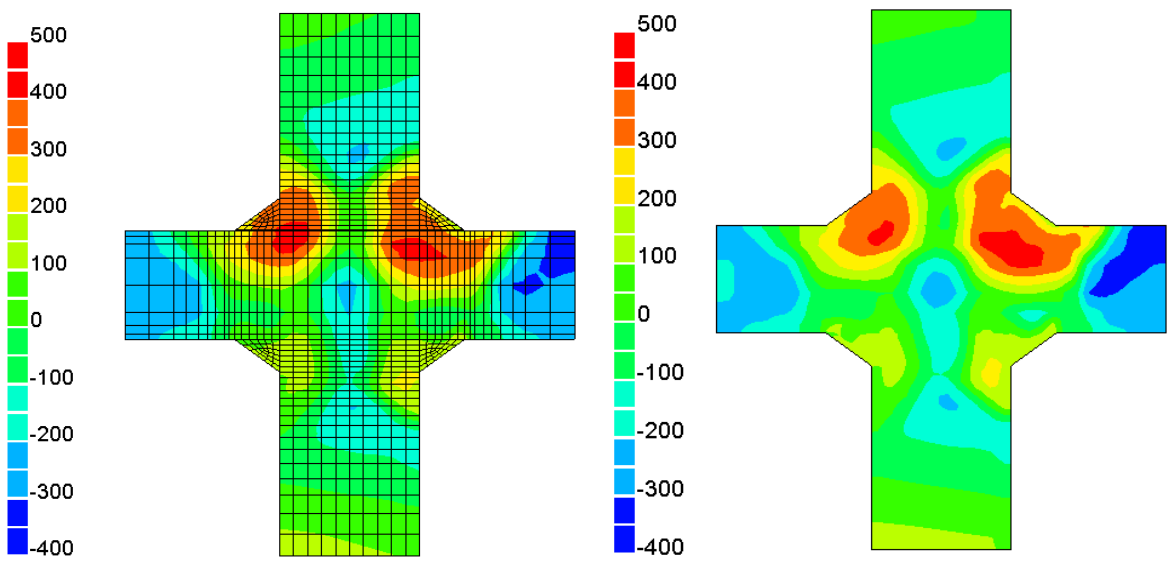

Fig. 7.14 Longitudinal stress at L-part: (a) Original residual stress (b) Reproduced by contour method

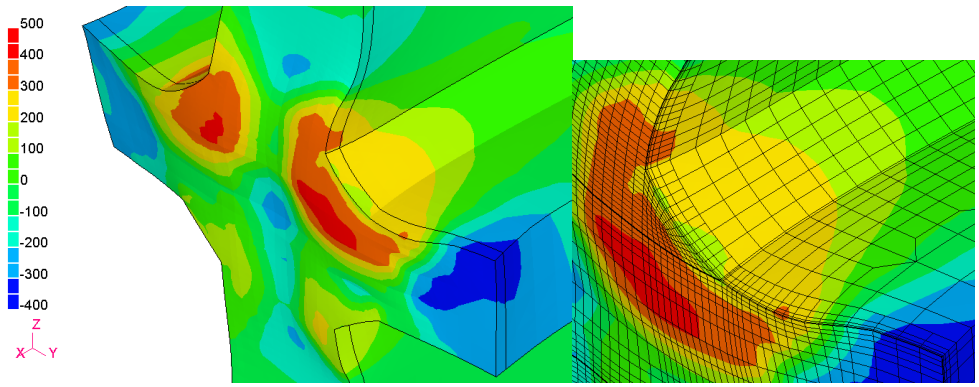

Fig. 7.15 Longitudinal stress by contour method (Deformation scaled by 100 times)

The isotropic view of reproduced longitudinal stress in L-part is shown in **Fig. 7.15**. It can be seen that, the displacement normal to plane due to cutting was reversed in the elastic analysis by contour method. The stress concentrates on the cut plane, and the stress decrease in the region away from the plane. Smooth distribution of stress across the refined elements can be observed, which suggest high accuracy of the mesh refining method.

To be clearer, the stress distribution along two lines were evaluated in **Fig. 7.16**. Good agreement between results of contour method and thermal elastic-plastic FEM is confirmed.

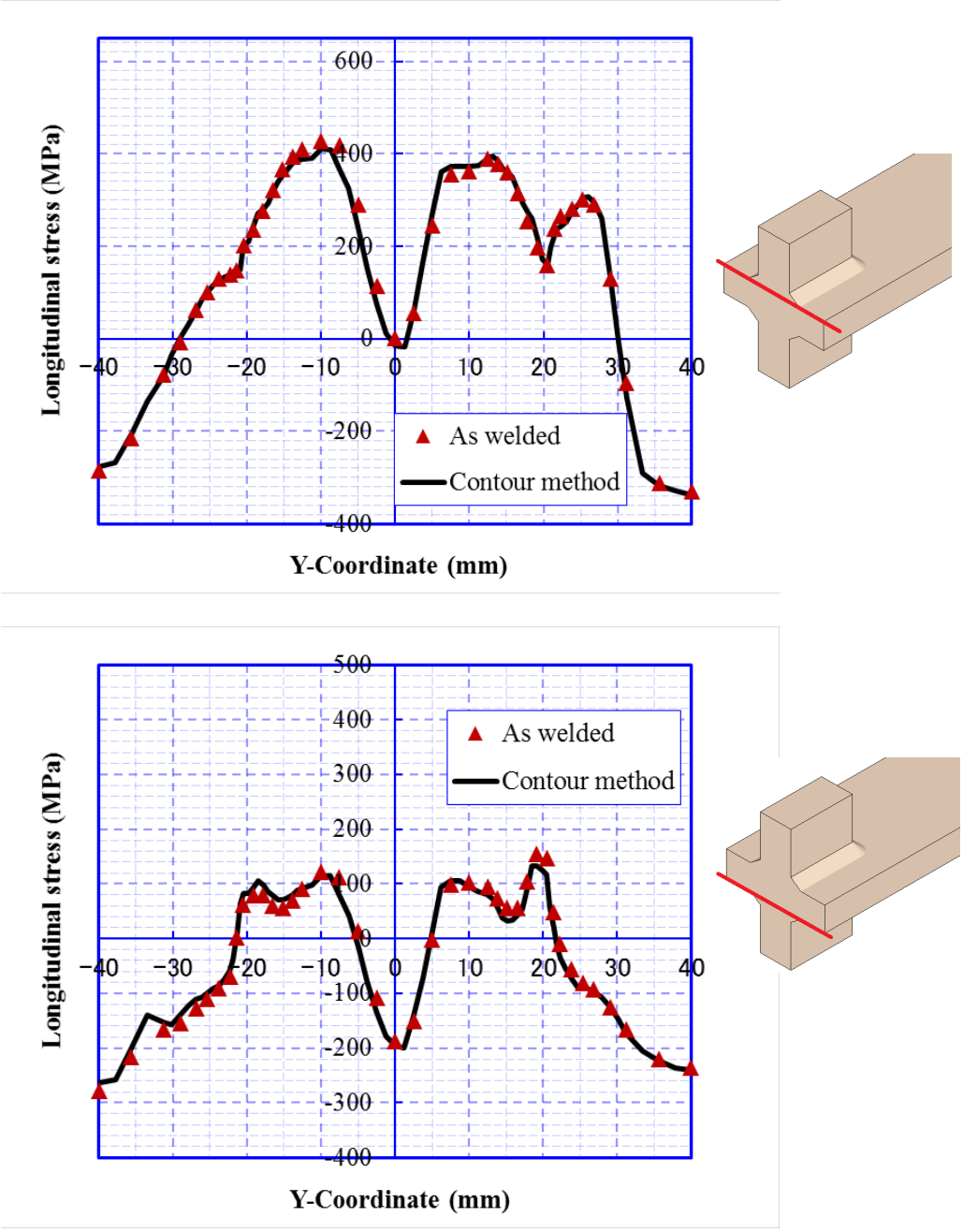

Fig. 7.16 Comparison between welding residual stress and reproduced by contour method

7.3 New contour method based on inherent strain theory

The above example has shown the effectiveness of the conventional contour method which simply use one of the separated parts to reproduce the residual stress. It can be inferred that, the constraint of separated parts are different if the original model is not cut symmetrically. The accuracy of reproduced residual stress depends on which part to use by the contour method. Relevant investigation is conducted in this section. Another case was considered, the cutting plane was shift to X=-45mm to verify this

effect. As shown in **Fig. 7.17**, the welded gusset joint is cut near the edge of web plate. Similar to previous numerical examples, five levels of mesh refinement have been carried out. Elements near the cut plane were subdivided in three directions in the first level of refining. And the newly generated elements were subdivided in X direction in the following levels of refining. The stiffness of the elements in the cut layer was reduced to very small, and the residual stresses on them were removed. The deformation after cutting is shown in **Fig. 7.18**, which apparently indicates that, the deformation on two sides of the cutting plane is very much different, especially at the regions near the web plates.

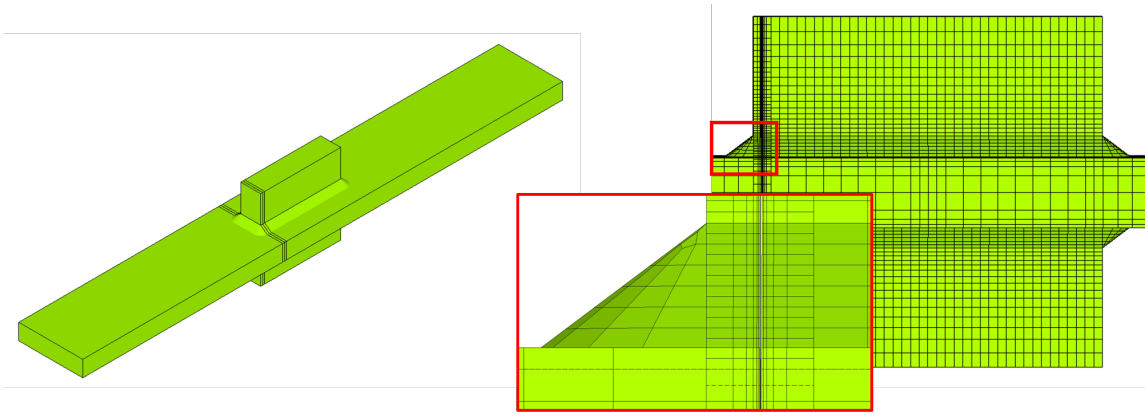

Fig. 7.17 Gusset welding joint with cutting near the edge of web: (a) Geometry (b) Mesh

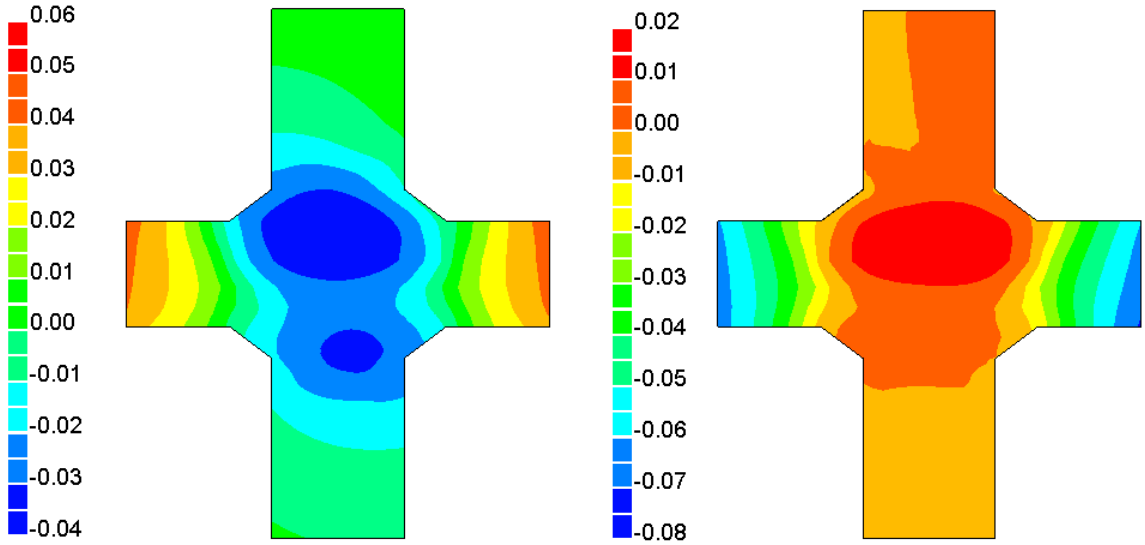

Fig. 7.18 Elastic deformation produced during cutting process: (a) L-part (b) R-part

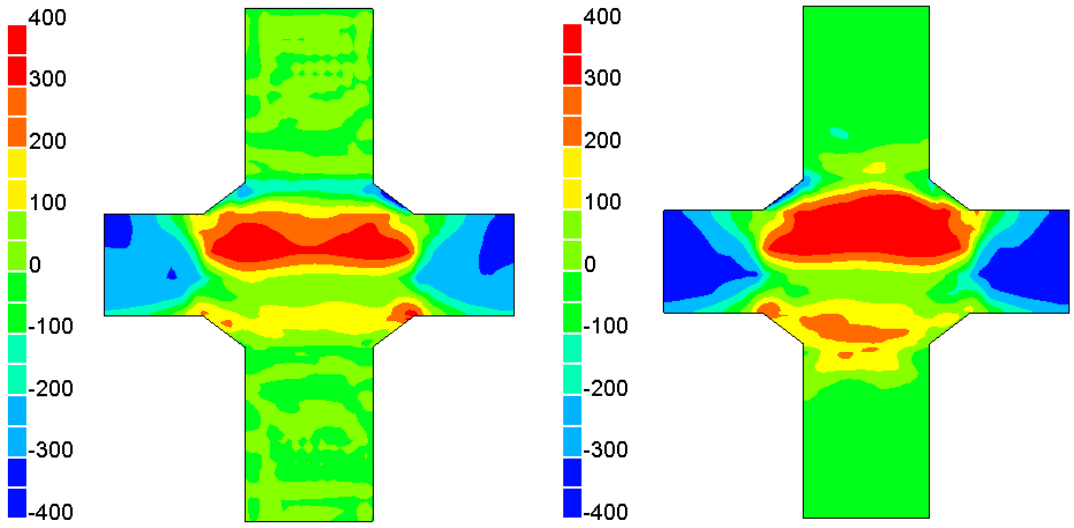

(a) (b)

Fig. 7.19 Reproduced longitudinal stress by contour method: (a) L-part, (b) R-part

The reproduced stress field by means of conventional contour method is plot in **Fig. 7.19**. Though relative good agreement can be found in the flange plate, the stress distribution has large discrepancy in the root of web plate. The isotropic view of reproduced longitudinal stress in L-part is shown in **Fig. 7.20**.

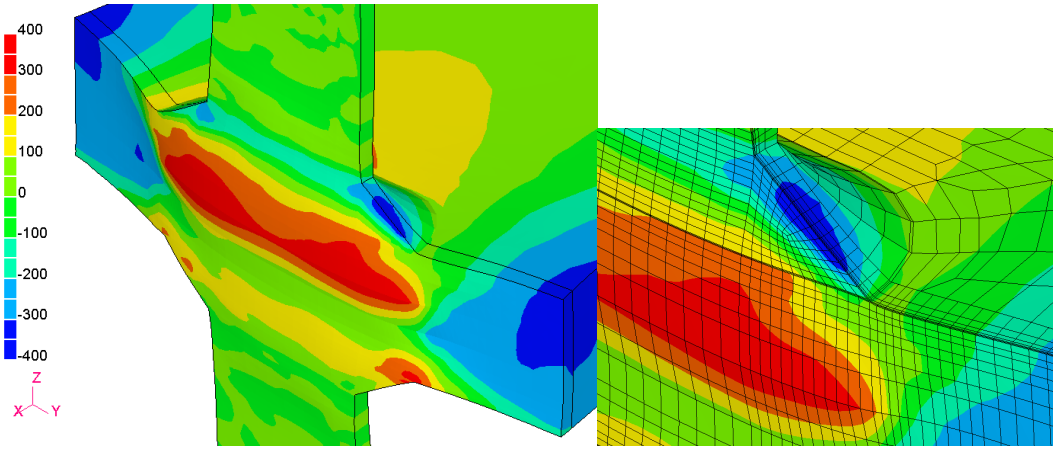

Fig. 7.20 Longitudinal stress by contour method (Deformation scaled by 100 times)

The longitudianl stress in the L-part and R-part was evaluated, and the stress profiles along a typical line are shown in **Fig. 7.21**. The predicted residual stress has similar tendency with original welding residual stress, however there is large deviation in the magnitudes. This is a result of asymmetry of the geometries after cutting.

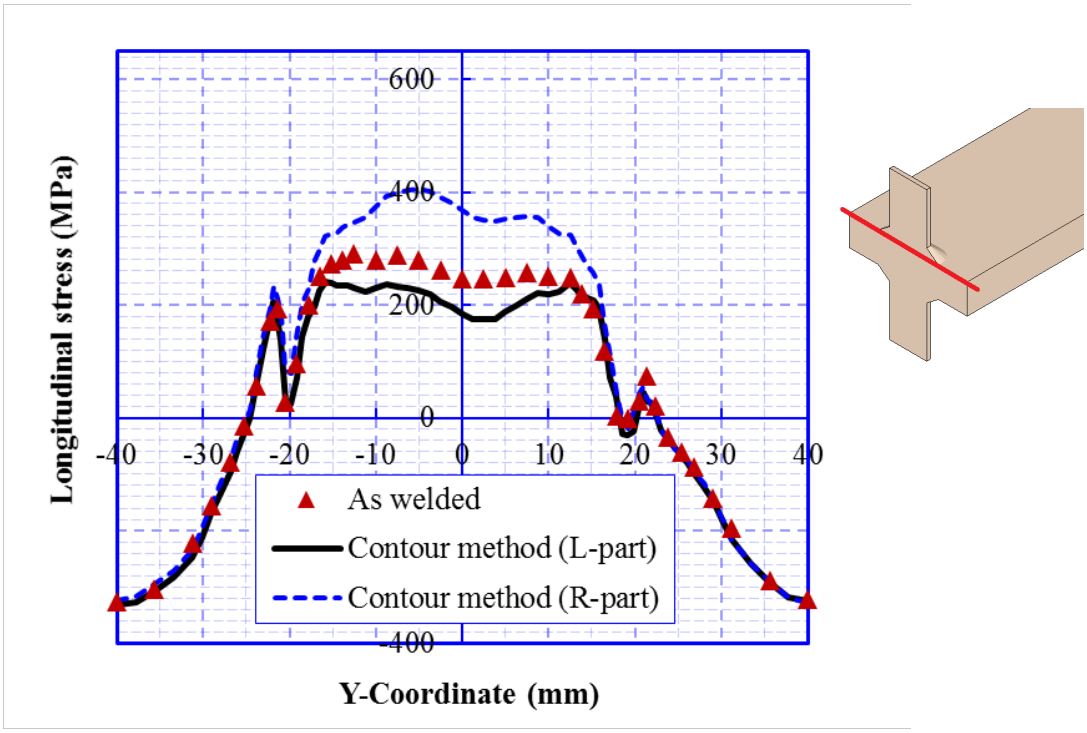

Fig. 7.21 Comparison between welding residual stress and those by conventional contour method

In order to obtain the residual stress in arbitrary position of the welding joint, it is necessary to consider the cutting deformations simultaneously in the analysis by contour method. The non-uniform gap between the two distorted surfaces should be closed when reproducing stress as shown in **Fig. 7.22**. In this research, the inherent strain method was employed to fulfill this purpose. The difference of cutting released deformation (inherent deformation) between two parts are converted into strain of cut layer, and then elastic analysis is carried out with this initial strain on a stress-free FE model. The reproduced residual stress using this new contour method was shown in **Fig. 7.23**. Very similar stress distribution between original residual stress and reproduced one can be observed.

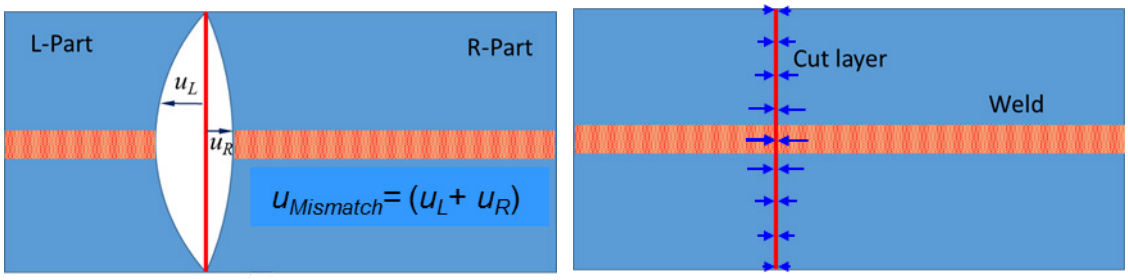

(a) (b)

Fig. 7.22 Concept of inherent strain induced by cutting (a) Plate after cutting (b) Plate by closing mismatch

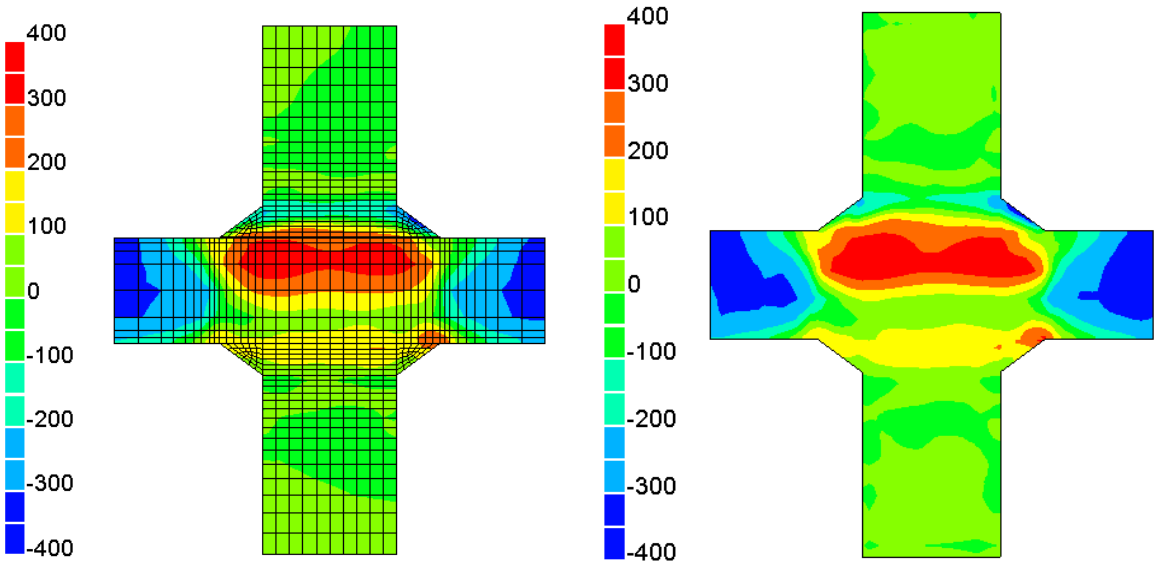

(a) (b)

Fig. 7.23 Longitudinal stress at L-part: (a) Original residual stress (b) Reproduced by new contour method

The isotropic view of reproduced longitudinal stress in L-part is shown in **Fig. 7.24**. It is interesting that longitudinal stress in the weld is mostly in compressive state, which is different from the case at the middle cross section in **Fig. 7.14**.

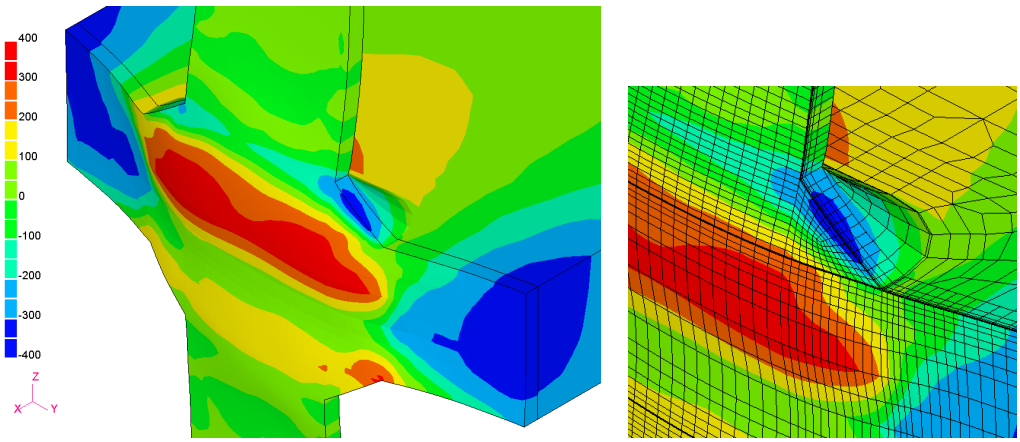

Fig. 7.24 Longitudinal stress by new contour method (Deformation scaled by 100 times)

In order to examine the accuracy of reproduced stress quantitatively, the stress profiles along two lines were evaluated, as shown in **Fig. 7.25.** It can be observed that globally accurate results can be achieved by the new contour method. The local deviated points existed near the weld toe and root. This is because the residual stress was analyzed by a coarser mesh and transferred to a finer mesh (multi-level) by

mapping. There is some extent of loss of numerical accuracy as mapping does not guarantee global equilibrium. The error is avoidable in practical case, since no mapping is necessary. Meanwhile, the stresses of elements are averaged on nodes, and the mesh size will influence the final results when the difference among adjacent element is large (the weld toe and root region is in the case). It is advisable to use uniformly fine mesh for elastic analysis by contour method, especially in the region near the weld line.

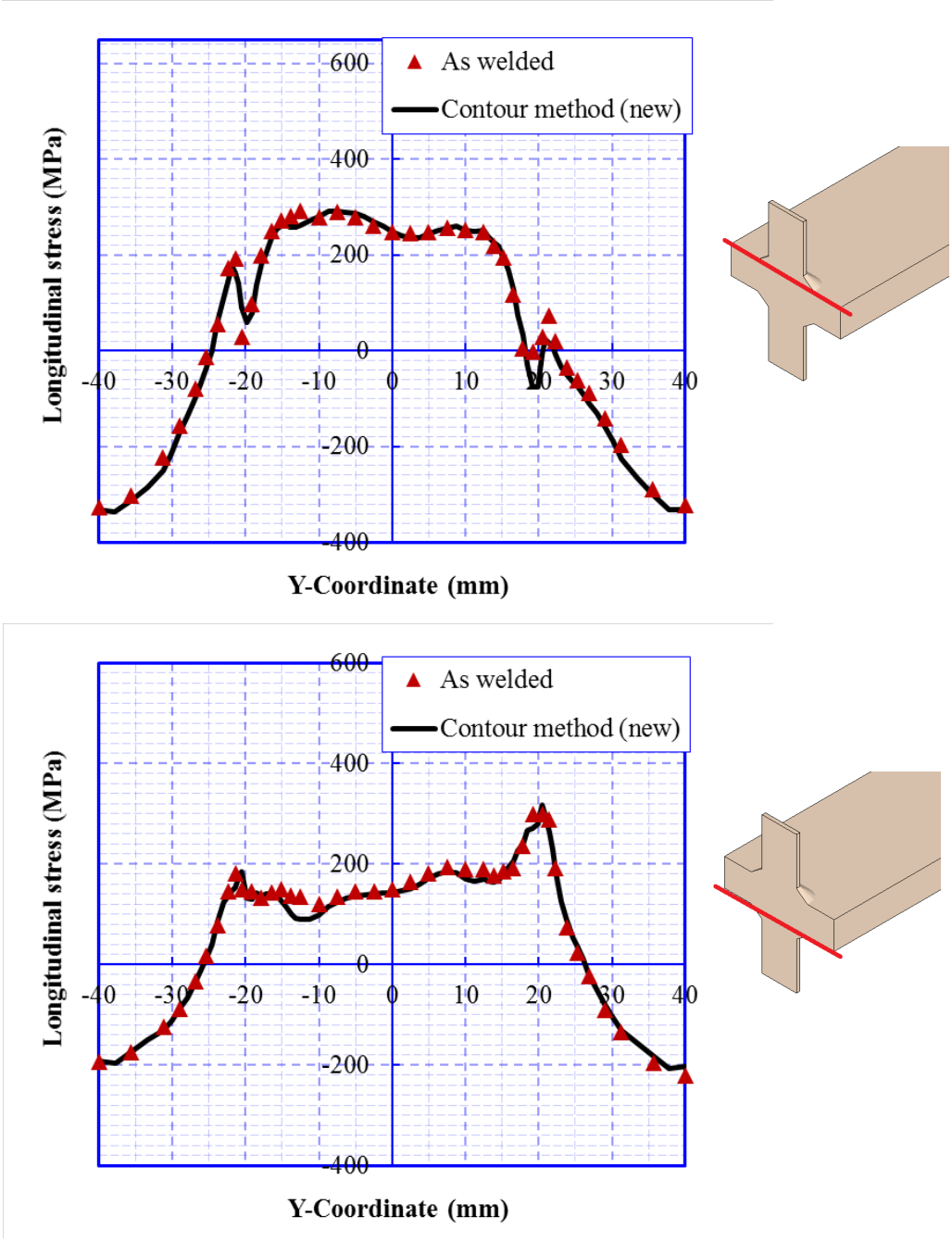

Fig. 7.25 Comparison between welding residual stress and reproduced by new contour method

7.4 Closure

The mesh refining method was extended to analyze problems of stress concentration and residual stress measurement by contour method. Through series of numerical study, it was confirmed that the welding residual stress is less sensitive to mesh size compared with stress concentration. In the case of rough estimation of fatigue life, the stress concentration has large influence on both crack initiation life and fracture life. To be cost-effective, the welding residual stress can be analyzed using a relatively coarse mesh, and then mapped onto a locally refined mesh. The region of refinement can be estimated by the static loading analysis. Qualitatively fatigue life can be predicted based on the refined mesh compared with the analysis using fine mesh for both welding residual stress and stress concentration calculation.

Mesh refining method has also shown advantage in reproducing welding residual stress by contour method. The multi-level refinement enables the modeling of cut of a thin layer very easy. Numerical validation was carried out using a gusset welding joint. Accurate reproduction of residual stress on middle cross section was confirmed by conventional contour method. Nevertheless, the accuracy of reproduced welding stress depends on the symmetry of welding joint after cutting. Cutting near the edge of the web plate was simulated, and the residual stresses were numerically measured on the parts which are cut out separately. Different results were obtained by the conventional contour method. In this study, the contour method based on inherent strain was proposed to overcome the deficiency. The elastic deformation occurred on the two parts were converted into strain, and the strain was introduced into the full welding joint at a stress-free state to reproduce the residual stress. Good agreement has been found between the original residual stresses and the reproduced one. The effectiveness of the contour method based inherent strain theory was validated.

Chapter 8 Conclusions and outlook

In the present study, several efficient and accurate transient thermal elastic-plastic finite element methods for large scale welding and line heating problems have been developed. Computation procedures were described in details for each method, and experimental and numerical examples have been shown to validate the approaches. The conclusions of the study are summarized as follows:

(1) An exhaustive review about computational welding mechanics was made, with focus on recent advance in numerical methods for accelerating computation. In addition, the facing challenges in solving large scale problems was addressed.

(2) From the viewpoint of temperature induced nonlinearity, the refining method was proposed to reduce the number of degrees of freedom in welding/heating problems. The multi-level refinement is developed based on node property, and interface between elements at different refining level is connected by transformation matrix. Flexible refinement in single or multiple direction is also available, which makes the computation more efficient. The proper values of mesh size and time increment is estimated by simple equations based on the conservation and continuity of heat input.

(3) In order to keep accuracy for stress and strain, dynamic mesh refining method is proposed with the idea of background mesh. Two different schemes in updating solution on background mesh are introduced. Refinement criterion based on analytical temperature distribution are employed in the research.

- In the first scheme, stiffness and equations are always assembled and solved on the computational mesh, and solutions are just recorded on background mesh. Both computation time and required physical memory are reduced, while the refinement was just limited to one level.
- In the second scheme, global stiffness and equations are also assembled and solved on background mesh, respectively. Multi-level refinement can be performed, and the computation can be further accelerated at the cost of computer memory.
- Fillet welding joints in different scale were analyzed by the two scheme respectively. The results revealed that DMRM can reduce the computation time to about 1/9 for a model consisting of 326,400 elements. The acceleration ratio almost linearly increase with ratio of number of elements in computational mesh and background mesh.

(4) In this study, two efficient schemes for temperature analysis were proposed and investigated. Based on the computational results, the following conclusions can be drawn:

- Dynamic mesh refining method can accurately trace the temperature history at

each point, and computation time is greatly reduced.

- ◆ Heat transfer localization method can predict the temperature distribution around the heat source and dual mesh analysis is proposed to recover the accuracy for outer region.
- ◆ Acceleration of computation was observed when the model scale grows larger. It is very efficient to apply the proposed methods in large scale structure.
- ◆ The temperature analysis of a stiffener model with over 1 million elements has been completed in 8.3 hours and 5.1 hours with DMRM and HTLM, respectively.
- ◆ The CPU time and physical memory of temperature analysis has been dramatically reduced by the proposed computation schemes.

(5) The existing advanced method — iterative substructure method was extended to larger scale analysis by combining with the concept of inherent strain. Also, a modified iterative substructure method (mod-ISM) with consideration of the large deformation theory was developed. As a main point of this study, dynamic mesh refining method and modified ISM were successfully combined to solve large scale thermo- mechanical problems.

- ◆ The welding deflection for a lap joint computed under large deformation theory agreed well with the measured one. The modified ISM shows a good accuracy in computation of large deformation problem and consumes much less time than the standard FEM.
- ◆ Three levels of refining was realized to analyze a line heating problem, large amount of DOFs were reduced in the computational mesh. By dynamic mesh refining method, the acceleration ratio over ABAQUS is about 40 times.
- ◆ By analyzing a flange-to-pipe welding model with 207,090 unknowns, it was demonstrated that, the computation time of latest version of DMRM* consumes just 1/56 of the time that used by ABAQUS, while the solution accuracy of the two codes are comparable.

(6) To demonstrate the performance of proposed method, typical large scale welding problems were analyzed. Computations on multi-pass thick welding joint, line heating on rectangular flat plate, welding of stiffened panel structures were included in this research.

- ◆ The rectangular plate with 33 heating lines model were analyzed under both small and large deformation theory. Significant difference in deformation magnitude was observed for the two cases. The computation was accomplished within 4 days by DMRM with single CPU.
- ◆ Transient thermal elastic-plastic analysis was realized on a large stiffened panel welded structure which has nearly 5 million DOFs. The initial gap was also investigated on its effect on final structural deformation. Good agreement between

numerical simulation and experiment results were confirmed.

- The effectiveness of i-ISM is examined taking welding of thick multi-pass weld joint as examples. The reduction of the computational time reaches 72 % in the case of welding on large-scale thick plate which contains around one million elements.

(7) The stress concentration problem was analyzed by refining method for high resolution. Mesh refining method has also shown advantage in reproducing welding residual stress by contour method. Following findings can be drawn:

- Rough fatigue life estimation reveals that, the stress concentration has large influence on both crack initiation life and fracture life.
- The welding residual stress is less sensitive to mesh size compared with stress concentration problem.
- To balance the cost of computation, fatigue life can be predicted by refining local region and mapping welding residual stress.
- In the framework of contour method, geometrical symmetry of welding joint after cutting is important in calculation of residual stress.
- The proposed new contour method based on inherent strain theory is effective in reproducing welding residual stress in more general cases such as asymmetric geometry.

Future works

Although the presented large deformation problems have been successfully solved using thermo-mechanical analysis. However, for some of practical cases, if plates are very thin and the structure is complex, the analysis tends to be unstable at bifurcation points. The severe numerical difficulty could interrupt the computation for current codes. Investigation on transient stability analysis such as arc length method and explicit method should be conducted to overcome this problem.

Fatigue analysis with simulation of crack initiation and propagation can be implemented in the framework of mesh refining and extended finite element method (X-FEM). Since the accuracy of X-FEM relies heavily on mesh size, the DMRM is very useful to zoom the local stress field. As illustrated in chapter 7.2, the fatigue strength evaluation can be improved by detailed residual stress and load-induced stress. The current approach shows great potential in analyzing practical welding and fatigue problems.

For complex welded structures, the assembly process induced effects such as gap, contact and constraint may greatly influence the welding deformation. Accurate

modeling of those factors in three-dimensional case requires additional interface elements and very robust solution control. It may be possible to simplify the modeling by some case study using elaborate numerical examples.

Finally, the memory consumption of proposed methods tends to be large in solving practical scale structure, due to the feature of implicit method. Due to data scattering in memory, the computation will slow down in case of solving large scale problem. A hybrid analysis methodology by combing explicit method and implicit method is promising. The instability problem can also be well solved in this framework, and meanwhile, the efficiency and accuracy is guaranteed.

Acknowledgement

First and foremost, I would like to express my sincere gratitude to my supervisor, Professor Hidekazu Murakawa, for his intellectual guidance and constant encouragement during my research. With patience and prudence, he labored through drafts of this thesis and pointed out defects in my theorizing. His innovative insight, rigorous attitude in science and hard working sprit have impressed me and will inspire me in my future study and research.

My cordial thanks go to Associate Professor Hisashi Serisawa for contacting me before I came to Japan and giving me valuable advices in the weekly seminar. I also want to express my gratitude to Professor Sherif Rashed, Associate Professor Keiji Nakacho, and Special Researcher Kawahara Atsushi for their fruitful discussion and comments. Especially, Prof. Fujikubo and Prof. Osawa are acknowledged for valuable suggestions and reviewing the thesis. They shared with me their idea and knowledge, without which I could not well complete the thesis.

I am very grateful to Prof. Ma, for his great help in my doctoral course and also for providing me a chance to conduct research work in JSOL. Many valuable advices and experiences are received from Prof. Ma in the past three years.

And I also express my gratitude to Ms. Noriko Fujimoto, for her kind assistance in many aspects related to study and my stay at Japan. I am also very grateful to all my lab mates, who have given me a lot of help and courage during my stay at the university.

The financial support from the Japanese Government (MONBUKAGAKUSHO: MEXT) is gratefully acknowledged.

Last but not the least; big thanks go to my family in China who has given me a lot of love and support. I am very grateful for their understanding of my studying abroad. I would like to express special thanks to my wife for her support during my study.

Reference

[1] Rosenthal D. (1941) Mathematical theory of heat distribution during welding and cutting.Welding Journal, 21(5): 220- 234

[2] Tanaka S. (1943) A study on heat conduction of a moving heat source. Journal Japan Welding Society, 13(9): 347-359.

[3] Rykalin N. N., The calculation of thermal processes in welding. Mashgiz (1951) translated into English by Z. Paley and C. M. Adams, Jr., 1963

[4] Okerblom N. O., (1958) The calculations of deformations of welded metal structures, London, Her Majesty's Stationary Office

[5] Vinokurov V. A., (1977) Welding stresses and distortion: determination and elimination. British Library Lending Division (original Russian version, Mashinostroenie, Moscow, 1968).

[6] Brian P. L. T. (1961) A finite-difference method of high-order accuracy for the solution of three-dimensional transient heat conduction problems. AIChE Journal, 7(3): 367-370.

[7] Wilson E. L., Nickell R. E. (1966) Application of the finite element method to heat conduction analysis. Nuclear Engineering and Design, 4(3): 276-286.

[8] Ueda Y., Yamakawa T. (1971) Analysis of thermal elastic-plastic stress and strain during welding by finite element method, Transactions of the Japan Welding Society, 2-2, 186-196

[9] Hibbitt H. D., Marcal P. V. (1973) A numerical, thermo-mechanical model for the welding and subsequent loading of a fabricated structure. Computers & Structures, 3(5): 1145-1174.

[10] Friedman E. (1975) Thermomechanical analysis of the welding process using the finite element method. Journal of Pressure Vessel Technology, 97(3): 206-213.

[11] Andersson B. A. B. (1978) Thermal stresses in a submerged-arc welded joint considering phase transformations. Journal of Engineering Materials and Technology, 100(4): 356-362.

[12] Masubuchi K. (1980) Analysis of welded structures: Residual stresses, distortion, and their consequences. First edition.

[13] Ueda Y., Takahashi E., Fukuda K. (1976) Multipass welding stresses in very thick plates and their reduction from stress relief annealing. Transactions of JWRI. 5(2): 179-189

[14] Rybicki E. F., Schmueser D. W., (1978) Stonesifer R W, et al. A finite-element model for residual stresses and deflections in girth-butt welded pipes. Journal of Pressure Vessel Technology, 100(3): 256-262.

[15] Rybicki E. F., Kanninen M. F. (1977) A finite element calculation of stress intensity factors by a modified crack closure integral. Engineering Fracture Mechanics, 9(4): 931-938.

[16] Maddox S. J. (1975) An analysis of fatigue cracks in fillet welded joints. International Journal of Fracture, 11(2): 221-243.

[17] Andersson B., Karlsson L. (1981) Thermal stresses in large butt-welded plates. Journal of Thermal Stresses, 4(3-4): 491-500.

[18] Parker A. P. (1982) Stress intensity factors, crack profiles, and fatigue crack growth rates in residual stress fields. ASTM STP, 776: 13-31.

[19] Kanninen M. F., Brust F. W., Ahmad J., et al. (1982) The numerical simulation of crack growth in weld-induced residual stress fields. Springer US

[20] Ueda Y., Kim Y. C., Garatani K., Yamakita T., Bang H. S. (1986). Mechanical characteristics of repair welds in thick plate (Report I): Distributions of three-dimensional welding residual stresses and plastic strains and their production mechanisms (Welding Mechanics, Strength & Design). Transactions of JWRI, 15(2), 359-368.

[21] Tekriwal P., Mazumder J. (1988) Finite element analysis of three-dimensional transient heat transfer in GMA welding. Welding Journal, 67(5): 150-156.

[22] Karlsson R.I., Josefson B.L., (1990) Three-dimensional finite element analysis of temperatures and stresses in a single-pass butt-welded pipe, J. Pressure Vessel Technol. 112-1: 76-84

[23] Wang J., Qi X., Zhong X. Ueda Y., Murakawa H. , (1994) Three dimensional simulation of welding deformations by FEM. Journal of Shanghai Jiaotong University, 6

[24] Fujimoto T., (1970) A method for analysis of residual welding stresses and deformations based on the inherent strain : A theoretical study of residual welding stresses and deformations (Report 1), Welding Society Journal 39(4), 236-252

[25] Ueda Y., Fukuda K., Tanigawa M. (1979) New measuring method of three dimensional residual stresses based on theory of inherent strain (Welding Mechanics, Strength & Design). Transactions of JWRI, 8(2): 249-256.

[26] Hill M. R., Nelson D. V. (1995) The inherent strain method for residual stress

determination and its application to a long welded joint. ASME-Publications-PVP, 318: 343-352.

[27] Ueda Y., Yuan M. G. (1993) Prediction of residual stresses in butt welded plates using inherent strains. Journal of Engineering Materials and Technology, 115(4): 417-423.

[28] Yuan M. G., Ueda Y. (1996) Prediction of residual stresses in welded T-and I-joints using inherent strains. Journal of Engineering Materials and Technology, 118(2): 229-234.

[29] Nakacho K., Ohta T., Ogawa N., et al. (2007) Measurement of welding residual stresses of reactor vessel by inherent strain method. Measurement of residual stresses of pipe-plate penetration joint. Quarterly Journal of the Japan Welding Society 40(5): 581-589

[30] Ma N., Murakawa H., Luo Y., Deng D., (2009) Measurement of three dimensional residual stresses in rolled clad plates and welded joints of a chemical tank structure. Transactions of JWRI , 38(2): 79-86.

[31] Murakawa H., Luo Y., Ueda Y., (1996) Prediction of welding deformation and residual stress by elastic FEM based on inherent strain (first report)–mechanism of inherent strain production. Journal of the society of Naval Architects of Japan, 180: 739-751.

[32] Wang R., Zhang J., Serizawa H., Murakawa H. (2009) Study of welding inherent deformations in thin plates based on finite element analysis using interactive substructure method. Materials & Design, 30(9): 3474-3481.

[33] Liang W., Deng D., Sone S., Murakawa H. (2005). Prediction of welding distortion by elastic finite element analysis using inherent deformation estimated through inverse analysis. Welding in the World, 49(11-12), 30-39.

[34] Murakawa H., Deng D., Ma N., (2010) Concept of inherent strain, inherent stress, inherent deformation and inherent force for prediction of welding distortion and residual stress. In: Proceedings of the International Symposium on Visualization in Joining and Welding Science, Osaka, Japan, 115–116.

[35] Hata M., Itoh S., Sugihiro T., Yamashita Y., Kamio A., Shibahara M., Mochizuki M. (2012). Investigation of factors influencing welding deformation of ship block by inherent strain analysis using idealized explicit FEM. Journal of Physics: Conference Series, 379(1): 012055

[36] Wang J., Rashed S., Murakawa H., Luo Y. (2013) Numerical prediction and mitigation of out-of-plane welding distortion in ship panel structure by elastic FE

analysis. Marine Structures, 34: 135-155.

[37] Wang J., Rashed S., Murakawa H., Shibahara M. (2011) Investigation of buckling deformation of thin plate welded structures. Proceedings of International Society of Ocean and Polar Engineering. 125‑131.

[38] Moshaiov A., Vorus W. S. (1987) The mechanics of the flame bending process: theory and applications, Journal of Ship Research, 31(4): 269-281

[39] Nomoto T., Ohmori T., Sutoh T., Enosawa M., Aoyama K., Saitoh M. (1990) Development of simulator for plate bending by line-heating, Journal of The Society of Naval Architects of Japan, 168: 527-535

[40] Shin J. G., Moshaiov A. (1991) Modified strip model for analyzing the line heating method-part 1: Elastic plates, Journal of Ship Research, 35(2): 172-182.

[41] Moshaiov A., Shin J. G. (1991) Modified strip model for analyzing the line heating method-part 2: Thermo-elastic-plastic plates, Journal of Ship Research, 35(3): 266-275

[42] Ueda Y., Murakawa H., Rashwan A. M., Okumoto Y., Kamichika R. (1994) Development of computer-aided process planning system for plate bending by line heating,(Report 3) –relation between heating condition and deformation, Journal of Ship Production, 10(4): 248-257

[43] Ueda Y., Murakawa H., Rashwan A. M., Okumoto Y., Kamic R. (1994) Development of computer-aided process planning system for plate bending by line heating (Report 1) - Relation between final form of plate and inherent strain. Journal of Ship Production, 10(1): 59-67.

[44] Ueda Y., Murakawa H., Rashwan A. M., Okumoto Y., Kamichika R. (1994) Development of computer-aided process planning system for plate bending by line heating, (Report 2) - Practice for plate bending in shipyard viewed from aspect of inherent strain, Journal of Ship Production, 10(4): 239-247.

[45] Ueda Y., Murakawa H., Rashwan A. M., Okumoto Y., Kamichika R. (1993) Development of computer-aided process planning system for plate bending by line heating (Report 4), Transactions of Japan Welding Research Institute, 22(2): 305-313.

[46] Tango Y., Ishiyama M., Nagahara S., Nagashima T., Kobayashi J. (2003) Automated line heating for plate forming by IHI-ALPHA system and its application to construction of actual vessels : System Outline and Application Record to date, Journal of The Society of Naval Architects of Japan, 193: 85-9

[47] Shin J. G., Ryu C. H., Lee J. H., Kim W. D. (2003) User-friendly, advanced line

heating automation for accurate plate forming, J. Ship Prod., 19(1): 8-15.

[48] Shin J. G., Ryu C. H., Nam J. H. (2004) A comprehensive line-heating algorithm for automatic formation of curved shell plates. J. Ship Prod., 20(2): 69-78.

[49] Tango Y., Ishiyama T., Suzuki H. (2011) IHIMU-alpha a fully automated steel plate bending system for shipbuilding, IHI Engineering Review, 44(1): 6-11.

[50] Vega A., Escobar E., Fong A., Ma N., Murakawa H. (2013) Analysis and prediction of parallel effect on inherent deformation during the line heating process. Computer Modeling in Engineering & Sciences, 90(3): 197-210.

[51] Vega A., Osawa N., Rashed S., Murakawa H. (2010) Analysis and prediction of edge effect on inherent deformation of thick plates formed by line heating. Computer Modeling in Engineering & Sciences, 69(3): 261-279.

[52] Vega A., Rashed S., Tango Y., Ishiyama M., Murakawa H. (2008) Analysis and prediction of multi-heating lines effect on plate forming by line heating, CMES Journal: Computer Modeling in Engineering & Sciences, 28(1): 1-14.

[53] Mochizuki M., Enomoto K., Okamoto N., Saito H., Hayashi E. (1993) Welding residual stresses at the intersection of a small diameter pipe penetrating a thick plate. Nuclear Engineering and Design, 144(3): 439-447.

[54] Brickstad B, Josefson B L. (1998) A parametric study of residual stresses in multi-pass butt-welded stainless steel pipes. International Journal of Pressure Vessels and Piping, 75(1): 11-25.

[55] Itoh S., Sengel M., Shibahara M., Serizawa H., Murakawa H. (2007) Influence of various factors on distortion of pipes under butt and fillet welding, Mathematical Modelling of Welding Phenomena, 8: 1141-1154

[56] Maekawa A., Kawahara A., Serizawa H., Murakawa H. (2013) Residual stress study in dissimilar metal welds of a PWR pressurizer surge nozzle: validation of developed fast analysis method and examination of safe-end length effect. In ASME 2013 Pressure Vessels and Piping Conference. American Society of Mechanical Engineers.

[57] Brown S. B., Song H. (1993) Rezoning and dynamic substructuring techniques in FEM simulations of welding processes, ASME J. Engrg Ind., 155: 415-423

[58] Lindgren L. E., Haggblad H. A., McDillb J. M. J., Oddy A. S. (1997) Automatic remeshing for three-dimensional finite element simulation 0f welding, Comput. Methods Appl. Mech. Engrg., 147(3): 401-409

[59] Duranton P., Devauxa J., Robin V., Gilles P., Bergheau J.M. (2004) 3D modelling

of multipass welding of a 316L stainless steel pipe, J. Mater. Process. Technol., 153-154: 457-463

[60] Goldak J .A., Mocanita M., Aldea V., Zhou J ., Downey D. and Zypchen A. (1999) Is real time CWM feasible? Recent progress in CWM; 5th International Seminar Numerical Analysis of Weldability IIW Com. IX, Graz-Seggau, Austria

[61] Souloumiac B., Boitout F., Bergheau J. (2001) A new local‐global approach for the modelling of welded steel component distortions, in: Mathematical Modelling of Weld Phenomena 6, Institute of Materials, Minerals and Mining, Graz, Austria.

[62] Hamide M., Elisabeth M., Michel B. (2008) Adaptive mesh technique for thermal ‐metallurgical numerical simulation of arc welding processes. International journal for numerical methods in engineering, 73(5): 624-641.

[63] Murakawa H., Oda I., Itoh S., Serizwa H., Shibahara M., Nishikawa H. (2004) Iterative substructure method for fast FEM analysis of mechanical problems in welding, Preprints of the National Meeting of JWS, 75: 274-275

[64] Itoh S., Shibahara M., Serizawa H., Murakawa H. (2009) Development of hierarchical multi-grid method and its application to the iterative substructure method. The Nineteenth International Offshore and Polar Engineering Conference. International Society of Offshore and Polar Engineers.

[65] Shibahara M., Ikushima K. (2010) Development of analytical method for welding mechanics using idealized explicit FEM, Transactions of JWRI, 39(2): 384-386

[66] Ikushima K., Itoh S., Shibahara M. (2013) Development of parallelized idealized expplicit FEM using GPU, Journal of Japan Welding Society, 31(1): 23-32

[67] Qiao D, Zhang W, Feng Z. (2012) High-temperature constitutive behavior of austenitic stainless steel for weld residual stress modeling. ASME Pressure Vessels and Piping Conference. American Society of Mechanical Engineers, 1229-1236.

[68] Goldak J., Chakravarti A., Bibby M. (1984) A new finite element model for welding heat sources. Metallurgical transactions B, 15(2): 299-305.

[69] Kiyoshima S., Deng D., Ogawa K., Yanagida N., Saito K., (2009) Influences of heat source model on welding residual stress and distortion in a multi-pass J-groove joint. Comp. Mater. Sci. 46(4): 987-995.

[70] Murakawa H., Sano M., Wang J. (2012) Influence of root gap and tack weld on transverse shrinkage during welding. Trans JWRI, 41(1): 65-77.

[71] Deng D.A., (2009) FEM prediction of welding residual stress and distortion in carbon steel phase transformation effects. Material & Design, 30: 359‐366.

[72] Goldak J., Oddy A., Gu M., Ma W., Mashaie A., Hughes E. (1992) Coupling heat transfer, microstructure evolution and thermal stress analysis in weld mechanics. In Mechanical Effects of Welding, Springer Berlin Heidelberg, 1-30.

[73] Benzley S. E. (1995) A comparison of all-hexahedra and all tetrahedral finite element meshes for elastic & elastoplatic analysis. Proceedings 4th International Meshing Round table, Sandia National Labs, 179-181

[74] Wang E., Thomas N., Rainer R. (2004) Back to elements-tetrahedra vs. hexahedra. International ANSYS Conference Proceedings, Munich, Germany,

[75] Feulvarch E., Roux J.C., Bergheau J.M. (2011) A simple and robust moving mesh technique for the finite element simulation of Friction Stir Welding, Fifth International Conference on Advanced Computational Methods in Engineering, Belgium

[76] Calvo N.A., Idelsohn S.R. (2000) All-hexahedral element meshing: Generation of the dual mesh by recurrent subdivision, Comput. Methods. Appl. Mech. Engrg. 182(3): 371-378.

[77] Zhang Y.J., Bajaj C. (2006) Adaptive and quality quadrilateral/hexahedral meshing from volumetric data, Comput. Methods. Appl. Mech. Engrg. 195(9): 942-960.

[78] Hughes T.J.R., Cottrell J.A., Bazilevs Y. (2005) Isogeometric analysis: CAD, finite elements, NURBS, exact geometry and mesh refinement, Comput. Methods. Appl. Mech. Engrg. 194(39): 4135-4195.

[79] Liu Y., Murakami S., Kanagawa Y. (1994) Mesh-dependence and stress singularity in finite element analysis of creep crack growth by continuum damage mechanics approach, Eur. J. Mech. A-Solid 13(3): 395-418.

[80] Chen W., Deng X. (2000) Performance of shell elements in modeling spot-welded joints, Finite Elem. Anal. Des. 35(1): 41-57.

[81] Michael W. (2013) Simufact.welding-High end software solution for welding analysis, IIW International Conference on "Automation in Welding", Essen, Germany

[82] Seshaiyer P., Suri M. (2000) hp submeshing via non-conforming finite element methods. Comput. Methods. Appl. Mech. Engrg. 189(3): 1011-1030.

[83] Chen Y., Li L., Fang J., Feng X. (2003) Numerical analysis of energy effect in laser-TIG hybrid welding. J. Mater. Sci. Technol., 19: 23-26

[84] Deng D. (2009) FEM prediction of welding residual stress and distortion in

carbon steel considering phase transformation effects. Materials & Design, 30(2): 359-366.

[85] Okagaito T., Ohji T., Miyasaka F. (2004) UV radiation thermometry of TIG weld pool–development of UV radiation thermometry (Report 1). Quart J Jpn Weld Soc 22(1): 21–6.

[86] Osawa N., Hashimoto K., Sawamura J., et al. (2007) Development of heat input estimation technique for simulation of shell forming by line-heating. Computer Modeling in Engineering and Sciences, 20(1): 43.

[87] Deng D., Liang W., Murakawa H. (2007) Determination of welding deformation in fillet-welded joint by means of numerical simulation and comparison with experimental measurements. Journal of Materials Processing Technology, 183(2): 219-225.

[88] Tsirkas S. A., Papanikos P., Kermanidis T. (2003) Numerical simulation of the laser welding process in butt-joint specimens. Journal of Materials Processing Technology, 134(1): 59-69.

[89] Shi Y. W., Chen B. Y., Zhang J. X. (1990) Effects of welding residual stresses on fatigue crack growth behaviour in butt welds of a pipeline steel. Engineering Fracture Mechanics, 36(6): 893-902.

[90] Murti V., Valliappan S. (1986) Numerical inverse isoparametric mapping in remeshing and nodal quantity contouring, Comput. Struct., 22(6): 1011-1021

[91] Deng D., Luo Y., Serizawa H., Shibahara M., Murakawa H. (2003) Numerical simulation of residual stress and deformation considering phase transformation Effects, Trans. JWRI, 32(2): 325-333

[92] Runnemalm H., Hyun S. (2000) Three-dimensional welding analysis using an adaptive mesh scheme. Computer methods in applied mechanics and engineering 189(2): 515-523.

[93] Radaj D. (1992) Heat effects of welding: Temperature field, residual stress, distortion, Springer-Verlag, 54-55

[94] Ueda Y., Takahashi E., Fukuda K., Nakacho K. (1974) Transient and residual stresses in multi-pass welded butt joints of 15cm thick plate, J. Jpn. Weld. Soc., 44(5): 466-474

[95] Deng D., Murakawa H. (2006) Numerical simulation of temperature field and residual stress in multi-pass welds in stainless steel pipe and comparison with experimental measurements, Comput. Mater. Sci., 37(3): 269-277.

[96] Ando Y., Yagawa G., Hayase Y. (1982) Evaluation of induction heating stress improvement (IHSI) treatment applied to nuclear primary piping. International Journal of Pressure Vessels and Piping, 10(5): 399‑406.

[97] Deng D., Murakawa H., Liang W. (2007) Numerical simulation of welding distortion in large structures. Computer methods in applied mechanics and engineering, 196(45): 4613-4627

[98] Ueda Y., Murakawa H., Ma N. (2012) Welding deformation and residual stress prevention, Butterworth-Heinemann, Elsevier.

[99] Nishikawa H., Serizawa H., Murakawa H. (2007) Actual application of FEM to analysis of large scale mechanical problems in welding. Science and Technology of Welding & Joining 12(2): 147-152.

[100] Osawa N., Hashimoto K., Sawamura, J., Kikuchi J., Deguchi Y., Yamaura T. (2007) Development of heat input estimation technique for simulation of shell forming by line-heating. Computer Modeling in Engineering & Sciences, 20(1): 43-53.

[101] Osawa N., Hashimoto K., Sawamura J., Tanaka H. (2008) GA-based heat input estimation technique for simulation of shell forming by line-heating. Proc. 18th International Offshore and Polar Engineering Conference, 4: 285-290

[102] Murakawa H., Ma N., Huang H. (2015) Iterative substructure method employing concept of inherent strain for large-scale welding problems, Welding in the World, 59(1): 53-63.

[103] Ma N. (2015) Implicit/Explicit FEM and CPU/GPU parallel computations for materials forming, welding mechanics and structure strength, 6th Int. Conf. on Welding Science and Engineering, Beijing

[104] Gadallah R., Murakawa H. (2014) Validation of the contour method considering the in-plane displacements at the cut surface. Transactions of JWRI, 43(2): 53-63.

[105] Ueda Y., Murakawa H., Ma N. (2012) Welding deformation and residual stress prevention, Butterworth-Heinemann, Elsevier.

[106] Kaviany M. (2002) Principles of heat transfer. John Wiley & Sons, 269-271

[107] Murakawa H., et al. (2015) Engineering tool for rough estimation of fatigue life based on simulation of welding residual stress - Application to weld joint made of low transformation temperature welding materials, 68th Annual Assembly of IIW, Doc.X-1817-15

Publications related to the thesis

Journal paper

[1] Hui Huang, Hisashi Serizawa, Jiangchao Wang, Hidekazu Murakawa, Development of Thermal Elastic-plastic FEM for Line Heating with Remeshing Technique, Quarterly Journal of the Japan Welding Society, Vol. 31 (2013) No. 4, 134s-137s

[2] Ninshu Ma, Liqun Li, Hui Huang, Shuai Chang, Hidekazu Murakawa, Residual Stresses in Laser-Arc Hybrid Welded Butt-joint with Different Energy Ratios, Journal of Materials Processing Technology, 2015, 220: 36-45

[3] Hidekazu Murakawa, Ninshu Ma, Hui Huang, Iterative substructure method employing concept of inherent strain for large scale welding problems, Welding in the world, 01/2015, 59(1): 53-63

[4] Ninshu Ma, Hui Huang, Hidekazu Murakawa. Effect of jig constraint position and pitch on welding deformation. Journal of Materials Processing Technology, 2015, 221: 154-162

[5] Hui Huang, Hidekazu Murakawa, Dynamic Mesh Refining and Iterative Substructure Method for Fillet Welding Thermo-Mechanical Analysis, Computer Modeling in Engineering and Sciences 09/2015; 106(3):187-201

[6] Hui Huang, Ninshu Ma, Tadafumi Hashimoto, Hidekazu Murakawa, Welding deformation and residual stresses in arc welded lap joints by modified iterative analysis, Science and Technology of Welding & Joining 10/2015, 20(7):571-577.

[7] Hui Huang, Jiandong Wang, Liqun Li, Ninshu Ma, Prediction of laser welding induced deformation in thin sheets by efficient numerical modeling, Journal of Materials Processing Technology 01/2016; 227:117-128.

Conference papers

[1] Hui Huang, Hidekazu Murakawa, An Efficient Remeshing Method for Simulation of Line Heating on Ship Plates, TEAM 2013, Sep. 9-12, 2013, Keelung, Taiwan

[2] Hui Huang, Hidekazu Murakawa, Efficient computation schemes for large scale thermal analysis in welding, The 5th International Conference on Welding Science and Engineering (WSE 2013), 3-5 October, Weihai, China

[3] Hui Huang, Hidekazu Murakawa, Development of Dynamic Mesh Refining Method for Large Scale Thermal and Mechanical Analysis in Welding and Line Heating, Transactions of JWRI 42(1), 63-70, 2013-06

[4] Hui Huang, Hidekazu Murakawa, Dynamic Mesh Refining Method for Welding Simulation of Large Scale Structures, Proceedings of the 1st International Joint Symposium on Joining and Welding,(2013),499-503

[5] Hui Huang, Ninshu Ma, Shijian Yuan, Hidekazu Murakawa, Analysis of Welding Deformation and Residual Stress in Automotive Engine Cradle by i-ISM and DMRM, Preprints of Japan Welding Society, 2014 Spring meeting, Tokyo, Vol. 94 (2014.04.22-2014.04.24), 206-207

[6] Hui Huang, Ninshu Ma, Hidekazu Murakawa (2014, August 7). Fast Prediction of Welding Distortion Using ISM and i-ISM with Experimental Validation. International Society of Offshore and Polar Engineers, (The Twenty-fourth International Ocean and Polar Engineering Conference, 15-20 June, Busan, Korea), Vol. 4, pp. 55-60

[7] Hui Huang, Ninshu Ma, Hidekazu Murakawa, Effect of Jig Position and Pitch on Welding deformation, Preprints of Japan Welding Society, 2014 Autumn meeting, Toyama, vol.95(2014.09.10-2014.09.12), 372-373

[8] Liqun Li, Ninshu Ma, Hui Huang, Shuai Chang, Hidekazu Murakawa, Deformation and Residual Stress Comparison between Mismatch and Normal Butt-Joints with Laser-Arc Hybrid Welding, Visual-JW 2014, Nov 26-28, Osaka, pp. 107-108

[9] Hui Huang, Ninshu Ma, Seiichiro Tsutsumi, Hidekazu Murakawa, Comparison of Welding Deformation and Residual Stresses at Jig Constraint Condition and Non-Constraint Condition , Visual-JW 2014, Nov 26-28, Osaka, pp. 127-128

[10] Tadafumi Hashimoto, Ninshu Ma, Hui Huang, Hidekazu Murakawa, Experimental Measurement and Numerical Computation of Residual Stresses in Lap Welded Joints, Visual-JW 2014, Nov 26-28, Osaka, pp. 158-159

[11] Hui Huang, Hidekazu Murakawa, Influence of Preparation Procedures on Residual Stresses in Welded Joint Specimen for Toughness Test, The Twenty-fifth International Ocean and Polar Engineering Conference, 20-26 June, Kona, Hawaii, USA; 06/2015, Vol.4, 148-153

[12] Hui Huang, Ninshu Ma, Xianqin Yin, Masatoshi Murayama, Quantitative study on welding distortion reduction by temporary tacking on base plate, Preprints of Japan Welding Society, 2015 Autumn meeting, Hokkaido, vol.97(2015.09.02-2015.09.04), 412-413

[13] Hui Huang, Jiandong Wang, Liqun Li, Ninshu Ma, Hidekazu Murakawa, A hybrid iterative substructure and multi-level refining method for laser welding thermo-mechanical analysis, The 6th International Conference on Welding Science and Engineering (WSE 2015), Sep. 20-23, Beijing, China

[14] T. Miyazaki, H. Huang, S. Tsutsumi, H. Murakawa, J.D. Wang, L.Q. Li, N. Ma, Measurement of welding residual stress in thin and thick plate using Contour method, The 6th International Conference on Welding Science and Engineering (WSE 2015), Sep. 20-23, Beijing, China